Elucidating Mechanisms of Immune Suppression in Mouse and Human Pancreatic Cancer

by

Samantha Blake Kemp

A dissertation submitted in partial fulfillment
of the requirements for the degree of
Doctor of Philosophy
(Molecular and Cellular Pathology)
in the University of Michigan
2021

Doctoral Committee:

Professor Celina G. Kleer, Co-Chair
Professor Marina Pasca di Magliano, Co-Chair
Professor Howard C. Crawford
Assistant Professor Timothy L. Frankel
Associate Professor Sriram Venneti

Samantha Blake Kemp

sbsaylor@umich.edu

ORCID iD: 0000-0002-1505-4015

Dedication

To Elaine H. Glahn. This work is done in your memory.

Acknowledgements

I owe a great deal of thanks to many individuals who have helped me reach this milestone. I first thank my mentors, Dr. Howard Crawford and Dr. Marina Pasca di Magliano, who have been instrumental in my growth as both a scientist and an individual. Marina, it is with your help that I have learned how to think big and ask important questions. I have also learned the importance of work-life balance from you and aim to develop that skill moving forward. Howard, you have pushed me to think critically and deeply about what my work means and why it is important. You have also taught me the importance of taking breaks and coming back with a fresh perspective. You have both taught me to push myself and seek a career that I never thought I was capable of. Deciding to attend the University of Michigan under both of your guidance was one of the best decisions I could have made.

I next thank my committee members, Dr. Timothy Frankel, Dr. Celina Kleer, and Dr. Sriram Venneti who helped guide my work over the years. Your outside perspective and expertise made me think about data and questions from a different angle and pushed my work forward.

I would not be where I am today without the support of the lab members from both the Crawford and Pasca di Magliano lab. From the Crawford lab I thank past lab members Dr. Mackenzie Goodwin, Dr. Ethan Abel, and Dr. Kenneth Takeuchi who trained me in my early days in the lab. Thank you to current lab members, Dr. Hui-Ju Wen, Dr. Simone Benitz, Daniel Salas-Escabillas, Amanda Pacheco, and Daniel Long who have given me

critical feedback on my work and have provided help along the way. I owe special thanks to two recently graduated members of the Crawford lab. To Dr. Jeanine Ruggeri and Dr. Meggie Hoffman thank you both for teaching me the basics when I first started in the lab and for being wonderful friends. Meggie, working closely with you was a highlight of my PhD and I look forward for us to continue to work together.

From the Pasca di Magliano lab I thank past lab members, Dr. Paloma Garcia, and Dr. Heather Schofield for helping me feel welcome and comfortable when I first joined the lab. I thank current lab members, Dr. Yaqing Zhang, Dr. Joyce Thompson, Dr. Wei Yan, Rosa Menjivar, Ashley Velez-Delgado and Kristee Brown for their help in experiments over the years in the lab. To Veerin Sirihorachai and Katelyn Donahue thank you for all of your bioinformatics help. Veerin, your cat pictures really kept me going some days. To Fatima Lima, thanks for all of your help. I am so honored to have had the opportunity to mentor you. To Carlos Espinoza, thank you for helping me with every mouse experiment I performed and keeping it fun while we worked. To Dr. Zeribe Nwosu, thank you for your help and critical analysis of my work. To Dr. Eileen Carpenter thank you for always being happy to guide me and for being a friend I can count on. And finally, thank you to Dr. Nina Steele, I would not have been able to make it through graduate school without you. I am so lucky to have met you. You have helped me grow as a scientist and have pushed me to realize my potential. You are my best friend, and I am so excited for both of our futures.

I owe a very large thank you to the entire pancreatic cancer group, PanTERA, at the University of Michigan. Thank you to every member who attended my talks and gave feedback on my work. To Dr. Filip Bednar, thank you for always taking the time to listen and help me with my work. Thank you to Dr. Costas Lyssiotis for your excitement towards

my projects and your insightful feedback. From the Lyssiotis lab I thank past lab members, Dr. Christopher Halbrook and Dr. Barbara Nelson for always being happy to help.

My work has only been possible because of great collaborations. I thank Dr. Lonnie Shea and his lab members, Dr. Grace Bushnell. Dr. Aaron Morris, and Dr. Sophia Orbach for their support and guidance on our scaffold project. I thank Dr. Arvind Rao and Stephanie The for bioinformatics support along the way. These collaborations pushed me outside of my comfort zone and allowed me to learn new techniques that will be beneficial as I continue my career.

I would like to thank my PhD department, Molecular and Cellular Pathology (MCP). I owe thanks to our program director Dr. Zaneta Nikolovska-Coleska, for her support and guidance. I would also like to thank our program administrator, Laura Labut, for always being available to help and answer any questions I had. The support from MCP made my transitions throughout graduate school seamless.

I owe a very special thanks to my undergraduate mentor, Dr. Tracy Deem. Without your support I would not be here today. It was your excitement for science and your willingness to teach me when I knew nothing that inspired me to pursue a scientific career. To my best friends since middle school, Jessica Isleib and Tabatha Chandler. I treasure the memories we were able to create while I was in graduate school. Our trips to visit each other kept me going even when things were very tough. Being able to see you both was always a reminder to take breaks and enjoy life.

I owe sincere gratitude to my family. Without the constant love and support from you all I would not be here where I am. To my aunt and uncle, Michael and Rebeca Glahn, thank you for your encouragement as I grew up and for being so supportive of my

accomplishments. Thank you to my wonderful younger brother, Hunter, I am so lucky to have someone as caring as you in my life. You always checked in with me and asked how everything was going. Listening to voicemails you would leave was always a highlight of my week. To my grandfather, I have learned how to always be kind. You have supported me since I was a child, and that support has only grown. I can always come to you with any problem. As I moved away from home, I realized how important and unwavering your support is. And most importantly, I thank my mom. I learned hard work and dedication from you. You raised me to always think for myself. Without us realizing it, you prepared me for a career in science where I have to be able to think outside the box. You have supported me in every way imaginable. I would call you if I was happy or if I was in tears over something and you always prioritized me no matter what else you had going on. You are my best friend, and I cannot express how thankful I am that you are my mother.

Finally, thank you to my husband, Parker. I am not sure how you even dealt me with me some days. You were always there for me during the highs and the lows of graduate school. We have grown together so much over the years and we have only grown closer. Thank you for dealing with my craziness and for being my unwavering support system in life. I know together, along with our pets Cali and Sake, we can accomplish anything. You mean everything to me, and I am excited for our future.

Table of Contents

Dedication ii

Acknowledgements iii

List of Figures x

Abstract xiv

Chapter 1 Introduction 1

Pancreatic cancer overview 1

PDA tumor microenvironment 3

Myeloid-epithelial crosstalk promotes immune suppression 11

Myeloid cells establish the pre-metastatic niche and promote metastatic disease 15

Macrophages drive resistance to chemotherapy 17

Myeloid cell compensatory responses 18

Myeloid single cell transcriptomics 19

Summary and dissertation overview 21

Chapter 2 Multi-modal Mapping of the Tumor and Peripheral Blood Immune Landscape in Human Pancreatic Cancer 24

Abstract 24

Introduction 25

Results 27

Discussion 42

Acknowledgments 44

Author contributions 45

Methods 46

Figures 57

Chapter 3 Apolipoprotein E Promotes Immune Suppression Through NF-κB Mediated CXCL1 Production in Pancreatic Cancer 82

Abstract 82

Introduction 83

Results 84

Discussion 94

Materials and Methods 97

Author contributions 106

Acknowledgments 107

Figures 109

Chapter 4 Pancreatic Cancer is Marked by Complement-high Tumor Associated Macrophages in Primary and Metastatic Tumors and Blood Monocytes 124

Abstract 124

Introduction 125

Results 127

Discussion 137

Materials and Methods 140

Author Contributions 148

Acknowledgments 148

Figures 150

Chapter 5 Discussion and Future Directions 168

Multi-modal Mapping of the Tumor and Peripheral Blood Immune Landscape in Human Pancreatic Cancer 168

Apolipoprotein E promotes immune suppression through NF-kB mediated CXCL1 production in pancreatic cancer 171

Pancreatic cancer is marked by complement-high tumor associated macrophages in primary and metastatic tumors and blood monocytes 174

Summary 177

Figures 178

Bibliography 183

List of Figures

Figure 2.1 CyTOF and multiplex fluorescent immunohistochemistry (mfIHC) mapping can be readily performed on patient tumor samples. 58

Figure 2.2 CyTOF and multiplex fluorescent immunohistochemistry (mfIHC) mapping reveals heterogeneous immune infiltration in human pancreatic cancer. 60

Figure 2.3 Single cell RNA sequencing reveals heterogenous immune infiltration in PDA tissue. 62

Figure 2.4 Single cell RNA sequencing reveals heterogenous expression of immune checkpoints in PDA tissue. 64

Figure 2.5 Single Cell RNA Sequencing of PDA PBMCs reveals heterogeneous cellular composition and expression of immune checkpoints. 66

Figure 2.6 Single cell RNA sequencing reveals exhausted $CD8^+$ T cell phenotype in PDA patients is defined by the immune checkpoint *TIGIT*. 67

Figure 2.7 Single cell RNA sequencing reveals 3 $CD8^+$ T cell populations: effector, exhausted, and memory $CD8^+$ T cells. 68

Figure 2.8 Single cell RNA sequencing of pancreatic tissues reveals *TIGIT* is differentially expressed in NK cells from PDA patients and is a defining marker of Tregs. 70

Figure 2.9 Single cell RNA sequencing reveals distinct myeloid and dendritic cell subsets. 72

Figure 2.10 Single cell RNA sequencing of myeloid subsets in human pancreatic cancer. 74
Figure 2.11 Predicted ligand receptor mapping in PDA patients demonstrate myeloid and non-immune cell types as sources of immune checkpoint ligands. 76
Figure 2.12 CyTOF and immunofluorescence protein validation of immune checkpoint expression in human pancreatic tissues and PBMCs. 78
Figure 2.13 Immunofluorescence of immune checkpoints in pancreatic tumors. 79
Figure 2.14 CyTOF analysis of PBMCs from healthy, chronic pancreatitis, and PDA patients. 81
Figure 3.1 Systemic *APOE* levels are elevated in PDA and correlate to patient survival. 110
Figure 3.2 *APOE* is highly expressed in the stroma of human PDA tumors. 111
Figure 3.3 APOE is highly expressed by tumor-associated macrophages. 112
Figure 3.4 APOE expression is lost when oncogenic *Kras* is extinguished. 113
Figure 3.5 Loss of APOE results in reduced tumor burden and fibrosis. 114
Figure 3.6 Histological changes in APOE deficient mice. 115
Figure 3.7 Mice deficient in APOE have fewer monocytic-MDSCs and increased $CD8^+$ T cell infiltration. 116
Figure 3.8 Loss of APOE alters macrophage polarization. 117
Figure 3.9 APOE regulates *Cxcl1* expression in tumor cells and fibroblasts. 119
Figure 3.10 Cxcl1 is highly expressed in mouse PDA tumors. 120
Figure 3.11 APOE upregulates NF-kB signaling. 121
Figure 3.12 APOE regulates tumor cell *Cxcl1* production via NF-kB signaling. 123

Figure 4.1 Immune characterization in liver, blood, and biomaterial scaffolds in tumor-bearing mice. 150
Figure 4.2 Biomaterial scaffolds harbor an immune-dense microenvironment in response to an orthotopic model of PDA. 151
Figure 4.3 Identification of a pancreatic cancer-specific gene signature. 152
Figure 4.4 Heterogenous immune signature in tumor-bearing mice. 153
Figure 4.5 Identification of two distinct macrophage subsets in scaffold infiltrate. 154
Figure 4.6 Single cell RNA sequencing analysis on scaffold associated macrophages. 155
Figure 4.7 Macrophages in mouse pancreatic cancer tumors overexpress *TREM2* and complement genes. 157
Figure 4.8 Single cell RNA sequencing analysis on mouse PDA macrophages. 158
Figure 4.9 Cq-TAMs and Chil-TAMs are elevated in the iKras* p53* model of pancreatic cancer. 160
Figure 4.10 Immune infiltration in iKras* and iKras* p53* mice. 161
Figure 4.11 Macrophages in human pancreatic cancer tumors overexpress *TREM2* and complement genes. 162
Figure 4.12 TAM populations are heterogenous in human PDA tumors. 163
Figure 4.13 Macrophages in human liver metastases express high levels of *TREM2* and complement genes and are distinct from primary tumor macrophages. 164
Figure 4.14 Single cell RNA sequencing of human liver metastases. 165
Figure 4.15 Complement genes mark one population of circulating monocytes in PDA patients. 166

Figure 4.16 Complement-high myeloid cells are elevated in the blood of pancreatic cancer patients. 167
Figure 5.1 Depletion of TIGIT did not alter tumor growth in an orthotopic mouse model of PDA. 178
Figure 5.2 Immunotherapy approaches in APOE deficient mice. 179
Figure 5.3 LDLR knockdown results in reduced p65 nuclear translocation. 180
Figure 5.4 Bone marrow-derived TAMs upregulate complement components and *Trem2* compared to M0 macrophages. 181
Figure 5.5 C1Q levels in human PDA serum. 182

Abstract

Pancreatic ductal adenocarcinoma (PDA) is one of the most lethal human malignancies. Currently, PDA has a dismal 5-year survival rate of 10% and is projected to become the second leading cause of cancer related deaths by 2030. PDA is overwhelming resistant to chemotherapy, radiotherapy, and immunotherapy appraoches. The only cure is surgical resection that only 20% of patients are eligible to receive. Unfortunately, 80% of patients who undergo surgery ultimately relapse with metastatic disease. It is critical to understand the biology underlying PDA for progress to be made. PDA tumors are characterized by a robust fibroinflammatory stroma that constitutes the bulk of the tumor volume. This rich tumor microenvironment (TME) is comprised of vasculature, nerves, extracellular matrix (ECM) components, fibroblasts and immune cells. The immune infiltration in PDA is immunosuppressive in nature. While immune checkpoint blockade has proven beneficial in other cancers, that benefit has not extended to PDA, due to this robust immune suppression. This dissertation will focus on mechanisms for immune suppression in both mouse and human PDA.

First, I discuss T cell mediated mechanisms for immune suppression in human PDA. We used a multimodal approach of multiplex immunohistochemistry, mass cytometry, and single cell RNA sequencing to map the immune landscape in human PDA. With this approach we provided further evidence that the T cell infiltration and further the expression of immune checkpoints in PDA is heterogenous. We discovered the previously underappreciated immune checkpoint TIGIT is elevated in human PDA tumors and

correlated with exhausted T cells compared to effector T cells. This work highlighted the importance of evaluating TIGIT as a potential therapeutic target and presented the importance of precision medicine when considering immune therapy.

Secondly, this dissertation focuses on myeloid-mediated mechanisms of immune suppression. This dissertation has two chapters on using mouse and human models to elucidate the role of myeloid cells in PDA immune suppression. I first discuss the role of Apolipoprotein E (ApoE) in mediating immune suppression via NF-κB signaling. Using our human single cell RNA sequencing dataset, we show ApoE is expressed highly in macrophages and serum levels stratify survival. Mechanistically, loss of ApoE results in smaller tumors and increased T cell infiltration. We determined our T cell phenotype was mediated by CXCL1 secretion via NF-κB signaling. We next evaluated myeloid cells systemically in PDA. We performed single cell RNA sequencing on biomaterial scaffolds, that serve as a synthetic metastatic niche, mouse and human primary tumors, human liver metastases and human peripheral blood to obtain a comprehensive evaluation of the systemic immune system changes in response to a primary PDA tumor. In this work, we discovered a population of monocytes/macrophages that highly expressed complement genes (*C1QA*, *C1QB*) that is elevated in PDA.

Taken together, this dissertation uses both mouse and human systems to map the immune landscape in PDA. We have identified novel proteins of interest in mediating immune suppression. Further work is necessary to evaluate functional implications as well as translational potential.

Chapter 1 Introduction[1,2]

Pancreatic cancer overview

Pancreatic ductal adenocarcinoma (PDA) is one of the most lethal human malignancies with a five-year survival rate of only 10% (Siegel et al., 2020). PDA is projected to become the second-leading cause of cancer related deaths by 2030 (Rahib et al., 2014). This poor prognosis is due in part to the majority of patients presenting with metastatic disease and overwhelming resistance to chemotherapy and radiotherapy approaches. The only potential cure for PDA is surgical resection, for which only 20% of patients are eligible, and ultimately 80% of these patients will relapse with metastatic disease (Kleeff et al., 2016). Current frontline therapies are the chemotherapy regimens FOLFIRINOX or gemcitabine/nab-paclitaxel, which modestly extend survival (Conroy et al., 2011; Conroy et al., 2018; Von Hoff et al., 2013). The main genetic drivers of PDA are mutations in *KRAS* (Almoguera et al., 1988; Hata et al., 2018), along with loss of tumor suppressors (*TP53*, *SMAD4*, INK4*A*) (Hezel et al., 2006; Maitra and Hruban, 2008). Both acinar cells and ductal cells within the healthy pancreas can give rise to PDA, however acinar cells appear to have a higher propensity for transformation (Kopp et al., 2012).

---

[1] Sections of Chapter 1 have been submitted for a review article at *Cellular and Molecular Gastroenterology and Hepatology*. Article is entitled, "Myeloid cell mediated immune suppression in pancreatic cancer" (2021).

[2] Author list: Samantha B. Kemp, Marina Pasca di Magliano*, Howard C. Crawford*
*Corresponding authors

Acinar cells go through a plastic transdifferentiation process called acinar to ductal metaplasia (ADM), which gives rise to pancreatic intraepithelial lesions (PanINs), and ultimately cancer formation (Storz, 2017). These stages of progression of human PDA have been recapitulated in genetically engineered mouse models that target oncogenic Kras expression to the pancreas, combined with inactivation of tumor suppressors (Aguirre et al., 2003; Hingorani et al., 2003; Hingorani et al., 2005).

PDA is characterized by a dense fibroinflammatory stroma. This robust stroma consists of fibroblasts, vasculature, nerves, extra-cellular matrix (ECM) components, and infiltrating immune cells (Chu et al., 2007). The immune cells within the tumor microenvironment (TME) are immunosuppressive in nature (Clark et al., 2007). Within the TME, there is a large infiltration of myeloid cells that prevent T cell responses (Clark et al., 2007). PDA patients with greater T cell infiltration (Balachandran et al., 2017) and fewer myeloid cells (Sanford et al., 2013) have more favorable survival outcomes. As such, there is an inverse correlation between myeloid cells and T cells in PDA (Clark et al., 2007; Steele et al., 2020).

Immune therapy has revolutionized cancer treatment, however, that benefit has so far not extended to PDA (Brahmer et al., 2012; Royal et al., 2010). Immune checkpoint therapy acts through re-activating T cell effector functions through blockade of the immune checkpoints programmed cell death 1 (PD-1) or cytotoxic T lymphocyte antigen 4 (CTLA-4) that results in reduced tumor burden in other solid tumors (Waldman et al., 2020). However, immune therapy is not effective in PDA, in part due to this robust immune suppression. It is imperative we understand the biology underlying pancreatic cancer immune suppression.

PDA tumor microenvironment

The PDA TME contains a robust infiltration of fibroblasts and various immune cell populations. There is a complex cellular crosstalk that acts to both restrain and promote carcinogenesis depending on the context. The primary cell types within the TME that are explored in this thesis include fibroblasts, T cells, and myeloid cells.

Fibroblasts

Fibroblasts are a mesenchymal cell type that have distinct functions in both normal physiology and carcinogenesis. In normal physiology fibroblasts are quiescent until activated to perform wound healing and tissue repair through the deposition of extracellular matrix components (Kalluri, 2016). When fibroblasts become activated they express high levels of alpha-smooth muscle actin (α-SMA) and are considered myofibroblasts (Hinz et al., 2001). Fibroblasts associated with the tumor are termed cancer-associated fibroblasts (CAFs). While α-SMA is highly expressed by fibroblasts it does not mark all fibroblasts. CAFs are heterogenous and have both tumor promoting and tumor restricting functions (Garcia et al., 2020).

The main subsets of CAFs in the PDA TME include inflammatory CAFs (iCAFs), myofibroblastic CAFs (myCAFs), and antigen presenting CAFs (apCAFs) (Elyada et al., 2019; Ohlund et al., 2017). myCAFs often reside in close proximity to tumor cells and are defined by high expression of α-SMA (Ohlund et al., 2017). In contrast, iCAFs are found further from tumor cells and secrete inflammatory mediators, such as interlekin-6 (IL-6) to promote carcinogenesis (Ohlund et al., 2017). myCAFs and iCAFs utilize different signaling pathways (Biffi et al., 2019). Formation of myCAFs is primarily through

transforming growth factor beta (TGF-β) signaling, while iCAF formation utilizes the Janus-kinase/signal transducer and activator of transcription (JAK/STAT) pathway. Inhibition of JAK in a mouse model of PDA resulted in a shift from iCAF to myCAF phenotype, highlighting the plasticity of CAFs and provided evidence for selective targeting of CAF subsets (Biffi et al., 2019). While CAFs have been shown to promote carcinogenesis in some studies, there is also existing literature providing evidence that CAFs restrain tumor growth (Lee et al., 2014; Mathew et al., 2014; Ozdemir et al., 2014; Rhim et al., 2014). Taken together these data suggest CAFs play a complex, and context dependent role in the PDA TME.

CAFs also have immunosuppressive abilities (Feig et al., 2013; Garcia et al., 2020; Kraman et al., 2010). Fibroblast activated protein (FAP) is broadly expressed on fibroblasts and FAP^+ CAFs mediate immune suppression through secretion of the chemokine CXCL12 (Feig et al., 2013). Targeting the CXCL12-CXCR4 axis resulted in increased T cell infiltration, allowing the tumor to be sensitized to immune therapy approaches (Feig et al., 2013). Further, inhibition of CXCR4 in PDA patients increased tumoral T cell infiltration (Biasci et al., 2020).

T cells

T cells possess anti-tumor abilities, however there is a paucity of T cells in PDA. Patients who do have a high infiltration of T cells though, have more favorable survival outcomes (Carstens et al., 2017). T cells are part of the adaptive immune response and have multiple subsets including $CD8^+$ and $CD4^+$ T cells. $CD4^+$ T cells can be further divided into Th1, Th2, and Th17 subsets (Zhou et al., 2020). Another subset of $CD4^+$ T

cells are regulatory T cells (Tregs) that are defined by expression of CD25 and forkhead box P3 (FOXP3). $CD4^+$ T cells are critical for the formation of PDA tumorigenesis by suppressing $CD8^+$ T cells (Zhang et al., 2014). Further, Tregs are abundant in PDA and are known to have immunosuppressive abilities (Clark et al., 2007). However, ablation of Tregs in a mouse model of PDA did not relieve immune suppression as hypothesized (Zhang et al., 2020). Rather, Treg depletion accelerated carcinogenesis through a compensatory infiltration of immunosuppressive myeloid cells, highlighting the complex cellular crosstalk in the PDA TME (Zhang et al., 2020).

$CD8^+$ T cells can be further divided into naïve, memory, effector and exhausted T cells (van der Leun et al., 2020). Effector $CD8^+$ T cells have cytotoxic functions that produce perforin, granzymes, and interferon gamma (IFN-γ) to control infection and further, have anti-tumor abilities (Sarkar et al., 2008). However, PDA tumors have a high infiltration of exhausted $CD8^+$ T cells rather than effector $CD8^+$ T cells (Steele et al., 2020). Exhausted $CD8^+$ T cells represents a state of dysfunction (van der Leun et al., 2020). In both viral infection as was as cancer, exhausted $CD8^+$ T cells upregulate the immune checkpoints, programmed cell death protein 1 (PD-1), lymphocyte-activating 3 (LAG3), T cell immunoglobulin and mucin domain-containing protein 3 (TIM-3), and T cell immunoreceptor with Ig and ITIM domains (TIGIT) (Steele et al., 2020; Wherry et al., 2007). Reactivation of effector T cell function can be attained through immune checkpoint blockade, however this has not shown success in PDA as it is an immunologically “cold” tumor (Saka et al., 2020). Further work is required to understand T cell biology in PDA that contributes to immune suppression.

Myeloid cells

PDA with a high density of myeloid cells is correlated with worse overall survival (Ino et al., 2013; Tsujikawa et al., 2017). In normal physiology, myeloid cells develop from hematopoietic stem cells (HSCs) in the bone marrow in a process called myelopoiesis (Messmer et al., 2015). Myeloid cells refer to all $CD45^+$ $CD11b^+$ cells, but further differentiate into distinct cell subsets: macrophages, granulocytes, mast cells, and dendritic cells (DCs). Macrophages within the tumor are referred to as tumor-associated macrophages (TAMs) and have distinct features compared to normal macrophages that will be discussed in detail below. Granulocytes can be further divided into eosinophils, basophils and neutrophils. Within the TME, neutrophils and monocytes are often in an immature state referred to as a myeloid-derived suppressor cell (MDSC).

Within the TME, macrophages are the most abundant immune cell population (Noy and Pollard, 2014). Macrophages are an innate immune cell type and originate from either infiltrating monocytes or embryonic progenitors (Wynn et al., 2013). Macrophages perform multiple physiological functions, including phagocytosis to eliminate debris, antigen-presentation, and cytokine secretion to recruit other immune cells to the site of injury. Macrophages are defined by expression of $CD11b^+$ $CD68^+$ $EMR1^+$ in humans and $CD11b^+$ $CD68^+$ $F4/80^+$ in mice. Macrophages are plastic cells that exist on a spectrum of differentiation states. Past definitions have classified macrophages into two main subtypes on each extreme of the spectrum. M1 or classically activated macrophages perform anti-tumor functions and can be induced through IFN-γ and toll-like receptor (TLR) stimuli (Qian and Pollard, 2010). M1 macrophages are characterized by high expression of interleukin 12 (IL-12), tumor necrosis factor (TNF), and inducible nitric oxide

synthase (iNOS). M2 or alternatively activated macrophages perform pro-tumor functions (Mantovani et al., 2002) and can be induced through the cytokines IL-4 and IL-13 (Gordon, 2003). M2 macrophages lose their antigen presentation abilities and act to instead suppress the immune response, through a variety of mechanisms, as will be discussed.

There is a negative correlation between macrophage infiltration and patient survival in PDA (Ino et al., 2013; Kurahara et al., 2011), providing further evidence for the pro-tumor function of macrophages in cancer. The M1/M2 classification is an oversimplification that is helpful for broad description but does not accurately describe the *in vivo* heterogeneity of TAMs. TAMs within the tumor are derived from either infiltrating monocytes or embryonically derived, tissue-resident macrophages (Zhu et al., 2017). Further, the heterogeneity of TAM origin has functional implications, where monocyte derived TAMs have increased antigen-presentation abilities, while embryonically derived TAMs shape the fibrotic response (Zhu et al., 2017). Within the TME, TAMs conform to neither the M1 nor the M2 phenotype, but rather have traits of both polarization states (Qian and Pollard, 2010).

A large body of work in PDA has been performed on targeting TAMs specifically. Due to the plasticity of macrophages, TAM targeted therapy aims to reprogram them to their anti-tumor functions. The colony-stimulating factor 1/colony-stimulating factor 1 receptor (CSF1/CSF1R) axis recruits and polarizes immunosuppressive TAMs. CSF1R is the major lineage regulator for all macrophage subsets (Qian and Pollard, 2010). PDA tumors are infiltrated by $CSF1R^+$ macrophages (Candido et al., 2018; Zhu et al., 2014). Inhibition of CSF1R resulted in reduced tumor burden and an increase in T cell infiltration,

providing evidence that targeting TAMs relieves immune suppression in the TME (Candido et al., 2018; Mitchem et al., 2013). Further, CSF1R inhibition sensitizes PDA to either PD-1 or CTLA-4 antagonists (Zhu et al., 2014), suggesting that while single agent immunotherapy is not sufficient to reduce tumor burden, immune checkpoint blockade in combination with TAM modulating therapies can effectively reverse immune suppression.

The CCL2/CCR2 chemokine axis is critical for the genesis of TAMs. CCL2 produced by tumor cells recruits $CCR2^+$ monocytes from the bone marrow to the circulation that then differentiate into TAMs after entering the tumor tissue (Shi and Pamer, 2011). PDA patients with high levels of circulating monocytes have worse overall survival rates (Sanford et al., 2013). Tumor cells secrete the chemokine CCL2, which recruits $CCR2^+$ monocytes. Monocytes in circulation do not possess the same immunosuppressive abilities as TAMs, suggesting the cellular crosstalk in the TME is critical for this function (Sanford et al., 2013). CCR2 blockade in mice resulted in retention of $CCR2^+$ monocytes in the bone marrow, impairing tumor growth (Sanford et al., 2013). CCR2 blockade with gemcitabine further impaired tumor growth (Sanford et al., 2013). Similarly, in a PDA clinical trial, patients with borderline resectable and locally advanced disease were treated with a combination of FOLFIRINOX and CCR2 antagonist (Nywening et al., 2016). After treatment, patients had reduced circulating $CCR2^+$ monocytes and subsequently fewer TAMs in the tumor, as well as increased $CD8^+$ T cells (Nywening et al., 2016).

Taken together, these studies highlight the tumor promoting role of TAMs in the PDA TME. Macrophage targeted therapy is promising as it synergizes with frontline

chemotherapy and immunotherapy regimens to reactivate effector T cell responses and reduce tumor burden.

MDSCs are immature myeloid cells with immunosuppressive functions. MDSCs can be further classified into two main subsets, polymorphonuclear-MDSCs/granulocytic-MDSCs (PMN-MDSCs/G-MDSCs) and mononuclear-MDSCs (M-MDSCs). These subsets are phenotypically distinct. PMN-MDSCs have more resemblance to granulocytes/neutrophils, while M-MDSCs closely resemble monocytes. In mice, MDSCs are broadly defined by $CD11b^{+}$ $Gr\text{-}1^{+}$, with Ly-6C and Ly-6G used to delineate MDSC subsets (Bronte et al., 2016). To accurately define MDSCs in mice the recommended definitions are: $CD11b^{+}$ $Ly6C^{lo}$ $Ly6G^{+}$ for PMN-MDSCs and $CD11b^{+}$ $Ly6C^{hi}$ $Ly6G^{-}$ for M-MDSCs (Bronte et al., 2016). Given their phenotypic differences, human PMN-MDSCs, which closely mirror granulocytes/neutrophils are defined by $CD11b^{+}$ $CD14^{-}$ $CD15^{+}$ or $CD11b^{+}$ $CD14^{-}$ $CD66b^{+}$, while human M-MDSCs, which are more similar to monocytes are defined by $CD11b^{+}$ $CD14^{+}$ HLA-$DR^{-/lo}$ $CD15^{-}$ (Bronte et al., 2016). While PMN-MDSCs and M-MDSCs are the major MDSC subsets, there are MDSCs that share markers of both subsets and represents a progenitor state. This third MDSC subset is called early stage-MDSCs (e-MDSCs) and has yet to be functionally evaluated in PDA (Bronte et al., 2016). While MDSCs are unique from their mature myeloid counterparts, neutrophils and monocytes, controversy remains on separating PMN-MDSCs from neutrophils. Currently, there are no markers to distinguish the immature PMN-MDSCs from mature neutrophils, and the only possible method of separation is via density centrifugation (Marvel and Gabrilovich, 2015). M-MDSCs differ from monocytes as they express low HLA-DR, and differ from TAMs as they do not express F4/80 (Veglia et al.,

2018). Distinction between neutrophils and PMN-MDSCs remains challenging and distinctive markers are needed. Importantly, MDSCs need to be further defined through functionality.

MDSCs perform their immune suppressive functions through multiple mechanisms. The main method is through the depletion of the essential amino-acid, L-arginine, from the TME (Bronte and Zanovello, 2005; Gabrilovich and Nagaraj, 2009). MDSCs produce high levels of the enzyme Arginase 1 (ARG1), that metabolizes L-arginine, resulting in T cell inhibition (Rodriguez and Ochoa, 2008). When considering MDSC function, it is important to also take into account that MDSCs exist in two main subsets. PMN-MDSCs comprise the largest percentage of MDSCs found in the blood and the tumor, compared to M-MDSCs (Youn et al., 2008). Despite M-MDSCs making up a smaller portion of the tumor, they often have an increased immunosuppressive function than PMN-MDSCs (Trovato et al., 2019). PMN-MDSCs and M-MDSCs have different immunosuppressive functions. While both MDSC subsets express high amounts of ARG1, PMN-MDSCs produced high amounts of reactive oxygen species (ROS) and low nitric oxide (NO), while M-MDSCs produced high NO and low ROS (Youn et al., 2008). The immunosuppressive function of M-MDSCs is in part due to tumor cell-derived prostaglandin E2 (PGE2) activating p50, a NF-kB subunit that results in increased iNOS production (Porta et al., 2020).

Due to the immunosuppressive nature of MDSCs, there has been a significant amount of work targeting these cells within the PDA TME. Early work targeted MDSCs through administration of zoledronic acid (Melani et al., 2007) which acts to reduce MDSCs. Administration of zoledronic acid in a PDA mouse model resulted in delayed

tumor growth, enhanced survival and increased $CD8^+$ T cell infiltration (Porembka et al., 2012). CXCR2 is a receptor found on neutrophils/MDSCs and regulates the recruitment of MDSCs to the TME (Highfill et al., 2014). Inhibition of CXCR2 in a genetically engineered mouse model of pancreatic cancer resulted in extended survival, an increase in T cell infiltration, and synergy with immunotherapy (Steele et al., 2016). MDSCs are also recruited to the tumor through tumor-cell derived GM-CSF secretion. Neutralization of GM-CSF resulted in a reduction in MDSC recruitment and subsequently reduced tumor growth in PDA tumors (Bayne et al., 2012; Pylayeva-Gupta et al., 2012). Depletion of just the PMN-MDSC subset resulted in tumor cell death and increased $CD8^+$ T cell infiltration, suggesting ablation of just one MDSC subset was sufficient enough to reverse immune suppression (Stromnes et al., 2014). Though they have not been yet targeted in PDA, it will be interesting to examine the effects of depleting M-MDSCs given their enhanced immunosuppressive nature.

Myeloid-epithelial crosstalk promotes immune suppression

Myeloid cells do not act alone in this tumor promoting phenotype. The TME in PDA has a complex cellular crosstalk that promotes carcinogenesis. In this section I will explore mechanisms of cellular crosstalk specifically between myeloid cells and epithelial cells that activate signaling pathways that enhance immune suppression.

Myeloid cells play a critical role in promoting pancreatic carcinogenesis (Liou et al., 2015; Liou et al., 2013; Zhang et al., 2017b; Zhang et al., 2017c). Myeloid cell ablation, using CD11b promoter driven expression of the diphtheria toxin receptor (DTR) followed by DT treatment (Duffield et al., 2005) in a PDA mouse model driven by the inducible

expression of *Kras* (iKras) (Collins et al., 2012a) causes regression of early PanIN lesions, preceded by reduced ERK activity in the neoplasia (Zhang et al., 2017c). While *KRAS is* the main genetic driver of PDA, it is not sufficient to induce carcinogenesis without additional activation of epidermal growth factor receptor (EGFR) to amplify mitogen-activated protein kinase (MAPK) signaling in the epithelium (Ardito et al., 2012; Collins et al., 2014). Of note, myeloid cells in the neoplastic pancreas express high levels of the EGFR ligands, heparin-binding EGF-like growth factor (HB-EGF) and epiregulin (EREG), suggesting that they promote the initial stages of pancreatic carcinogenesis by stimulating epithelial EGFR. Conversely, oncogenic *Kras* expression in the epithelium also alters macrophage polarization (Zhang et al., 2017c). Extinguishing *Kras* expression in the iKras model resulted in decreased expression of Arginase 1 (*Arg1*) and the EGFR ligand, HB-EGF (*Hbegf*) in the myeloid compartment, with subsequent loss of EGFR (*Egfr*) expression in the epithelial compartment. These data suggest that KRAS/EGFR/MAPK signaling regulates myeloid cell infiltration and polarization prior to PanIN formation, which in turn promotes epithelial transformation and progression of the neoplasia.

In addition to its early role in PDA formation, EGFR also regulates immune suppression in frank carcinoma (Li et al., 2020a; Zhang et al., 2017b). Myeloid cells ablation from pre-existing tumors resulted in reduced tumor burden, providing evidence that myeloid cells drive carcinogenesis in both early and late stages of disease (Zhang et al., 2017b). Myeloid cells secrete HB-EGF, an EGFR ligand, that activates EGFR/MAPK signaling in tumor cells leading to increased PD-L1 expression (Zhang et al., 2017b). Further, ablation of EGFR in PDA tumors sensitized tumors to chemo- and

immunotherapy (Li et al., 2020a). Treatment with the EGFR inhibitor, Erlotinib, reduced tumoral myeloid cells, increased $CD8^+$ T cells, and enhanced response to immunotherapy (Li et al., 2020a). These studies suggest a role for EGFR/MAPK in promoting carcinogenesis and myeloid-mediated immune suppression.

Nuclear factor-kB (NF-κB) is a transcription factor with known diverse function in regulation of the immune system (Zhang et al., 2017a). Dysregulated NF-κB signaling can lead to inflammatory conditions such as cancer (Gilmore, 2006). Along with *KRAS*, NF-κB is constitutively active in PDA patients (Ling et al., 2012; Maier et al., 2013). NF-κB is activated through release of inhibitory κB (IκB) proteins, usually sequestered in the cytoplasm, that activate IκB kinase (IKK), resulting in active gene transcription of downstream target genes. The IKK complex is made up of two kinases, IKKα and IKKβ, and an additional subunit, NEMO/IKKγ (Israel, 2010). Inactivation of IKKβ in PDA tumors reduced infiltration of macrophages and MDSCs, and blocked carcinogenesis, extending survival (Ling et al., 2012). This initial study provided evidence that NF-kB is not only critical for PDA formation, but also mediated myeloid cell infiltration in the tumor.

In addition to *KRAS* and MAPK, NF-κB activation is critical in the early formation of PDA. Macrophages are additionally critical in the early stages of carcinogenesis. To further understand potential mechanisms behind macrophages and tumor initiation, one study co-cultured primary mouse acinar cells with macrophages and observed increased ADM formation (Liou et al., 2013). Further analysis of the macrophage conditioned media revealed that tumor necrosis factor (TNF) promotes ADM formation via NF-κB signaling, suggesting a role for NF-κB in the earliest stages of carcinogenesis (Liou et al., 2013).

NF-κB signaling additionally activates GM-CSF secretion (Schreck and Baeuerle, 1990). GM-CSF is a cytokine that functions to recruit MDSCs as described earlier (Bayne et al., 2012; Pylayeva-Gupta et al., 2012). Human PDA tumor cells treated with chemotherapy (Gemcitabine or 5-FU) had increased levels of GM-CSF (Takeuchi et al., 2015). Further, human tumor cells treated with gemcitabine have increased NF-κB activity. Monocytes cultured with chemotherapy treated tumor cells promotes differentiation into immunosuppressive MDSCs (Takeuchi et al., 2015). Taken together, these data suggest one possible mechanism for chemoresistance in PDA is active NF-κB signaling in tumor cells, which promotes an immunosuppressive myeloid phenotype, exacerbating disease.

NF-κB activates the expression of the chemokines CXCL1, CXCL2, and CXCL5, which in turn recruits $CXCR2^+$ MDSCs, resulting in T cell suppression (Burke et al., 2014; Chao et al., 2016; Ijichi et al., 2011). PDA patients have a heterogenous infiltration of T cells (Carstens et al., 2017). Recent work identified CXCL1 as one mediator for T cell heterogeneity in the PDA TME (Li et al., 2018a). Overexpression of tumor cell-derived *Cxcl1* increases myeloid infiltration, specifically the G-MDSCs, and fewer infiltrating $CD8^+$ T cells, providing further evidence on the immunosuppressive role of CXCL1 in the TME (Li et al., 2018a). Furthermore, ablation of *Cxcl1* in tumor cells resulted in fewer G-MDSCs and a subsequent increase in $CD8^+$ T cells, allowing the tumors to be sensitized to immunotherapy (Li et al., 2018a).

There is complex cellular crosstalk between tumor cells and myeloid cells that suppresses T cell infiltration and function in the TME. Multiple pathways are implicated in this immune suppressive phenotype. Work thus far targeting this tumor-myeloid

interaction is compelling as it sensitizes tumors to immunotherapy approaches, highlighting the translational implications for PDA patients.

Myeloid cells establish the pre-metastatic niche and promote metastatic disease

The majority of PDA patients present with metastatic disease and for those patients, limited therapeutic options are available. The liver is the most common site for metastatic dissemination in PDA. Pancreatic tumor cells disseminate early in carcinogenesis, prior to progression to carcinoma (Rhim et al., 2012). Despite the severity of metastatic disease, the process of metastasis is inefficient (Malanchi et al., 2011). A key barrier to tumor cell dissemination and survival in distal organs is the requirement of support from stromal cells (Nielsen et al., 2016). Inflammation is critical for progression of the primary tumor (Coussens and Werb, 2002), but is also critical for tumor cell dissemination (Rhim et al., 2012). Myeloid cells colonize these distal sites prior to the arrival of the tumor cells in principle to create a hospitable environment for tumor cell growth (Hiratsuka et al., 2002; Hiratsuka et al., 2006; Kaplan et al., 2005; Lee et al., 2019a), in a concept termed the pre-metastatic niche.

Currently, few studies have been performed evaluating the pre-metastatic niche in PDA. One study showed macrophages that are recruited to the liver secrete granulin, which in turn activates myofibroblasts creating a permissive environment for tumor cell survival (Nielsen et al., 2016). Exosomes from tumor cells were identified as another mediator that promotes formation of the liver pre-metastatic niche in PDA (Costa-Silva et al., 2015). Tumor derived exosomes are taken up by Kupffer cells, resident liver macrophages, resulting in increased fibrotic deposition in the liver and increased

macrophage accumulation (Costa-Silva et al., 2015). This stromal accumulation prepares the liver for ultimate tumor cell survival. Macrophage migration inhibitory factor (MIF) was determined to be the primary exosome cargo driving the pre-metastatic niche formation. As such, MIF ablation prevented formation of the pre-metastatic niche and subsequently reduced liver metastasis (Costa-Silva et al., 2015). Interleukin-6 / Signal transducer and activator of transcription 3/ serum amyloid A (IL-6/STAT3/SAA) signaling is another critical mechanism for the formation of the liver pre-metastatic niche (Lee et al., 2019a). Rather than tumor-cell mediated formation of the pre-metastatic niche, this study identifies hepatocytes as an additional driver of the pre-metastatic niche (Lee et al., 2019a). Genetic ablation of individual components of IL-6/STAT3/SAA signaling resulted in fewer macrophages and PMN-MDSCs (Ly-6G^{+}), preventing metastatic dissemination. The concept of the pre-metastatic niche is an important question that is relatively unexplored in PDA. Each of these studies provide a framework to explain the role myeloid cells play in pre-metastatic formation. Identifying methods to interfere with myeloid function has the potential to mitigate metastasis of this highly aggressive cancer.

In addition to their role in tumorigenesis and pre-metastatic niche preparation, myeloid cells have been implicated in migration and invasion of metastatic disease in many cancer types (Condeelis and Pollard, 2006; Pollard, 2004; Qian and Pollard, 2010). CCR2 (Sanford et al., 2013) and CXCR2 (Steele et al., 2016) inhibition have been shown to reduce metastatic dissemination in PDA through ablation of monocytes/macrophages and MDSCs, respectively. MDSC depletion in mouse PDA tumors converted the tumor from the highly invasive basal subtype to the less aggressive classical subtype and extended survival (Bailey et al., 2016; Steele et al., 2016). Further, pharmacological

depletion of macrophages with liposomal clodronate impaired angiogenesis and reduced metastasis formation in mice with PDA (Griesmann et al., 2017). Myeloid cells are thus critical for both the formation of the pre-metastatic niche and metastatic dissemination.

Macrophages drive resistance to chemotherapy

Given that immune therapy has so far not been beneficial in PDA, frontline therapy remains chemotherapy regimens, though they have marginal efficacy (Burris et al., 1997; Conroy et al., 2011; Goldstein et al., 2015; Von Hoff et al., 2013). Current standard-of-care chemotherapy regimens for PDA patients include gemcitabine/nab-paclitaxel and FOLFIRINOX. However, PDA tumors are highly chemoresistant. A broad approach of depleting all myeloid cells using CD11b-DTR mouse treated with DT resulted in tumors being sensitized to gemcitabine (Halbrook et al., 2019), suggesting myeloid cells can be targeted to revert chemoresistance. Further, dual inhibition of TAMs ($CCR2^{+}$) and MDSCs (CXCR2+) resulted in increased efficacy of FOLFIRINOX (Nywening et al., 2018).

Macrophages within the PDA TME have alternative activation and express less antigen presenting MHC II (Schreiber et al., 2011), suggesting that macrophages could be reprogrammed to perform their role as antigen presenting cells. Activation of CD40 with an agonist in combination with gemcitabine activated TAMs and resulted in reduced tumor burden in a cohort of patients (Beatty et al., 2011). Paralleling the human trials, mouse models of PDA are also resistant to single agent immune checkpoint blockade, however combined chemo- and immunotherapy approaches have shown success. Combination therapy of gemcitabine/nab-paclitaxel and αCD40 agonist, sensitized PDA

tumors to αPD-1 and αCTLA-4 immunotherapy (Winograd et al., 2015). This combined chemo- and immunotherapy approach, GAFCP (gemcitabine, nab-paclitaxel/abraxane, αCD40 agonist, αPD-1, αCTLA-4) is currently under clinical trial for patients with PDA ((NCT03214250, NCT02588443). Further, the effectiveness of the GAFCP chemo- and immunotherapy can be predicted based on the amount of CD8+ T cell infiltration, with tumors rich in CD8+ T cells correlating with increased therapeutic response (Li et al., 2018a).

Myeloid cell compensatory responses

I have highlighted a myriad of reports targeting monocytes/macrophages and MDSCs in PDA, however It has become clear that these approaches, while beneficial often result in a compensatory response of the other myeloid cell subsets. Two studies in PDA report a compensatory increase in monocyte and macrophage subsets when MDSCs are depleted (Nywening et al., 2018; Stromnes et al., 2014). To prevent compensatory myeloid infiltration, another approach is to target all myeloid cells via integrin CD11b on their surface. While antagonists for CD11b exist (Jaeschke et al., 1993; Rogers et al., 1998), they have not been well tolerated in patients due to toxicity (Dove, 2000). Rather, an alternative approach to activate CD11b rather than antagonize has shown promise in preventing inflammation (Maiguel et al., 2011). The small molecule CD11b agonist reduced inflammation in a mouse model of PDA (Panni et al., 2019). CD11b agonism reduced myeloid infiltration, increased T cell infiltration and sensitized tumors to both chemotherapy and immunotherapy (Panni et al., 2019). While the total number of myeloid cells was reduced with CD11b agonism, macrophages that remained

were reprogrammed, reducing the expression of a number of immunosuppressive genes (Arginase 1, IL-10, TGF-b) and increasing antigen-presentation abilities, leading to activation of classical-DCs (cDCs) and subsequent T cell infiltration (Panni et al., 2019). CD11b agonism is one potential avenue to avoid myeloid cell compensation when targeting a select myeloid cell subset.

Further, myeloid cells compensate for depletion of regulatory T cells (Tregs), another immunosuppressive cell type in the PDA TME (Zhang et al., 2020). In this study, depletion of Tregs did not reverse immune suppression as hypothesized, but rather accelerated tumor progression, in part due to a compensatory infiltration of immunosuppressive myeloid cells (Arginase 1, Chitinase3-like-3/YM1). This sustained immunosuppression was reduced through inhibition of the myeloid receptor CCR1, providing further indication that myeloid cells promote tumor progression and have complex and compensatory roles in the PDA TME.

Myeloid single cell transcriptomics

Recent single cell RNA sequencing efforts in PDA have revealed significant heterogeneity within myeloid cell subsets that confirm the M1/M2 designation is an oversimplification. Analysis of human PDA tumor samples compared to adjacent normal pancreas tissue identified populations of neutrophils, classical monocytes/macrophages, resident macrophages, and alternatively activated macrophages (Elyada et al., 2019). *MARCO*, *APOE*, and *SPP1*, *C1QA* emerged as novel macrophage markers that warrant further evaluation in PDA (Elyada et al., 2019). Another study identified similar myeloid populations in human PDA compared to adjacent normal pancreas tissue with similar

gene expression profiles (Steele et al., 2020). Further, myeloid cells are shown to have heterogenous expression of immune checkpoint receptors (*LGALS9*, *CD274*, *PVR*, *CSF1R*, *SRPA*, *HLA-DQA1*) (Steele et al., 2020). Putative immune checkpoint interactions were upregulated in PDA compared to adjacent normal samples, and these interactions were heterogenous across patients. Given the overwhelming lack of response to immunotherapy approaches, these data suggest the heterogeneity of immune checkpoints across patients is a contributing factor and we should consider the possibility of precision medicine in immune-modulatory appraoches.

Two studies used single cell transcriptomics analysis to evaluate the immune response during PDA progression (Hosein et al., 2019; Schlesinger et al., 2020). Consistent with previous reports, macrophages were identified as one of the major immune cells infiltrating early lesions. Through unbiased clustering, 3 macrophage populations were identified in early lesions, while only 2 macrophage populations were identified in late/tumor samples (Hosein et al., 2019). The macrophage population only found in early lesion samples had expression of *Fn1*, *Lyz1*, and *Ear1*, suggesting this population is involved in wound repair (Hosein et al., 2019). There was not an equivalent macrophage population to this one seen in the late-stage tumor samples, suggesting macrophage populations change over the course of disease progression. In a separate study, macrophages from late lesions compared to early lesion samples had an increase in the chemokines, *Cxcl1*, *Cxcl2*, and *Ccl8,* which have known roles in recruitment of MDSCs (*Cxcl1*, *Cxcl2*) and macrophages (*Ccl8*), suggesting sustained infiltration of myeloid cells as carcinogenesis progresses (Schlesinger et al., 2020). Further, these macrophages upregulated markers of alternative activation (*Mrc1*), further supporting the

concept that macrophage polarization changes in later stages of PDA. Importantly these combined efforts have revealed novel myeloid cells markers with potential functional importance in PDA.

Summary and dissertation overview

Frustratingly, PDA remains refractory to current therapies. One of the challenges in treating PDA patients is the robust immunosuppressive TME that characterizes the disease. There is an inverse correlation between myeloid cells and T cells in the PDA TME, with a large myeloid infiltration and a paucity of T cells correlating with worse survival outcomes. Shifting this balance and reprogramming the immune cells to perform anti-tumor functions has been of prime interest to the PDA field. In this dissertation I present new hypotheses and findings behind mechanisms of immune suppression.

In Chapter 2 I present a comprehensive immune mapping in human PDA. There has been a surge of single cell RNA sequencing publications in the last several years. In PDA, these single cell analyses focused primarily on fibroblasts and epithelial cells. Our work was the first in PDA to focus on the immune cells in both tumors and peripheral blood in patients compared to healthy controls (Steele et al., 2020). This work highlighted the heterogeneity of the immune infiltration in PDA, an important point to consider for precision medicine approaches. Further, these data provide rationale for why current immune therapy appraoches are not successful. Here we show that PDA patients have an increased number of exhausted $CD8^+$ T cells compared to effector T cells. And that the immune checkpoints, PD-1 and CTLA-4 are uniformly expressed across exhausted and effector $CD8^+$ T cells, while TIGIT is the sole immune checkpoint that defines exhausted $CD8^+$ T cells. Using a putative ligand receptor mapping approach, we identified

the TIGIT-PVR axis is upregulated in PDA patients, highlighting its role in disease and its targetable potential. For translational relevance we assessed $TIGIT^+$ and $PD\text{-}1^+$ $CD8^+$ T cells in patient matched blood and tumor and discovered TIGIT and not PD-1 had a positive correlation between the blood and tissue. These data revealed complex heterogeneity in PDA patients and that TIGIT is an understudied immune checkpoint with translational potential in PDA. The human PDA dataset from Chapter 2 was used to generate the hypotheses discussed in Chapters 3 and 4.

In Chapter 3 I present Apolipoprotein E (ApoE) as a novel mediator of immune suppression in PDA. ApoE has been extensively evaluated in cardiovascular and Alzheimer's disease (Mahley, 2016). There have also been contradictory reports on the role of ApoE in carcinogenesis in acute myeloid leukemia (AML) and melanoma (Deng et al., 2018; Tavazoie et al., 2018). Using the human PDA dataset in Chapter 2 we identified ApoE as being upregulated in the stroma of PDA patients. ApoE is expressed specifically in macrophages and iCAFs in the TME. Based on the literature of macrophages and iCAFs in PDA we hypothesized that ApoE promoted immune suppression. Patients with high plasma levels of ApoE had worse survival outcomes, providing further evidence in its role in accelerating carcinogenesis. In this work, we used a syngeneic, orthotopic mouse model of PDA and showed ApoE regulates immune suppression. Mice deficient in ApoE had smaller tumors, fewer M-MDSCs, and an increase in tumoral $CD8^+$ T cells. The T cell infiltration was driven by NF-κB mediated Cxcl1 and Cxcl5 secretion from tumor cells. The mechanism of CXCL1 mediating T cell infiltration has been established (Li et al., 2018a), and our work provides evidence that ApoE is critical in this mechanism. These data highlight a novel role for ApoE in promoting immune suppression in PDA.

In Chapter 4 I present a novel gene signature that is systemically elevated in both mouse and human PDA. One of the challenges for PDA patients is that most present with metastatic disease, for which there is no cure. The immune response has been well studied at the primary tumor in PDA, but how the immune system is altered systemically has not been well described. In this work we used biomaterial scaffolds, which serve as a synthetic metastatic niche, blood, livers, and primary tumors from multiple mouse models, as well as blood, liver metastases, and primary tumor samples from human PDA patients to get a comprehensive evaluation of the systemic changes to the immune response in PDA. We identified two distinct macrophages populations, one defined by Chil3 (Chil-TAMs) and the other defined by complement component genes (Cq-Tams) that exist systemically. Further, the complement components, *C1QA* and *C1QB,* as well as *TREM2* were upregulated systemically in PDA compared to normal controls. These data suggest a novel role for the complement system in PDA that has yet to be fully elucidated. Our single cell RNA sequencing analysis in this work further identified the complexity of macrophages in PDA and uncovered novel markers for future evaluation.

In Chapter 5 I discuss how the hypotheses and findings from Chapters 2, 3, and 4 contribute to the PDA field and suggest future directions for each project.

Chapter 2 Multi-modal Mapping of the Tumor and Peripheral Blood Immune Landscape in Human Pancreatic Cancer[3,4]

Abstract

Pancreatic ductal adenocarcinoma (PDA) is characterized by an immune-suppressive tumor microenvironment that renders it largely refractory to immunotherapy. We implemented a multimodal analysis approach to elucidate the immune landscape in PDA. Using a combination of CyTOF, single-cell RNA sequencing, and multiplex immunohistochemistry on patient tumors, matched blood, and non-malignant samples, we uncovered a complex network of immune-suppressive cellular interactions. These experiments revealed heterogeneous expression of immune checkpoint receptors in individual patient's T cells and increased markers of $CD8^+$ T cell dysfunction in advanced disease stage. Tumor-infiltrating $CD8^+$ T cells had an increased proportion of cells expressing an exhausted expression profile that included upregulation of the immune checkpoint *TIGIT*, a finding that we validated at the protein level. Our findings point to a

---

[3] Data from Chapter 2 have been published in *Nature Cancer* in a manuscript entitled, "Multimodal Mapping of the Tumor and Peripheral Blood Immune Landscape in Human Pancreatic Cancer" (2020).

[4] Author list: Nina G. Steele[+], Eileen S. Carpenter[+], Samantha B. Kemp[+], Veerin Sirihorachai[+], Stephanie The, Lawrence Delrosario, Jenny Lazarus, El-ad David Amir, Valerie Gunchick, Carlos Espinoza, Samantha Bell, Lindsey Harris, Fatima Lima, Valerie Irizarry-Negron, Daniel Paglia, Justin Macchia, Angel Ka Yan Chu, Heather Schofield, Erik-Jan Wamsteker, Richard Kwon, Allison Schulman, Anoop Prabhu, Ryan Law, Arjun Sondhi, Jessica Yu, Arpan Patel, Katelyn Donahue, Hari Nathan, Clifford Cho, Michelle A. Anderson, Vaibhav Sahai, Costas A. Lyssiotis, Weiping Zou, Benjamin L. Allen, Arvind Rao, Howard C. Crawford[*], Filip Bednar[*], Timothy L. Frankel[*], Marina Pasca di Magliano[*]
[+] Equal author contribution
[*]Corresponding authors

profound alteration of the immune landscape of tumors, and to patient-specific immune changes that should be taken into account as combination immunotherapy becomes available for pancreatic cancer.

Introduction

Pancreatic ductal adenocarcinoma (PDA), one of the deadliest human malignancies, is distinguished by an extensive and complex tumor microenvironment (TME) containing abundant infiltrating immune cells. Immunotherapy clinical trials using checkpoint inhibitors PD-1 and CTLA4 as single agents have been unsuccessful (Brahmer et al., 2012; Royal et al., 2010), but recent clinical trials using combination of immune regulatory agents have shown positive initial results (NCT02588443), indicating the need to target multiple components of the stroma and better understand the immune landscape of human PDA. The prevalence of $CD8^+$ T cells varies across patients (Stromnes et al., 2017). Deconvolution of bulk RNA sequencing data from The Cancer Genome Atlas (TCGA) stratified tumors based on their cytolytic index, including a high cytolytic index group (Balli et al., 2017). These data indicate that the $CD8^+$ T cell landscape in pancreatic tumors might be more complex than previously believed, and the mechanisms of immune suppression may vary across patients. While pancreatic cancer is most often diagnosed when locally invasive or metastatic, most existing datasets are limited to surgical samples representing earlier stages of the disease.

The presence and distribution of cytotoxic T cells in PDA has important prognostic correlations; $CD8^+$ T cells in proximity to PDA cells correlate with increased overall survival (Carstens et al., 2017). Further, analysis of rare long-term PDA survivors revealed persistence of T cell clones specific to tumor antigens (Balachandran et al.,

2017). Conversely, infiltration of myeloid cells, specifically tumor associated macrophages, negatively correlates with prognosis (Tsujikawa et al., 2017), consistent with an immune-suppressive role of these cells (Vonderheide, 2018). $CD4^+$ T cells are abundant within tumors, with a prevalence of regulatory T cells (Clark et al., 2007); their nature in human PDA is currently poorly understood. Similarly, our understanding of other immune cell types within tumors is limited.

Here, we used multiple, complementary approaches [mass cytometry (CyTOF), single-cell RNA sequencing (scRNA seq), and multiplex fluorescent immunohistochemistry (mfIHC)] to investigate the immune landscape of pancreatic tumors from a collection of samples that included both surgical and fine needle biopsy samples, as well as matched patient blood. Our work adds an in-depth immune characterization to complement recent single cell characterization on pancreatic tumor cells (Chan-Seng-Yue et al., 2020; Moncada et al., 2020) and cancer associated fibroblasts (Biffi et al., 2019; Dominguez et al., 2020; Elyada et al., 2019). We observed that immune landscapes in each individual patient were heterogeneous, although some common features emerged. Cytotoxic T cells in patients displayed an exhausted gene expression signature, which was progressively more pronounced in advanced disease. The specific combinations of immune checkpoint genes expressed in each patient's $CD8^+$ T cells was unique. Tumor infiltrating $CD8^+$ T cell had a higher proportion of cells expressing genes previously associated with T cell exhaustion, and these cells had enriched expression of the immune checkpoint *T-cell immunoglobulin and ITIM domains* (*TIGIT*) (Manieri et al., 2017). Predicted interaction analysis (Cohen et al., 2018; Zhang et al., 2019a) revealed multiple potential cellular interactions upregulated in tumors

compared with non-malignant tissue. Overall, our study provides a wealth of hypothesis-generating data to benefit the PDA community at large.

Results

CyTOF and multiplex immunohistochemistry mapping reveal heterogeneous immune infiltration in human pancreatic cancer

To map the immune infiltration in pancreatic cancer, we performed CyTOF on 10 pancreatic tumor samples and 8 samples from non-malignant pancreas specimens [Whipple pancreaticoduodenectomy (n=2), distal pancreatectomy (n=4), partial pancreatectomy (n=1) or endoscopic fine needle biopsy (n=3)]. Clinical pathology review provided the diagnosis for samples (**Fig. 2.1A**); histology of surgical specimens is shown in **Fig. 2.1B**. Our validated antibody panel contained 30 immune markers (Bendall et al., 2011). We used the Astrolabe Cytometry platform for batch correction to account for differences in the timing of sample acquisition, and selected live singlets for downstream analysis (Amir et al., 2019; Nowicka et al., 2017).

Principal component analysis (PCA) showed a minor shift between adjacent or normal pancreas and tumor samples (**Fig. 2.2A),** indicating differences in immune cell composition. To visualize the distribution of cell populations within individual samples, we utilized unbiased hierarchical clustering algorithms (Nowicka et al., 2017), along with supervised annotation (**Fig. 2.2B**,**C** and **Fig. 2.1C,D**). While adjacent/normal samples contained mostly non-immune cells, tumor samples had an abundance of immune cells (**Fig. 2.2C**). Multiple immune populations were elevated in tumor samples: myeloid cells, B cells, NK cells, $CD4^+$ T cells, regulatory T cells and $CD8^+$ T cells (**Fig. 2.2D** and **Fig.**

2.1E). We observed an inverse correlation between the percentage of myeloid cells and $CD8^+$ T cells (**Fig. 2.2E**), consistent with previous observation in mouse models and in agreement with the notion that myeloid cells are a key immunosuppressive component in pancreatic cancer (Clark et al., 2007; Panni et al., 2019; Stromnes et al., 2014; Stromnes et al., 2017; Zhang et al., 2017b).

To measure immune composition in undisturbed tissue and define the spatial relationships between immune cells in the microenvironment, we performed seven-color multiplex fluorescent immunohistochemistry (mfIHC) on a formalin fixed paraffin embedded tissue tumor microarray (TMA) comprised of 71 PDA and 34 chronic pancreatitis samples, as previously described (Lazarus et al., 2018) (**Fig. 2.1F**). Representative images from individual samples are shown in **Fig. 2.2F**, **Fig. 2.1G-H**. Chronic pancreatitis samples contained a higher epithelial cell component than the PDA samples. Conversely, immune cell infiltration was more abundant in PDA tissue **(Fig. 2.2G)**. In agreement with our CyTOF analysis, mfIHC demonstrated an increase in Tregs ($FOXP3^+$) and macrophages ($CD163^+$). However, unlike in the CyTOF data, $CD8^+$ T cells did not change (**Fig. 2.2G**), likely reflecting differences in the control tissues (chronic pancreatitis versus adjacent/normal pancreas). Individual patient tumors were variable in terms of $CD8^+$ T cell infiltration. As in the CyTOF data, we observed a negative correlation between $CD8^+$ T cells and myeloid cells in PDA samples **(Fig. 2.2H** and **2.2E**) (Clark et al., 2007; Tsujikawa et al., 2017), supporting a key immunosuppressive role of this cell population (Beatty et al., 2015; DeNardo and Ruffell, 2019; Elyada et al., 2019; Nywening et al., 2018; Panni et al., 2019; Sanford et al., 2013; Zhang et al., 2017b; Zhu et al., 2017;

Zhu et al., 2014). Overall, our data show a complex microenvironment and considerable variability across individual patients.

Single cell RNA sequencing reveals a complex immune landscape with heterogeneous expression of immune checkpoints and ligands in the pancreatic cancer microenvironment

We performed single cell RNA sequencing (scRNA seq) on 16 PDA samples, including surgical (n=6) and fine needle biopsy specimens (n=10) (**Fig. 2.3A**). All the patients were treatment-naïve at the time of sample acquisition. We also included three non-malignant pancreas samples (1196, 1258, 19732) from patients undergoing surgery for duodenal adenoma, ampullary carcinoma, or adjacent to PDA, respectively, where an uninvolved portion of pancreas was included in the resection (as determined by pathologic evaluation). To capture a window into the systemic immune response in PDA patients, we also collected peripheral blood mononuclear cells (PBMCs) from these patients and healthy subjects (**Fig. 2.3A**, *right panel*).

In total, we sequenced 8541 cells from adjacent/normal samples and 46,244 from PDA, while from the blood samples we sequenced 14,240 cells from 4 healthy subjects, and 55,873 cells from 16 PDA patients. To define and visualize cell subpopulations, we batch corrected our tumor and blood sequencing samples (**Fig. 2.3B**) and then used unbiased clustering and a dimensionality reduction through Uniform Manifold Approximation and Projection (UMAP) (**Fig. 2.4A** and **Fig. 2.5A**). We identified each subpopulation based on published lineage markers (**Fig. 2B** and **Fig. 2.5B**). We observed variability in the total immune cell composition of individual tumors, and in the relative

abundance of individual immune cell components similar to CYTOF and mfIHC data (**Fig. 2.3C** and **2.3D).**

We identified abundant pro-inflammatory cells in the PDA microenvironment including $CD8^+$ T cells and natural killer cells (NK) (**Fig. 2.4A**). To gather insight into the possible mechanisms preventing anti-tumor immune responses, we profiled average expression of immune checkpoint receptors and ligands by cell type, both in tumors and PBMCs of PDA patients (**Fig. 2.4C** and **Fig. 2.5C**). We observed expression of multiple immune checkpoint receptors in T and NK cell subsets, while myeloid populations were enriched for their corresponding ligands (**Fig. 2.4C**). $CD8^+$ T cells had elevated *ICOS, TIGIT, PDCD1* and *LAG3*, among others, but relatively low expression of *CTLA4*. *CTLA4*, as well as all other checkpoints except for *LAG3*, was high in $CD4^+$ T cells. NK cells also had elevated *CD47, TIGIT, TNFRSF18* and *LAG3*, and modest expression of *PDCD1*. The expression of checkpoint ligands was heterogeneous, with epithelial cells mainly expressing *PVR* and *LGALS9* (encoding for *PVR* and *GALECTIN 9*, ligands for *TIGIT* and *HAVCR2*(*TIM3)* respectively). Myeloid and dendritic cells expressed several genes encoding checkpoint ligands, including *SIRPA, LGALS9, PVR,* and *ICOSLG* (**Fig. 2.4C**). Similarly, in PBMC samples, $CD4^+$ T cells, $CD8^+$ T cells and NK cells had elevated expression of multiple immune checkpoint receptors (*TIGIT* was elevated in all three cellular compartments), and granulocytes, monocytes and B cells, plasma cells and dendritic cells expressed the ligands (**Fig. 2.5C**). We also detected expression of immune checkpoint ligands in other non-immune cell types, which included fibroblasts, endocrine, and endothelial cells (**Fig. 2.4C**). Our single cell data revealed a complex, patient-specific

landscape of immune checkpoint ligand and receptor expression across multiple immune and non-immune cell types.

Tumor-infiltrating CD8$^+$ T cells have a distinct gene expression profile, with progressive dysfunction in advanced disease

Cytotoxic T cells are a fundamental component of anti-tumor immune responses and the target of immunotherapy (for review see (Rosenberg, 2014)). To gather deeper insight into the functional status of tumor-infiltrating CD8$^+$ T cells, we investigated their transcriptional profile. To investigate patient-specific variability, we mapped the average expression of immune checkpoint receptors in CD8$^+$ T cells in each individual patient's tumor and blood samples (**Fig. 2.4D** and **Fig. 2.5D**). Infiltrating CD8$^+$ T cells expressed markedly distinct immune checkpoint profiles in individual patient samples, both in tumors and blood (**Fig. 2D** and **Fig. 2.5D**). In tumor samples, *LAG3* was elevated in patients 1141, 1294, 1261 and 1229. Patient 1229 (locally advanced) also had high expression of *ICOS, CTLA4, TIGIT* and *CD47*. Conversely, patient 1261 (also locally advanced), had elevated *CD27, LAG3, PDCD1, HAVCR2, TNFRSF18, CSF1, TIGIT, CD40LG, CD47* and *CD28*, but not *CTLA4*. The immune checkpoint landscape did not cluster by disease stage, and while some metastatic patients had high expression of multiple immune checkpoints (3210) others expressed only a limited subset (1253). Analysis of circulating CD8$^+$ T cells revealed a similarly complex landscape, but no clear overall correlation in the expression of individual checkpoints between patient tumor and blood T cells at a gene expression level (**Fig. 2.5D**).

We then investigated tumor-infiltrating $CD8^+$ T cells compared to $CD8^+$ T cells in normal/adjacent tissue. By functional annotation, we observed pathways relating to cell cytotoxicity, chemokine signaling, T cell receptor signaling, and antigen processing were significantly enriched in PDA samples, compared to adjacent/normal tissue $CD8^+$ T cells, an indication that immune responses had been elicited in the tumors (**Fig. 2.4E**). We performed unbiased clustering of the $CD8^+$ T cell gene expression signatures in patients. Circulating $CD8^+$ T cells gene expression patterns did not clearly segregate by disease stage (**Fig. 2.5E**). We then performed an unbiased differential expression analysis on the tissue-infiltrating $CD8^+$ T cells in tumors versus adjacent/normal tissue. This analysis revealed distinct expression patterns in healthy versus tumor infiltrating total $CD8^+$ T cells (**Fig 2.4F**). We noted that the $CD8^+$ T cells in adjacent/normal samples clustered together, while tumor-infiltrating $CD8^+$ T cell signatures spanned a spectrum in individual samples. Some tumor signatures partially resembled non-malignant tissue and others were greatly diverging. Interestingly, upon clinical annotation, we discovered that the divergence from the normal signature was more pronounced in samples from advanced disease stage. When we considered which genes were differentially expressed across the groups, we observed an increase in T cell activation and trafficking markers (*GZMB, GZMA, KLF2*) (Balli et al., 2017; Carlson et al., 2006; Stromnes et al., 2017) in tumor $CD8^+$ T cells, compared to adjacent/normal tissues. Further, T cell exhaustion markers such as *EOMES* and *GZMK* were low in healthy $CD8^+$ T cells, and elevated in the majority of tumor $CD8^+$ T cell samples (Li et al., 2018b; Wherry et al., 2007). The only immune checkpoint receptor identified as differentially overexpressed in tumor-infiltrating $CD8^+$ T cells, compared to $CD8^+$ T cells in adjacent/normal tissue, was *TIGIT*, a gene encoding a

receptor belonging to the Ig superfamily (Manieri et al., 2017). Overall, comparison of the transcriptional profile of tumor and adjacent/normal infiltrating $CD8^+$ T cells revealed unique profiles of expression of immune checkpoint genes in individual patients. However, some common features emerged, such as expression of activation markers, as well as an exhausted gene expression signature which progressively increased with advanced disease stage.

Tumor infiltrating $CD8^+$ T cells include an expanded exhausted population characterized by TIGIT expression

Distinct populations of tumor infiltrating $CD8^+$ T cells have been described (Jansen et al., 2019). Given the progressive dysfunction of tumor-infiltrating $CD8^+$ T cells, we hypothesized that the transcriptional profile shift might be caused by changes in $CD8^+$ populations. By unbiased clustering, we distinguished 6 populations of *CD8A*-expressing T cells in both adjacent/normal and PDA samples (**Fig. 2.6A**). To identify sub-populations, we plotted the top expressed genes per cluster (**Fig. 2.6B**), and compared them with published signatures of $CD8^+$ T cells subtypes (Wherry et al., 2007). We identified two populations of effector $CD8^+$ T cells (T_{eff}), expressing *PRF1* and *GZMB*; a population of likely memory (mem)/ precursor effector (pec) $CD8^+$ T cells ($T_{mem/pec}$) expressing *CCR6* (Kondo et al., 2007); and two populations of exhausted $CD8^+$ T cells (T_{ex}) expressing *EOMES*, *GZMK*, and *TIGIT* (**Fig. 2.6C, Fig. 2.7A** and average expression heatmap in **Fig. 2.7C**). Interestingly, comparison of tumor infiltrating versus adjacent/normal $CD8^+$ T cells revealed a relative increase in exhausted T cells and memory T cells, with converse reduction of effector T cell levels (**Fig. 2.6D** and **Fig. 2.7B**). We then examined expression

of immune checkpoints and immune activation markers across $CD8^+$ T cell subsets, and observed uniform expression of *PDCD1*, *HAVCR2* and *LAG3* (**Fig. 2.6C),** while *TIGIT* was enriched in exhausted and memory $CD8^+$ T cells. We found that 13.3% of effector $CD8^+$ T cells, compared to 44.2% of exhausted $CD8^+$ T cells expressed TIGIT. To compare gene expression changes within distinct clusters of $CD8^+$ T cells, we performed two separate differential expression analyses. We first compared PDA effector $CD8^+$ T cells to adjacent/normal effector $CD8^+$ T cells, and we found that *GZMA* and *GZMB* were higher in tumor infiltrating effector $CD8^+$ T cells, suggesting T cell activation (**Fig. 2.6E**). *RORA* expression, a marker associated with effector T cells, was also upregulated (Wherry et al., 2007) (**Fig. 2.6E**), consistent with an ongoing immune response. We then compared PDA exhausted $CD8^+$ T cells to adjacent/normal exhausted $CD8^+$ T cells and tumor infiltrating exhausted $CD8^+$ T cells had higher expression of *EOMES* and *KLF2*, markers of exhaustion (Wherry et al., 2007) (**Fig. 2.6F**).

Our data suggest that exhausted $CD8^+$ T cells are abundant in pancreatic tumors, and that their exhausted phenotype is more profound than the equivalent population in adjacent/normal tissue. Further, *TIGIT* was the sole immune checkpoint receptor that specifically defined exhausted $CD8^+$ T cells.

A complex landscape of NK and $CD4^+$ T cells cell subsets in pancreatic cancer

Similar to effector $CD8^+$ T cells, NK cells display cytotoxic activity and express immune checkpoint receptor (**Fig. 2.4C**), however these cells are not well defined in human PDA (Ducimetiere et al., 2019). Unsupervised sub-clustering of NK cells revealed three populations (**Fig. 2.8A** and **2.8B**). Along with the three NK cell subsets, we found

two additional populations that we labeled cluster 1 and 2, which expressed *NKG7, CD3E,* and *CD8A*. While these cells did not cluster with the CD8 T cells based on their transcriptional profile, they could potentially be highly cytolytic CD8 T cells expressing some NK markers (Arlettaz et al., 2004; McMahon et al., 2002). A "NK" cell population expressing *CD8A* was identified in a recent PDA scRNA-seq paper (Elyada et al., 2019). Highly variable gene expression analysis highlighted differences among subpopulations (**Fig. 2.8B**). In NK subsets we detected expression of markers of antigen presentation (*HLA-DRA*), cytolytic activity (*PRF1, GZMB*), and chemokines/chemokine receptors (*CCL3, IL7R*), in agreement with a recently published characterization of human NK cells by single cell RNA sequencing (Smith et al., 2020). NK cluster 1 was enriched for immune checkpoint *HAVCR2*, while NK cluster 3 expressed high levels of immune checkpoint *TNFRSF4* (**Fig. 2.8B** and **2.8C**). We then performed differential gene expression analysis and unbiased clustering of individual patient samples to compare tumor infiltrating NK cells with NK cells in non-tumor tissue. The signatures of tumor-infiltrating and non-tumor NK cells were not as divergent as was the case for $CD8^+$ T cells, and, with one exception (1324), resectable tumor samples clustered closely with the non-tumor samples (**Fig. 2.8D**). However, advanced disease samples had a different expression signature than healthy counterparts, with increased expression of activation markers such as *GZMA* and elevated expression of two immune checkpoint genes, *TIGIT* and *HAVCR2*. The role of NK cells in PDA is not well understood; our findings set the stage for future functional studies on the role of NK cells in this disease.

We then investigated $CD4^+$ T cells, a complex population that includes regulatory T cells, and plays a fundamental role in regulating pancreatic carcinogenesis (Chan-

Seng-Yue et al., 2020; Hoffman et al., 2020; Jang et al., 2017; Li et al., 2020b; Oakes et al., 2020; Perusina Lanfranca et al., 2020; Zhang et al., 2020; Zhang et al., 2014). Unlike the $CD8^+$ T and NK cells, we could not perform differential expression on $CD4^+$ T cells as we did not capture enough cells from adjacent/normal tissue samples; instead we focused on studying the tumor-infiltrating component. We identified 13 transcriptionally distinct populations of $CD4^+$ T cells, although many of the different clusters tended to merge together (**Fig. 2.8E**). A highly enriched gene analysis of $CD4^+$ subsets revealed expression of naïve T cell markers *CCR7* and *SELL* (Sckisel et al., 2017) in cluster 0 and expression of regulatory T cell marker *FOXP3* in cluster 3 (**Fig. 2.8F**). As expected, based on previous studies, *CTLA4* was highly expressed within Tregs (Bengsch et al., 2017) (**Fig. 2.8G**). Specific immune checkpoint genes were highly expressed in individual clusters, such as *TNFRSF18* and *PDCD1. TIGIT* appeared as a top expressed gene in Tregs (**Fig. 2.8F**), although it was also expressed in other clusters more sparsely (**Fig. 2.8G).** The other clusters did not correspond to known subsets of $CD4^+$ T cells, and were relatively similar to one another, a possible reflection of low transcriptional activity of non-Treg $CD4^+$ T cells. Taken together, these analyses suggest multiple immune checkpoint receptors are expressed in $CD4^+$ and NK cell subsets. In particular, the immune checkpoint *TIGIT* was differentially overexpressed on tumor-infiltrating PDA $CD8^+$ T cells, regulatory T cells and NK cells.

Myeloid and dendritic cells are an important source of immune checkpoint ligands in human PDA

We next analyzed myeloid cells, which are an important source of immune checkpoint ligands in PDA. By unbiased clustering, we identified 6 transcriptionally distinct populations of myeloid cells. (**Fig. 2.9A).** We observed an abundant granulocyte population expressing *CXCR1* and *CXCR2, FCGR3B* and *S100A8* (**Fig. 2.9B**). Consistent with previous studies (Biffi et al., 2019; Elyada et al., 2019; Sanford et al., 2013), we detected resident macrophages and alternatively activated macrophages (*MARCO*$^{+}$), and classical monocytes (**Fig. 2.9A** and **2.9B**). We also observed an additional myeloid population, denoted as alternatively activated macrophages 2, that resembled alternatively activated macrophages and was uniquely defined by abundant expression of *CHIT1* and multiple immune checkpoint ligands (**Fig. 2.9A, 2.9B** and **Fig. 2.10A**). We next mapped immune checkpoint ligand expression within specific myeloid compartments and observed heterogeneous expression of immune checkpoints in specific clusters (**Fig. 2.9C**). Differential expression analysis between adjacent/normal and tumor-infiltrating myeloid sub-clusters revealed multiple upregulated checkpoint ligands. *LGALS9,* the ligand for *HAVCR2* (encoding for TIM3*)*, was significantly increased within alternatively activated macrophages, while *SIRPA*, the ligand for *CD47*, was higher in PDA granulocytes compared to granulocytes in adjacent/normal tissue (**Fig. 2.9D**). *PVR*, the ligand for *TIGIT* was enriched in total macrophages (**Fig. 2.9D**). Average expression heatmaps of macrophages (**Fig. 2.10B**) and granulocytes (**Fig. 2.10C**) demonstrated that the expression of immune checkpoint ligands was highly variable in individual patients.

Dendritic cells (DCs) cells are professional antigen presenting myeloid cells, and support anti-tumor activity by stimulating T cells; their relative rarity in PDA is one of the

potential causes for ineffective immune responses in this disease (Hegde et al., 2020). Clustering analysis revealed multiple populations of tumor-infiltrating DCs (**Fig. 2.9E**). We found two populations of plasmacytoid DCs (*IRF8, GZMB*) and two populations of Langerhans-like DCs (*CD207*, *CD1A*) as previously described (Elyada et al., 2019)(**Fig. 2.9F** and **2.11A**). Langerhans-like DC2 had robust expression of *IL22RA2*, also known as IL22BP, and the IL-22-IL22BP axis is known to be a crucial mediator of tumorigenesis in the colon (Huber et al., 2012) and pancreas (Perusina Lanfranca et al., 2020). We also detected a population of conventional DC1s (*CLEC9A, IRF8*) (Biffi et al., 2019; Collin and Bigley, 2018; Elyada et al., 2019), and two additional populations of potential conventional DC2s that expressed immune checkpoint ligand *SIRPA* (**Fig. 2.9F** and **2.11A**). We also detected two unique populations of activated DCs (*LAMP3*, *CCL22*) (Elyada et al., 2019) (**Fig. 2.9F** and **2.11A**). We then plotted the average expression of known immune checkpoint ligands in the different DC subsets. We discovered that activated DC1 had elevated expression of nearly all the immune checkpoint ligands, including *PVR* (**Fig. 2.11B**), suggesting that in pancreatic tumors some subsets of DCs may be immunosuppressive (Veglia and Gabrilovich, 2017).

Mapping predicted interactions and tissue heterogeneity in pancreatic cancer samples by single cell sequencing

To explore potential cross-talk between T/NK and myeloid populations, we applied a predicted interaction algorithm (Cohen et al., 2018) based on known ligand-receptor (LR) pairs interacting with high affinity (Ramilowski et al., 2015). We curated the list to specifically add immune checkpoints and limit the receptor-ligand pairs to cytokines,

chemokines and specific signaling pathways. We first plotted all the receptor-ligand interactions that were statistically higher in tumor versus non-malignant samples, based on the level of ligand expression, and observed a complex landscape of potential interactions involving multiple cell types (**Fig. 2.10D**). We then visualized upregulated ligands in macrophages (**Fig. 2.11C**), granulocytes (**Fig. 2.11D**), dendritic cells (**Fig. 2.11E**), endothelial cells (**Fig. 2.11F**) and epithelial cells (**Fig. 2.11G**) and mapped the predicted binding partners in CD4, CD8, and NK cells. Among interactions upregulated in cancer compared to adjacent/normal, we detected known putative immune suppressive interactions, such as those mediated by the chemokine receptors *CXCR2* in granulocytes and *CCR2* in macrophages (DeNardo and Ruffell, 2019; Sanford et al., 2013). Predicted interactions mediated by *IL1A* and *IL1B* with their receptor encoding genes *IL1R1* and *IL1R2* were also upregulated, consistent with their known roles in pancreatic cancer (Das et al., 2020; Elyada et al., 2019; Ohlund et al., 2017). Multiple putative interactions linked T and NK cells to myeloid immune checkpoint ligands, which is consistent with a key role for myeloid cells in establishing immune suppression in pancreatic cancer (for review see (Vonderheide, 2018)). Predicted immune checkpoint-mediated interactions such as *ICOS/ICOSLG* and *SIRPA/CD47* were among those upregulated in pancreatic cancer compared to healthy/adjacent tissue. *TIGIT/PVR* interactions were elevated between macrophages and $CD4^+$ T cells, $CD8^+$ T cells and NK cells (**Fig. 2.11C**). Interestingly, the putative *TIGIT/PVR* interaction was also elevated between tumor endothelial and epithelial cells, T cell and NK cell subsets (**Fig. 2.11F, 2.11G**). We then endeavored to investigate the expression of other genes involved in the TIGIT pathway. We investigated the expression of TIGIT's costimulatory counter receptor, DNAM1 (CD226), which

competes for PVR and PVRL2 and promotes T cell activation (Fourcade et al., 2018). We found that while TIGIT was significantly increased on PDA $CD8^+$ T cells (P= 4.8E-32), CD226 expression was not altered in $CD8^+$ T cells between adjacent/normal and PDA cells (**Fig. 2.11H**). CD96 and PVRIG act similarly to TIGIT, inhibiting T cell activation. Expression analysis showed that mRNA levels of these receptors were not altered between adjacent/normal and PDA $CD8^+$ T cells (**Fig. 2.11H**). PVRL2 encodes a second ligand for TIGIT, although it binds with a lower affinity compared to PVR (Yu et al., 2009). We detected expression of *PVRL2* in epithelial, myeloid, and endothelial cells (**Fig. 2.11I**). TIGIT, CD96, PVRIG, and CD226 were mainly expressed by T and NK cells in PDA tissue (**Fig. 2.11I**). We then investigated the Adenosine pathway, because of its immune suppressive role (Maj et al., 2017). We profiled this pathway in tumor samples and found expression of the adenosine receptor *ADORA1* in epithelial and mast cells, *ADORA2B* in epithelial, mast cells, and dendritic cells, ADORA3 in dendritic, mast, and myeloid cells (**Fig. 2.10E**).

The expression of multiple immune checkpoints has been previously described in pancreatic cancer (Balli et al., 2017). Since a deconvolution approach was used, the specific immune cell types expressing receptors and ligands could not be assessed. In contrast, our analysis provides a comprehensive view of the multiple, redundant potential immune suppressive interactions within the pancreatic cancer microenvironment.

TIGIT protein expression is increased on T and NK cells in pancreatic cancer, and its expression in the tumors correlates with matched blood

To determine whether mRNA expression of immune checkpoints was reflected by protein levels, we performed mass cytometry on tumor and normal/adjacent uninvolved tissue samples (**Fig. 2.12A**). TIGIT expression was elevated in tumor-infiltrating $CD8^+$ T cells in the majority of samples, albeit not all, while PD1 and LAG3 were not significantly altered (**Fig. 2.12A**). Interestingly, we detected an increase in expression in PD-1 ligand, PD-L1, in $CD68^+$ macrophages from PDA patients (**Fig. 2.13B**). CTLA4 expression was significantly increased in $CD4^+$ T cells in most PDA samples versus adjacent/normal tissues (**Fig. 2.12B**). $TIGIT^+$ $CD4^+$; $CD25^+$ T cells were more frequent in PDA samples, compared to controls (**Fig. 2.12B**). Similarly, $TIGIT^+$ NK cells ($CD56^+$) were more frequent in PDA, although this finding is limited by the small number of samples analyzed (**Fig. 2.12C**). In one patient, where matched tumor and uninvolved adjacent tissue were analyzed, we observed a higher frequency of TIGIT expression on both $CD8^+$ and $CD4^+$ T cells in the tumor (**Fig. 2.12D**). We then performed immunostaining for both TIGIT and PVR on patient tissue *in situ* (**Fig. 2.12E**) and observed TIGIT in $CD8^+$ T cells, and PVR (red) in epithelial and stromal cells (**Fig. 2.12E** and single channels shown in **Fig. 2.13A**).

Lastly, as we observed that TIGIT was commonly upregulated in tumors, we investigated whether protein expression of TIGIT in blood correlated with the individual patient's tumor, an attractive possibility given the relatively easy accessibility of blood samples. We performed CyTOF on the peripheral white blood cell (PBMC) component in 36 pancreatic cancer patients, 18 healthy volunteers, and 8 patients with chronic pancreatitis (**Fig. 2.14A)**. Cellular subtyping and frequency of circulating immune cells present are shown in **Fig. 2.14B-E.** Principal component analysis failed to show any major distinction between our three patient populations (**Fig. 2.14G**). Blood from both PDA and

chronic pancreatitis patients had fewer circulating $CD8^+$ T cells, but higher expression of TIGIT $CD8^+$ T cells **(Fig. 2.12F, 2.12G** and **Fig. 2.14F).** PD1 and CTLA4 protein expression was elevated in PDA circulating $CD8^+$ and $CD4^+$ T cells, respectively, compared to healthy subjects (**Fig. 2.12G**). We then analyzed the subset of patients for whom we had matched mass cytometry of tumor and PBMCs and found a positive correlation of TIGIT expression, but not PD1 expression, in $CD8^+$ T cells (**Fig. 2.12H** and **2.12I**). Thus, different immune checkpoint molecules are prevalent in individual patients, and further validation of potential targets, including TIGIT, is warranted.

Discussion

Recent reports examining gene expression in pancreatic tumors by scRNAseq or high content *in situ* hybridization have largely focused on the complexity of the fibroblast populations, (Dominguez et al., 2020; Elyada et al., 2019; Ligorio et al., 2019) however the heterogeneity of the immune reaction in PDA at a single cell level remained unclear. We have used a multi-modal approach combining CyTOF (Amir et al., 2019; Bendall et al., 2011), multiplex immunohistochemistry, and scRNA seq to map the immune infiltration, as well as the systemic immune response through patient blood, in human PDA (Stuart and Satija, 2019).

Multiparameter mapping of the TME demonstrated a highly heterogeneous immune infiltration in individual patients, consistent with previous reports (Stromnes et al., 2017), suggesting that immune-modulatory therapies should potentially be targeted to specific individuals based on their checkpoint expression profile within tumors. Both CyTOF and mfIHC also revealed an inverse correlation between infiltration of myeloid

and $CD8^+$ T cells. scRNA seq analysis suggests that $CD8^+$ T cells express markers of exhaustion at levels that increase in advanced stages of disease, consistent with a recent study of peripheral T cells in pancreatic cancer patients showing diminished fitness (Xu et al., 2019). Importantly, we included fine needle biopsy samples for both single cell sequencing and CyTOF, which allowed us to study the immune infiltration in patients with unresectable advanced stages of disease. These tumors included $CD8^+$ T cells with a more pronounced exhaustion signature compared with early-stage patients, a possible indication of progressive immune dysfunction.

We found differential expression of *TIGIT*, both at the gene and at the protein level, in patient $CD8^+$ T cells. We chose to focus on TIGIT in particular as one example of an immune checkpoint ligand/receptor pair given our ability to evaluate this relatively understudied checkpoint across multiple modalities. *TIGIT* expression was enriched specifically within $EOMES^{high}$ $CD8^+$ T cells, or exhausted T cells, similar to recent findings in human prostate, bladder, and kidney cancer (Jansen et al., 2019). *TIGIT* was also elevated in NK cells within the tumor, where its role is less understood, although there is at least some evidence TIGIT inhibition in NK cells might be beneficial (Zhang et al., 2018). Elevated *TIGIT* expression is a feature of Tregs, and again its role in this cell population is not well understood. However, it has been proposed that inhibition of TIGIT on Tregs may suppress the secretion of the immunosuppressive cytokine IL-10 (Manieri et al., 2017). The expression of TIGIT, and other immune checkpoint receptors in multiple cellular compartments, as well as the observation that expression of immune checkpoints is highly heterogeneous across patients, will have to be further investigated as new combination immunotherapy approaches are devised for preclinical testing. Further, it is

interesting to note that multiple cellular compartments express a variety of immune checkpoint ligands in a similar heterogeneous manner. At the protein level, we validated that PVR, the ligand for TIGIT, was expressed in tumor, endocrine, and endothelial cells (while low in non-malignant acinar cells). PVR and other immune checkpoint ligands were also upregulated in myeloid subsets, supporting the notion of myeloid cells as key mediators of immune suppression in PDA. Intriguingly, TIGIT protein expression in the blood correlated with TIGIT expression in the tumors of individual patients, although a similar correlation was not observed for other immune checkpoints such as PD-1. Of note, while functional studies on the role of TIGIT in different patients and different cellular compartments within each tumor are still needed, TIGIT blocking agents are available and are currently being evaluated in clinical trials (Solomon and Garrido-Laguna, 2018).

In summary, our study provides a multimodal characterization of the immune landscape in PDA, highlights the complexity of this disease in human patients, and provides a resource for future functional studies.

Acknowledgments: We thank Matthew Cochran and Terry Wightman at the Flow Cytometry core at the University of Rochester Medical Center and Andrea Michelle Gunawan at the Indiana University Simon Cancer Center Flow Cytometry for their support in cell CyTOF acquisition. We thank Vinicius Motta and Kevin Brown from Fluidigm for their assistance with panel design. We would like to thank Patricia Schnepp and Aquila Ahmed for their assistance with CyTOF experimental design. We would also like to thank Tricia Tamsen and Judy Opp from the University of Michigan Advanced Genomics Core. We would like to thank David Hill and Michael Czerwinski for their input on designing single cell analysis pipelines. We would very much like to thank Amir Gilado and Ido Amit

for their expertise in building our pancreatic interactome network. We would like to thank the Tissue Procurement Center at the University of Michigan. Thanks to Ed Stack formerly with Perkin Elmer for assistance with initial R introduction and basic training using inForm 2.3.0 and earlier versions. and staining strategies. We thank Philip Turncliff for the excellent graphics. We also thank Jason Spence for the VE-cadherin antibody gift.

Funding: This project was supported by NIH/NCI grants R01CA151588, R01CA198074, U01CA224145, and the American Cancer Society to MPdM. This work was also supported by the University of Michigan Cancer Center Support Grant (P30CA046592), including an Administrative Supplement to HCC and MPdM. FB was funded by the Association of Academic Surgery Joel Roslyn Award. TLF was funded by K08CA201581. SK was supported by T32-GM113900 and NS, VS, KD were supported by T32-CA009676. EC is supported the American College of Gastroenterology Clinical Research Award and by T32-DK094775. NS is a recipient of the American Cancer Society Postdoctoral Award PF-19-096-01 and the Michigan Institute for Clinical and Healthy Research (MICHR) Postdoctoral Translational Scholar Program fellowship award. AR and ST were supported by institutional startup funds from the University of Michigan, a gift from Agilent Technologies, NCI grant R37CA214955 and a Research Scholar Grant from the American Cancer Society (RSG-16-005-01). The funders had no role in study design, data collection and analysis, decision to publish, or preparation of the manuscript.

Author contributions: MPdM directed the study. TF, FB, and HC assisted with study design and analysis. MPdM, NS, EC, and SK developed the study concept, and were responsible for study design. JL, LD, VIN and SB stained and analyzed and TLF

coordinated the multiplex immunohistochemistry. VG, EC, EJW, RK, AS, AP, RL, JY, AP, HN, CC, MA, HS procured human tissue and assisted with clinical data collection. VG and EC maintained the database of human biospecimens. NS, EC, SK, DP, JM, CE, FL processed samples for CyTOF. EC, VS, JM, CE, DP, LH processed samples for single cell RNA sequencing. FB developed an R pipeline for CyTOF analysis. EDA analyzed CyTOF PBMC data. AR, ST and AC developed bioinformatic analysis pipelines and carried out the interactome analysis. VRS, NS, SK, KD analyzed single cell RNA sequencing data. NS, SK, EC analyzed the CyTOF data. VS, CL, BLA, AR, HS, WZ, HC, FB, TF, CC, KD, EDA, provided study guidance and feedback on the manuscript. NS, EC, SK, and MPdM wrote the manuscript, which was then edited by all the co-authors. All the co-authors approved the final version of the manuscript prior to submission.

Methods

Study Approval and Patient Consent

Patient Selection/Sample procurement: Medical chart review was used to screen for potential study patients with pancreatic disease at the University of Michigan. Fine needle biopsies: Patients over the age of 18 referred for diagnostic endoscopic ultrasound of a pancreas mass lesion suspected of PDA were consented according to IRB HUM00041280 or HUM00025339. Up to 2 extra passes using at 22 Gauge SharkCore™ needle were taken for research after biopsy obtained for clinical use. Surgical specimens: Surgical specimens of either tumor tissue or adjacent normal pancreas were obtained from patients referred for Whipple procedure or distal pancreatectomy according to IRB

HUM00025339. Blood collection: Up to 40 cc of whole blood were collected pre-procedurally or intra-operatively for all patients consented. For patients not undergoing interventional procedures (i.e. chemotherapy visit), only whole blood was collected.

Multiplex fluorescent immunohistochemistry (mflHC) imaging, cell segmentation, and basic phenotyping

Images were taken using the Mantra™ Quantitative Pathology Work Station (Akoya Biosciences). One image was taken of each patient core. All cube filters were used for each image capture (DAPI, CY3, CY5, CY7, Texas Red, Qdot) and the saturation protection feature was utilized. After all images were acquired, images were analyzed using inForm® Cell Analysis™ software versions 2.3.0 and 2.4.2 (Akoya Biosciences). Using this software, chronic pancreatitis specimens and PDA specimens were batch analyzed by their separate diagnoses. Cell segmentation was completed using DAPI as a basis of cell location and size and all cells segmented into the following subsets (nucleus, cytoplasm, and membrane). Using the automated training software, basic phenotypes (T cells, tumor epithelial cells, other cells, $CD163^+$ cells) were created. Software output consisting of mean fluorescent intensity (mfi) of each antibody-fluorophore pair, basic phenotypes, and x and y coordinates were acquired for further processing. A total of 34 chronic pancreatitis patients and 71 PDA patients were included in this study.

Cytometry Time-of-Flight (CyTOF) Immune Phenotyping and Data Analysis

For CyTOF, we collected 8 samples from non-malignant pancreas specimens, including non-involved pancreas tissue adjacent to a duodenal adenoma (1196, (patient ID)), ampullary carcinoma (1258), insulinoma (19-700), and non-involved pancreas tissue adjacent to PDA (1172, 19-262, 19-561, 19-732, 1252), all obtained surgically (**Fig. 2.3A**). PDA samples were collected from either surgical (n=7) or fine needle biopsy (FNB) (n=3) procedures, and clinical annotation is shown in **Fig. 2.3A**. Human patient tissues from FNB or surgery were immediately placed into DMEM media supplemented with Y27632 (Rho-Kinase inhibitor) for transport to the laboratory. Tissues were mechanically minced and enzymatically digested with collagenase P (1mg/mL DMEM) at 37 degrees Celsius with gentle shaking and subsequently filtered through a 40μm mesh to obtain single cells. Whole blood was collected pre-operatively into two 10mL EDTA tubes. EDTA tubes were inverted 10 times before centrifugation at room temperature (RT), 1700 x g for 20 minutes. Serum was removed and using a P1000 tip, the white layer of PBMCs at the interface between serum and RBCs was removed and placed into 15mL falcon tube. PBMCs were washed in 3X volume PBS centrifuged at RT, 300 x g for 15 minutes. Following centrifugation, the supernatant was removed, and 10ml ACK lysis buffer was added to lyse RBCs for 10 minutes at RT. Following this, PBMCs were centrifuged at 300 x g for 5 minutes. PBMC and tissue samples were washed twice with MaxPar® PBS (Fluidigm) prior to Cell-ID™ Cisplatin (Live/Dead staining). Cell-ID™ Cisplatin reagent (1.67μM) was incubated with tissue and PBMCs single cell suspensions for 5 minutes at RT. To quench this reaction, 4mL of Cell Staining Buffer (Fluidigm) was added to each sample and samples were centrifuged at 300 g for 5 minutes. The supernatant was removed, and cells were washed with 2 mL of MaxPar® Cell Staining Buffer. Cell fixation was achieved

by removing the supernatant, and re-suspending the cell pellet in residual volume, prior to the addition of freshly prepared cell fixation buffer (1.6% Methanol-free Formaldehyde; Thermo Fisher 28906 in MaxPar® PBS) for 10 minutes at RT. After fixation, samples were washed twice with 2mL of MaxPar® Cell Staining Buffer and centrifuged at 300 g for 5 minutes. Samples were re-suspended in 1mL MaxPar® Cell Staining Buffer and stored at 4 degrees Celsius for up to one week prior to staining. Up to 3 million cells per sample were stained with cell surface antibody cocktail (All antibodies were purchased from Fluidigm and used at the following dilutions: (CD3 (1:200); CD19 (1:300); CD15 (1:400); CD163 (1:100); CD64 (1:100); CD16 (1:400); LAMP1 (1:100); CD66b (1:200); CCR2 (1:200); TIGIT (1:100); PD-1 (1:100); PD-L1 (1:100); CD8a (1:200); CD33 (1:200); CD45RO (1:200); CD34 (1:100); CD45RA (1:100); CD206 (1:100); CD25 (1:100); CTLA-4 (1:100); CD68 (1:100); PD-L2 (1:100); HLA-DR (1:400); CD14 (1:100); CD4 (1:100); CD11b (1:200); CD45 (1:200); LAG3 (1:100); CD23 (1:100); CD56 (1:100)), in 100µl volume of MaxPar® Cell Staining Buffer for 30 minutes at room temperature. After being washed once in 1mL MaxPar® Cell Staining Buffer cells were re-suspended in 2mL cell intercalation solution (125 nM Cell-ID Intercalator-Ir in MaxPar® Fix and Perm Buffer) and shipped to either the Flow Cytometry core at the University of Rochester Medical Center or the Indiana University Simon Cancer Center Flow Cytometry where CyTOF2 Mass Cytometer cell acquisition was performed.

CyTOF Data Preprocessing

Normalized FCS files were analyzed using the Premium CytoBank Software V7.3.0 (cytobank.org). Data were checked for quality of staining and normalized by the use of

internal bead standards. Live singlet cells were identified using the combination of Ir191 DNA Intercalator, Event Length, and Pt195 Cisplatin staining intensity channels. Filtered live single cells were exported as new FCS files for downstream analysis.

CyTOF Analysis

Unbiased identification of cellular subpopulations was performed in parallel using multiple approaches – visualization through FlowSOM-viSNE in R, where an initial FlowSOM clustered cells into 100 initial nodes, followed by the ConsensusClusterPlus package which, along with manual annotation helped to further consolidate the clusters based on cell surface marker expression (Nowicka et al., 2017), or Astrolabe Cytometry Platform (Astrolabe Diagnostics, Inc.), where single-cell data was clustered using the FlowSOM R package (Van Gassen et al., 2015) and labeled using the Ek'Balam algorithm (Amir et al., 2019). The hierarchical clustering for all heatmaps uses the Pearson's correlation as a distance metric. Differential abundance analysis was performed using the edgeR V3.11 R package (McCarthy et al., 2012; Robinson et al., 2010). We used a combination of manual gating validation and unbiased approaches to analyze our datasets and included samples with >3000 live singlets in clustering algorithms.

Treatment of Batch Effects

In order to avoid batch effects within the data analysis, the Astrolabe Cytometry Platform did not compare numerical intensities between samples (Amir et al., 2019). Each sample was analyzed separately, and then comparisons were done using either cell frequencies (such as comparing T Cell counts) or qualitative values ("CD3 high" versus "CD3 low").

The underlying assumption was that a given subset was the same regardless of if underlying marker intensity has shifted; in other words, a T Cell was defined as a T Cell whether the $CD3^+$ peak was centered around a transformed intensity of 4, or a transformed intensity of 6. This mirrors the approach utilized in manual gating analysis.

t-SNE Visualization

For the t-SNE maps in **Fig. 2.14B/C**, each sample was uniformly downsampled into at most 10,000 cells. Samples were then concatenated, and the complete data set was uniformly downsampled into at most 500,000 cells. t-SNE algorithm was run using the Rt-SNE package: https://github.com/jkrijthe/Rt-SN.

Single-cell RNA sequencing

Tissues were mechanically minced and enzymatically digested with collagenase P (1mg/mL DMEM) and subsequently filtered through a 40μm mesh to obtain single cells. Dead cells were removed using MACS® Dead Cell Removal Kit (Miltenyi Biotec Inc.). Single-cell cDNA libraries were prepared and sequenced at the University of Michigan Sequencing Core using the 10x Genomics Platform. Samples were run using paired end 50 cycle reads on HiSeq 4000 or the NovaSeq 6000 (Illumina) to a depth of 100,000 reads. The raw data were processed and aligned by the University of Michigan DNA Sequencing Core. Cellranger count version 3.0.0 with default settings was used, with an initial expected cell count of 10,000. In all cases the hg19 reference supplied with the cellranger software was used for alignment. R Studio V3.5.1 and R package Seurat version 3.0 was used for single cell RNA-seq data analysis. Data were initially filtered to

only include all cells with at least 200 genes and all genes in greater than 3 cells. Data were initially normalized using the NormalizeData function with a scale factor of 10,000 and the LogNormalize normalization method. Variable genes were identified using the FindVariableFeatures function. Data were assigned a cell cycle score using the CellCycleScoring function and a cell cycle difference was calculated by subtracting the S phase score from the G2M score. Data were scaled and centered using linear regression on the counts and the cell cycle score difference. PCA was run with the RunPCA function using the previously defined variable genes. Violin plots were then used to filter data according to user-defined criteria. All tissue samples were batch corrected through the R package Harmony V1.0 (https://github.com/immunogenomics/harmony). Harmony is a flexible multi-dataset integration algorithm for scRNA-seq by correcting the low-dimensional embedding of cells from principal component analysis (PCA). It first uses soft clustering to find potential clusters, and then uses a soft k-means clustering algorithm to find clusters that favors the cells from multiple datasets and penalizes for any specified unwanted technical or biological factors. It then learns a simple linear adjustment function by computing cluster-specific linear correction factors, such as individual cell-types and cell state, from the cluster-specific centroids from each dataset. Each cell is weighted and corrected by its cell-specific linear factor. It then iterates the clustering and correction until the cell cluster assignments are stable. We used Harmony V1.0 to integrate our scRNA-seq patient data, correcting for individual scRNA-seq Run IDs (as each individual patient was each their own Run ID). Cell clusters were identified via the FindNeighbors and FindClusters function using a resolution of 1.2-2 for all samples and Uniform Manifold Approximation and Projection (UMAP) clustering algorithms were performed.

FindAllMarkers table was created and clusters were defined by user-defined criteria. Code is publicly available on GitHub.com (https://github.com/PascaDiMagliano-Lab/MultimodalMappingPDA-scRNASeq).

Interactome

Ligand and receptor pairs were defined based off of a curated literature supported list in Ramilowski et al (Ramilowski et al., 2015). The average of expression of ligands and receptors (LR) in all the population for each group were calculated. LR pairs in each group (adjacent/normal and PDA) were determined to be expressed by setting the median average expression for all groups as a threshold. LR's above the threshold were considered as expressed in the group. LR pairs were then filtered out if the ligand and receptor in the LR pairs were not expressed in both groups. Differences of the LR's between groups were determined using Wilcoxon ranked test, and p-values were adjusted for multiple comparisons with the Bonferroni correction method. LR's were considered significantly different if the $p < 1.0x10^{-4}$. LR pairs were then sorted by the adjusted ligand expression p-value. The interactomes were visualized using the Circos software V0.69-9 and the heatmap values within the circos plots displays the average expression of each ligand/receptor within the PDA tissues (Krzywinski et al., 2009).

Immunofluorescent staining

Patient tissue slides were rehydrated in xylene, 100% ethanol, 95% ethanol, then running deionized water sequentially. Antigen retrieval was performed with sodium citrate, pH 6.0. Tissue was blocked in 10% donkey serum overnight at 4°C. Primary antibodies

(PVR/CD155 (1:100, Cell Signaling Technology), VE-Cadherin/CD144 (1:250, R&D), FOXP3 (1:100, Cell Signaling), Vimentin (1:100, Cell Signaling), CD163 (1:100, Novus Biologicals), or Pan Cytokeratin-488 (1:250, Thermo Fisher Scientific) were diluted in 5% donkey serum in PBST (DS/PBST) and incubated overnight at 4°C. For tissue co-stained for TIGIT-FOXP3 and PVR-Vimentin: the tyramide signal amplification kit with Alexa Fluor 488 (Thermo Fisher Scientific) was used following the manufacturer's recommendation to enhance signaling for PVR and FOXP3. Samples underwent a second citrate antigen retrieval and were then multiplexed with TIGIT and Vimentin following the aforementioned standard IFC protocol. A 1% BSA block was used throughout the TSA protocol and subsequent multiplex staining. Tissue was mounted with DAPI ProLong™ Gold Antifade Mountant (Thermo Fisher Scientific) and subsequently imaged by confocal microscopy on a Leica SP5.

Statistical Analysis and Reproducibility

Significance was evaluated by the following statistical analyses: two-tailed, parametric, unpaired Student's *t*-test, Student's *t*-test with Welch's correction, Wilcoxon rank-sum test, or a Mann–Whitney *U*-test in GraphPad Prism (version 7) or JMP Pro software (version 14). The data were presented as means ± standard error (SEM) or means ± standard deviation (STDV). A p value of $p<0.05$ was considered statistically significant. Pearson correlation coefficients were used to measure R and R^2. Intergroup comparisons (differential expression) of scRNA seq was performed using Wilcoxon ranked test and p-values were adjusted for multiple comparisons with the Bonferroni correction method. For the interactome analysis, differences of the ligand and receptors between groups were

determined using Wilcoxon ranked test, and p-values were adjusted for multiple comparisons with the Bonferroni correction method. Ligand/Receptor pairs were considered significantly different if the $p < 1.0x10^{-4}$. Ligand/Receptor pairs were then sorted by the adjusted ligand expression p-value. No statistical method was used to predetermine sample sizes, experiments were not randomized and mass cytometric analysis of samples was not blinded. No data were excluded from the analyses. Each patient is considered an independent biological sample in the analyses. For comparison of differential abundance analysis of mass cytometry data, the edegR package (version 3.11) was used.

Data Availability

All raw data are publicly available without restrictions. All mass cytometry data used for this publication have been deposited in the FlowRepository. All fcs files of tissue (tumor and adjacent normal) have been uploaded to FlowRepository Experiment FR-FCM-Z2S4 and PBMC files have been uploaded to FlowRepository Experiment FR-FCM-Z2S3. Single cell RNA sequencing data with clinical metadata are available at NIH dbGAP database under the accession phs002071.v1.p1. Deidentified single cell RNA sequencing data are available at NIH GEO database under the accession GSE155698. Source data are available for this study. All other data supporting the findings of this study are available from the corresponding author on reasonable request.

Code Availability

Code is publicly available on GitHub.com (https://github.com/PascaDiMagliano-Lab/MultimodalMappingPDA-scRNASeq).

Figures

Figure 2.1

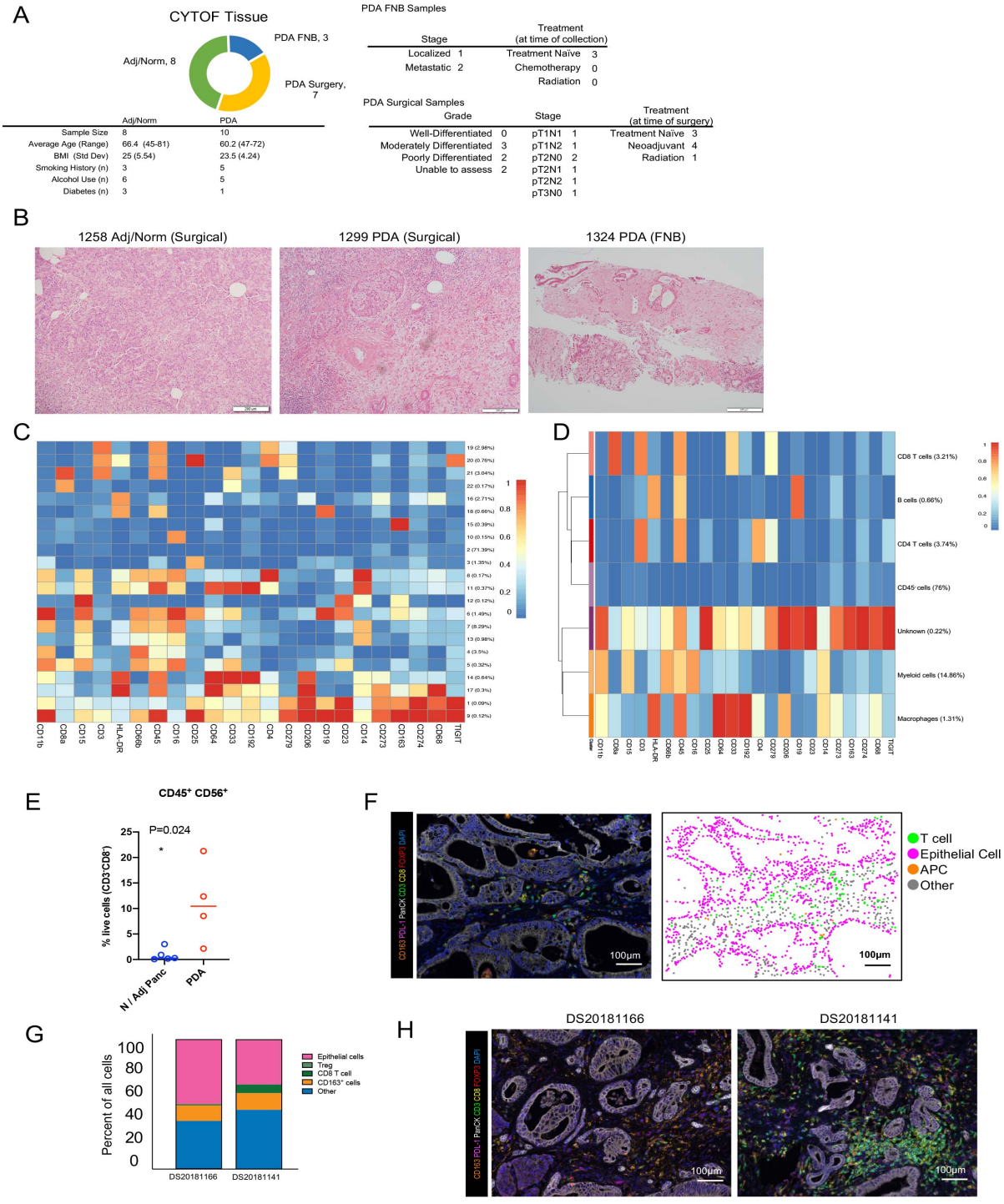

Figure 2.1 CyTOF and multiplex fluorescent immunohistochemistry (mfIHC) mapping can be readily performed on patient tumor samples.
(A) Patient breakdown and tumor characteristics of CyTOF performed on 8 adj/norm pancreas and 10 PDA tumor samples (surgical (7) vs. fine needle biopsy (FNB) (3)). (B) Representative H&E stains of samples DS20191258 (Adj/Norm), DS20191299 (PDA tumor from surgical resection), and DS20191324 (PDA tumor from fine needle biopsy). (C) The ConsensusClusterPlus and FlowSOM R packages were used to define the initial 22 clusters identified in the tissue CyTOF samples. (D) Final heatmap demonstrating marker expression used to define cell populations. (E) Manual gating of CD3-CD8A-CD45+CD56+ NK cells in adjacent/normal and PDA tissue samples, n=5 adjacent/normal tissue samples and n=4 PDA tissue samples. Two-sided Student's t-test was performed to compare between groups and asterisk indicates a p value of less than 0.05 was considered significant. For manual gating of NK cells n=5 for adj/norm and n=4 for PDA patient samples. (F) mfIHC composite image of PDA (left). Phenotype map with the following basic phenotypes at their x and y coordinates: T cell (green), epithelial cells (pink), APCs (orange), other cells (grey) (right). 71 individual PDA and 34 individual chronic pancreatitis subjects were examined in this analysis. (G) Relative cellular composition by quantitation of mfIHC of representative surgical PDA tissue of additional patients DS20181166 (PDA tumor from distal pancreatectomy), DS20181141 (PDA tumor from distal pancreatectomy) (H) Corresponding mfIHC images of DS20181166, and DS20181141.

Figure 2.2

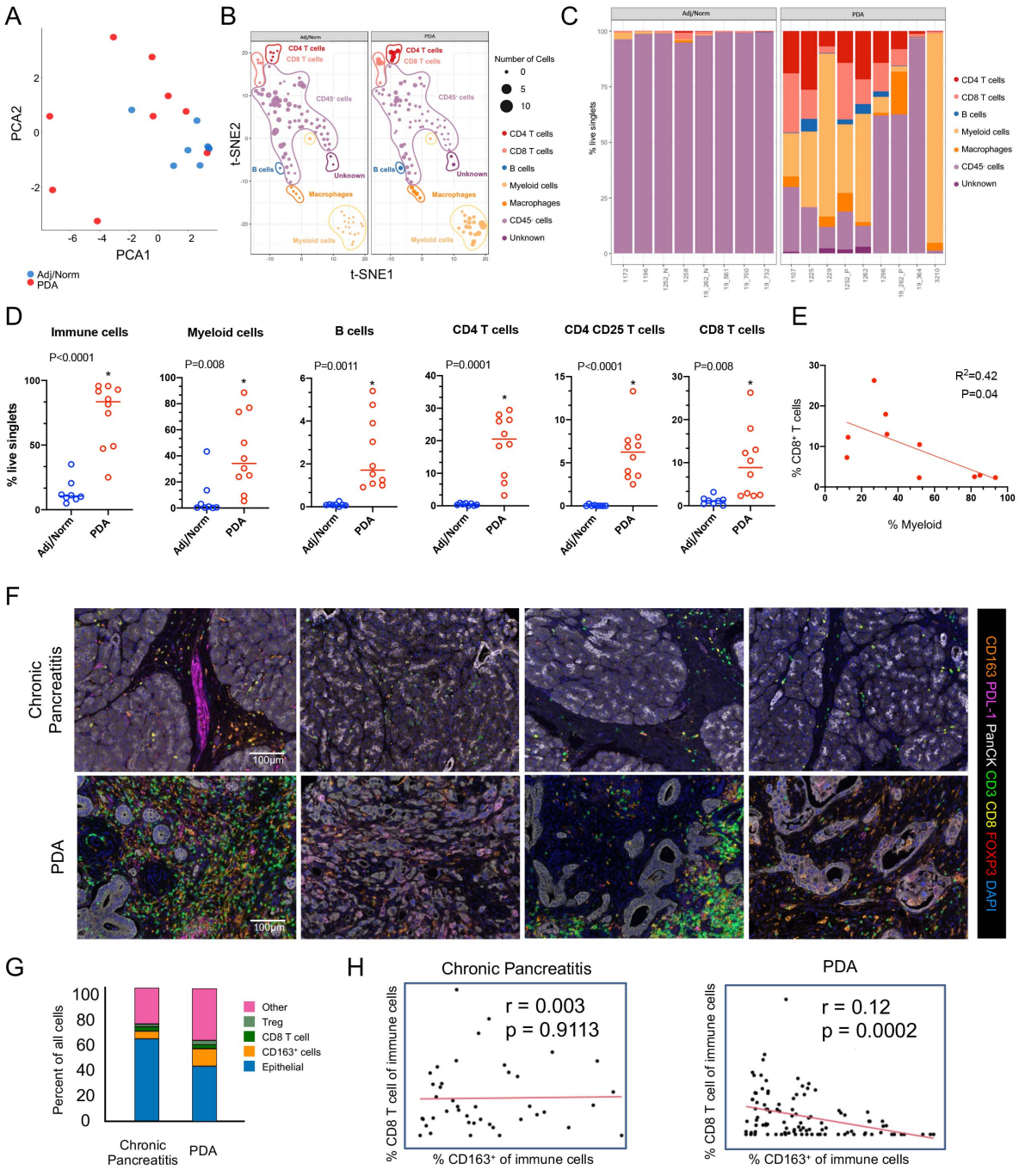
A
PCA2
PCA1
Adj/Norm
PDA
B
t-SNE2
t-SNE1
CD4 T cells
CD8 T cells
CD45- cells
B cells
Unknown
Macrophages
Myeloid cells
Number of Cells
0
5
10
CD4 T cells
CD8 T cells
B cells
Myeloid cells
Macrophages
CD45- cells
Unknown
C
Adj/Norm
PDA
% live singlets
CD4 T cells
CD8 T cells
B cells
Myeloid cells
Macrophages
CD45- cells
Unknown
D
Immune cells
Myeloid cells
B cells
CD4 T cells
CD4 CD25 T cells
CD8 T cells
P<0.0001
P=0.008
P=0.0011
P=0.0001
P<0.0001
P=0.008
% live singlets
Adj/Norm
PDA
E
R2=0.42
P=0.04
% CD8+ T cells
% Myeloid
F
Chronic Pancreatitis
PDA
100μm
CD163 PDL-1 PanCK CD3 CD8 FOXP3 DAPI
G
Percent of all cells
Other
Treg
CD8 T cell
CD163+ cells
Epithelial
Chronic Pancreatitis
PDA
H
Chronic Pancreatitis
r = 0.003
p = 0.9113
% CD8 T cell of immune cells
% CD163+ of immune cells
PDA
r = 0.12
p = 0.0002
% CD8 T cell of immune cells
% CD163+ of immune cells

Figure 2.2 CyTOF and multiplex fluorescent immunohistochemistry (mfIHC) mapping reveals heterogeneous immune infiltration in human pancreatic cancer.
(A) PCA analysis comparing intensity of marker staining of n=8 normal or adjacent pancreata tissue samples (blue) compared to n=9 PDA tumor samples (red). (B) Merged adj/norm panc (left) and PDA (right) t-SNE analysis of defined cell clusters from CyTOF analysis on tissue samples. The size of the dot represents the number of cells in the cluster. Each color represents a cell population: CD4 T cells (red), CD8 T cells (pink), B cells (blue), Myeloid (light orange), Macrophages (orange), CD45- cells (light purple), Unknown (purple). (C) Bar plot representation from FlowSOM CyTOF analysis of n=8 adj/norm tissue samples and n=9 PDA tumor samples. Analysis was only performed on samples with greater than 3,000 live singlets. (D) Manual quantitation of total immune cells (CD45+), myeloid cells (CD11b+), CD4+ T cells, CD8+ T cells, potential Tregs (CD4+ CD25+), and B cells. Manual gating included n=8 adj/norm patients and n=10 PDA patients per group. Asterisk denotes a p-value less than 0.05 determined by two-sided Student's t-test. (E) Correlation plot of total CD11b+ myeloid cells compared to total CD8+ T cells. (F) mfIHC composite images of formalin-fixed, paraffin-embedded tissue specimens from four different patients with chronic pancreatitis (top row) and four patients with PDA (bottom row). Antibodies and colors are as follows: CD163 (orange), PD-L1 (magenta), Pancytokeratin (PanCK; white), CD3 (green), CD8 (yellow), FOXP3 (red), and DAPI (blue). (G) Comparison of cellular infiltration between n=34 chronic pancreatitis patients and n=71 PDA patients (P-values: Other 0.0001, CD163+ cells 0.020, CD8+ T cells 0.3483, Treg <0.0001, Epithelial <0.0001). (H) Correlation between percentage of CD8+ T cells and CD163+ cells in chronic pancreatitis and PDA.

Figure 2.3

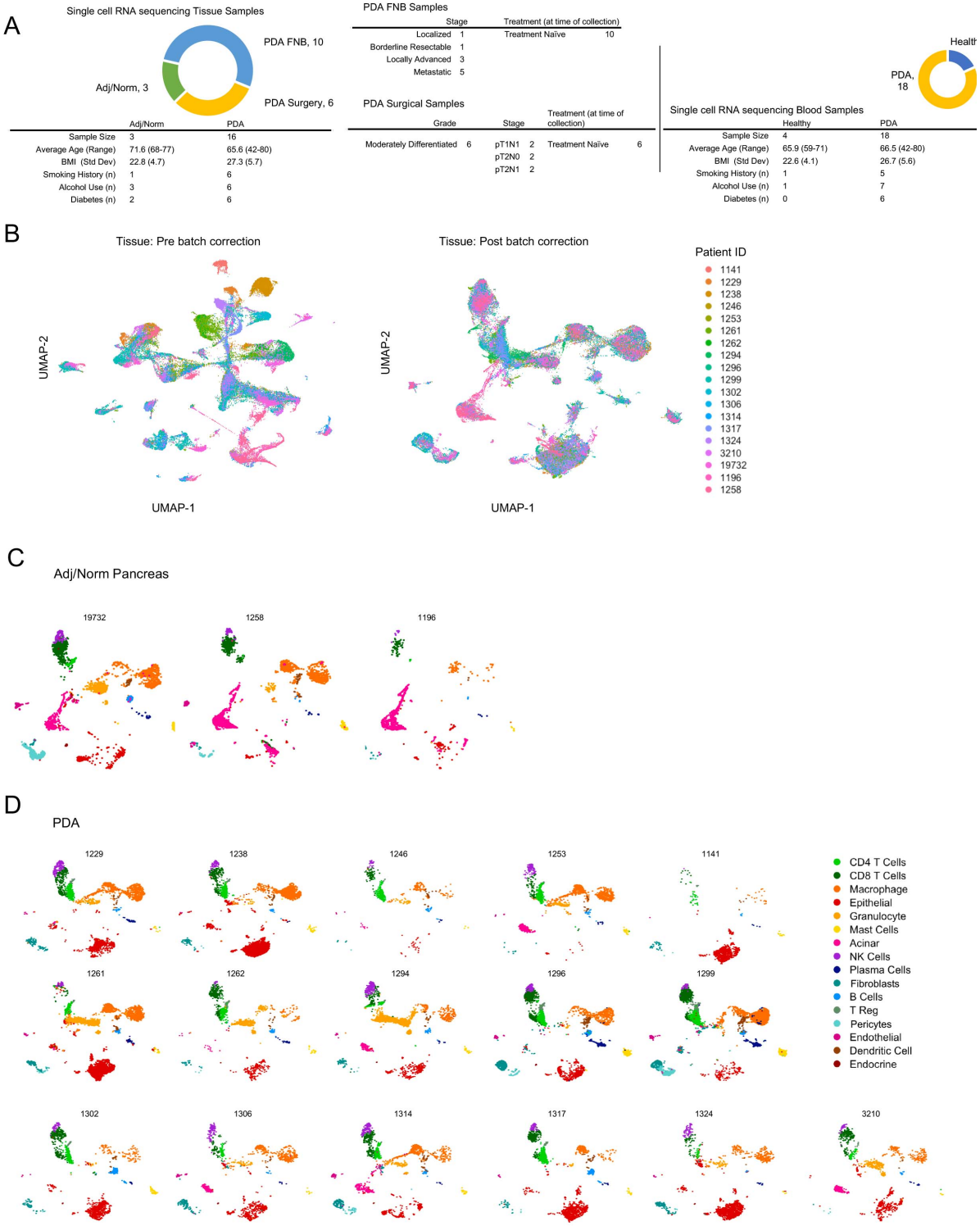
A
Single cell RNA sequencing Tissue Samples
Adj/Norm, 3
PDA FNB, 10
PDA Surgery, 6
Adj/Norm PDA
Sample Size 3 16
Average Age (Range) 71.6 (68-77) 65.6 (42-80)
BMI (Std Dev) 22.8 (4.7) 27.3 (5.7)
Smoking History (n) 1 6
Alcohol Use (n) 3 6
Diabetes (n) 2 6
PDA FNB Samples
Stage
Localized 1
Borderline Resectable 1
Locally Advanced 3
Metastatic 5
Treatment (at time of collection)
Treatment Naïve 10
PDA Surgical Samples
Grade
Moderately Differentiated 6
Stage
pT1N1 2
pT2N0 2
pT2N1 2
Treatment (at time of collection)
Treatment Naïve 6
Single cell RNA sequencing Blood Samples
PDA, 18
Healthy PDA
Sample Size 4 18
Average Age (Range) 65.9 (59-71) 66.5 (42-80)
BMI (Std Dev) 22.6 (4.1) 26.7 (5.6)
Smoking History (n) 1 5
Alcohol Use (n) 1 7
Diabetes (n) 0 6
B
Tissue: Pre batch correction
Tissue: Post batch correction
UMAP-1
UMAP-2
Patient ID
1141
1229
1238
1246
1253
1261
1262
1294
1296
1299
1302
1306
1314
1317
1324
3210
19732
1196
1258
C
Adj/Norm Pancreas
19732
1258
1196
D
PDA
1229
1238
1246
1253
1141
1261
1262
1294
1296
1299
1302
1306
1314
1317
1324
3210
CD4 T Cells
CD8 T Cells
Macrophage
Epithelial
Granulocyte
Mast Cells
Acinar
NK Cells
Plasma Cells
Fibroblasts
B Cells
T Reg
Pericytes
Endothelial
Dendritic Cell
Endocrine

Figure 2.3 Single cell RNA sequencing reveals heterogenous immune infiltration in PDA tissue.
(A) Single cell RNA sequencing tissue sample breakdown (n = 3 Adj/Norm tissue, n=10 PDA tissue from fine needle biopsy, and n=6 PDA tissue from surgical resection), patient clinical data, and tumor characteristics (grade and stage) (Left panel). Breakdown of sequenced PBMC samples with corresponding patient clinical data (Right panel). (B) UMAP of the merged tissue colored by Patient ID prior to batch correction (Left panel) and post batch correction (Right panel). (C) UMAP of 3 individual adjacent/normal samples and (D) 16 PDA tissues. We distinguished two epithelial populations: tumor cells and acinar cells. In the non-epithelial compartment, we identified fibroblasts, pericytes, $CD8^+$ T cells, $CD4^+$ T cells, Tregs, NK cells, B cells, plasma cells, mast cells, macrophages, granulocytes, dendritic cells, endothelial cells, and a small endocrine population.

Figure 2.4

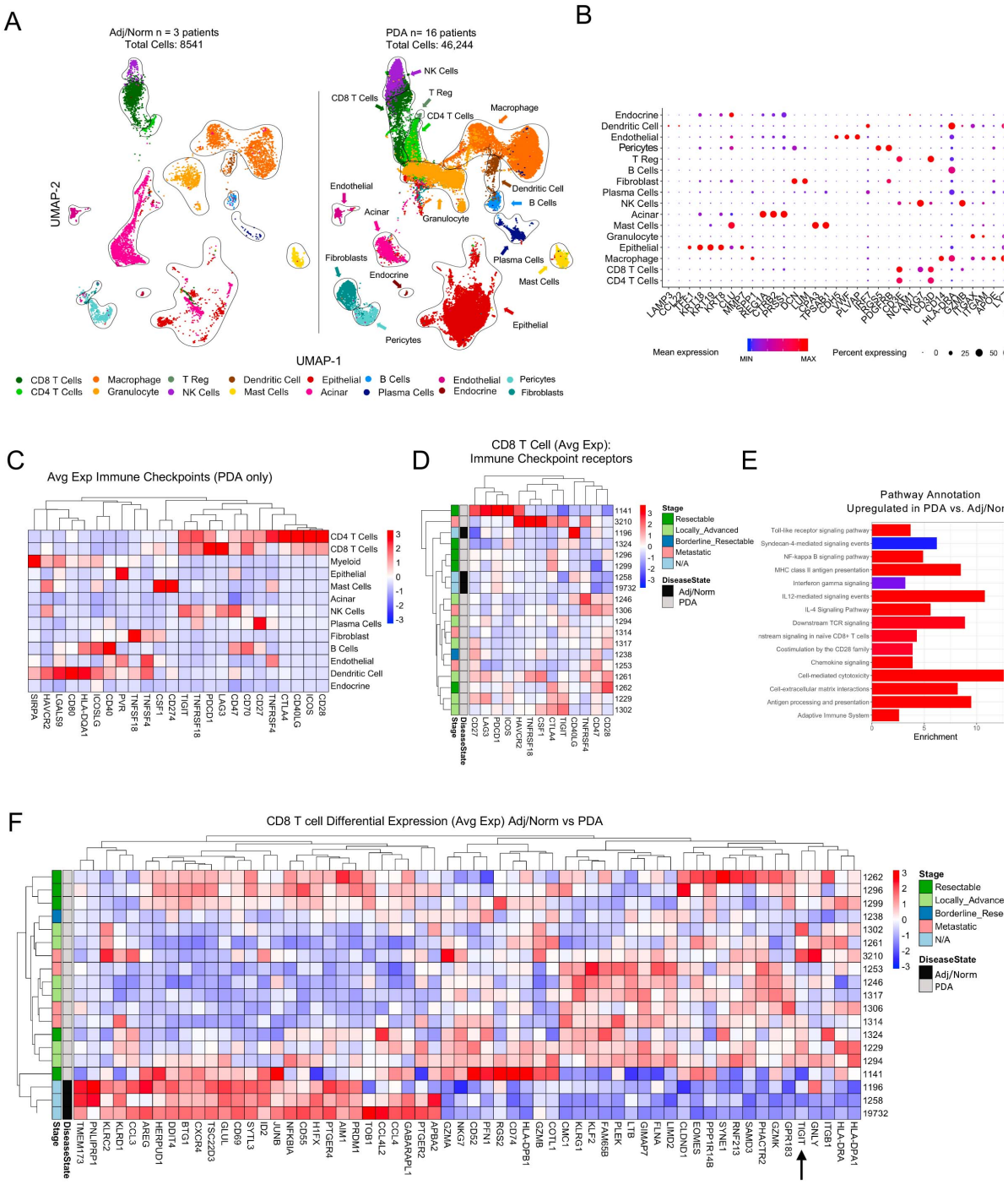
A
Adj/Norm n = 3 patients
Total Cells: 8541
PDA n= 16 patients
Total Cells: 46,244
UMAP-2
UMAP-1
CD8 T Cells
CD4 T Cells
Macrophage
Granulocyte
T Reg
NK Cells
Dendritic Cell
Mast Cells
Epithelial
Acinar
B Cells
Plasma Cells
Endothelial
Endocrine
Pericytes
Fibroblasts
B
Mean expression
MIN
MAX
Percent expressing
C
Avg Exp Immune Checkpoints (PDA only)
D
CD8 T Cell (Avg Exp):
Immune Checkpoint receptors
Stage
Resectable
Locally_Advanced
Borderline_Resectable
Metastatic
N/A
DiseaseState
Adj/Norm
PDA
E
Pathway Annotation
Upregulated in PDA vs. Adj/Nor
Enrichment
F
CD8 T cell Differential Expression (Avg Exp) Adj/Norm vs PDA

Figure 2.4 Single cell RNA sequencing reveals heterogenous expression of immune checkpoints in PDA tissue.
(A) UMAP on 3 adjacent/normal pancreas (left) and 16 PDA patient (right) tissues. Populations identified as follows: acinar (pink), epithelial (red), fibroblasts (dark and light teal), $CD8^+$ T cells (dark green), $CD4^+$ T cells, (neon green), Tregs (light green), NK cells (purple), B cells (light blue), plasma cells (dark blue), mast cells (yellow), macrophages (dark orange), granulocytes (light orange), dendritic cells (brown), endothelial cells (dark pink), and endocrine (dark red). (B) Dot plot of key markers used to define the identified cell populations. Color of dot represents average expression, while the size of the dot represents percent expression. Dot plot represents merged n=3 adj/norm patients and n=16 PDA patients gene expression of lineage markers. (C) Average expression of immune checkpoint ligands and receptors in the identified cell populations in n=16 tumor tissue samples. (D) Average expression of immune checkpoint receptors on $CD8^+$ T cells in n=16 PDA patients and n=3 adj/norm patients merged tissues. (E) Pathway annotations from gene set enrichment analysis (GSEA) using the R package *clusterprofiler* in n=16 PDA samples compared to n=3 adj/norm samples. The color of the bar represents the p-value adjusted for multiple comparisons using the Benjamini Hochberg method. Enrichment score is plotted on the x-axis. (F) Unbiased differential expression between $CD8^+$ T cells from adj/norm pancreas (black) and PDA (grey). Significantly up- and down-regulated genes are plotted as average expression per patient. This analysis was performed on all $CD8^+$ T cells found in the adjacent/normal and PDA tissue. Disease stage is plotted on the left: resectable (green), locally advanced (light green), borderline resectable (blue), metastatic (pink), N/A (light blue).

Figure 2.5

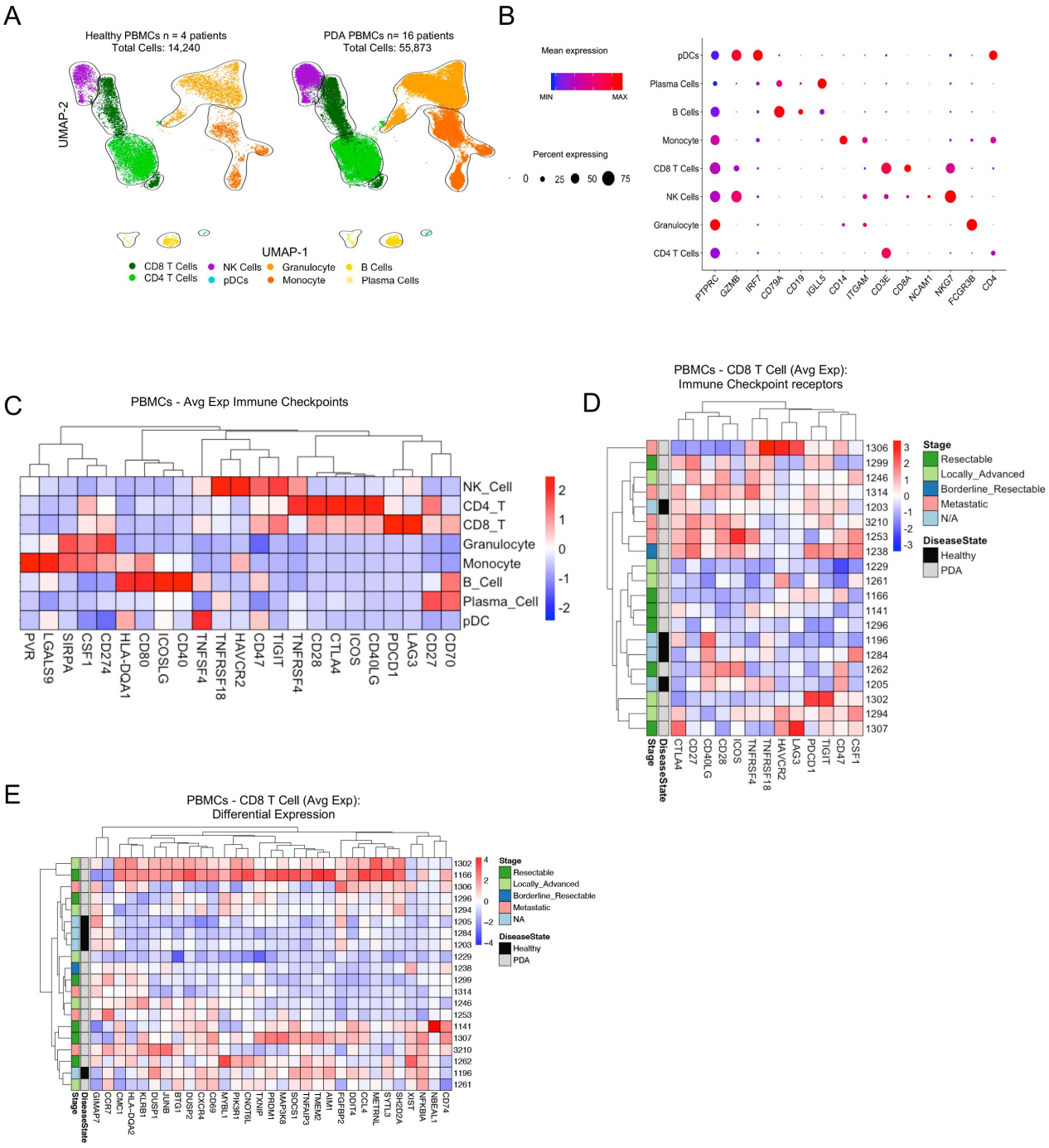
A
Healthy PBMCs n = 4 patients
Total Cells: 14,240
PDA PBMCs n= 16 patients
Total Cells: 55,873
UMAP-2
UMAP-1
CD8 T Cells
CD4 T Cells
NK Cells
pDCs
Granulocyte
Monocyte
B Cells
Plasma Cells
B
Mean expression
MIN
MAX
Percent expressing
0
25
50
75
pDCs
Plasma Cells
B Cells
Monocyte
CD8 T Cells
NK Cells
Granulocyte
CD4 T Cells
PTPRC
GZMB
IRF7
CD79A
CD19
IGLL5
CD14
ITGAM
CD3E
CD8A
NCAM1
NKG7
FCGR3B
CD4
C
PBMCs - Avg Exp Immune Checkpoints
NK_Cell
CD4_T
CD8_T
Granulocyte
Monocyte
B_Cell
Plasma_Cell
pDC
PVR
LGALS9
SIRPA
CSF1
CD274
HLA-DQA1
CD80
ICOSLG
CD40
TNFSF4
TNFRSF18
HAVCR2
CD47
TIGIT
TNFRSF4
CD28
CTLA4
ICOS
CD40LG
PDCD1
LAG3
CD27
CD70
D
PBMCs - CD8 T Cell (Avg Exp):
Immune Checkpoint receptors
Stage
Resectable
Locally_Advanced
Borderline_Resectable
Metastatic
N/A
DiseaseState
Healthy
PDA
Stage
DiseaseState
CTLA4
CD27
CD40LG
CD28
ICOS
TNFRSF4
TNFRSF18
HAVCR2
LAG3
PDCD1
TIGIT
CD47
CSF1
E
PBMCs - CD8 T Cell (Avg Exp):
Differential Expression
Stage
Resectable
Locally_Advanced
Borderline_Resectable
Metastatic
NA
DiseaseState
Healthy
PDA
Stage
DiseaseState
GIMAP7
CCR7
CMC1
HLA-DQA2
KLRB1
DUSP1
JUNB
BTG1
DUSP2
CXCR4
CD69
MYBL1
PIK3R1
CNOT6L
TXNIP
PRDM1
MAP3K8
SOCS1
TNFAIP3
TMEM2
AIM1
FGFBP2
DDIT4
CCL4
METRNL
SYTL3
SH2D2A
XIST
NFKBIA
NBEAL1
CD74

Figure 2.5 Single Cell RNA Sequencing of PDA PBMCs reveals heterogeneous cellular composition and expression of immune checkpoints.
(A) Merged UMAP plots of PBMCs from 4 healthy donors and 16 PDA patients (total of 70,113 cells). CD8 T cells (green), CD4 T cells (light green), NK cells (purple), pDCs (blue), Granulocyte (light orange), Monocyte (orange), B cells (yellow), Plasma cells (light yellow). (B) Dot plot analysis of key markers to define the 8 identified cell populations. Color of dot represents average expression, while the size of the dot represents percent expression. Dot plot represents merged healthy (n=4) and PDA (n=16) patient gene expression of PBMC lineage markers. (C) Average expression of immune checkpoint ligands and receptors in the identified cell populations in merged blood samples. (D) Average expression of immune checkpoint receptors on $CD8^+$ T cells in merged PBMCs. (E) Average expression of differentially expressed genes in $CD8^+$ T cells comparing healthy (black) to PDA (grey) PBMCs. Disease stage is plotted on the left.

Figure 2.6

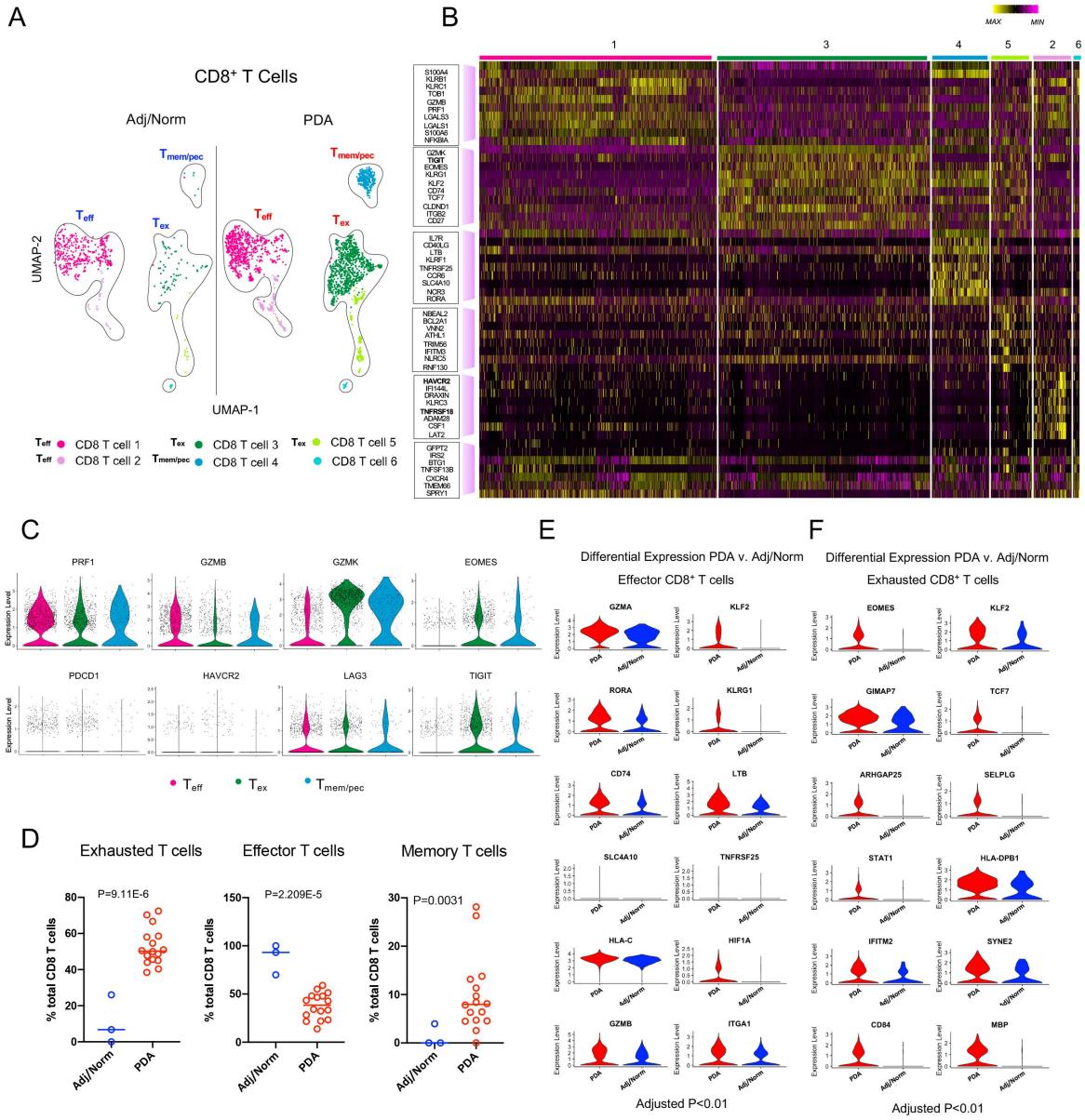

Figure 2.6 Single cell RNA sequencing reveals exhausted CD8⁺ T cell phenotype in PDA patients is defined by the immune checkpoint *TIGIT*.
(A) UMAP analysis of CD8⁺ T cells from n=3 adjacent/normal pancreas samples (left) and n=16 PDA tumors (right). The 6 identified subsets of CD8⁺ T cells were collapsed into potential memory (blue), effector (pink) and exhausted (green). (B) Single cell resolution heatmap analysis of top 10 genes for each identified CD8⁺ T cell subset. (C) Violin plots of normalized expression for selected markers mapped across the CD8⁺ T cell subsets. (D) Quantitation of potential exhausted (p=9.11E-6), effector (p=2.209E-5) and memory (p=0.0031) T cells in adjacent/normal pancreas and PDA patients, plotted as % total CD8⁺ T cells. Plots represent n=3 adj/norm and n=16 PDA patients. Two-sided Student's *t*-test was performed to compare between groups and a p value of 0.05 or less was considered statistically significant. Panel of genes differentially expressed in (E) effector and (F) exhausted CD8⁺ T cells in PDA (red) compared to adjacent/normal pancreas (blue). Plots represent n=3 adj/norm and n=16 PDA patients. Violin plots are shown as normalized expression. All violin plots in (E) and (F) have an adjusted p-value of p<0.01 and are considered statistically significant.

Figure 2.7

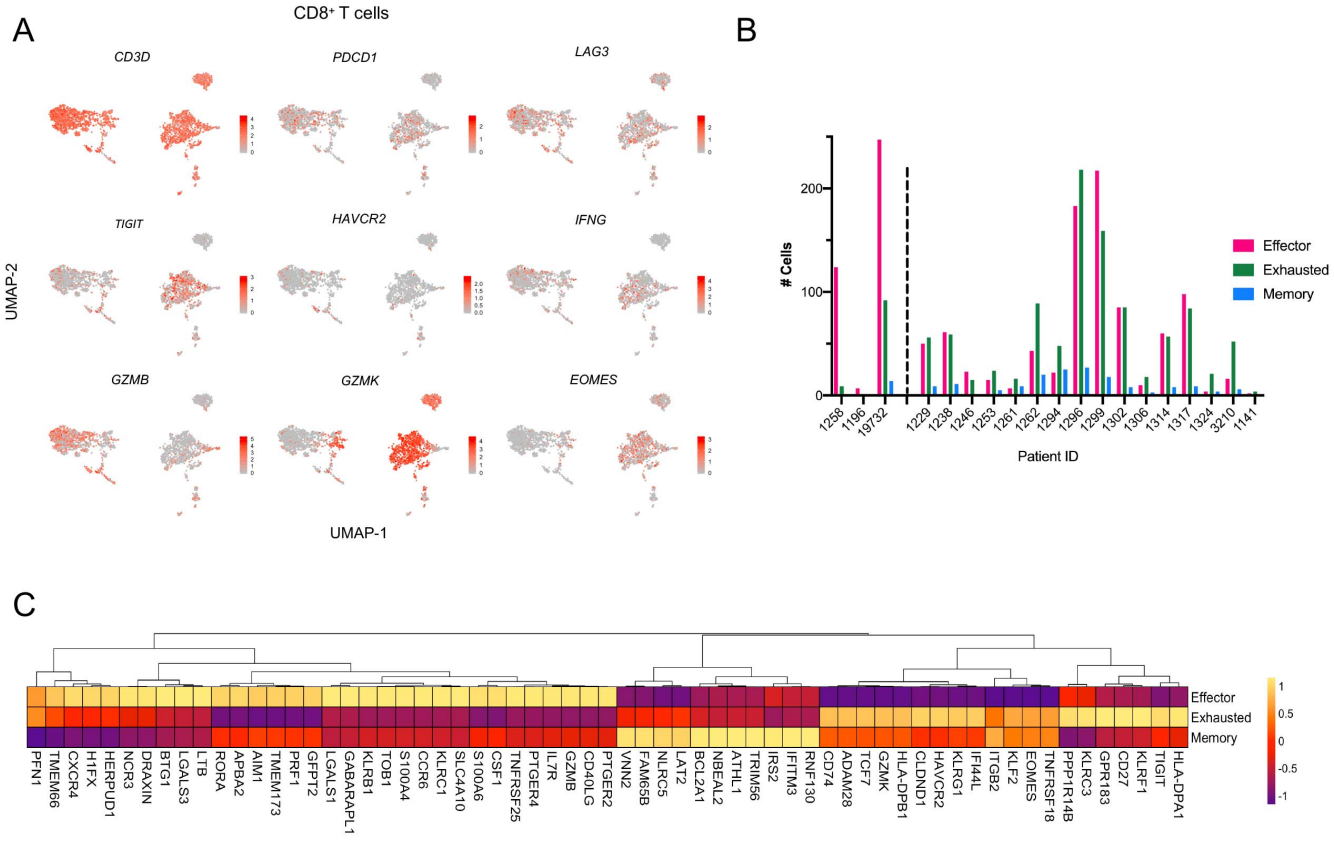

Figure 2.7 Single cell RNA sequencing reveals 3 CD8⁺ T cell populations: effector, exhausted, and memory CD8⁺ T cells.

(A) Feature plots of immune checkpoints (*PDCD1, LAG3, TIGIT, HAVCR2)*, activation markers (*IFNG, GZMB)*, and exhaustion markers *(GZMK, EOMES)* in CD8⁺ T cells. (B) Number of effector (pink), exhausted (green), and memory (blue) CD8⁺ T cells captured in each individual tissue sample by scRNA seq. (C) Average scaled expression heatmap of highly enriched genes by potential effector, exhausted, and memory cell populations. (n = 3 Adj/Norm tissue and n= 16 PDA tissue for panels A-C).

Figure 2.8

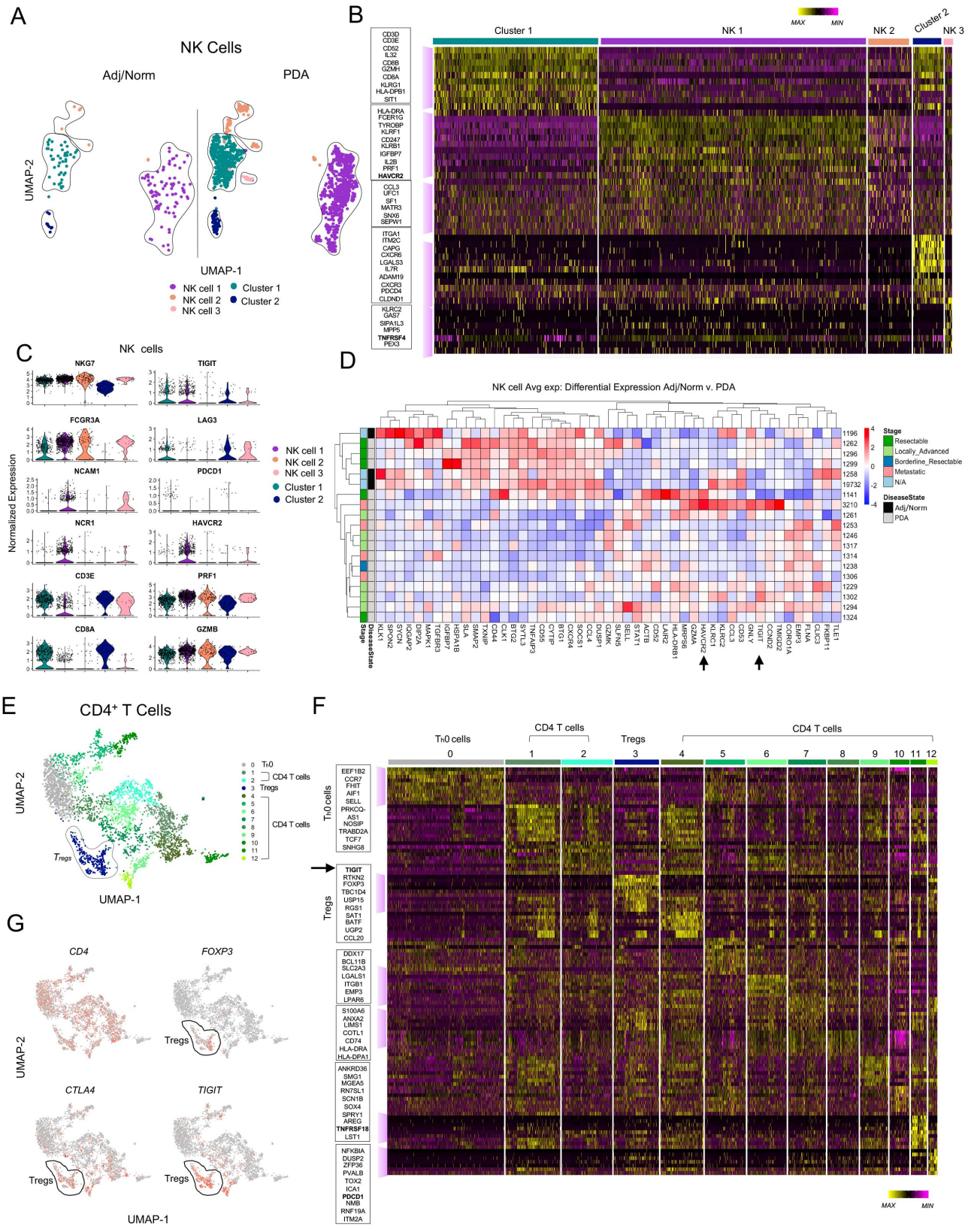
A
NK Cells
Adj/Norm
PDA
UMAP-2
UMAP-1
NK cell 1
NK cell 2
NK cell 3
Cluster 1
Cluster 2
B
MAX
MIN
Cluster 1
NK 1
NK 2
Cluster 2
NK 3
C
NK cells
NKG7
TIGIT
FCGR3A
LAG3
NCAM1
PDCD1
NCR1
HAVCR2
CD3E
PRF1
CD8A
GZMB
Normalized Expression
D
NK cell Avg exp: Differential Expression Adj/Norm v. PDA
Stage
Resectable
Locally_Advanced
Borderline_Resectable
Metastatic
N/A
DiseaseState
Adj/Norm
PDA
E
CD4⁺ T Cells
UMAP-2
UMAP-1
Tregs
Tn0
CD4 T cells
F
Tn0 cells
CD4 T cells
Tregs
G
CD4
FOXP3
CTLA4
TIGIT
UMAP-2
UMAP-1
Tregs

Figure 2.8 Single cell RNA sequencing of pancreatic tissues reveals *TIGIT* is differentially expressed in NK cells from PDA patients and is a defining marker of Tregs.
(A) Merged UMAP of 5 identified subsets of NK cells from adjacent/normal pancreas (left) and PDA (right). Plots represent n=3 adj/norm and n=16 PDA patients. (B) Single cell resolution heatmap of each NK cell subset identified. Immune checkpoints (*HAVCR2, TNFRSF4)* are bolded. (C) Violin plots of normalized average expression within NK cell subsets demonstrating specific lineage markers for NK cells (such as *NCAM1/FCGR3A*) and immune checkpoint receptors. (D) Unbiased differential average expression of merged NK cells from adjacent/normal pancreas (black) and PDA (grey). Disease stage is plotted on the left. (E) Merged UMAP of all $CD4^+$ T cells with 13 identified cell subsets. Naïve $CD4^+$ T cells are denoted as T_h0 (*CCR7*$^+$) and Tregs as Tregs (*FOXP3*$^+$). All other subsets are denoted as CD4 T cells. (F) Single cell resolution heatmap of each $CD4^+$ T cell subset. Boxes on the left designate naïve $CD4^+$ T cells (T_h0) and the $CD4^+$ T cell subsets that are defined by immune checkpoint expression (*TIGIT, TNFRSF18, PDCD1*). (G) Feature plots of *CTLA4* and *TIGIT* in regulatory $CD4^+$ T cells (outlined). In all panels, plots represent n=3 adj/norm and n=16 PDA patients.

Figure 2.9

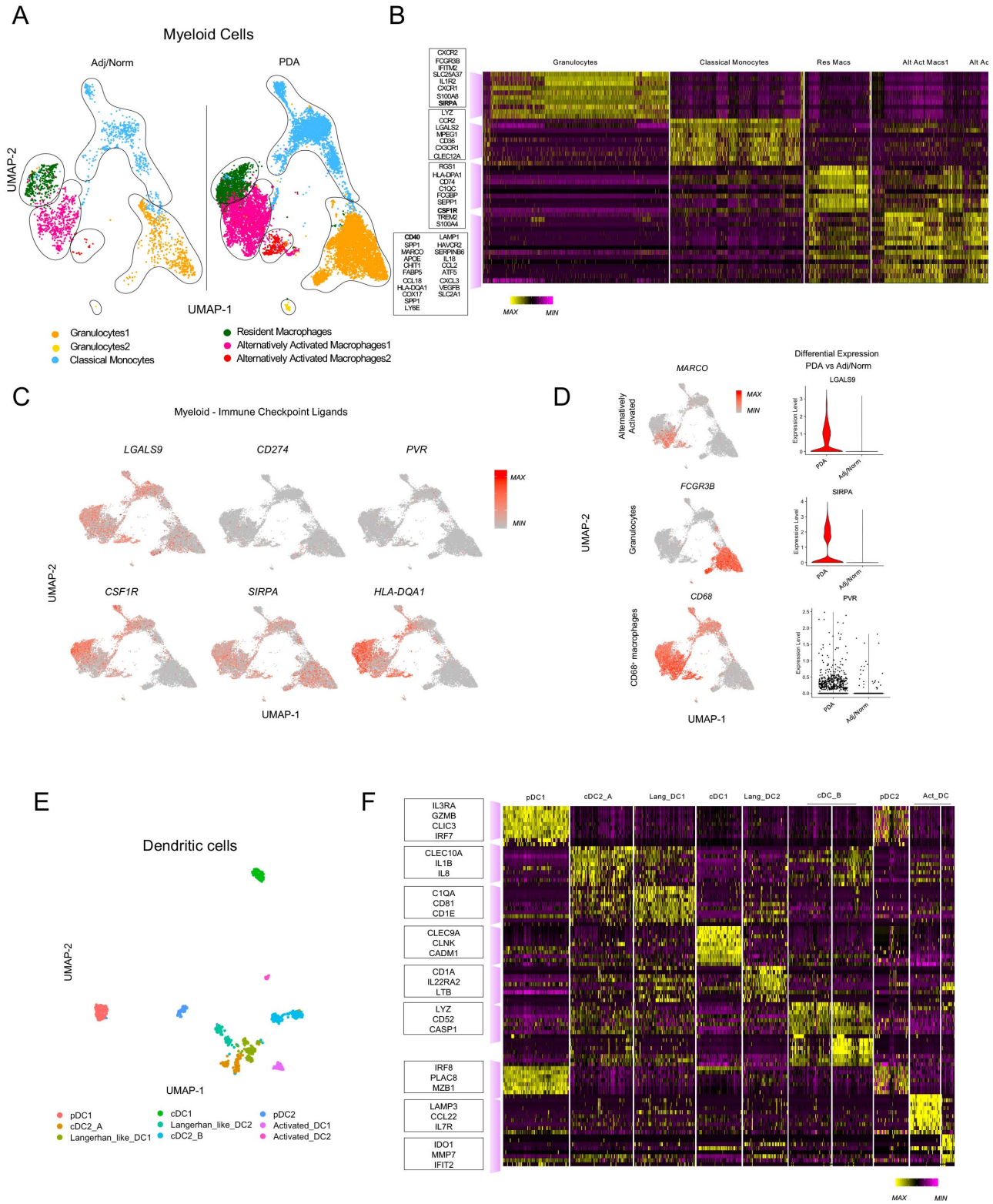
A
Myeloid Cells
Adj/Norm
PDA
UMAP-2
UMAP-1
Granulocytes1
Granulocytes2
Classical Monocytes
Resident Macrophages
Alternatively Activated Macrophages1
Alternatively Activated Macrophages2
B
Granulocytes
Classical Monocytes
Res Macs
Alt Act Macs1
Alt Ac
CXCR2 FCGR3B IFITM2 SLC25A37 IL1R2 CXCR1 S100A8 SIRPA
LYZ CCR2 LGALS2 MPEG1 CD36 CX3CR1 CLEC12A
RGS1 HLA-DPA1 CD74 C1QC FCGBP SEPP1 CSF1R TREM2 S100A4
CD40 SPP1 MARCO APOE CHIT1 FABP5 CCL18 HLA-DQA1 CCR17 SPP1 LY6E
LAMP1 HAVCR2 SERPINB6 IL18 CCL2 ATF5 CXCL3 VEGFB SLC2A1
MAX
MIN
C
Myeloid - Immune Checkpoint Ligands
LGALS9
CD274
PVR
CSF1R
SIRPA
HLA-DQA1
MAX
MIN
UMAP-2
UMAP-1
D
MARCO
Alternatively Activated
FCGR3B
Granulocytes
CD68
CD68- macrophages
UMAP-2
UMAP-1
MAX
MIN
Differential Expression
PDA vs Adj/Norm
LGALS9
SIRPA
PVR
Expression Level
PDA
Adj/Norm
E
Dendritic cells
UMAP-2
UMAP-1
pDC1
cDC2_A
Langerhan_like_DC1
cDC1
Langerhan_like_DC2
cDC2_B
pDC2
Activated_DC1
Activated_DC2
F
pDC1
cDC2_A
Lang_DC1
cDC1
Lang_DC2
cDC_B
pDC2
Act_DC
IL3RA GZMB CLIC3 IRF7
CLEC10A IL1B IL8
C1QA CD81 CD1E
CLEC9A CLNK CADM1
CD1A IL22RA2 LTB
LYZ CD52 CASP1
IRF8 PLAC8 MZB1
LAMP3 CCL22 IL7R
IDO1 MMP7 IFIT2
MAX
MIN

Figure 2.9 Single cell RNA sequencing reveals distinct myeloid and dendritic cell subsets.
(A) Merged UMAP of 6 identified myeloid cell subsets in adjacent/normal pancreas (left) and PDA (right). (B) Single cell resolution heatmap of each myeloid cell subset identified. Boxes on the left designate the top expressing genes for each myeloid subset. (C) Selected feature plots of the immune checkpoints, *LGALS9, CD274, PVR, CSF1R, SIRPA, HLA-DQA1* in myeloid cells. (D) Selected feature plots of markers that define alternatively activated macrophages, granulocytes, and total macrophage subsets (left) and violin plots of immune checkpoint ligands that are upregulated in PDA patients (right). (E) UMAP analysis of dendritic cells in merged normal/adjacent pancreas and PDA. (F) Top ten highly enriched gene signature analysis of dendritic cell subclusters identifying potential DC subsets, including plasmocytoid DCs (pDCs), Langerhans-like DCs (Lang_DCs), conventional DCs (cDCs), and activated DCs (Act_DCs). In all panels, plots represent n=3 adj/norm and n=16 PDA patients.

Figure 2.10

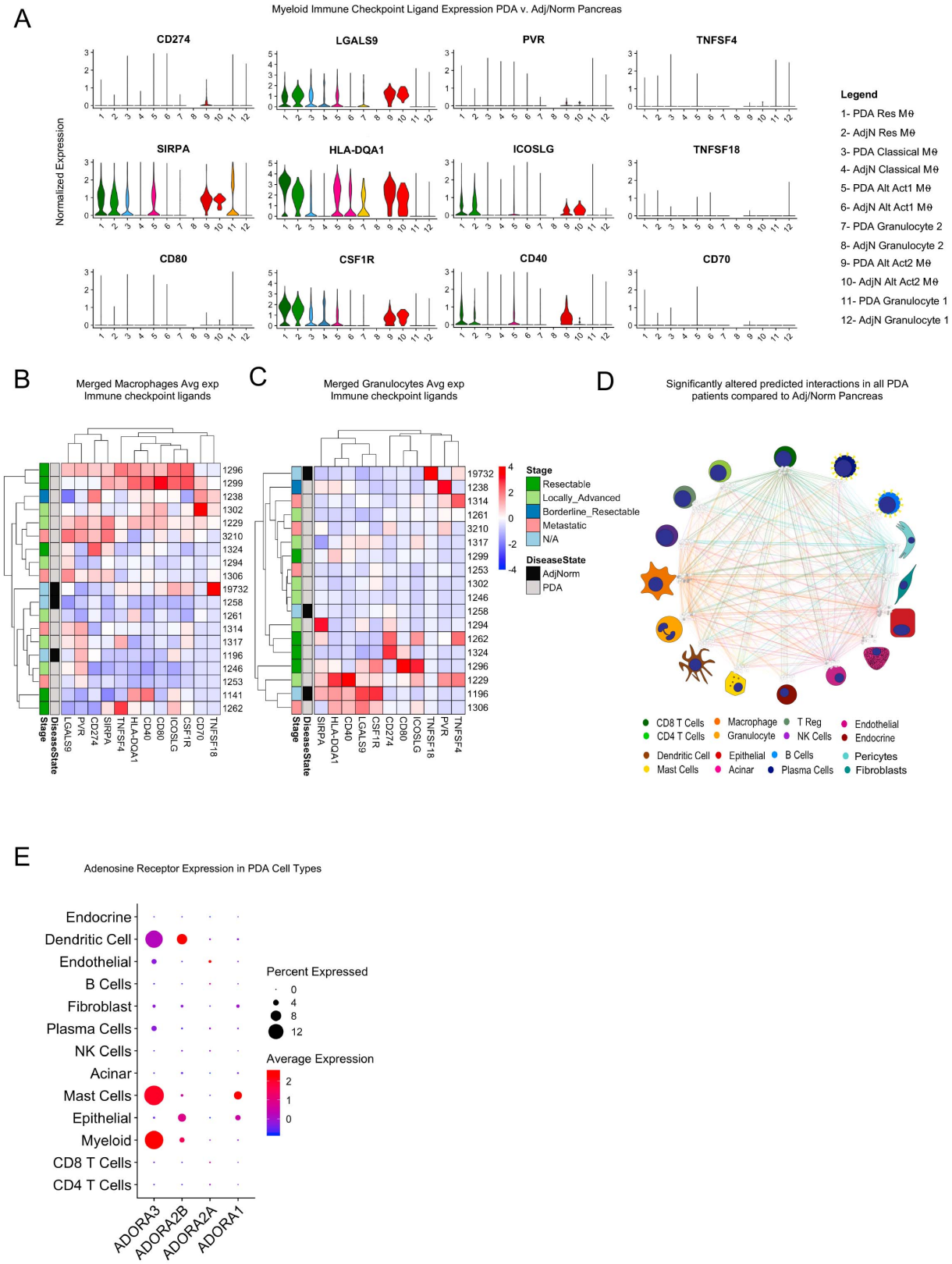
A
Myeloid Immune Checkpoint Ligand Expression PDA v. Adj/Norm Pancreas
CD274
LGALS9
PVR
TNFSF4
SIRPA
HLA-DQA1
ICOSLG
TNFSF18
CD80
CSF1R
CD40
CD70
Normalized Expression
Legend
1- PDA Res Mϕ
2- AdjN Res Mϕ
3- PDA Classical Mϕ
4- AdjN Classical Mϕ
5- PDA Alt Act1 Mϕ
6- AdjN Alt Act1 Mϕ
7- PDA Granulocyte 2
8- AdjN Granulocyte 2
9- PDA Alt Act2 Mϕ
10- AdjN Alt Act2 Mϕ
11- PDA Granulocyte 1
12- AdjN Granulocyte 1
B
Merged Macrophages Avg exp
Immune checkpoint ligands
C
Merged Granulocytes Avg exp
Immune checkpoint ligands
Stage
Resectable
Locally_Advanced
Borderline_Resectable
Metastatic
N/A
DiseaseState
AdjNorm
PDA
D
Significantly altered predicted interactions in all PDA
patients compared to Adj/Norm Pancreas
CD8 T Cells
CD4 T Cells
Macrophage
Granulocyte
T Reg
NK Cells
Endothelial
Endocrine
Dendritic Cell
Mast Cells
Epithelial
Acinar
B Cells
Plasma Cells
Pericytes
Fibroblasts
E
Adenosine Receptor Expression in PDA Cell Types
Endocrine
Dendritic Cell
Endothelial
B Cells
Fibroblast
Plasma Cells
NK Cells
Acinar
Mast Cells
Epithelial
Myeloid
CD8 T Cells
CD4 T Cells
ADORA3
ADORA2B
ADORA2A
ADORA1
Percent Expressed
Average Expression

Figure 2.10 Single cell RNA sequencing of myeloid subsets in human pancreatic cancer.
(A) Violin Plots illustrating comparison of immune checkpoint ligands in myeloid clusters in PDA vs. adjacent normal/pancreas samples. (B) Average expression heatmap of checkpoint ligands in merged macrophages (all cells expressing *CD68* within the myeloid population) and (C) merged granulocytes (all cells expressing *FCGR3B* within the myeloid population*)*. Left panels denote disease state (adjacent/normal vs. PDA tissue) and stage. (D) Map of all putative ligand receptor differential interactions that are upregulated in 16 PDA compared to 3 adjacent/normal pancreas. The line color denotes cellular source of the ligand, and putative interactions were visualized in Cytoscape® V3.7.1. (E) Dot plot analysis showing expression of adenosine receptors in PDA tumor cell types. Red indicates high expression, blue low expression, and the size of the dot is relative to the percent that marker is expressed. Dot plot represent n=16 PDA patient gene expression of adenosine receptors.

Figure 2.11

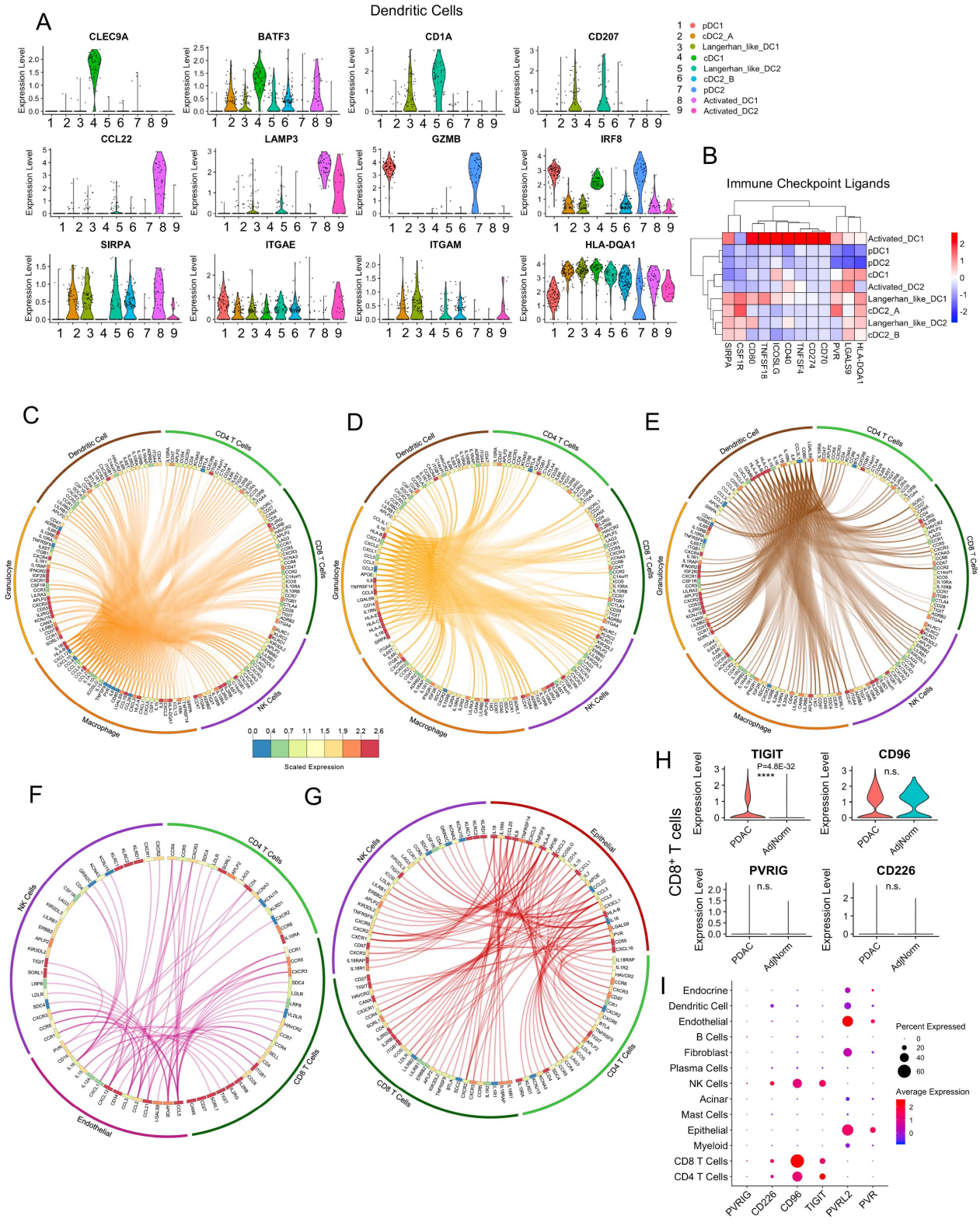
A
Dendritic Cells
CLEC9A
BATF3
CD1A
CD207
CCL22
LAMP3
GZMB
IRF8
SIRPA
ITGAE
ITGAM
HLA-DQA1
Expression Level
1 pDC1
2 cDC2_A
3 Langerhan_like_DC1
4 cDC1
5 Langerhan_like_DC2
6 cDC2_B
7 pDC2
8 Activated_DC1
9 Activated_DC2
B
Immune Checkpoint Ligands
Activated_DC1
pDC1
pDC2
cDC1
Activated_DC2
Langerhan_like_DC1
cDC2_A
Langerhan_like_DC2
cDC2_B
SIRPA
CSF1R
CD80
TNFSF18
ICOSLG
CD40
TNFSF4
CD274
CD70
PVR
LGALS9
HLA-DQA1
C
D
E
Dendritic Cell
CD4 T Cells
CD8 T Cells
NK Cells
Macrophage
Granulocyte
Scaled Expression
F
G
Endothelial
H
TIGIT
P=4.8E-32
****
CD96
n.s.
PVRIG
n.s.
CD226
n.s.
CD8+ T cells
PDAC
AdjNorm
I
Endocrine
Dendritic Cell
Endothelial
B Cells
Fibroblast
Plasma Cells
NK Cells
Acinar
Mast Cells
Epithelial
Myeloid
CD8 T Cells
CD4 T Cells
PVRIG
CD226
CD96
TIGIT
PVRL2
PVR
Percent Expressed
Average Expression

Figure 2.11 Predicted ligand receptor mapping in PDA patients demonstrate myeloid and non-immune cell types as sources of immune checkpoint ligands.
(A) Violin plots, where each dot represent a single cell, of select dendritic cell lineage markers across all 9 identified subsets. (B) Immune checkpoint ligand expression heatmap within dendritic subclusters. (C) Circos plot map of all putative ligand receptor interactions that are upregulated in PDA macrophages, (D) granulocytes, (E) dendritic cells, (F) endothelial cells (G) epithelial cells compared to adjacent/normal pancreas visualized by circos plot using the Circos software V0.69-9 (circos.ca). The heatmap within the circos plots is the scaled average expression of each gene within PDA tissue cell populations. The interactions plotted are those in which the expression level of either the ligand, the receptor, or both are increased in expression in PDA samples compared to adjacent/normal tissue. (H) Violin plots for the normalized expression of *TIGIT*, *CD96*, and *CD226* in $CD8^+$ T cells in PDA (red) compared to adjacent/normal pancreas (blue). Between adj/norm and PDA groups, the asterisk indicates $P<0.0001$, and exact $P=4.8E-32$. For Figure 6 panels A through H, n=3 adj/norm samples were examined and n=16 PDA patients were analyzed. (I) Dot plot analysis of TIGIT family members within PDAC tissue. Color of dot represents average expression, while the size of the dot represents percent expression. Dot plot represent n=16 PDA patients gene expression.

Figure 2.12

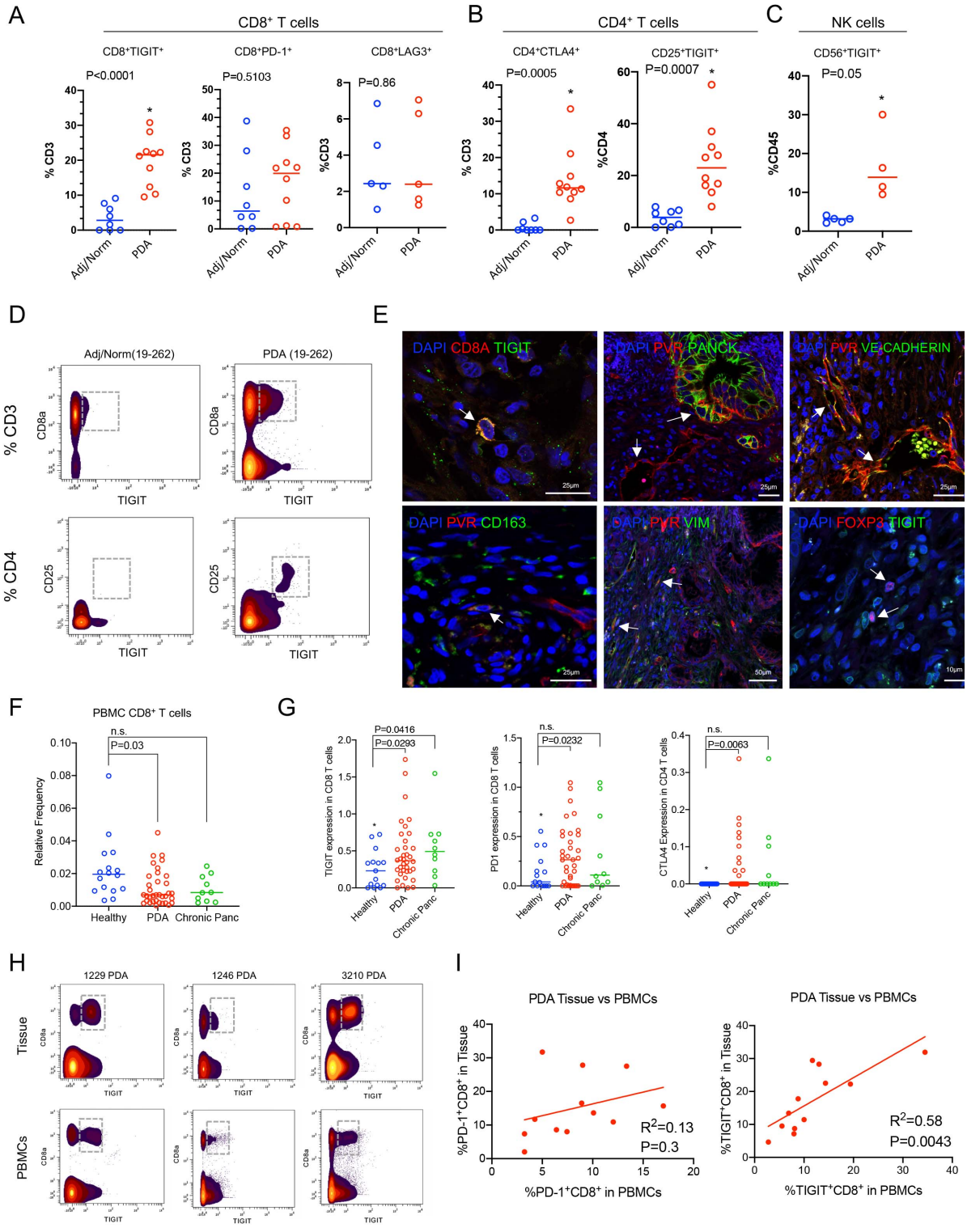
A
CD8⁺ T cells
CD8⁺TIGIT⁺
P<0.0001
CD8⁺PD-1⁺
P=0.5103
CD8⁺LAG3⁺
P=0.86
% CD3
%CD3
Adj/Norm
PDA
B
CD4⁺ T cells
CD4⁺CTLA4⁺
P=0.0005
CD25⁺TIGIT⁺
P=0.0007
%CD4
C
NK cells
CD56⁺TIGIT⁺
P=0.05
%CD45
D
Adj/Norm(19-262)
PDA (19-262)
% CD3
% CD4
CD8a
CD25
TIGIT
E
DAPI CD8A TIGIT
DAPI PVR PANCK
DAPI PVR VE-CADHERIN
DAPI PVR CD163
DAPI PVR VIM
DAPI FOXP3 TIGIT
F
PBMC CD8⁺ T cells
n.s.
P=0.03
Relative Frequency
Healthy
PDA
Chronic Panc
G
P=0.0416
P=0.0293
TIGIT expression in CD8 T cells
n.s.
P=0.0232
PD1 expression in CD8 T cells
P=0.0063
CTLA4 Expression in CD4 T cells
H
1229 PDA
1246 PDA
3210 PDA
Tissue
PBMCs
I
PDA Tissue vs PBMCs
%PD-1⁺CD8⁺ in Tissue
%PD-1⁺CD8⁺ in PBMCs
R²=0.13
P=0.3
%TIGIT⁺CD8⁺ in Tissue
%TIGIT⁺CD8⁺ in PBMCs
R²=0.58
P=0.0043

Figure 2.12 CyTOF and immunofluorescence protein validation of immune checkpoint expression in human pancreatic tissues and PBMCs.
Manual gating of CyTOF for immune checkpoints, including (A) TIGIT (n=8 adj/norm pancreas samples, n=10 PDA tumors), PD-1 (n=8 adj/norm pancreas samples, n=10 PDA tumors), and LAG3 (n=5 adj/norm pancreas samples, n=5 PDA tumors) in $CD8^+$ T cells, (B) CTLA4 in $CD4^+$ T cells (n=8 adj/norm pancreas samples, n=10 PDA tumors) and TIGIT in $CD25^+$ $CD4^+$ potential Tregs (n=8 adj/norm, n=10 PDA), and (C) $CD56^+$ NK cells in n=5 adjacent/normal pancreas samples and n=4 PDA tumor tissues. In Figure 7A-C two-sided Student's *t*-tests were performed and a p value of <0.05 was considered statistically significant. (D) Representative individual CyTOF biaxial density plots from normal adjacent and PDA tissue of a matched patient (19-262) of TIGIT expression in both CD8 T cells (as a percentage of total $CD3^+$ cells) and $CD25^+$ potential Tregs (as a percentage of $CD4^+$ cells). (E) PDA patient tissues, where 3 individual patient tumors were examined independently per staining analysis, were stained with antibodies against TIGIT with either CD8A ($CD8^+$ T cells) or FOXP3 (Tregs), and PVR with Pan-cytokeratin (epithelial cells), VE-cadherin (endothelial cells), CD163 (myeloid), or Vimentin (fibroblasts). (F) Quantitation of the percentage of $CD8^+$ T cells (of total live cells) from CyTOF of healthy, PDA, and chronic pancreatitis patient PBMCs. Quantitation of PBMC CyTOF data represent n=16 healthy, n=36 PDA, and n=10 chronic pancreatitis patients. In the healthy versus chronic pancreatitis comparison, the n.s. P value = 0.0702. (G) TIGIT and PD-1 transformed protein expression within $CD8^+$ T cells of healthy, PDA, and chronic pancreatitis patient PBMCs, and for the comparison between healthy and the chronic pancreatitis patients the n.s. P=0.1224. CTLA4 expression in $CD4^+$ T cells of healthy (n=16), PDA (n=36), and chronic pancreatitis (n=10) patient PBMCs, and for the comparison between healthy and the chronic pancreatitis patients the n.s. P=0.1216. In Figure 7F-G two-sided Student's *t*-tests were performed and a p value of <0.05 was considered statistically significant. (H) Representative biaxial plots of TIGIT expression in $CD8^+$ T cells in the tumor tissue and matched blood of three PDA patients (1229, 1246, 3210). (I) Correlation of CyTOF data from PDA patient tissue versus matched PBMC $CD8^+$ T cells expressing TIGIT and PD-1 (of total $CD3^+$ cells).

Figure 2.13

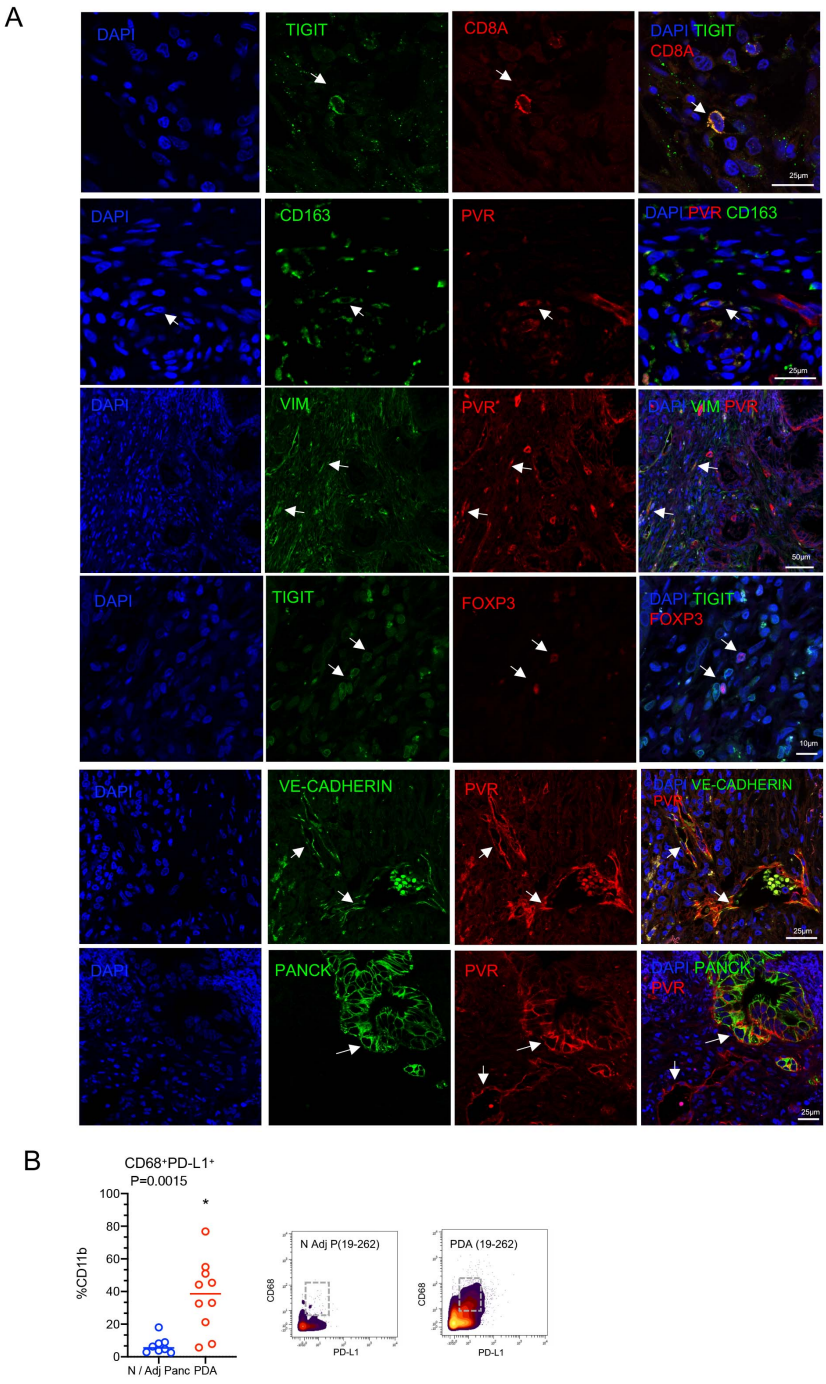

Figure 2.13 Immunofluorescence of immune checkpoints in pancreatic tumors.
(A) Individual channels of immunofluorescent staining of patient tissues with antibodies specific for TIGIT/CD8A, TIGIT/FOXP3, PVR/Pan-cytokeratin, PVR/CD163, PVR/Vimentin, and PVR/VE-cadherin. Three individual patient tumors were examined independently per staining analysis. (B) Manual gating of PD-L1$^+$ CD68$^+$ macrophages in normal adjacent (n=8) and PDA (n=10) tissue. Two-sided Student's *t*-test was performed, and asterisk indicates a p value of <0.05 was considered statistically significant. Representative individual CyTOF biaxial density plots from normal adjacent and PDA tissue of a matched patient (19-262) of PD-L1 expression in CD68$^+$ macrophages (as a percentage of total CD11b$^+$ cells).

Figure 2.14

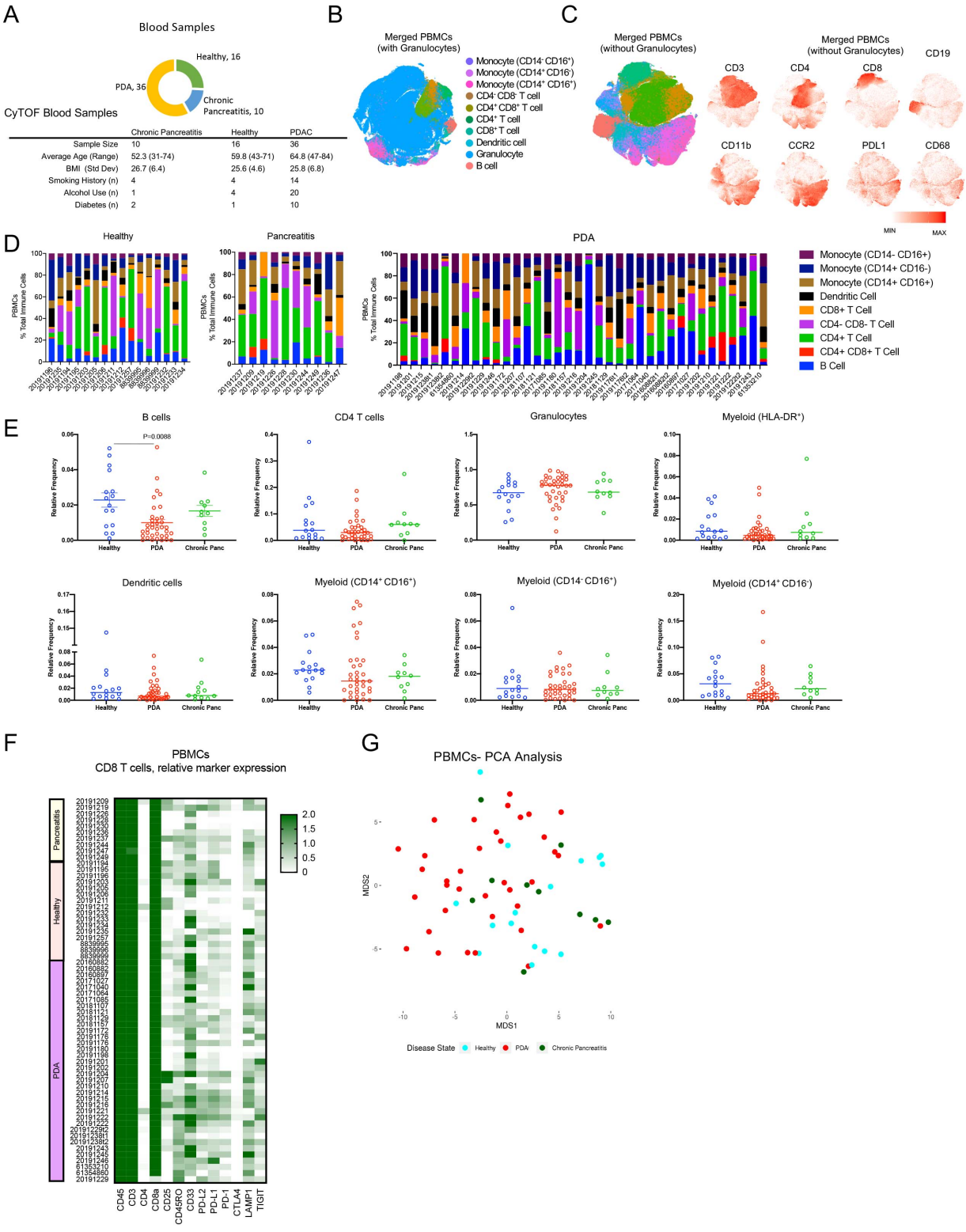
A
Blood Samples
Healthy, 16
PDA, 36
Chronic Pancreatitis, 10
CyTOF Blood Samples
Chronic Pancreatitis
Healthy
PDAC
Sample Size 10 16 36
Average Age (Range) 52.3 (31-74) 59.8 (43-71) 64.8 (47-84)
BMI (Std Dev) 26.7 (6.4) 25.6 (4.6) 25.8 (6.8)
Smoking History (n) 4 4 14
Alcohol Use (n) 1 4 20
Diabetes (n) 2 1 10
B
Merged PBMCs (with Granulocytes)
Monocyte (CD14- CD16+)
Monocyte (CD14+ CD16-)
Monocyte (CD14+ CD16+)
CD4- CD8- T cell
CD4+ CD8+ T cell
CD4+ T cell
CD8+ T cell
Dendritic cell
Granulocyte
B cell
C
Merged PBMCs (without Granulocytes)
Merged PBMCs (without Granulocytes)
CD3
CD4
CD8
CD19
CD11b
CCR2
PDL1
CD68
MIN
MAX
D
Healthy
Pancreatitis
PDA
PBMCs % Total Immune Cells
Monocyte (CD14- CD16+)
Monocyte (CD14+ CD16-)
Monocyte (CD14+ CD16+)
Dendritic Cell
CD8+ T Cell
CD4- CD8- T Cell
CD4+ T Cell
CD4+ CD8+ T Cell
B Cell
E
B cells
P=0.0088
CD4 T cells
Granulocytes
Myeloid (HLA-DR+)
Dendritic cells
Myeloid (CD14+ CD16+)
Myeloid (CD14- CD16+)
Myeloid (CD14+ CD16-)
Relative Frequency
Healthy
PDA
Chronic Panc
F
PBMCs
CD8 T cells, relative marker expression
Pancreatitis
Healthy
PDA
2.0
1.5
1.0
0.5
0
CD45
CD3
CD4
CD8a
CD25
CD45RO
CD33
PD-L2
PD-L1
PD-1
CTLA4
LAMP1
TIGIT
G
PBMCs- PCA Analysis
MDS2
MDS1
Disease State
Healthy
PDA
Chronic Pancreatitis

Figure 2.14 CyTOF analysis of PBMCs from healthy, chronic pancreatitis, and PDA patients.
(A) Patient breakdown and characteristics of CyTOF performed on patient blood samples (n = 16 healthy patients, n = 10 chronic pancreatitis patients, and n=36 PDA patients). (B) t-SNE analysis of CyTOF of all merged PBMC samples with granulocytes ($CD66b^+$). (C) t-SNE analysis of CyTOF of all merged PBMC samples without granulocytes. Key marker t-SNE feature plots of CD3 (total T cells), CD4 (Helper $CD4^+$ T cells), CD8 (Cytotoxic T cells), CD19 (B cells), CD11b (Myeloid cells), CCR2, PDL-1, and CD68 (Macrophage marker). (D) Bar plots of relative cell type abundance (B cell, $CD4^+/CD8^+$ T cell, $CD4^+$ T cell, $CD4^-/CD8^-$ T cell, Dendritic cell, $CD14^+/CD16^+$ Monocyte, $CD14^+/CD16^-$ Monocyte, and $CD14^-$ $CD16^+$ Monocyte) from CyTOF of PBMCs of healthy, chronic pancreatitis, and PDA patients. (E) Quantification of unbiased analysis (Astrolabe pipeline) of PBMC immune populations in n=16 healthy patients, n=36 PDA patients, and n=10 chronic pancreatitis patients. Two-sided Student's *t*-tests were performed to compare between groups and a p value of <0.05 was considered significant. (F) Relative CyTOF marker expression in $CD8^+$ T Cells from PDA tumor tissue. (G) PCA analysis of PBMCs at different disease states. Healthy (neon blue), PDA (red), and Chronic Pancreatitis (green).

Chapter 3 Apolipoprotein E Promotes Immune Suppression Through NF-κB Mediated CXCL1 Production in Pancreatic Cancer[5,6]

Abstract

Pancreatic ductal adenocarcinoma (PDA) is a lethal malignancy with few effective therapeutic options. PDA is characterized by an extensive fibroinflammatory stroma that includes abundant infiltrating immune cells. Tumor-associated macrophages (TAMs) are prevalent within the stroma and a key driver of immunosuppression. TAMs in human and murine pancreatic cancer are characterized by elevated expression of Apolipoprotein E (ApoE). ApoE is an apolipoprotein that mediates cholesterol metabolism and has known roles in cardiovascular disease and Alzheimer's disease. However, its role in pancreatic cancer has not been studied. We found that ApoE is also elevated in peripheral blood monocytes in PDA patients, and plasma protein levels stratify patient survival. To elucidate ApoE's functional role within the pancreatic cancer microenvironment, we orthotopically implanted mouse pancreatic cancer cells into syngeneic wild type or in $ApoE^{-/-}$ mice and observed reduced tumor growth in $ApoE^{-/-}$ mice. We then characterized tumors by histology and Mass Cytometry (CyTOF) and observed an increase in $CD8^{+}$ T

---

[5] Data from Chapter 3 have been submitted for publication at *Cancer Research* in a manuscript entitled, "Apolipoprotein E promotes immune suppression through NF-κB mediated CXCL1 production in pancreatic cancer" (2021).

[6] Author list: Samantha B. Kemp, Eileen S. Carpenter, Zeribe C. Nwosu, Nina G. Steele, Katelyn L. Donahue, Amanda Pacheco, Ashley Velez-Delgado, Rosa E. Menjivar, Fatima Lima, Stephanie The, Carlos Espinoza, Daniel Long, Yaqing Zhang, Costas A. Lyssiotis, Arvind Rao, Marina Pasca di Magliano*, Howard C. Crawford*
*Corresponding authors

cells in tumors from ApoE$^{-/-}$ mice. Mechanistically, we found that ApoE induces the expression of *Cxcl1* and *Cxcl5* – known immunosuppressive factors – in pancreatic cancer cells, through LDL receptor and NF-κB signaling. Taken together, our study reveals a novel immunosuppressive role of ApoE in the PDA microenvironment.

Introduction

Pancreatic ductal adenocarcinoma (PDA) is a lethal malignancy with a 5-year survival rate of only 10% (Siegel et al., 2020). PDA is characterized by a dense, fibroinflammatory stroma that includes abundant cancer-associated fibroblasts (CAFs) and infiltrating immune cells (Zhang et al., 2019c). These cell populations engage in a complex cellular crosstalk that results in a highly immunosuppressive tumor microenvironment (TME) (Clark et al., 2007). Re-activation of the immune response through checkpoint blockade has provided benefit for patients with other malignancies, but not for PDA patients, likely due to its insufficiency to overcome this robust immune suppression (Brahmer et al., 2012; Royal et al., 2010). A large body of work has determined that infiltrating myeloid cells are a key driver for the establishment of a suppressive immune TME (Mitchem et al., 2013; Stromnes et al., 2014; Zhang et al., 2017b; Zhu et al., 2017; Zhu et al., 2014). The myeloid compartment of the TME includes immature myeloid cells – or myeloid-derived suppressor cells (MDSCs) – and tumor-associated macrophages (TAMs) that block cytotoxic T cell-mediated immune responses (Clark et al., 2007).

Apolipoprotein E (ApoE/APOE) is secreted at high levels by hepatocytes (Bouma et al., 1988) and macrophages (Werb et al., 1986) throughout the body to mediate lipid

metabolism (Mahley, 1988). ApoE has been extensively studied in inflammatory conditions such as Alzheimer's disease and atherosclerosis (Mahley, 2016). Recently, a role for ApoE in carcinogenesis has emerged (Ren et al., 2019), but its role in pancreatic cancer is currently undefined. We thus investigated the functional role of ApoE in the PDA tumor microenvironment.

In this study, we show that *APOE* is expressed predominately by tumor-associated macrophages and fibroblasts in both mouse and human pancreatic cancer. Mice deficient in ApoE have reduced tumor burden, less fibrosis and an alteration in innate and adaptive immune infiltration. While we observed no change in macrophage infiltration or polarization status, mice deficient in ApoE had fewer monocytic-MDSCs and regulatory T cells (Tregs), suggesting loss of immunosuppressive cell populations. Conversely, mice deficient in ApoE had increased tumor infiltrating $CD8^+$ T cells. Bulk RNA sequencing of pancreatic tumor cells treated with recombinant ApoE showed upregulation of the chemokines *Cxcl1* and *Cxcl5*. Tumor-cell derived Cxcl1 has been shown to negatively regulate T cell infiltration in pancreatic cancer (Li et al., 2018a). Gene set enrichment analysis revealed that addition of ApoE upregulated NF-κB signaling in tumor cells. Further, inhibition of NF-κB signaling resulted in reduced induction of *Cxcl1* and *Cxcl5*. We propose that ApoE regulates T cell infiltration by upregulating tumor-cell derived chemokines mediated by activation of NF-κB signaling.

Results

Systemic *APOE* levels are elevated in PDA and correlate to patient survival

APOE has been extensively studied in cardiovascular disease and Alzheimer's disease, but its role in cancer is not fully elucidated. To determine which cell types express APOE in specific cellular compartments in human pancreatic cancer, we interrogated a human single cell RNA sequencing dataset (Steele et al., 2020), comprised of 16 PDA patient tumor tissue and 3 adjacent normal pancreas samples (**Fig. 3.1A**). In human tumors, *APOE* was highly expressed in myeloid cells and fibroblasts, as previously reported (Elyada et al., 2019) (**Fig. 3.1B** and **Fig. 3.2A**). Within the myeloid population, *APOE* was enriched in macrophage and alternatively activated macrophage populations, compared to the other myeloid populations, which had sparse expression of *APOE* (**Fig. 3.1C** and **3.1D**). Additionally, *APOE* was significantly elevated specifically in macrophages from human PDA compared to adjacent normal samples (**Fig. 3.1E**). Within the fibroblast population we identified a population of myofibroblastic-CAFs (myCAFs) and inflammatory-CAFs (iCAFs) that have been well described (Ohlund et al., 2017) (**Fig. 3.1F** and **Fig. 3.2B**). *APOE* was enriched in human iCAFs compared to myCAFs (**Fig. 3.1G**). However, unlike the macrophages, fibroblast expressed *APOE* did not differ between normal and cancer samples (**Fig. 3.1H**).

We next wanted to assess *APOE* expression in other sequencing datasets. Using published laser capture microdissection (LCM) data from matched epithelial and stromal samples from human pancreatic cancer (Maurer et al., 2019), we confirmed *APOE* was upregulated specifically in the stroma compared to the epithelium (**Fig. 3.2C**). We then utilized The Cancer Genome Atlas (TCGA) pancreatic cancer dataset comprised of 150 patients and stratified patients into *APOE* low and *APOE* high and observed a correlation between *APOE* expression and expression of *MARCO* and *TREM2*, markers of

alternatively activated macrophages (**Fig. 3.2D**) (Turnbull et al., 2006; van der Laan et al., 1999). To confirm the *APOE* high tumor signature is associated with macrophages we overlaid the top 250 genes of *APOE* high PDA tumors from two datasets (TCGA and International Cancer Genome Consortium (ICGC)) with that of *APOE*$^{+}$ macrophages from single-cell RNA sequencing of 16 human PDA tumors (Steele et al., 2020) (**Fig. 3.2E**). We found 26 genes that overlapped across all the datasets, strengthening the correlation between *APOE* expression and expression of other known macrophage markers (*C1QA, C1QB, MSR1, TREM2, HAVCR2, CD74)* (**Fig. 3.2E**).

We assessed the systemic alterations of *APOE* expression using a dataset of 16 human peripheral blood mononuclear cell (PBMC) samples and 4 healthy donors (Steele et al., 2020). Interestingly, of four distinct monocyte populations identified, one subset (monocyte population/cluster 1) was highly enriched for *APOE* expression (**Fig. 3.2F** and **3.2G**). Finally, *APOE* expression was increased in the peripheral monocytes of PDA patients, compared to healthy individuals, suggesting that elevated monocyte *APOE* expression represents a systemic response to the tumor (**Fig. 3.1I**). We then analyzed plasma samples from 15 healthy donors, 17 chronic pancreatitis patients, and 155 PDA patients and did not see a statistically significant increase in APOE concentration at the protein level in PDA plasma compared to healthy donors or chronic pancreatitis plasma (**Fig. 3.1J**). However, we observed outliers with very high APOE concentration among the pancreatic cancer plasma samples. We thus stratified patients based on APOE plasma levels and performed survival analysis. We found high plasma levels of APOE correlated with shorter survival (**Fig. 3.1K**). These data show that ApoE gene expression

is elevated in the monocytes and macrophages of PDA patients, and protein levels correlate with poor survival, suggesting that it may play a functional role in the disease.

APOE is highly expressed by tumor-associated macrophages

To determine if APOE plays a functional role in PDA, we turned to an established murine model of the disease, where 7940b cells, derived from the *Kras*$^{LSL\text{-}G12D/+}$; *Trp53*$^{LSL\text{-}R172H/+}$; *Pdx1-Cre* (KPC) mouse model of pancreatic cancer (Hingorani et al., 2005), were implanted directly into the pancreas of syngeneic mice. We then evaluated ApoE expression by immunostaining, and found it elevated in mouse tumors compared to the healthy pancreas controls, similar to our findings in human samples (**Fig. 3.3A** and **3.3B**). To determine the source of *ApoE* within the TME we performed single cell RNA sequencing on orthotopic KPC tumors (**Fig. 3.3C** and **Fig. 3.4A**) and, consistent with the human data, we detected highest expression of *ApoE* in macrophages, followed by fibroblasts (**Fig. 3.3D**). We next performed co-immunofluorescence staining for ApoE, macrophages (F4/80) and fibroblasts (alpha-smooth muscle actin (aSMA)) and confirmed ApoE expression most often overlapped with F4/80^{+} macrophages (**Fig. 3.3E**). Further, APOE^{+} macrophages were elevated in the orthotopic KPC tumor compared to the normal pancreas (**Fig. 3.4B**).

Macrophages are plastic cells that exist on a spectrum of polarization from an inflammatory state (referred to as M1) to an immunosuppressive state (referred to as M2) (Orecchioni et al., 2019). TAMs are distinct from both M1 and M2 macrophages, although they share markers with both (Chen et al., 2019). To determine which macrophage population produces ApoE, we performed an *in vitro* macrophage polarization assay. We

treated bone-marrow derived macrophage cultures with either M-CSF, LPS, IL-4 or pancreatic tumor cell conditioned media (CM) to polarize to M0, M1, M2, and TAM respectively (**Fig. 3.3F**) and assessed ApoE expression in the various conditions. Strikingly, ApoE was specifically upregulated in TAMs compared to other macrophage populations (**Fig. 3.3G**). In addition, ApoE protein was robustly secreted by TAMs and was absent in the culture media derived from ApoE $^{-/-}$ TAMs, as a negative control (**Fig. 3.3H**). Finally, we utilized the well-established iKras* mouse model of pancreatic neoplasia (Collins et al., 2012a), where oncogenic *Kras* expression is inducible and reversible. We induced oncogenic Kras* expression, followed by induction of acute pancreatitis, and harvested after 3 weeks of continuous oncogenic Kras expression, or from mice where oncogenic Kras was expressed for three weeks and then inactivated for three or seven days (**Fig. 3.4C**). We then stained the pancreata for ApoE. We observed elevated expression of ApoE in iKras* pancreata after 3 weeks of oncogenic Kras expression, when iKras* mice present with low-grade neoplasia, compared to control pancreata (**Fig. 3.4D** and **Fig. 3.4E**). Further, ApoE expression decreased upon inactivation of oncogenic Kras expression. (**Fig. 3.4D** and **Fig. 3.4E**). Thus, ApoE is specifically upregulated in TAMs and the upregulation occurs early during carcinogenesis and depends upon epithelial expression of oncogenic Kras.

APOE ablation reduces tumor burden and reprograms the tumor microenvironment

To evaluate the function of ApoE, we utilized germline ApoE knock-out mice (ApoE $^{-/-}$) for orthotopic implantation of syngeneic 7940b KPC cells, compared to wild-type (WT) C57BL/6J controls (**Fig. 3.5A**). Mice deficient in ApoE had moderately, but significantly

smaller tumors at endpoint compared to their WT controls. (**Fig. 3.5B**). No major differences were noted by histopathology analysis (**Fig. 3.5C**). Immunohistochemical analysis revealed complete loss of ApoE within the tumor compared to WT mice, as expected (**Fig. 3.5D** and **3.5E**). We then measured levels of proliferation by Ki-67 staining and saw no statistical difference (**Fig. 3.6A** and **Fig. 3.6B**). However, levels of apoptosis by cleaved caspase 3 (CC3) staining were significantly increased in tumors implanted in ApoE $^{-/-}$ mice compared to controls (**Fig. 3.5D** and **3.5E**). We next assessed aSMA^{+} expression and observed loss of aSMA^{+} fibroblasts along with reduced collagen deposition visualized by Trichrome stain (**Fig. 3.5D** and **3.5E**). Given the association of ApoE with macrophages we next evaluated total infiltration of macrophages by F4/80 staining and found no difference in total numbers (**Fig. 3.6A** and **Fig. 3.6B**). However, we noted an increased infiltration of CD3^{+} T cells in ApoE $^{-/-}$ mice (**Fig. 3.6A** and **Fig. 3.6B**), suggesting changes in the immune microenvironment.

To expand the immune characterization, we performed mass cytometry (CyTOF) on tumors from WT and ApoE $^{-/-}$ mice (**Fig. 3.7A**). Unbiased clustering visualized through t-distributed stochastic neighbor embedding (t-SNE) revealed populations of macrophages, MDSCs, CD8 T cells, CD4 T cells and B cells along with a small population of non-immune cells (**Fig. 3.7B** and **Fig. 3.8A**). Manual gating of the identified populations revealed no significant difference in total immune cells (CD45^{+}), B cells (CD45^{+} CD19^{+}), total myeloid cells (CD45^{+} CD11b^{+}), macrophages (CD11b^{+} F4/80^{+}), or changes in macrophage sub-populations (F4/80^{+} CD206^{+}; F4/80^{+} PD-L1^{+}) (**Fig. 3.7C**). Macrophage polarization, determined by expression of Programmed death-ligand 1 (PD-L1/*Cd274*), Arginase 1 (*Arg1*), Cd206 (*Mrc1*) and inducible nitric oxide synthase (*Nos2*), did not differ

between tumors of WT and ApoE $^{-/-}$ mice (**Fig. 3.8B**). Further, we isolated bone marrow derived monocytes and polarized to TAMs in both WT and ApoE $^{-/-}$ mice and saw an increase in *Arg1*, and a decrease in *Cd274* and *Tnf-a*, suggesting loss of ApoE has minor effects on macrophage polarization *in vitro* (**Fig. 3.8C**).

Another prominent population identified in the tumor were putative MDSCs (immature myeloid cells). Murine MDSCs have multiple subsets defined by expression of Ly-6C^{+} and Ly-6G^{+} (Bronte et al., 2016). Granulocytic-MDSCs (Ly-6C^{+} Ly-6G^{+}) did not differ (**Fig. 3.7C**). However, the monocytic-MDSC subset (Ly-6C^{+} Ly-6G^{-}) was decreased in ApoE $^{-/-}$ mice compared to controls, suggesting a potential diminishment of immune suppression (**Fig. 3.7C**). To explore this possibility further, we evaluated T cell populations by manual gating and found an increase in total T cells (CD45^{+} CD3^{+}), CD4 T cells (CD3^{+} CD4^{+}) and CD8 T cells (CD3^{+} CD8^{+}) (**Fig. 3.7C**). Interestingly, there was also a decrease in potential regulatory T cells (CD4^{+} CD25^{+}) (**Fig. 3.7C**). We performed co-immunofluorescence staining and confirmed the increase in CD8+ T cells in ApoE $^{-/-}$ mice (**Fig. 3.7D**). Taken together, the loss of monocytic-MDSCs and regulatory T cells along with the increase in cytotoxic T cell infiltration in ApoE $^{-/-}$ mice provides evidence for a functional role of ApoE in contributing to immune suppression within the TME through regulation of T cell infiltration.

APOE regulates *Cxcl1* expression in tumor cells and fibroblasts

To gain mechanistic insight on the role of ApoE, we then explored its effect on pancreatic cancer cells. For this purpose, we added recombinant murine ApoE (rApoE) to 7940b KPC tumor cells and performed bulk RNA sequencing (RNA-seq) compared to

vehicle treated controls (**Fig. 3.9A**). Gene set enrichment analysis revealed upregulation of inflammatory associated transcriptional programs in tumor cells treated with rApoE (**Fig. 3.10A**). Differential expression analysis revealed tumor cells treated with ApoE had increased expression of the chemokine *Ccl2*, a chemoattractant for monocytes/macrophages and monocytic-MDSCs (Deshmane et al., 2009), and the chemokines *Cxcl1* and *Cxcl5*, which binds the Cxcr2 receptor expressed on granulocytic-MDSCs (granulocytes) (Kumar et al., 2016) (**Fig. 3.9A**). We next confirmed our bulk RNA-seq analysis by qPCR and detected a significant increase in *Cxcl1* and *Cxcl5* in tumor cells treated with recombinant ApoE (**Fig. 3.9B**). PDA patients with high CXCL1 plasma levels had reduced overall survival (**Fig. 3.9C**). We next utilized the ICGC pancreatic cancer dataset and stratified patients by low and high expression of *CXCL1* and *CXCL5* (**Fig. 3.10B**). Patients with high expression of *CXCL1* but not *CXCL5* had significantly reduced survival (**Fig. 3.10B**). Cxcl1 has been shown to inhibit T cell infiltration in pancreatic cancer (Li et al., 2018a), potentially by increasing the recruitment of immune suppressive myeloid cells expressing Cxcr2.

Cxcl1 and its family members *Cxcl2* and *Cxcl5* are expressed in multiple cell populations in the TME (**Fig. 3.9D**). In accordance with previous reports, Cxcl1 and Cxcl5 are expressed highly in both epithelial cell and fibroblasts, while Cxcl2 is highest in granulocytes (Steele et al., 2016) (**Fig. 3.9D**). Cxcl1 was elevated in the KPC tumor epithelium compared to the normal pancreas (**Fig. 3.10C**). Accordingly, we detected an increase in *Cxcl1* in both wild-type pancreatic fibroblasts (BLK6318) and cancer-associated fibroblasts (FB1) treated with ApoE (**Fig. 3.9E**). Interestingly, fibroblasts treated with ApoE had increased expression of the inflammatory cytokine interleukin-6

(*Il6*) (**Fig. 3.10D**), while aSMA (*Acta2)* did not differ (**Fig. 3.10E**). We next wanted to determine if our finding was consistent *in vivo*. We detected significantly reduced *Cxcl1* and a trend towards lower *Cxcl5* expression in tumors implanted in ApoE $^{-/-}$ mice (**Fig. 3.9F**). Additionally, immunohistochemical analysis, revealed less Cxcl1 in tumors from ApoE deficient mice (**Fig. 3.10F**). By co-immunofluorescence staining, we determined that Cxcl1 is reduced in both tumor cells and fibroblasts in tumors grown in ApoE $^{-/-}$ compared to tumors grown in WT mice (**Fig. 3.9G**).

Given that Cxcl1 is a granulocyte chemoattractant, we separated human PDA serum into APOE low and APOE high and used CyTOF to assess granulocyte (CD11b^{+} CD66b^{+} CD16^{+}) levels in the matched blood samples. We observed an increase in blood granulocytes in patients with high serum APOE (**Fig. 3.9H**).

ApoE is a secreted protein, and macrophages are one of the main sources (**Fig. 3.3H**). We thus assessed *in vitro* whether macrophage derived ApoE regulated Cxcl1 expression in cancer cells. Bone marrow derived monocytes were isolated from WT mice and ApoE $^{-/-}$ mice and polarized to TAMs. We then cultured tumor cells with macrophage conditioned-media from WT and ApoE $^{-/-}$ mice for 48 hours to ascertain the role of secreted factors in the macrophage media on tumor cell production of *Cxcl1*. Cxcl1 levels were measured by qRT-PCR in tumor cells alone and tumor cells cultured with WT or ApoE $^{-/-}$ macrophage conditioned media (**Fig. 3.9I**). Culture with WT macrophage conditioned media, induced higher *Cxcl1* expression in tumor cells, suggesting a secreted factor from macrophages regulates *Cxcl1* production from tumor cells (**Fig. 3.9I**). In contrast, tumor cells cultured with ApoE $^{-/-}$ macrophage failed to induce increased *Cxcl1* expression, and

adding rApoE to the media rescues *Cxcl1* induction, demonstrating that secreted ApoE is required for macrophage induction of tumor cell *Cxcl1* expression (**Fig. 3.9I**).

APOE regulates tumor cell *Cxcl1* production via NF-κB signaling

Given our finding that ApoE mediates expression of *Cxcl1* and *Cxcl5*, we next assessed which receptor was regulating this phenotype. ApoE has multiple known receptors, including low-density lipoprotein receptor (LDLR), low-density lipoprotein receptor-related protein 1 (LRP1), and low-density lipoprotein receptor-related protein 8 (LRP8) (Lane-Donovan and Herz, 2017). We used single cell RNA sequencing and detected *Ldlr, Lrp1*, and *Lrp8* expression on epithelial cells from orthotopic KPC tumors (**Fig. 3.11A**). *In vitro, Ldlr* was the highest expressed ApoE receptor in the 7940b KPC tumor cells (**Fig. 3.11B**). Further, single cell RNA sequencing of human PDA also revealed that *LDLR* is highly expressed on tumor cells relative to other cell types (**Fig. 3.11C**). Given these data, we then used small interfering RNA (siRNA) to knock-down LDLR in 7940b KPC tumor cells (**Fig. 3.12A**). Tumor cells with partial knock-down of LDLR had reduced induction of *Cxcl1* and *Cxcl5* expression when cells were treated with recombinant ApoE compared to the scrambled siRNA control (**Fig. 3.12B**). These data suggest ApoE mediates *Cxcl1* and *Cxcl5* expression via signaling through LDLR.

We next wanted to examine the intracellular signaling pathways that mediated ApoE-driven *Cxcl1* and *Cxcl5* expression. Gene set enrichment analysis of TCGA pancreatic cancer dataset revealed a positive correlation of APOE expression with NF-κB signaling components (**Fig. 3.11D**). Similar to the human enrichment analysis, we performed gene set enrichment analysis on KPC tumor cells treated with recombinant

ApoE and saw upregulation of complement, Kras signaling, inflammatory response pathways, as well as components of NF-κB signaling (**Fig. 3.11E**). Further, many NF-κB/cytokine signature genes were upregulated within pancreatic cancer cells treated with recombinant ApoE (**Fig. 3.12C**). We performed co-immunofluorescence staining for the NF-κB mediator p65 and the tumor cell marker, CK19, in 7940b KPC cells treated with recombinant ApoE compared to vehicle (**Fig. 3.12D**). We detected an increase in percent nuclear p65 with the addition of ApoE, suggesting tumor cells activate NF-κB signaling in response to ApoE treatment (**Fig. 3.12D**). Cxcl1 is activated by NF-κB signaling and ApoE has been shown to regulate NF-κB in acute myeloid leukemia (Deng et al., 2018). To assess the role of ApoE and NF-κB in PDA we next used a NF-κB inhibitor, BAY 11-7082 (Lee et al., 2012), which targets IKK to determine the effect of NF-κB inhibition on *Cxcl1* expression. As previously described, we saw an increase in *Cxcl1* and *Cxcl5* in tumor cells treated with recombinant ApoE (**Fig. 3.12E**). Treatment of the 7940b KPC cells with BAY 11-7082 significantly reversed the *Cxcl1* and *Cxcl5* induced by recombinant ApoE (**Fig. 3.12E**). Thus, ApoE may regulate tumor cell derived *Cxcl1* and *Cxcl5* expression, at least in part, through binding to LDLR and through NF-κB signaling activation.

Discussion

Here, we found that the apolipoprotein APOE is expressed in mouse and human pancreatic cancer. Further, we show that ApoE is secreted, and acts on tumor cells – at least in part through the LDL receptor – to induce secretion of Cxcl1 and Cxcl5. These cytokines are chemoattractants for MDSCs and consequently suppress cytotoxic T cell infiltration (Li et al., 2018a; Steele et al., 2016) (**Fig. 3.12F**). Absence of ApoE secretion

was associated with reduced expression of Cxcl1 in tumor cells and an increase in tumor-infiltrating T cells (**Fig. 3.12G**). Our work provides evidence that APOE mediates immune suppression by modulating T cell infiltration in the setting of pancreatic cancer.

Myeloid cells are a key driver of immune suppression in PDA and these myeloid-mediated mechanisms remain incompletely understood. Recent single cell sequencing efforts identified *ApoE* as part of a group of genes highly expressed by macrophages and, additionally, expressed by iCAFs in PDA (Elyada et al., 2019; Steele et al., 2020). Our data are consistent with previous reports on *ApoE* expression in both macrophages and fibroblasts and support the growing recognition that fibroblasts have an immunosuppressive role (Biffi et al., 2019; Elyada et al., 2019; Feig et al., 2013; Ohlund et al., 2017).

ApoE, among other apolipoproteins, inhibits T cell activation *in vitro* (Macy et al., 1983). While understudied in PDA, APOE-mediated regulation of the immune system has been evaluated in other cancers. Consistent with our data, APOE mediates T cell suppression in AML (Deng et al., 2018; Gui et al., 2019). In contrast, activation of ApoE in melanoma promotes cytotoxic T cell responses (Pencheva et al., 2012; Tavazoie et al., 2018), suggesting the function of APOE in cancer may be context dependent. The differences in ApoE function seen between PDA and melanoma could be due to the baseline immune reactivity in melanoma versus pancreatic cancer (Blando et al., 2019).

Our study highlights a previously undescribed mechanism of ApoE in mediating tumor cell crosstalk with the immune system in PDA. Our data suggest that ApoE signals directly to tumor cells to enhance expression of *Cxcl1* and *Cxcl5*. Cxcl1 and *Cxcl5* act as a chemoattractant for MDSCs. MDSCs in turn prevent T cell infiltration in PDA (Li et al.,

2018a). We further show that ApoE induction of *Cxcl1* and *Cxcl5* expression is at least partially dependent on its binding to the LDL receptor on tumor cells. ApoE signaling also leads to activation of NF-κB in tumor cells. Interestingly, inactivation of cholesterol signaling in a mouse model of pancreatic cancer results in delayed carcinogenesis and prolonged survival. When tumors do develop, they have basal-like features, possibly indicating that classical tumors are uniquely dependent on cholesterol (Gabitova-Cornell et al., 2020). An interesting consideration is that one of the physiological consequences of ablating ApoE is higher plasma cholesterol, suggesting that some of the *in vivo* phenotypes observed may have to do with suppressed tumor promotion.

While mice have only one variant of *APOE,* humans have three different variants *APOE2, APOE3,* and *APOE4*, with different functions (Mahley and Rall, 2000). In Alzheimer's disease *APOE4* is a risk factor for disease (Strittmatter et al., 1993), while *APOE2* plays a protective role (Corder et al., 1994). *APOE* genotype has not been extensively studied in cancer, but in one melanoma study, *APOE4* plays a favorable role in disease, while *APOE2,* has a worse outcome (Ostendorf et al., 2020). However, *APOE4* has the highest affinity for the LDL receptor suggesting it would further promote immune suppression in PDA (Yamamoto et al., 2008). Future studies will examine the role of *APOE* variants in human PDA.

Finally, we observed that higher serum APOE levels correlate to worse overall survival in pancreatic cancer patients. These findings suggest that APOE levels could be a useful prognostic marker for PDA patients. In summary, ApoE is highly expressed by macrophages and fibroblasts within the pancreatic cancer microenvironment; ApoE is

secreted and binds the LDL receptor on cancer cells, in turn inducing the expression of cytokines that mediate immune suppression in pancreatic cancer.

Materials and Methods

Study approvals

All animal experiments and procedures were performed at the University of Michigan under Protocol Number PRO00007983 and were in compliance with guidelines from the Institutional Animal Care & Use Committee (IACUC). All human research was performed according to ethical standards and guidelines approved by the University of Michigan Institutional Review Board (IRB). All patients provided written consent before procedures were performed. Peripheral blood was collected from patients over the age of 18 who received diagnostic endoscopic ultrasound for pancreatic mass under IRB HUM00041280 or surgical resection under IRB HUM00025339. Blood was also collected from known PDA patients at clinic visits or infusion visits for chemotherapy under HUM00025339. For all consented patients, up to 40 ml of whole blood was collected.

APOE expression analysis and human PDA stratification

RNA sequencing dataset of laser microdissection (LCM, 65 PDAC tumor epithelium vs 65 stroma samples) was downloaded from NCBI GEO (Accession number GSE93326) and used to determine the expression of APOE in tumors relative to stroma. For the stratification of patients tumors by APOE level, we used The Cancer Genome Atlas (TCGA) pancreatic adenocarcinoma RNA sequencing data (150 samples) downloaded from cBioPortal (https://www.cbioportal.org/) as well as microarray data from the

International Cancer Genome Consortium – Australia cohort (ICGC-AU, 269 samples) downloaded from https://dcc.icgc.org/projects/. Tumor samples in both datasets were split into two groups (APOE high and low). Genes differentially expressed between the two groups were determined using *limma* package in R software (v 3.5.2) with an adjusted $P<0.05$ as cut off for statistical significance.

Human and mouse single cell RNA sequencing

Single cell RNA sequencing analysis utilized the following datasets. Processed data for the human pancreatic cancer single cell RNA sequencing dataset are available at NIH Gene Expression Omnibus (GEO) database under the accession GSE155698 and raw data are available at the NIH dbGaP database under the accession phs002071.v1.p1 (Steele et al., 2020). Raw and processed data for the orthotopic KPC mouse single cell RNA sequencing dataset are available at GEO under the accession GSE158356. Downstream analysis was performed using Seurat V3.2.2 in R Studio V1.3.1093.

Human plasma isolation

Human PBMCs were isolated from whole blood as previously described (Steele et al., 2020). Briefly, whole blood was inverted 10 times and then underwent centrifugation at 1700 x g for 20 minutes at room temperature (RT). The plasma layer was then removed and stored in -80 °C.

Enzyme-linked immunosorbent assay (ELISA)

For detection of APOE in human plasma, Human Apolipoprotein E Human Elisa Kit (abcam, ab108813) was used. For detection of APOE in mouse macrophage media, Mouse Apolipoprotein E SimpleStep Elisa Kit (abcam, ab215086) was used. For detection of human CXCL1, Human CXCL1/GRO alpha Quantikine ELISA Kit (R&D systems, DGR00B) was used. ELISAs were performed according to manufacturing instructions. Mouse bone marrow cells were plated in 1:1 tumor cell conditioned media: DMEM with 10% FBS for seven days before media was removed. For APOE detection, human plasma was diluted 1:1000 and mouse macrophage media was diluted 1:100. Samples were plated in duplicate. Absorbance was read at 450 nm with wavelength correction at 570 nm. Final concentration was multiplied by the dilution factor. Survival analyses were performed on human APOE and CXCL1 plasma data. PDA patients were stratified by APOE or CXCL1 levels and survival analysis was performed using Log-rank (Mantel-Cox) test.

Animal experiments

Mice

Wild type C57/BL6J mice (Jackson Laboratory, 000664) and $ApoE^{-/-}$ mice (Jackson Laboratory, 002052) were used for animal experiments. All mice were housed in specific pathogen-free facilities at the University of Michigan Rogel Cancer Center.

Orthotopic transplantation models

For orthotopic transplantation into the pancreas, 5×10^4 7940b KPC cells were prepared in a 1:1 ratio of growth-factor reduced matrigel and DMEM supplemented with 10% FBS.

Mice were anesthetized using isoflurane and the surgical area was prepared using aseptic technique. A tumor cell suspension of 50 µl was injected directly into the pancreas using an insulin syringe, as previously described (Aiello et al., 2016).

Doxycycline treatment

iKras* mice (Collins et al., 2012a) were administered doxycycline chow (BioServ, F3949) to induce expression of *Kras^{G12D}* for 72 hours. Pancreatitis was then induced by two days of 8 intraperitoneal injections of caerulein (Sigma, 75 µg/kg) with continuous administration of doxycycline as previously described (Collins et al., 2012a). Doxycycline chow was administered for 3 weeks for Kras ON timepoint and then replaced with regular chow for Kras OFF timepoints. Littermate control mice lacking the full set of alleles also received caerulein and doxycycline at the indicated timepoints.

Histopathological analysis and quantification

Tissues were fixed overnight in 10% neutral buffered formalin, then transferred to 70% ethanol for paraffin embedding. Hematoxylin & Eosin was performed in accordance with manufacturing guidelines. Gomori Trichrome was performed in accordance with manufacturing guidelines (ThermoFisher, #87021). Immunohistochemical staining was performed using the Ventana Discovery Ultra XT autostainer and counterstained with hematoxylin. For immunofluorescent staining, tissues were de-paraffinized with xylene, followed by antigen retrieval. Slides were blocked with 1% bovine serum albumin (BSA) in PBS for 1 hour at RT. Primary antibody was diluted in blocking buffer and incubated overnight at 4 °C, followed by secondary antibody incubation (Alexa Fluor secondaries,

1:300) for 45 minutes at RT. Nuclei were counterstained with Prolong Diamond Antifade Mountant with DAPI (Invitrogen). For *in vitro* staining, tumor cells were grown on sterile, glass cover slips. Images were taken on the Olympus BX53F microscope with the Olympus DP80 digital camera and CellSens Standard software using the 20x and 40x objectives. Confocal images were imaged on LeicaSP5 or SP8 confocal microscope Leica Software at 63x objective. Image J, Fiji V2.0.0-rc-69/1.52p was used to quantify positive immunohistochemical stain. Quantification was done on at least three 20x magnification fields across three or more biological replicates.

Bone-marrow macrophage polarization

Bone marrow cells were isolated from mouse femurs and tibias and macrophage polarization was performed as previously described (Halbrook et al., 2019). Briefly, bone-marrow cells were isolated from C57BL/6J mice and cultured in macrophage differentiation media supplemented with 30% L929 conditioned media for 5 days. On day 6, macrophages were polarized for 24 hours using 10ng/mL murine macrophage colony-stimulating factor (M-CSF) (Peprotech, 315-02), 10ng/mL LPS (Enzo, ALX-581-011-L001), 10ng/mL murine interleukin-4 (IL-4) (Peprotech, 214-14), or 75% PDA conditioned media, for M0, M1, M2 and TAM polarization, respectively. For TAM only studies, bone-marrow cells were isolated and cultured in 50% PDA conditioned media for seven days, with additional media added on day 3.

Quantitative RT-PCR (qRT-PCR)

Tumor tissues were flash frozen in liquid nitrogen, then prepared for RNA extraction through incubation in RNA*later*-ICE (ThermoFisher, AM7030) overnight at -20 °C. Tissues and cell lines were mechanically disrupted in Buffer RLT (Qiagen, 79216). RNA was extracted according to RNeasy Plus Mini Kit manufacturing instructions (Qiagen, 74134). cDNA was synthesized using the High-Capacity cDNA Reverse Transcription Kit (ThermoFisher, 4368814). For qRT-PCR, samples were prepared with either Fast SYBR Green PCR Master Mix (Applied Biosystems, 4385612) or TaqMan Universal Mastermix (Applied Biosystems, 4364340). Amplifications were performed in triplicate. *Cyclophilin A/Ppia* was used for normalization.

Mass Cytometry (CyTOF)

Mouse tumors were mechanically and enzymatically (1mg/ml Collagenase P: DMEM) digested for 30 minutes at 37 °C with constant shaking. Samples were then washed with DMEM and 10% FBS and filtered through 100 μM mesh, followed by 40 μM mesh, to obtain a single cell suspension. Human PBMCs were isolated as previously described (Steele et al., 2020). Whole blood was inverted 10 times and then underwent centrifugation at 1700 x g for 20 minutes at RT. The top PBMC layer was then removed, washed with PBS, and underwent ammonium-chloride-potassium (ACK) lysis. PBMCs underwent a final wash and centrifugation. Mouse and human samples were prepared for CyTOF cell surface staining in accordance to manufacturing guidelines (Fluidigm, PN 400276 A4). Samples were first washed with Maxpar PBS (Fluidigm, 201058). Up to 1 million cells from the single cell suspension were then stained with Cell-ID Cisplatin (Fluidigm, #201064) 5 minutes at RT, to label dead cells. Cells were then washed with

Maxpar PBS and were stained with a panel of 16 surface mouse antibodies and 6 surface human antibodies for 30 minutes at room temperature. Samples were washed with Maxpar PBS twice then left pelleted in 1 mL Cell-ID Intercalator-IR (Fluidigm, 201192A). Samples were then shipped to the University of Rochester, Flow Cytometry Core, and acquired on the CyTOF 2. Files were normalized to internal bead controls. Downstream analysis was performed using the Premium CytoBank Software (cytobank.org). Live singlets were gated using the DNA Intercalator Ir191, event length, and Cisplatin Pt195. tSNE visualization was performed in CytoBank on representative samples.

Cell culture

KPC (C57/BL6) cell line: 7940b (A gift from Dr. Gregory Beatty, University of Pennsylvania). Fibroblast cell lines: BLK6318 was generated from a normal mouse (C57/BL6) pancreas. FB1 cancer-associated fibroblast line was generated from an iKras* p53* mouse (FVB/NJ) (Collins et al., 2012b) through fluorescence-activated cell sorting (FACS) on $PDGFRa^{+}$ $EpCAM^{-}$ cells. All cell lines underwent routine Mycoplasma testing using MycoAltert (Lonza, LT07-318). DMEM with 10% FBS and 1% penicillin/streptomycin (ThermoFisher, 15140163) was used for all cell lines. Murine recombinant ApoE (abcam, ab226314) was used at a concentration of 0.3µg/mL for all experiments. 50,000 -100,000 cells were plated into a 6-well dish and were allowed to adhere for 24 hours. Recombinant ApoE was spiked into the culture media for 1 to 48 hours, depending on experimental conditions. For NF-kB inhibition, cells were pre-treated with either 5 or 10uM BAY 11-7082 (abcam, ab141228) for 2 hours, before the addition of recombinant ApoE.

RNA sequencing analysis of APOE-treated cells

Cells were lysed in Buffer RLT (Qiagen, 79216). RNA was then extracted according to RNeasy Plus Mini Kit manufacturing instructions (Qiagen, 74134). RNA quality was determined using both NanoDrop results and RNA Integrity Number (RIN). All samples had a RIN >9 and underwent reverse transcription for cDNA synthesis. The University of Michigan Advanced Genomics Core prepared libraries and then underwent paired-end sequencing on the NovaSeq6000 (Illumina). Sample reads were aligned with HISAT2 v2.2.0 using prebuilt index of Mus musculus UCSC reference genome mm10 obtained from http://daehwankimlab.github.io/hisat2/download/. Gene assembly and quantification was done with Stringtie 2.1.1, counts of duplicated genes were averaged and differential gene expression was determined using *DESeq2* package (v 1.22.2) in R software after filtering out genes with low counts (i.e. total raw counts <20 across samples). Pathway enrichment and gene ontology analyses were performed with GSEA v4.0.3 (pre-ranked) using differentially expressed genes, and with DAVID v6.8 (https://david.ncifcrf.gov/summary.jsp). Bulk RNA sequencing data from this study are available at GEO under the accession GSE160592.

siRNA transfection

siRNA transfection was performed according to manufacturer instructions (Lipofectamine RNAiMAX Reagent Protocol, 2013). 7940b KPC cells were seeded at 60% confluency in a 6-well plate. The next day, two separate LDLR siRNA (Thermo, #s69153 and #s69154) or scrambled negative control (Thermo, 4390843) were diluted in Opti-MEM reduced

serum medium (Gibco, 31985062). Lipofectamine RNAiMAX transfection reagent (Thermo, 13778075) was diluted in Opti-MEM medium. Diluted siRNA was then mixed with diluted lipofectamine RNAiMAX at 1:1 ratio and incubated for 5 minutes at RT. siRNA and lipofectamine complexes were then added to adherent cells at a final concentration of 25 pmol. Cells were incubated for 48 hours at 37 °C.

Western blot analysis

Cells were lysed in RIPA buffer (Sigma) with protease (Sigma) and phosphatase (Roche) inhibitors. Protein samples were separated through electrophoresis on a 4-20% precast polyacrylamide gel (BioRad, 4561094) then transferred to PVDF membrane (BioRad, 1620177). Membranes were blocked with 5% milk for one hour at RT. Membranes were incubated with primary antibodies overnight at 4 °C, followed by secondary antibody incubation for 2 hours at RT. All incubations were performed under constant rocking. For protein detection, membranes were incubated in Western Lightning Plus-ECL (Perkin Elmer, 509049323) for 1 minute and then imaged using BioRad Chemidoc. Image J was used for quantitation of normalized protein expression.

Statistics

GraphPad Prism version 8.4.3 was used for statistical analyses and graphical representation. Data are presented as means ± standard deviation (SD). Two-tailed Student's t-test and One-way ANOVA with Turkey's test for multiple correction were performed for comparison between groups. A $p<0.05$ was considered statistically significant. Kaplan-Meier overall survival analysis was performed with log-rank test.

Data availability

Processed data for the human pancreatic cancer single cell RNA sequencing dataset are available at NIH Gene Expression Omnibus (GEO) database under the accession GSE155698 and raw data are available at the NIH dbGaP database under the accession phs002071.v1.p1 (Steele et al., 2020). Raw and processed data for the orthotopic KPC mouse single cell RNA sequencing dataset are available at GEO under the accession GSE158356. Bulk RNA sequencing data from this study are available at GEO under the accession GSE160592.

Author contributions

HCC and MPdM directed the study. HCC, MPdM, and SBK developed the study concept. ZCN analyzed human bulk RNA sequencing datasets (LCM, TCGA, ICGC). ST and AR developed bioinformatics pipelines. SBK, NGS, and ESC performed single cell RNA sequencing analyses. ESC consented patients and processed human peripheral blood for plasma collection. ESC, SBK, and ST analyzed human plasma ELISA data. SBK, NGS, CE, FL, and AVD performed *in vivo* mouse experiments. SBK, DL, and FL performed immunostainings. SBK performed image quantification. SBK, NGS, and FL imaged immunostainings. SBK, FL, KLD, AP, YZ, and RME performed *in vitro* experiments. SBK, CE, and NGS processed tissue for CyTOF. SBK analyzed CyTOF data. SBK, FL and AP processed samples for qRT-PCR. ZCN analyzed bulk mouse RNA sequencing dataset. EC, SBK, NGS, and CE processed human PBMCs for CyTOF. ESC, ST, and SBK analyzed human PBMC CyTOF data. YZ and NGS generated primary

mouse cell lines. CAL provided technical support and study guidance. SBK, MPdM, and HCC drafted the manuscript. All co-authors edited and approved the manuscript.

Acknowledgments

We thank the Advanced Genomics core at the University of Michigan. We thank the Flow Cytometry Core at the University of Rochester, specifically Matthew Cochran and Terry Wightman. For help with CyTOF panel design and analysis, we thank Kevin Brown and Vinicius Motta from Fluidigm. We thank El-ad Amir from Astrolabe Diagnostics for help in human CyTOF analysis. We thank Dr. Gregory Beatty, at the University of Pennsylvania, for his generous gift of the 7940b KPC cell line. We thank Michael Scales for generation of the BLK6318 mouse wild type fibroblast cell line. **Funding:** This study was funded by the NIH U01CA224145 to HCC and MPdM and the University of Michigan Cancer Center Support Grant (P30CA046592), including an Administrative Supplement to HCC and MPdM. This project was additionally supported by NIH/NCI grants R01CA151588, R01CA198074 and the American Cancer Society to MPdM. SBK was supported by NIH T32-GM113900 and NCI F31-CA247076. ZCN was supported by the Michigan Postdoctoral Pioneer Program, University of Michigan Medical School. ESC was supported by the American College of Gastroenterology Clinical Research Award and by T32-DK094775. NGS was funded by American Cancer Society Postdoctoral Award PF-19-096-01 and the Michigan Institute for Clinical and Healthy Research (MICHR) Postdoctoral Translational Scholar Program fellowship award. NGS and KLD were supported by T32-CA009676. CAL was supported by NIH grant R37CA237421. AR and ST were funded by institutional startup funds from the University of Michigan, a gift from

Agilent Technologies, NCI grant R37CA214955 and a Research Scholar Grant from the American Cancer Society (RSG-16-005-01). The funders had no role in the manuscript.

Figures

Figure 3.1

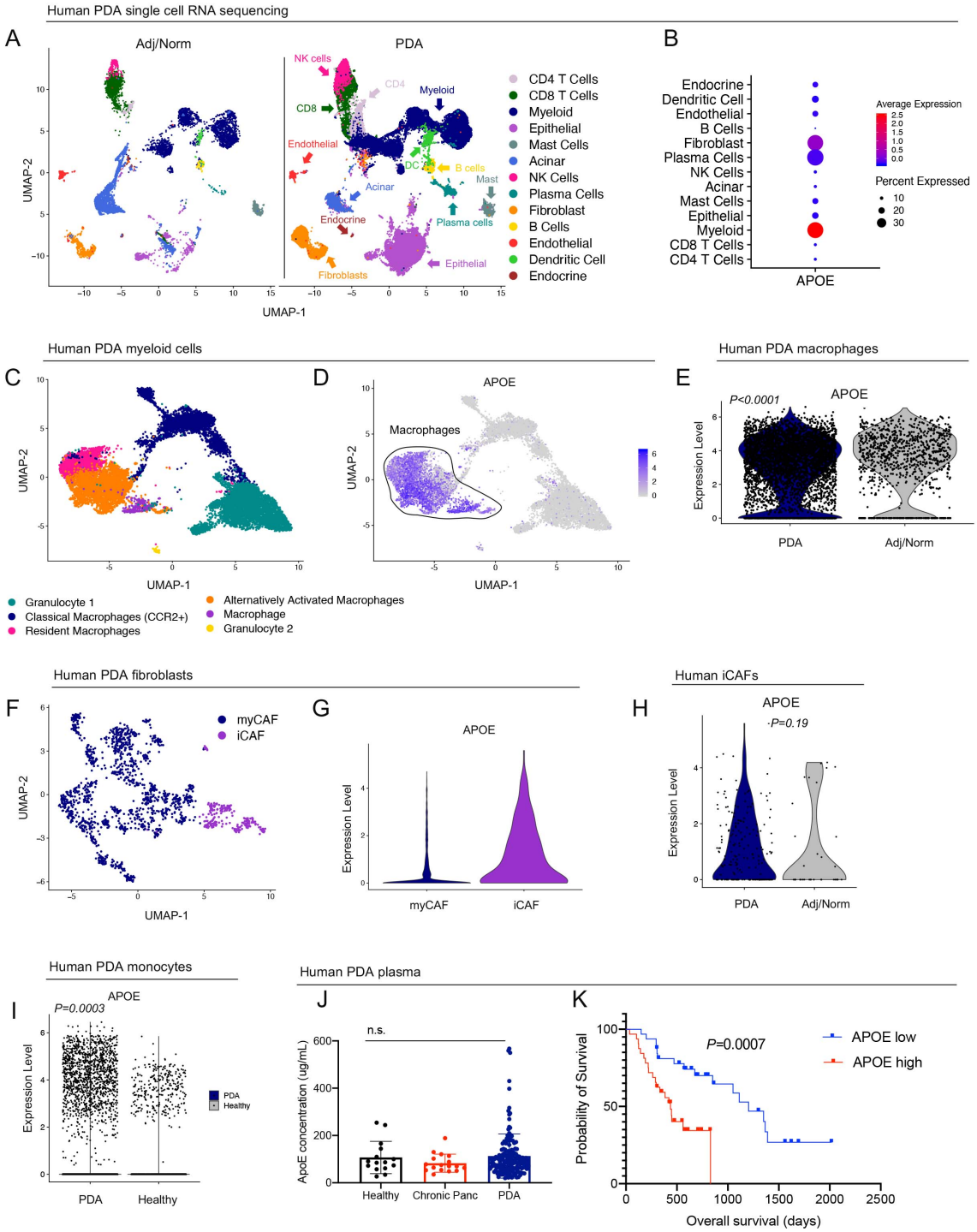

Figure 3.1 Systemic *APOE* levels are elevated in PDA and correlate to patient survival.
(A) UMAP analysis of the 13 identified cell populations in human adjacent/normal pancreas (n=3) and PDA tumors (n=16). (B) Dot plot of *APOE* in all identified cell populations in human single cell dataset. Color represents average expression. Size of the dot represents percent expressed. (C) UMAP visualization of 6 identified myeloid cell sub-populations in the human PDA tissue. (D) Feature plot of *APOE* expression in all identified myeloid cell populations in human PDA. Low expression is in grey, while high expression is in blue. Black outline denotes *APOE* positive macrophages. (E) Violin plot of normalized gene expression of *APOE* in PDA and adjacent normal pancreas macrophages in human PDA. Statistics were determined using non-parametric Wilcoxon rank sum test. (F) UMAP visualization of human PDA fibroblast sub-populations. (G) Violin plot of normalized gene expression of *APOE* in human myCAF and iCAF populations. (H) Violin plot of normalized gene expression of *APOE* in PDA and adjacent normal pancreas iCAFs in human PDA. Statistics were determined using non-parametric Wilcoxon rank sum test. (I) Violin plot of normalized expression of *APOE* in human monocytes. Statistics were determined using non-parametric Wilcoxon rank sum test. (J) Human APOE concentration (μg/mL) in plasma from healthy donors (n=15), chronic pancreatitis patients (n=17) and PDA patients (n=155). Statistics were determined using one-way ANOVA with Turkey's test for multiple comparisons. n.s. = not significant. (K) Survival analysis of PDA patients stratified by plasma APOE levels. APOE Low (n=32) and APOE High (n=32). Statistics were determined using Log-rank (Mantel-Cox) test.

Figure 3.2

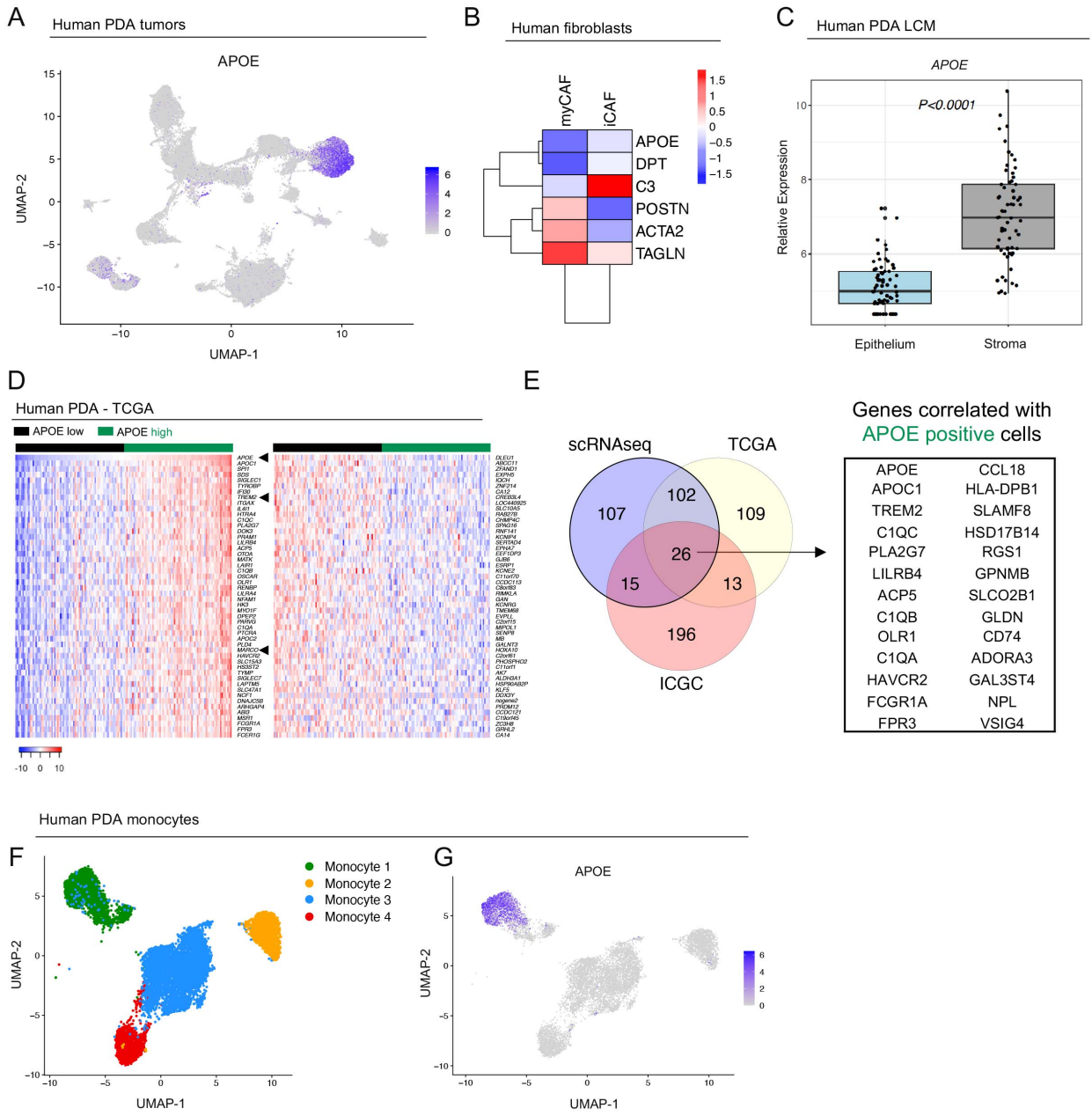

Figure 3.2 *APOE* is highly expressed in the stroma of human PDA tumors.
(A) Feature plot of *APOE* in human PDA tumor cell populations. Low expression is in grey, while high expression for *APOE* is in blue. (B) Average expression heatmap of myCAF (*TAGLN, ACTA2, POSTN*) and iCAF (*C3, DPT, APOE*) lineage markers. Low expression (blue) and high expression (red) of selected genes. (C) Relative *APOE* expression in epithelium (n=65) and stroma (n=65) compartments in human PDA samples from Laser Capture Microdissection PDA dataset. (D) Heatmaps of the top correlated genes in APOE low (n=75) and APOE high (n=75) patients from TCGA pancreatic cancer data. Arrowheads denote APOE, *TREM2,* and *MARCO*. (E) Venn diagram showing genes overlapping between the human scRNA seq *APOE*$^{+}$ macrophages and genes high in APOE high tumors from TCGA and ICGC datasets. The 26 overlapped genes that correlate with APOE positive cells are plotted on the right. (F) UMAP visualization of 4 identified monocyte populations in human PDA. (G) Feature plot of *APOE* in human PDA monocyte populations. Low expression is in grey, while high expression for *APOE* is in blue.

Figure 3.3

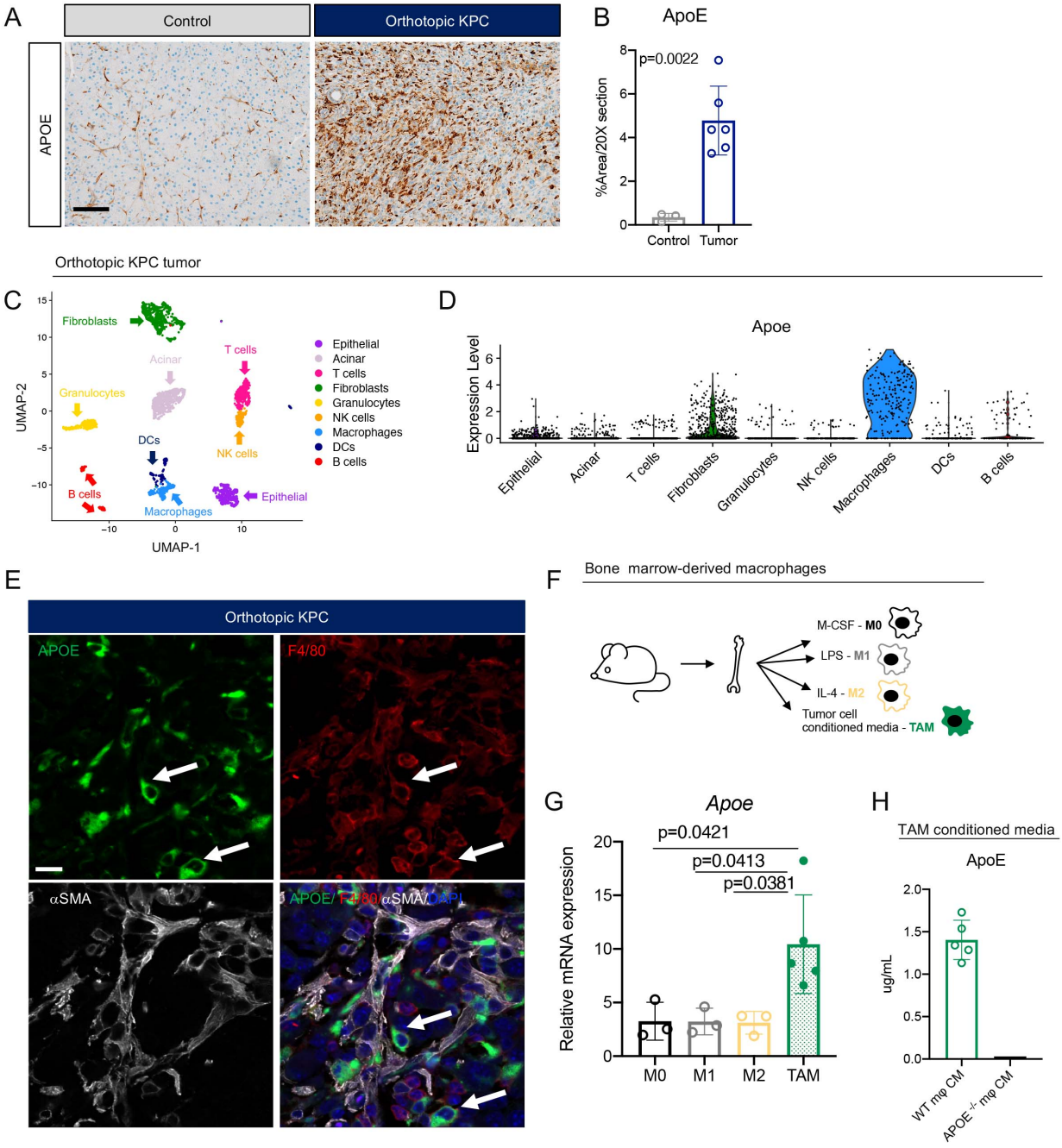

Figure 3.3 APOE is highly expressed by tumor-associated macrophages.
(A) Immunohistochemical analysis of APOE in normal mouse pancreas and orthotopic KPC tumor. Scale bars, 100 μm. (B) Quantitation of positive APOE staining as percent of area in a 20x field of view. Five fields of view are averaged per mouse. Control (n=3) and orthotopic tumor (n=6). Statistical significance was determined using two-tailed *t* test. (C) UMAP visualization of 9 identified populations in orthotopic KPC tumors (n=2). (D) Violin plot of normalized expression of *Apoe* in identified cell populations in orthotopic KPC tumors (n=2). (E) Co-immunofluorescence of orthotopic KPC tumor with single channels of APOE (green), F4/80 (red), aSMA (white) and merge to show APOE and F4/80 co-localization. Two examples of APOE and F4/80 co-localization are denoted by white arrows. Scale bars, 25 μm. (F) Experimental design for bone marrow derived macrophage polarization assay. (G) qRT-PCR analysis of *Apoe* mRNA levels relative to *Cyclophilin A* housekeeping in 4 macrophage conditions (M0, M1, M2, TAM). Statistical significance was determined using one-way ANOVA with Turkey's test for multiple correction. (H) ApoE concentration (μg/mL) in wild type TAM conditioned media (n=5) and ApoE$^{-/-}$ TAM conditioned media (n=1).

Figure 3.4

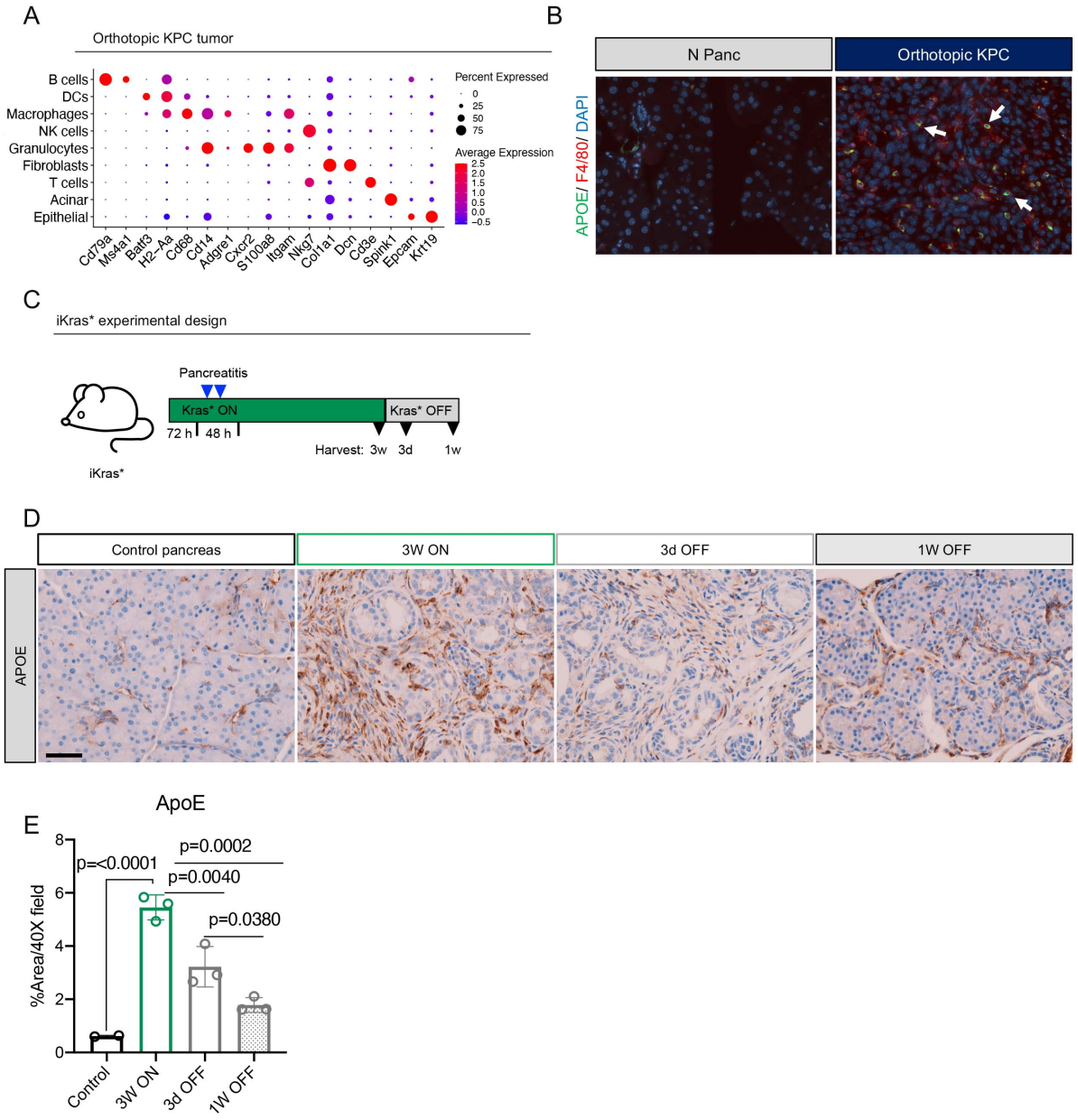

Figure 3.4 APOE expression is lost when oncogenic *Kras* is extinguished.
(A) Dot plot of lineage markers used to define identified cell populations in orthotopic KPC tumors (n=2). Color of the dot represents average expression. Size of the dot represents percent expressed. (B) Co-immunofluorescence staining on normal mouse pancreas (N Panc) and orthotopic KPC tumor for APOE (green), F4/80 (red) and DAPI (blue). White arrows denote APOE and F4/80 colocalization. Scale bars, 100 μm. (C) iKras* experimental design. (D) Immunohistochemical staining for APOE in mouse normal pancreas, pancreatic tissue after 3 weeks of oncogenic *Kras* expression, and removal of oncogenic *Kras* for 3 days and 1 week. Scale bars, 50 μm. (E) Quantitation of positive APOE staining as percent area in a 40x field. 5 images per mouse were averaged. Control (n=2), 3W ON (n=3), 3d OFF (n=3), and 1W OFF (n=3). W=week. d=day. Statistical significance was determined using one-way ANOVA with Turkey's test for multiple correction.

Figure 3.5

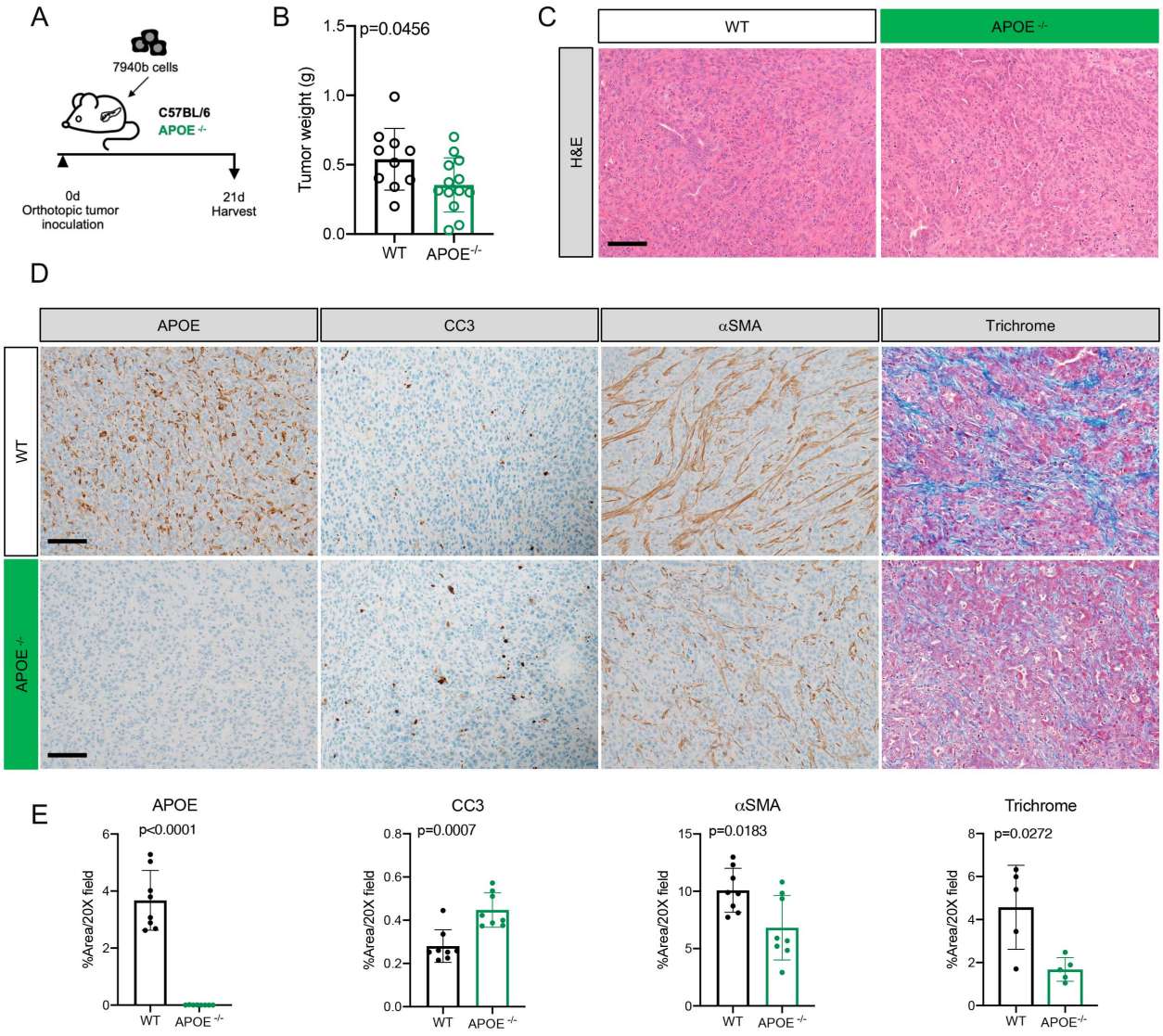

Figure 3.5 Loss of APOE results in reduced tumor burden and fibrosis.
(A) Experimental scheme for orthotopic transplantation of 7940b, KPC tumor cells. (B) Final tumor weight (g) in WT (n=10) and ApoE$^{-/-}$ (n=13) mice, Statistics were determined using two-tailed *t* test, with a $p<0.05$ considered statistically significant. (C) Representative images of Hematoxylin & Eosin (H&E) stain in WT and ApoE$^{-/-}$ mice. Scale bars, 100 µm. (D) Representative immunohistochemical staining for APOE, cleaved caspase 3 (CC3), aSMA, and Gomori Trichome in WT and ApoE$^{-/-}$ mice. Scale bars, 100 µm. (E) Quantitation of immunohistochemical stains as percent area per 20x field in WT (n= 5-8) and ApoE$^{-/-}$ mice (n=5-8). Statistics were determined by two-tailed *t* tests.

Figure 3.6

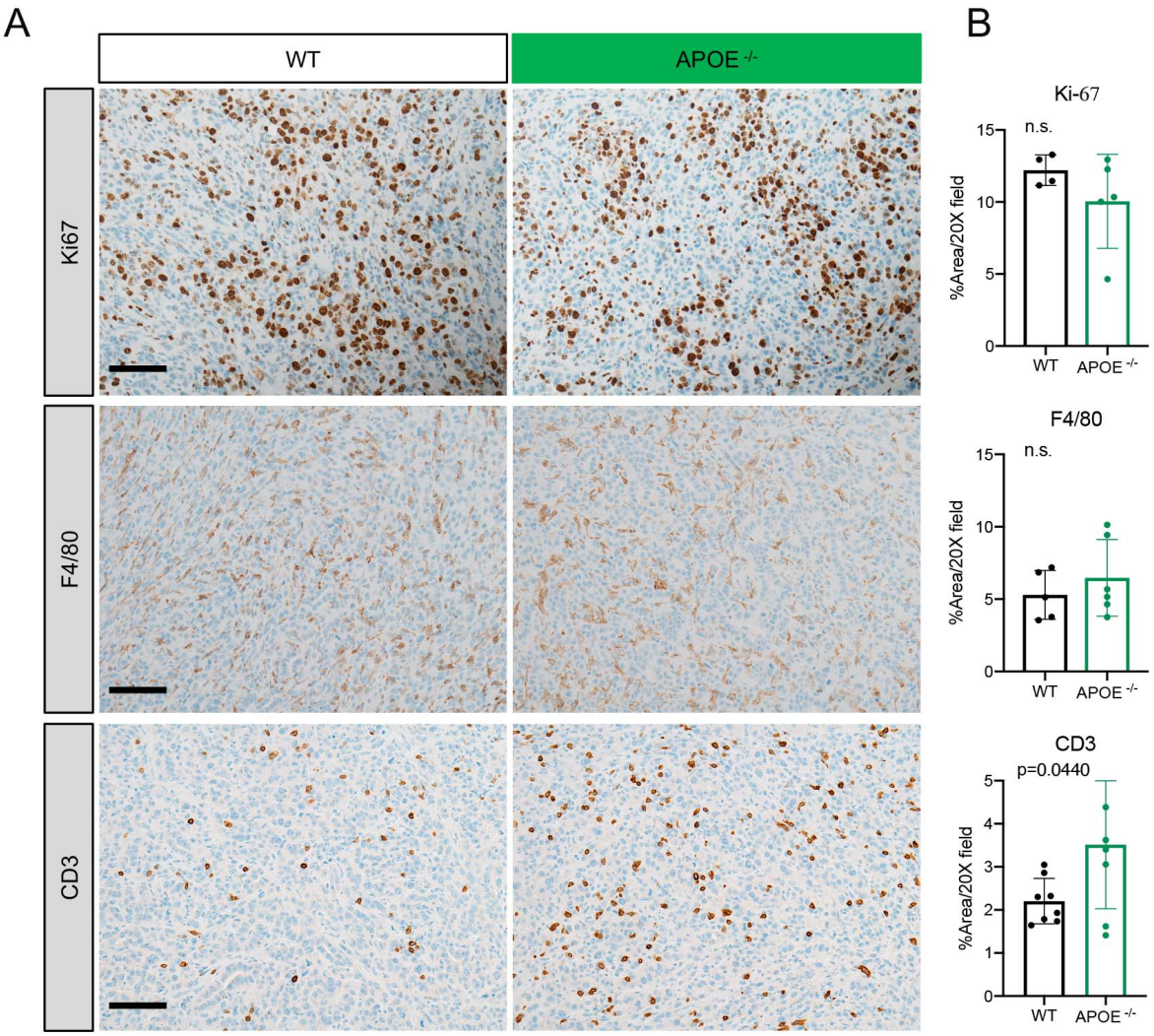

Figure 3.6 Histological changes in APOE deficient mice.
(A) Representative immunohistochemical staining for Ki-67, F4/80 and CD3 in WT and ApoE$^{-/-}$ mice. Scale bars, 100 μm. (B) Quantitation of positive immunohistochemical stain as percent area per 20x field in WT (n= 5) and ApoE$^{-/-}$ mice (n=5).

Figure 3.7

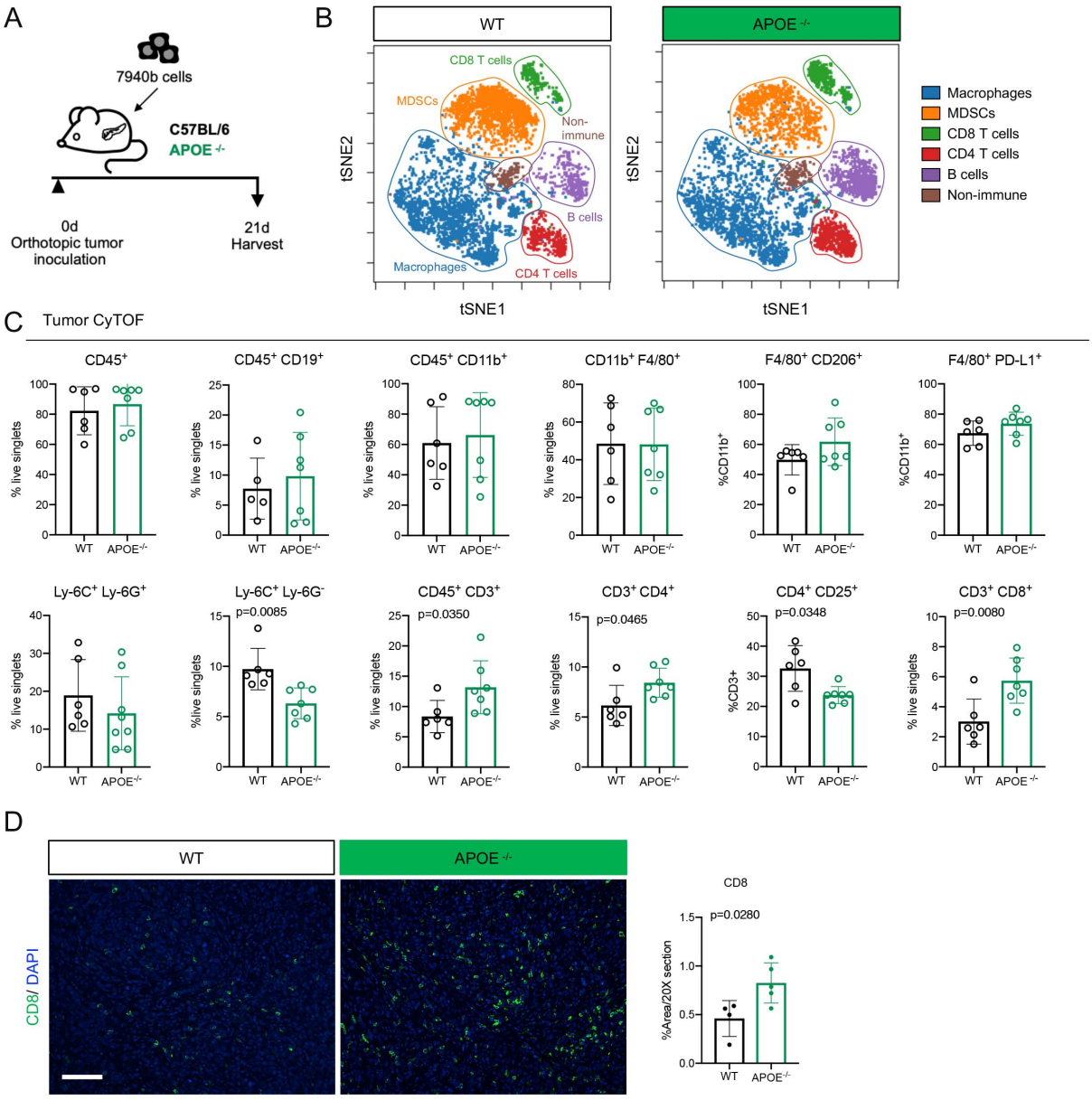

Figure 3.7 Mice deficient in APOE have fewer monocytic-MDSCs and increased CD8⁺ T cell infiltration.
(A) Experimental scheme for orthotopic transplantation of 7940b, KPC tumor cells. (B) tSNE visualization of the 6 cell populations identified using CyTOF in WT and ApoE$^{-/-}$ tumors. Populations identified include macrophages (blue), MDSCs (orange), CD8 T cells (green), CD4 T cells (red), B cells (purple) and non-immune (brown). (C) Manual gating quantitation of cell populations in WT (n=5-6) and ApoE$^{-/-}$ (n=7) tumors. Populations include total immune (CD45^{+}), B cells (CD45^{+} CD19^{+}), total myeloid (CD45^{+} CD11b^{+}), macrophages (CD11b^{+} F4/80^{+}), TAMs (F4/80^{+} CD206^{+}; F4/80^{+} PD-L1^{+}), granulocytic-MDSCs (Ly-6C^{+} Ly6G^{+}), monocytic-MDSCs (Ly-6C^{+} Ly-6G^{-}), total T cells (CD45^{+} CD3^{+}), CD4 T cells (CD3^{+} CD4^{+}), regulatory T cells (CD4^{+} CD25^{+}), and CD8 T cells (CD3^{+} CD8^{+}). (D) Representative immunofluorescence staining of CD8 (green) and DAPI (blue) in WT and ApoE$^{-/-}$ tumors. Scale bars, 100 μm. Quantitation of percent CD8 positive area in a 20x field in WT (n= 4) and ApoE$^{-/-}$ mice (n=5) (right panel). Statistics were determined by two-tailed *t* test.

Figure 3.8

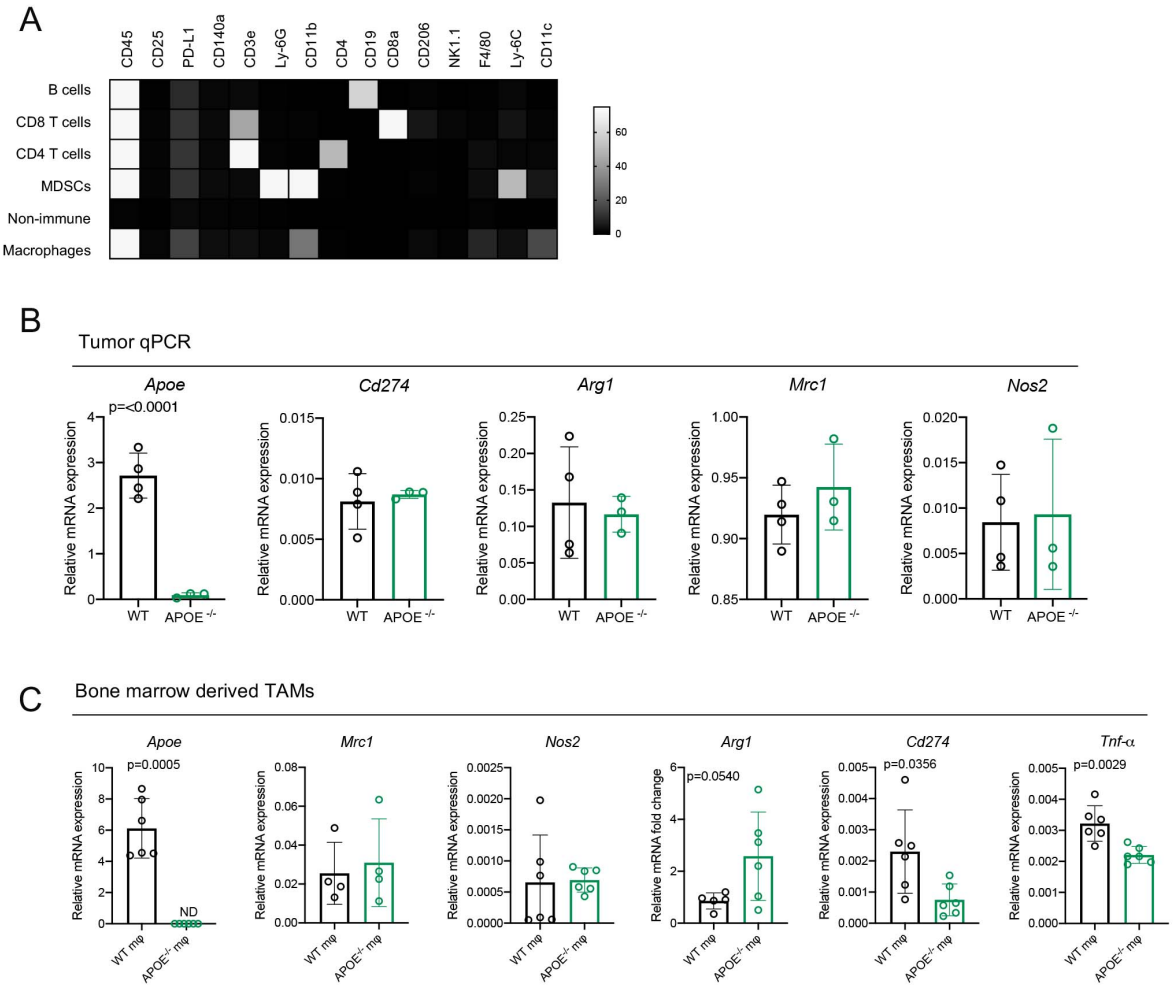

Figure 3.8 Loss of APOE alters macrophage polarization.
(A) Heatmap of lineage markers used to define cell populations. Low expression is in black, while high marker expression is in white. (B) qRT-PCR analysis of *ApoE, Cd274*, *Arg1*, *Mrc1*, *and Nos2* mRNA levels relative to *Cyclophilin A* housekeeping in WT (n=4) and ApoE$^{-/-}$ (n=3) tumors. Statistical significance was determined using two-tailed *t* tests. (C) qRT-PCR analysis of *ApoE, Mrc1*, *Nos2*, *Cd274*, *and Tnfa* mRNA levels relative to *Cyclophilin A* housekeeping in WT TAMs (n=4-6) and ApoE$^{-/-}$ TAMs (n=4-6) tumors. Statistical significance was determined using two-tailed *t* tests. ND = not detected.

Figure 3.9

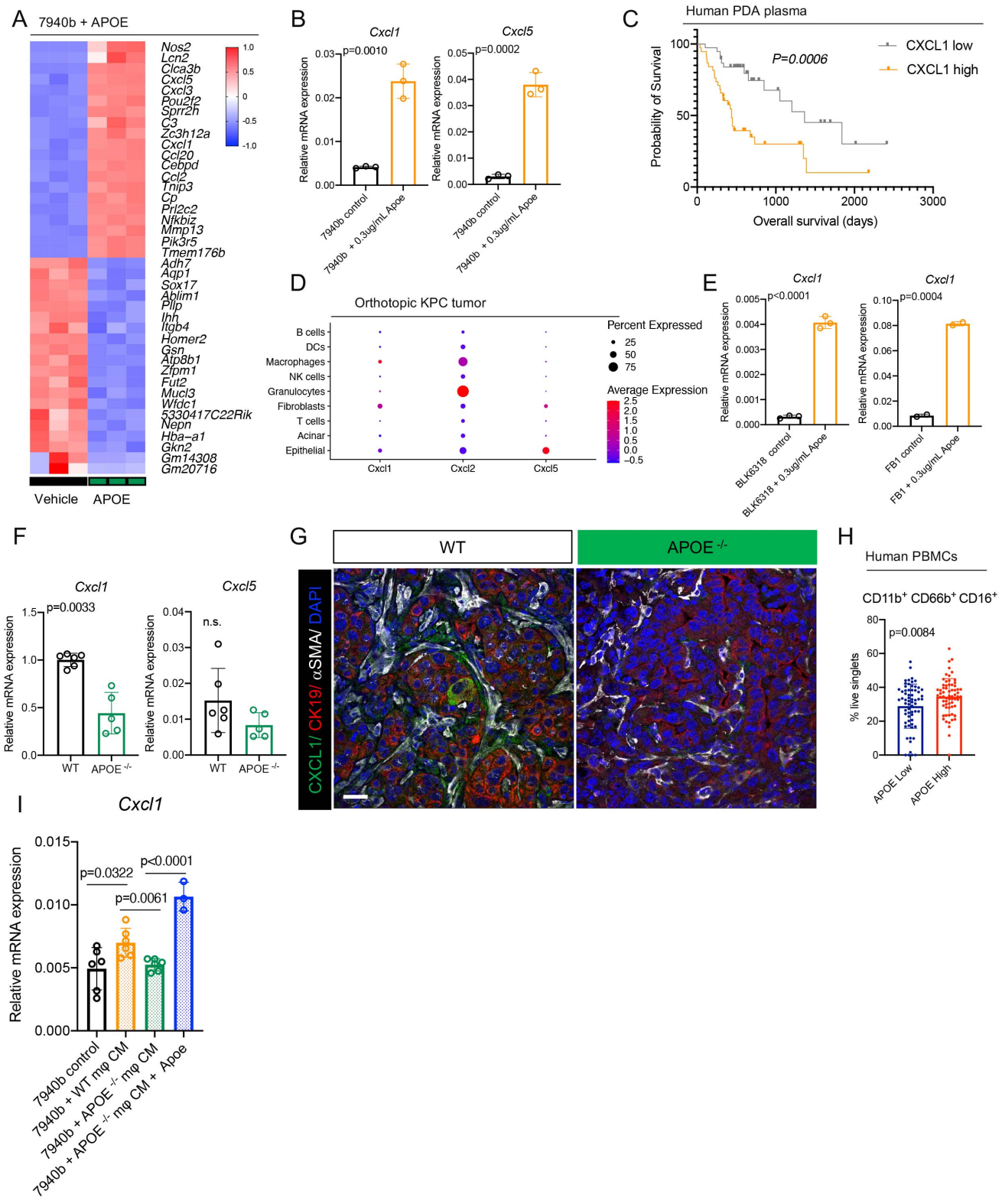
A
7940b + APOE
Nos2
Lcn2
Clca3b
Cxcl5
Cxcl3
Pou2f2
Sprr2h
C3
Zc3h12a
Cxcl1
Ccl20
Cebpd
Ccl2
Tnip3
Cp
Prl2c2
Nfkbiz
Mmp13
Pik3r5
Tmem176b
Adh7
Aqp1
Sox17
Ablim1
Plip
Ihh
Itgb4
Homer2
Gsn
Atp8b1
Zfpm1
Fut2
Mucl3
Wfdc1
5330417C22Rik
Nepn
Hba-a1
Gkn2
Gm14308
Gm20716
Vehicle
APOE
B
Cxcl1
p=0.0010
Relative mRNA expression
7940b control
7940b + 0.3ug/mL Apoe
Cxcl5
p=0.0002
C
Human PDA plasma
P=0.0006
CXCL1 low
CXCL1 high
Probability of Survival
Overall survival (days)
D
Orthotopic KPC tumor
B cells
DCs
Macrophages
NK cells
Granulocytes
Fibroblasts
T cells
Acinar
Epithelial
Cxcl1
Cxcl2
Cxcl5
Percent Expressed
Average Expression
E
Cxcl1
p<0.0001
BLK6318 control
BLK6318 + 0.3ug/mL Apoe
p=0.0004
FB1 control
FB1 + 0.3ug/mL Apoe
F
Cxcl1
p=0.0033
WT
APOE -/-
Cxcl5
n.s.
G
WT
APOE -/-
CXCL1/ CK19/ αSMA/ DAPI
H
Human PBMCs
CD11b+ CD66b+ CD16+
p=0.0084
% live singlets
APOE Low
APOE High
I
Cxcl1
p=0.0322
p<0.0001
p=0.0061
7940b control
7940b + WT mφ CM
7940b + APOE -/- mφ CM
7940b + APOE -/- mφ CM + Apoe

Figure 3.9 APOE regulates *Cxcl1* expression in tumor cells and fibroblasts.
(A) Heatmap of differentially expressed genes in *in vitro* 7940b KPC cells treated with vehicle (n=3) compared to 7940b KPC cells treated with 0.3 μg/mL murine recombinant APOE (n=3) for 48 hours. High expression is in red, while low expression is in blue. (B) qRT-PCR analysis of *Cxcl1* and *Cxcl5* mRNA levels relative to *Cyclophilin A* housekeeping in 7940b KPC cells treated with vehicle (n=3) or 0.3 μg/mL recombinant ApoE (n=3) for 48 hours. Statistics were determined using two-tailed *t* tests. (C) Survival analysis of PDA patients stratified by plasma CXCL1 levels. CXCL1 Low (n=38) and CXCL1 High (n=38). Statistics were determined using Log-rank (Mantel-Cox) test. (D) Dot plot for *Cxcl1*, *Cxcl2*, and *Cxcl5* in orthotopic KPC tumors (n=2). Color denotes average expression. Size of dot represents percent expression. (E) qRT-PCR analysis for *Cxcl1* mRNA levels relative to *Cyclophilin A* housekeeping in wild type fibroblasts (BLK6318) and cancer-associated fibroblasts (FB1), treated with vehicle (n=2-3) or 0.3 μg/mL recombinant ApoE (n=2-3) for 48 hours. Statistics were determined by two-tailed *t* tests. (F) qRT-PCR analysis of *Cxcl1* and *Cxcl5* mRNA levels relative to *Cyclophilin A* housekeeping in WT (n=6) and $ApoE^{-/-}$ (n=5) tumors. Statistical significance was determined using two-tailed *t* test. n.s. = not significant. (G) Co-immunofluorescence staining of CXCL1 (green), CK19 (red), aSMA (white), and DAPI (blue) in WT and $ApoE^{-/-}$ orthotopic KPC tumors. (H) Quantitation of human neutrophils ($CD11b^{+}$ $CD66b^{+}$ $CD16^{+}$) in the blood of PDA patients with low (n=65) versus high (n=65) plasma APOE levels. Statistics were determined by two-tailed *t* tests. (I) qRT-PCR analysis of *Cxcl1* mRNA levels relative to *Cyclophilin A* housekeeping in 7940b tumor cells alone control (n=6), 7940b cells cultured with WT macrophage conditioned media (n=6), 7940b cells cultured with $ApoE^{-/-}$ macrophage conditioned media (n=6), and 7940b cells cultured with $ApoE^{-/-}$ macrophage conditioned media with 0.3 μg/mL recombinant ApoE (n=3). Statistical significance was determined by two-tailed *t* tests between groups.

Figure 3.10

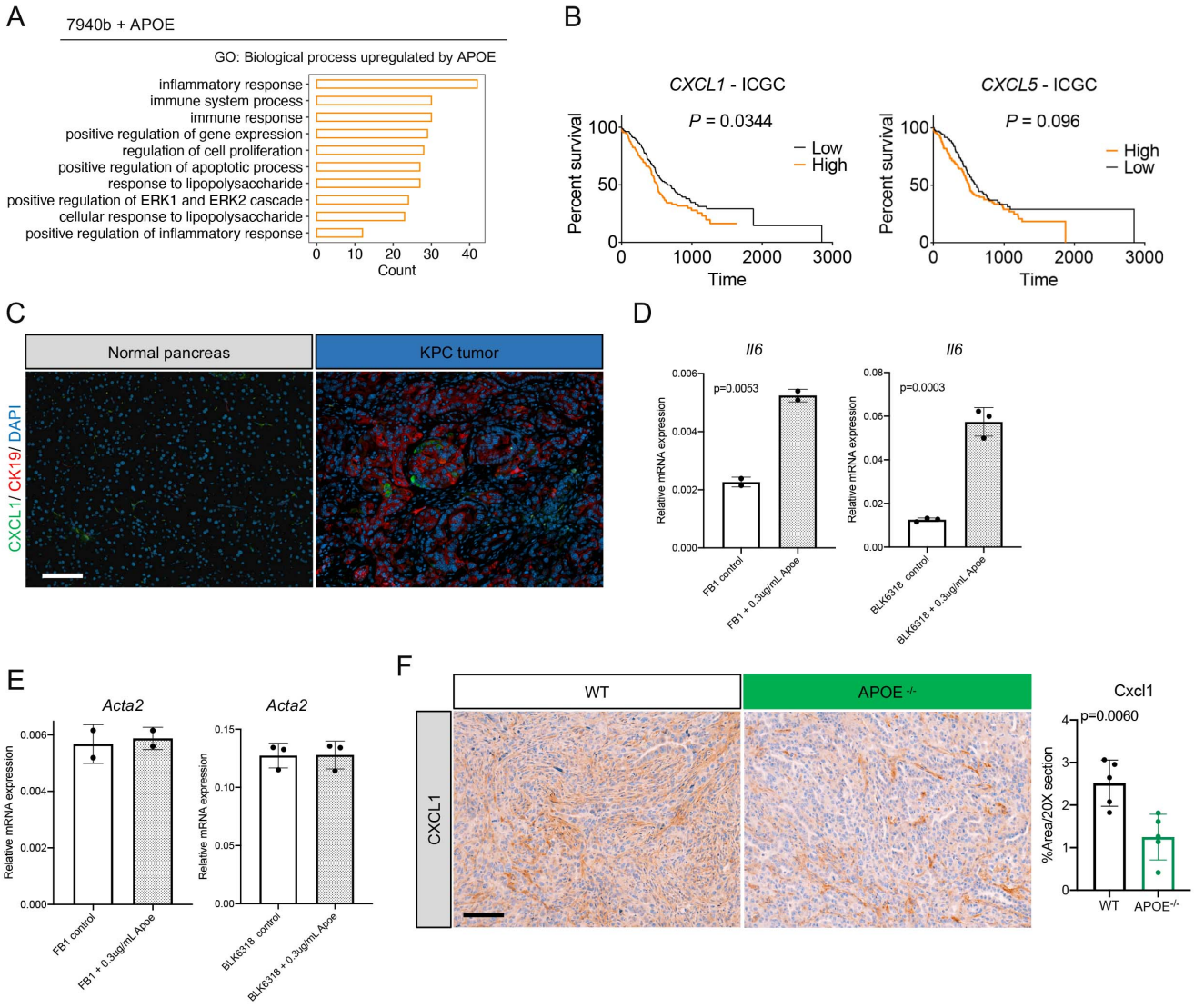

Figure 3.10 Cxcl1 is highly expressed in mouse PDA tumors.
(A) Biological processes upregulated in 7940b KPC cells treated with recombinant APOE. Derived from DAVID functional annotation platform using the top 500 genes induced by recombinant APOE. (B) Survival analysis of PDA patients from the ICGC dataset stratified by *CXCL1* (left) or *CXCL5* (right) expression levels. *CXCL1* low (n=154) and high (n=155). *CXCL5* low (n=154) and high (n=155). Statistics were determined by Log-rank (Mantel-Cox) test. (C) Representative co-immunofluorescence staining of CXCL1 (green), CK19 (red), and DAPI (blue) in mouse normal pancreas compared to mouse KPC tumor. Scale bars, 100 μm. (D) qRT-PCR analysis for *Il6* and (E) *Acta2* mRNA levels relative to *Ppia* housekeeping in wild type fibroblasts (BLK6318) and cancer-associated fibroblasts (FB1), treated with vehicle (n=2-3) or 0.3 μg/mL recombinant ApoE (n=2-3) for 48 hours. Statistics were determined by two-tailed *t* tests. (F) Representative immunohistochemical staining for CXCL1 in WT and ApoE$^{-/-}$ mice. Scale bars, 100 μm. Quantitation of positive CXCL1 staining as percent area per 20x field in WT (n= 5) and ApoE$^{-/-}$ mice (n=5). Statistics determined by two-tailed *t* tests.

Figure 3.11

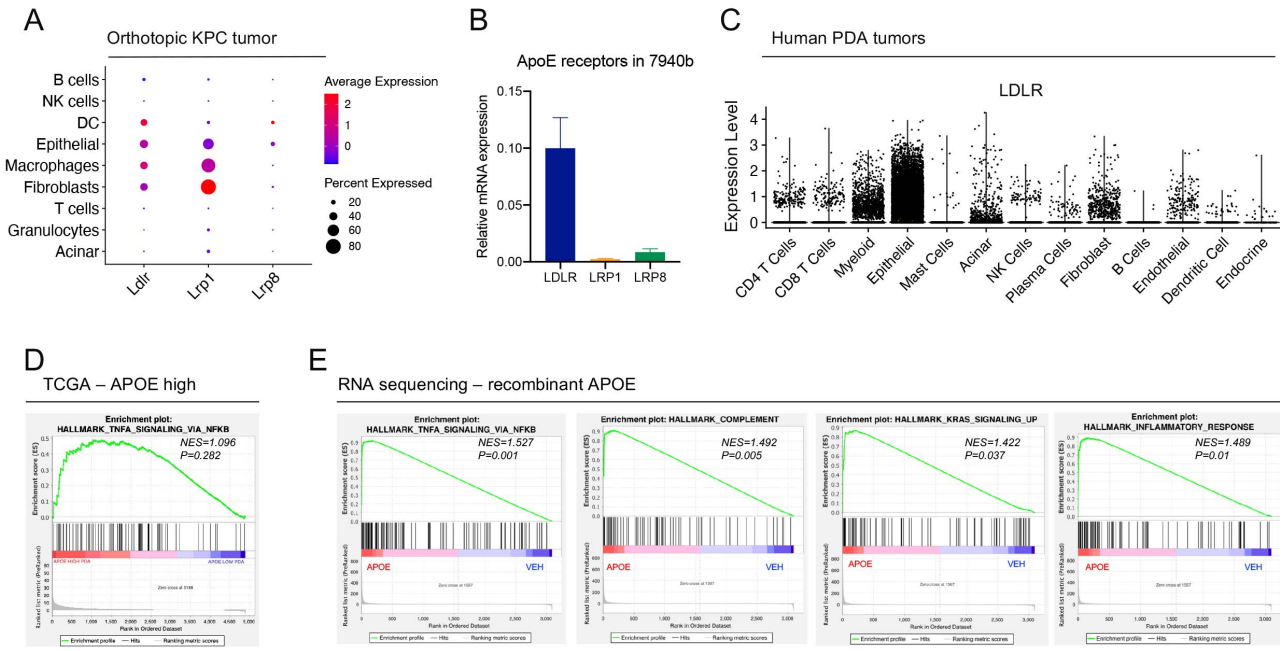

Figure 3.11 APOE upregulates NF-kB signaling.
(A) Dot plot of *Ldlr*, *Lrp1*, and *Lrp8* in orthotopic KPC tumors. Color represents average expression, while size of the dot represents percent expressed. (B) qRT-PCR analysis for *Ldlr*, *Lrp1*, and *Lrp8* mRNA levels relative to *Cyclophilin A* in 7940b KPC tumor cells *in vitro*. (C) Violin plot of normalized *LDLR* expression in human PDA. (D) Gene set enrichment analysis of NF-kB pathway enrichment in PDA TCGA APOE high tumors. (E) Gene set enrichment analysis of complement, NF-kB pathway, Kras signaling, and inflammatory response pathway enrichment in 7940b KPC cells treated with 0.3µg/mL recombinant ApoE (n=3) compared to vehicle (n=3) for 48 hours.

Figure 3.12

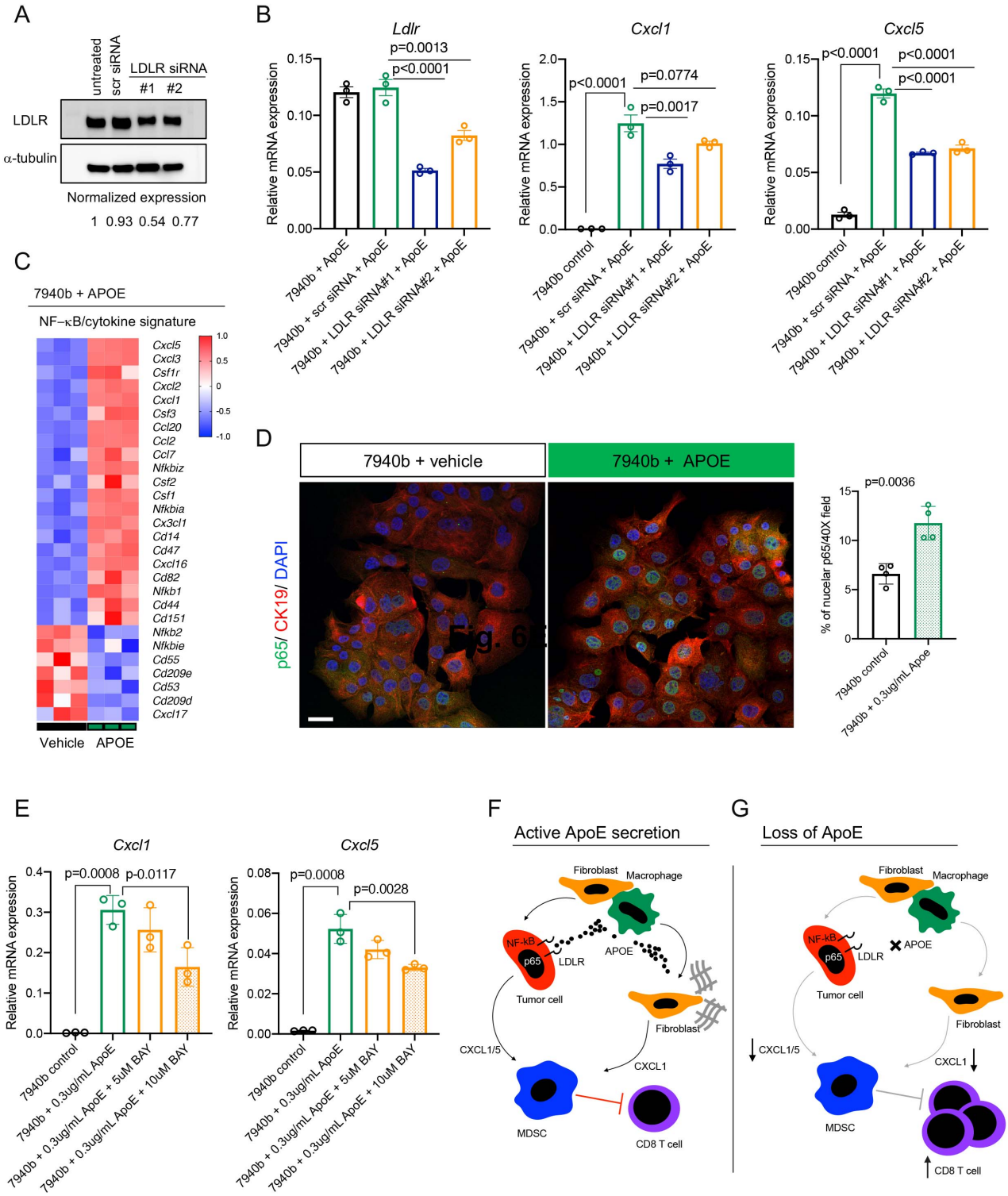
A
untreated
scr siRNA
LDLR siRNA
#1 #2
LDLR
α-tubulin
Normalized expression
1 0.93 0.54 0.77
B
Ldlr
p=0.0013
p<0.0001
Relative mRNA expression
7940b + ApoE
7940b + scr siRNA + ApoE
7940b + LDLR siRNA#1 + ApoE
7940b + LDLR siRNA#2 + ApoE
Cxcl1
p<0.0001
p=0.0774
p=0.0017
7940b control
Cxcl5
p<0.0001
p<0.0001
p<0.0001
C
7940b + APOE
NF−κB/cytokine signature
Cxcl5
Cxcl3
Csf1r
Cxcl2
Cxcl1
Csf3
Ccl20
Ccl2
Ccl7
Nfkbiz
Csf2
Csf1
Nfkbia
Cx3cl1
Cd14
Cd47
Cxcl16
Cd82
Nfkb1
Cd44
Cd151
Nfkb2
Nfkbie
Cd55
Cd209e
Cd53
Cd209d
Cxcl17
Vehicle APOE
D
7940b + vehicle
7940b + APOE
p65/ CK19/ DAPI
p=0.0036
% of nucelar p65/40X field
7940b control
7940b + 0.3ug/mL Apoe
E
Cxcl1
p=0.0008 p-0.0117
Cxcl5
p=0.0008
p=0.0028
7940b + 0.3ug/mL ApoE
7940b + 0.3ug/mL ApoE + 5uM BAY
7940b + 0.3ug/mL ApoE + 10uM BAY
F
Active ApoE secretion
Fibroblast
Macrophage
NF-kB
p65
LDLR
APOE
Tumor cell
Fibroblast
CXCL1/5
CXCL1
MDSC
CD8 T cell
G
Loss of ApoE
Fibroblast
Macrophage
NF-kB
p65
LDLR
APOE
Tumor cell
Fibroblast
CXCL1/5
CXCL1
MDSC
CD8 T cell

Figure 3.12 APOE regulates tumor cell *Cxcl1* production via NF-kB signaling.
(A) Representative western blot analysis of 7940b KPC tumor cells that were either untreated, treated with scrambled siRNA negative control, or treated with LDLR siRNA for 24 hours. a-tubulin was used for loading control. Normalized protein expression is denoted under each lane. (B) qRT-PCR analysis of *Ldlr*, *Cxcl1* and *Cxcl5* mRNA levels relative to *Cyclophilin A* housekeeping in 7940b KPC cells that underwent LDLR knockdown for 48 hours and were treated with 0.3 μg/mL recombinant ApoE (n=3) for 1 hour. Statistics were determined using one-way ANOVA with Turkey's test for multiple correction. (C) Heatmap of NF-kB/cytokine signatures in 7940b KPC cells treated with 0.3μg/mL recombinant ApoE (n=3) compared to vehicle (n=3) for 48 hours. High expression is in red and low expression is in blue. (D) Representative co-immunofluorescence staining of p65 (green), CK19 (red) and DAPI (blue) in 7940b tumor cells *in vitro* treated with vehicle or 0.3μg/mL recombinant ApoE for 48 hours. Scale bars, 25 μm. Quantitation of percent nuclear p65 in a 40x field in 7940b cells (n=4) and 7940b cells treated with 0.3μg/mL recombinant ApoE (n=4) for 48 hours. Statistics were determined through two-tailed *t* tests. (E) qRT-PCR analysis of *Cxcl1*, and *Cxcl5* mRNA levels relative to *Cyclophilin A* housekeeping in 7940b cells (n=3), 7940b cells treated with 0.3μg/mL recombinant ApoE for 2 hours (n=3), 7940b cells pre-treated with 5 μM BAY 11-7082 for 1 hour and then treated with 0.3μg/mL recombinant ApoE for 2 hours (n=3), and 7940b cells pre-treated with 10 μM BAY 11-7082 for 1 hour and then treated with 0.3μg/mL recombinant ApoE for 2 hours (n=3). Statistical significance was determined using one-way ANOVA with Turkey's test for multiple comparisons. (F) Working model. PDA tumors with active ApoE secretion regulate CXCL1 production from tumor cells and fibroblasts, which in turn recruits MDSCs, resulting in suppression of $CD8^+$ T cell infiltration. (G) PDA tumors with loss of ApoE secretion results in less CXCL1 production from tumor cells and fibroblasts, which in turn recruits fewer MDSCs, allowing for an increase in $CD8^+$ T cell infiltration.

Chapter 4 Pancreatic Cancer is Marked by Complement-high Tumor Associated Macrophages in Primary and Metastatic Tumors and Blood Monocytes[7,8]

Abstract

Pancreatic ductal adenocarcinoma (PDA) is accompanied by reprogramming of the local microenvironment, but changes at distal sites are poorly understood. Utilizing biomaterial scaffolds implanted into immunocompetent tumor-bearing and control mice, we identified a unique tumor-specific gene expression signature that includes high expression of *C1qa*, *C1qb* (complement components), as well as *Trem2*, *and Chil3.* Single cell RNA sequencing mapped these genes to two distinct macrophage populations in the scaffolds, one marked by elevated *C1qa*, *C1qb*, and *Trem2,* the other with high *Chil3.* In mice, corresponding populations of tumor associated macrophages (TAMs) were present at the primary tumor and were elevated in the tumor compared to the normal pancreas. We then analyzed single cell RNA sequencing from patient samples, and determined that elevated expression of *C1QA*, *C1QB*, and *TREM2* is elevated in human macrophages both at the primary tumor site and in liver

[7] Data from Chapter 4 have been submitted for publication at *Life Science Alliance* in a manuscript entitled, "Pancreatic cancer is marked by complement-high tumor-associated macrophages in primary and metastatic tumors and blood monocytes" (2021).

[8] Author list: Samantha B. Kemp, Nina G. Steele, Eileen S. Carpenter, Katelyn L. Donahue, Grace G. Bushnell, Aaron H. Morris, Stephanie The, Sophia M. Orbach, Veerin R. Sirihorachai, Zeribe C. Nwosu, Carlos Espinoza, Fatima Lima, Kristee Brown, Alexander A. Girgis, Valerie Gunchick, Yaqing Zhang, Costas A. Lyssiotis, Timothy L. Frankel, Filip Bednar, Arvind Rao, Vaibhav Sahai, Lonnie D. Shea, Howard C. Crawford*, Marina Pasca di Magliano*
*Corresponding authors

metastases. Single cell sequencing analysis of patient blood revealed a substantial enrichment of a monocyte population expressing the same gene signature, compared to healthy controls. Taken together, our study reveals a tumor-associated macrophage and monocyte population that is indicative of systemic immune changes in PDA patients.

Introduction

Pancreatic ductal adenocarcinoma (PDA) is a lethal malignancy with a dismal 5-year survival rate of only 10% (Siegel et al., 2020). PDA is characterized by an abundant, fibroinflammatory stroma. From the onset of carcinogenesis, the immune response to pancreatic cancer results in an immunosuppressive tumor microenvironment (TME) (Clark et al., 2007). Myeloid cells are abundant and heterogenous within the PDA TME and a key driver of an immune suppressive microenvironment (Mitchem et al., 2013; Stromnes et al., 2014; Zhang et al., 2017b; Zhu et al., 2017; Zhu et al., 2014). The primary tumor and metastatic sites are both characterized by tumor cell evasion of the immune response (Gonzalez et al., 2018; Hanahan and Weinberg, 2011). However, systemic alteration of the immune system by the primary tumor remains poorly understood. While the stochastic nature of metastasis greatly limits our ability to study the systemic responses to the primary tumor, recent advances in biomaterials engineering provide a novel opportunity to evaluate systemic response to PDA through the use of polycaprolactone scaffolds.

Biomaterial scaffolds have been used as a synthetic pre-metastatic niche in a breast cancer model (Aguado et al., 2017; Azarin et al., 2015; Bushnell et al., 2019; Rao et al., 2016). Additionally, scaffolds elicit a robust and dynamic immune infiltration in both

control and tumor settings, likely in response to scaffolds acting as a foreign body (Azarin et al., 2015; Rao et al., 2016). Scaffolds have been utilized more recently as a tool to allow for repeat sampling to obtain gene signatures that are predictive of disease and recurrence in mouse models of breast cancer and multiple sclerosis, an application of high clinical relevance (Morris et al., 2020a; Morris et al., 2020b; Oakes et al., 2020). Scaffolds, unlike the blood, allow for analysis of tissue-based immune response at distal sites.

In this study, we used engineered polymer scaffolds implanted into immune competent mice with orthotopic pancreatic tumors to generate an immune gene signature associated with pancreatic cancer. We found fundamental differences in the gene expression of cellular infiltrates derived from scaffolds in tumor-bearing versus non-tumor mice, with a tumor-specific signature including *Chil3*, *Trem2*, *C1qa* and *C1qb*. Single cell RNA sequencing identified changes primarily in macrophage gene expression and revealed two distinct populations of macrophages that were unique to tumor-bearing animals. While one macrophage population expressed *Chil3*, the other expressed *Trem2* and complement components *C1qa* and *C1qb* (complement-high macrophage). The complement-high macrophage population were present in primary tumors from mice and PDA patients, metastatic liver lesions, and expression of *C1QA*, *C1QB*, and *TREM2* was elevated in the blood of human PDA patients. Thus, we defined two-distinct systemically altered macrophage populations associated with PDA in mice and an enrichment of a complement-high macrophage/monocyte population in PDA patients.

Results

Biomaterial scaffolds harbor an immune-dense microenvironment in response to an orthotopic model of PDA

To understand the systemic immune changes in PDA, we first assessed the immune infiltration in the liver and peripheral blood of tumor-bearing animals compared to controls. Using an orthotopic model of pancreatic cancer, we implanted 7940b cells, derived from the *LSL-Kras*$^{G12D/+}$; *LSL-Trp53*$^{R172H/+}$; *Pdx1-Cre* (KPC) model of pancreatic cancer (Hingorani et al., 2005) on the C57BL/6J (BL/6) background, into the pancreas and performed mass cytometry (CyTOF) analysis. We found that livers and peripheral blood mononuclear cells (PBMCs) from tumor-bearing mice had an increase in total myeloid cells and myeloid cell subsets preceding the outgrowth of metastases, similar to previous reports (Lee et al., 2019b; Li et al., 2018a; Rhim et al., 2012; Sanford et al., 2013) (**Fig. 4.1A** and **4.1B**).

The immune cell changes in the blood and liver of tumor-bearing mice provided evidence of a systemic immune response to the tumor. We next used biologically inert polycaprolactone scaffolds to further study how tumors alter the systemic immune response in pancreatic cancer. We implanted scaffolds subcutaneously into BL/6 mice. One-week later 7940b (BL/6) cells were orthotopically transplanted into the pancreas, followed by removal of the scaffolds after 3 weeks (**Fig. 4.2A** and **Fig. 4.1C**). Control mice had subcutaneous scaffold implantation, followed by mock orthotopic surgery. After removal, scaffolds were examined by immunofluorescence staining to determine which cell populations colonized the scaffold. Tumor cells (CK19^{+}) were identified in the scaffold of tumor bearing animals while epithelial cells were rare/absent in healthy controls (**Fig.**

4.2B). We observed a stromal response in the tumor-bearing scaffold, characterized by accumulation of fibroblasts (aSMA) (**Fig. 4.2B**). In order to determine whether the immune response in the scaffold was distinct in tumor-bearing versus healthy mice, we performed CyTOF using a panel of immune markers. Visualization of the scaffold infiltrate by t-distributed stochastic neighbor embedding (t-SNE) in control and tumor-bearing animals revealed an abundant stromal response in both, with the majority of the infiltrate comprised of various myeloid subsets, including macrophage subsets and myeloid-derived suppressor cells (MDSCs) (**Fig. 4.2C**). Macrophage subsets were unbiasedly defined by expression of either the inflammatory marker, Ly-6C, the immune checkpoint, PD-L1, or the alternatively activated marker, CD206. While there was no difference in total myeloid ($CD45^+$ $CD11b^+$), MDSC ($CD11b^+$ $Ly\text{-}6G^+$ $Ly\text{-}6C^+$), or total macrophage ($CD11b^+$ $F4/80^+$) infiltration we observed an upward trend in specific macrophage populations ($CD11b^+$ $F4/80^+$ $CD206^+$; $CD11b^+$ $F4/80^+$ $PD\text{-}L1^+$) in scaffolds from tumor-bearing animals, compared to controls, similar to the findings in the liver (**Fig. 4.1A** and **4.1D**, **Fig. 4.2D**). In addition, tumor-bearing scaffolds had more endothelial cells ($CD45^-$ $PECAM1^+$) and fibroblasts ($CD45^-$ $PDGFRa^+$) than control scaffolds (**Fig. 4.2E**). Finally, we analyzed the adaptive immune populations, and observed that tumor-bearing scaffolds had fewer total T cells ($CD45^+$ $CD3^+$), and fewer $CD8^+$ T cells compared with control (**Fig. 4.1D**, **Fig. 4.2E**). Thus, cell composition data suggested that the microenvironment at a distal site was altered in tumor-bearing mice.

Identification of a pancreatic cancer-specific gene signature

To understand the nature of the systemic changes in tumor bearing mice, we isolated RNA from scaffolds implanted in control and tumor-bearing mice and used a RT-qPCR array (OpenArray®, OA) to assess a panel of 632 mouse inflammatory genes and 16 reference genes. Two computational approaches were used to assign numerical scores to the mice and distinguish healthy (black) from diseased (red) (**Fig. 4.3A)** (Morris et al., 2020a). Unsupervised hierarchical clustering analysis revealed that tumor-bearing scaffolds (red) clustered separately from control scaffolds (black) at the gene expression level (**Fig. 4.4A** and **4.4B**). We further observed that while the inflammatory signature of control scaffolds appeared rather uniform, there was distinct heterogeneity amongst the tumor-bearing scaffolds (**Fig. 4.4A**). We then analyzed the data to define a unique 21 gene signature indicative of disease (**Fig. 4.3B**). Tumor-bearing scaffolds had lower expression of interferon gamma (*Ifng*) and Killer Cell Lectin Like Receptor G1 (*Klrg1*), markers of T cell activation/effector T cells, and, conversely, upregulation of Coagulation Factor II Thrombin Receptor (*F2r)*, a marker of exhausted T cells (Wherry et al., 2007) (**Fig. 4.3B**). In addition, tumor-bearing scaffolds had upregulation of chitinase3-like-3 (*Chi3l3*/*Chil3*/*Ym1*), a gene elevated in tumor-associated macrophages (TAMs) (Georgoudaki et al., 2016) (**Fig. 4.3B)**. Bulk RNA analysis provided an indication that the immune composition and functional status might be altered systemically in mice bearing pancreatic cancer.

We next performed single cell RNA sequencing on cells isolated from the scaffolds extracted from control and tumor-bearing mice to understand gene expression changes at a cellular level. Using published lineage markers, we defined the captured cells (Elyada et al., 2019) (**Fig. 4.4C**). We performed downstream analysis on all captured stromal cells,

including cancer-associated fibroblast (CAF) subsets (myofibroblastic-CAFs (myCAF) and inflammatory-CAFs (iCAF)) (Ohlund et al., 2017), perivascular cells, natural killer (NK) cells, T cell subsets (CD4, CD8, double-negative (DN) T cells, and Regulatory T cells (Treg)), plasma cells, mast cells, dendritic cells (DCs) and myeloid cell subsets (granulocytes and macrophages) (**Fig. 4.3C**). Analysis of the scaffold gene profile further revealed cell type specific gene signatures (**Fig. 4.3D**). Given the changes in myeloid cells and macrophages in the liver and blood of tumor-bearing mice (**Fig. 4.1A** and **4.1B**) we subsequently focused on the scaffold-associated macrophages (SAMs). We detected expression of *Chil3* and Interleukin 6 Receptor (*Il6ra)* (**Fig. 4.3D**), which have both been identified as playing a role in polarization of alternatively activated macrophages (Liou et al., 2017; Mauer et al., 2014; Roszer, 2015). We further detected an increase in Chil3 in tumor-bearing livers compared to controls, providing further evidence that the scaffolds can in part mimic the natural metastatic site (**Fig. 4.4D** and **4.4E**).

Identification of two distinct macrophage subsets in scaffold infiltrate

We next compared the gene expression profile of scaffold-associated macrophages in tumor-bearing versus control. The differentially expressed genes (DEGs) corroborated the scaffold signature with lower expression of Interferon Regulatory Factor 7 (*Irf7)* and Signal Transducer and Activator of Transcription 1 (*Stat1)*, as well as increased expression of *Chil3* (**Fig. 4.5A**-**C**, and **4.3B**). In addition, tumor-bearing SAMs displayed a high expression of Complement C1q A chain and B chain (*C1qa* and *C1qb*) and Triggering Receptor Expressed on Myeloid Cells 2 (*Trem2)*, and a low expression of the antigen-presentation markers, *Cd74* as well as the Major Histocompatibility

Complexes, (*H2-D1*, *H2-Aa*, and *H2-Eb1)* compared to control SAMs (**Fig. 4.5A** and **4.5B**). Thus, SAMs from tumor-bearing mice at a distal site have distinct gene expression compared to controls. While *C1qa*, *C1qb* and *Trem2* are known drivers of alternatively activated macrophage polarization in a LPS-induced inflammation model (Benoit et al., 2012; Turnbull et al., 2006), little is known about their involvement in pancreatic cancer.

We next performed Uniform Manifold Approximation and Projection (UMAP) analysis on the scaffold-associated macrophages and identified two transcriptionally distinct macrophage populations in the control and tumor-bearing scaffold infiltrate (**Fig. 4.5D** and **Fig. 4.6A**). Unbiased analysis of the top genes defining each cluster identified *C1qa*, *C1qb*, and *Trem2* as markers of the scaffold-associated macrophages 1 (SAMs 1) population, whereas *Chil3*, Placenta Associated 8 (*Plac8)*, and *Ly6c2* emerged as markers of scaffold-associated macrophages 2 (SAMs 2) (**Fig. 4.6B** and **4.6C**, **Fig. 4.5E** and **4.5F**). SAMs 1 also had high expression of *Cd74* and Major Histocompatibility complexes (*H2-Eb1*, *H2-Aa*) (**Fig. 4.6D).** Taken together, scaffold-associated macrophages separated into two main populations and have a different gene expression pattern in tumor-bearing mice compared to SAMs from healthy mice.

Macrophages in mouse pancreatic cancer tumors overexpress *TREM2* and complement genes.

Having identified *Chil3*, *Trem2* and the complement genes, *C1qa* and *C1qb* as markers of scaffold-associated macrophages in tumor-bearing mice, we next investigated whether these macrophage subsets also exist in primary tumors. To this end, we performed single cell RNA sequencing on two primary mouse orthotopic PDA tumors. We

identified populations of epithelial cells, acinar cells, fibroblasts, and six immune cell populations, including macrophages (**Fig. 4.7A**, **Fig. 4.8A**). Compared to the other immune cells, the macrophages in the primary tumor (i.e. TAMs) exclusively exhibited high expression of the SAMs signature genes (*Chil3*, *Trem2, C1qa*, and *C1qb*), while *Plac8* and *Ly6c2* were broadly expressed across cell types (**Fig. 4.7B**). Unbiased clustering identified 2 distinct populations of macrophages in the primary tumor (**Fig. 4.7C**, **Fig. 4.8B**). Similar to the SAMs, the TAMs in the primary tumor separated into two populations; one with high expression of *Chil3*, *Plac8*, and *Ly6c2* (Chil-TAMs), and the other with high expression of *C1qa, C1qb, and Trem2* (Cq-TAMs) (**Fig. 4.7D**). Chil-TAMs had higher expression of the inflammatory macrophage markers, nitric oxide synthase 2 (*Nos2*) and tumor necrosis factor (*Tnf*) (Murray and Wynn, 2011), while Cq-TAMs had higher expression of the alternatively activated macrophage markers, *Mrc1* and *Cd163* (Roszer, 2015) (**Fig. 4.8C**).

We next compared TAMs from orthotopic KPC tumors (Tumor) to a normal mouse pancreas (N Panc) sample (**Fig. 4.7E**). We identified a population of Chil-TAMs, and Cq-TAMs, and an additional population of macrophages (TAM) (**Fig. 4.7E** and **Fig. 4.8D**). Similar to the findings in the scaffold, we identified an increase in the expression of Chil-TAM and Cq-TAM markers in orthotopic tumors compared to the normal pancreas (**Fig. 4.7F**). Further, we performed co-immunofluorescence and detected an elevation of Cq-TAMs ($C1q^{+}$ $F4/80^{+}$) in a KPC tumor as well as a KPC liver metastasis sample, compared to the normal pancreas (**Fig. 4.7G**).

Thus, these two distinct macrophage populations (Chil-TAMs and Cq-TAMs) are prevalent both at the primary tumor and systemically in response to pancreatic cancer in

mice. We next performed differential expression on macrophages from scaffolds compared to macrophages from orthotopic mouse tumors (**Fig. 4.8E**). Among the top differentially expressed genes was higher expression of *Arg1, Il1a*, and *Rgs1* in macrophages from scaffolds compared to the primary tumor, suggesting a possible role for these genes in systemic disease (**Fig. 4.8F**). We have shown that these macrophages are in part similar, but they also importantly retain distinct features.

Cq-TAMs and Chil-TAMs are elevated in the iKras* p53* model of pancreatic cancer.

We next sought to identify Chil-TAMs and Cq-TAMs in the iKras* and iKras* p53* genetically engineered mouse models that recapitulate the progression of human pancreatic cancer (Collins et al., 2012a; Collins et al., 2012b). We first subcutaneously implanted scaffolds into control and iKras* p53* mice and performed single cell RNA sequencing on the scaffold infiltrate (**Fig. 4.9A** and **Fig. 4.10A**). We observed an increase in *C1qa*, *C1qb*, and *Chil3*, but not *Trem2*, in the iKras* p53* scaffolds compared to control (**Fig. 4.9B**). Similar to the orthotopic scaffolds, we observed two distinct macrophage populations (**Fig. 4.9C**). SAMs 1 was defined by expression of *C1qa*, *C1qb*, and *Trem2*, while SAMs 2 was defined by expression of *Chil3*, *Plac8*, and *Ly6c2* (**Fig. 4.9C** and **4.9D**).

We next used single cell RNA sequencing to assess Chil-TAMs and Cq-TAMs in iKras* and iKras* p53* pancreas samples compared to the normal pancreas (**Fig. 4.10B** and **4.10C**). The macrophages unbiasedly clustered into three distinct macrophage populations (**Fig. 4.9E**). We again identified a population of Chil-TAMs and Cq-TAMs (**Fig. 4.9E** and **4.9F**). We further, identified a third population of macrophages that are defined by high expression of *Ccr2*, and the antigen-presentation markers, *Cd74* and *H2-*

Eb1 (**Fig. 4.10D**). The iKras* sample represents an early lesion timepoint, while the iKras* p53* represents a late lesion timepoint, allowing us to evaluate Chil-TAMs and Cq-TAMs during progression of PDA. We observed increased expression in Chil-TAM and Cq-TAM makers, along with a loss of CCR2-TAM markers in the iKras* p53* pancreas compared to iKras* and control samples (**Fig. 4.9G** and **Fig. 4.10E**). These data suggest that later stages of disease have an elevation in Chil-TAMs and Cq-TAMs.

Macrophages in human pancreatic cancer tumors overexpress *TREM2* and complement genes.

We next assessed the macrophage gene signature in human pancreatic cancer. Since there is no human ortholog for *Chil3*/*Ym1* (Kzhyshkowska et al., 2007) or *Ly6c2* (Lee et al., 2013), we focused on *TREM2* and the complement components, *C1QA* and *C1QB*. To assess the expression of *TREM2*, *C1QA*, and *C1QB* we queried a single cell RNA sequencing dataset including human normal / adjacent normal pancreas (n=3) and human PDA tumors (n=16) (Steele et al., 2020) (**Fig. 4.11A**). Consistent with our observation in mice, we saw the highest expression of *TREM2*, *C1QA*, and *C1QB* in human macrophages, while *PLAC8* was broadly expressed (**Fig. 4.11B)**. Further, these macrophages separated into two transcriptionally distinct subsets, that were consistent across patients (**Fig. 4.11C**; **Fig. 4.12A** and **4.12B**). One population was enriched for expression of *C1QA, C1QB*, and *TREM2* (CQ-TAMs), while the other population had high expression of *VCAN*, *FABP5*, and *RETN* (TAMs) (**Fig. 4.11D** and **Fig. 4.12A).** Paralleling the mouse data, *C1QA, C1QB*, and *TREM2* were upregulated in macrophages from human pancreatic cancer tumors compared to macrophages from non-malignant

pancreas (**Fig. 4.11E)**. CQ-TAMs were enriched at the primary tumor, suggesting that *C1QA, C1QB*, and *TREM2* identify a tumor-specific macrophage population in patient primary tumors.

Macrophages in human liver metastases express high levels of *TREM2* and complement genes.

To further address the role of CQ-TAMs in the systemic immune response, we next assessed the expression of the macrophage signature genes in liver metastasis samples from PDA patients (n=5). These samples were obtained through ultrasound guided percutaneous biopsy of a liver lesion in 5 individual PDA patients and processed for single cell RNA sequencing. Single cell RNA sequencing followed by UMAP visualization revealed a profound stromal response, including a substantial population of macrophages within the metastatic liver lesions (**Fig. 4.13A**, **Fig. 4.14A**). Similar to our scaffold and primary tumor data, the macrophages in the liver metastases had high expression of *C1QA*, *C1QB* and *TREM2* consistent with this macrophage population being part of a systemic response to a primary tumor (**Fig. 4.13B**). In addition, subsetting of the liver metastasis associated-macrophages confirmed the existence of two transcriptionally distinct macrophage populations (i.e. CQ-TAMs and TAMs), similar to the findings in the scaffolds in mice and primary tumors in mice and humans (**Fig. 4.13C)**. The signature genes *C1QA, C1QB*, and *TREM2* had highest expression in CQ-TAMs compared to TAMs (**Fig. 4.13D**, **Fig. 4.14B**). CQ-TAMs are present at both the primary tumor and systemic locations in humans. Similar to our analysis in mice, we next performed differential expression analysis on macrophages from human liver metastases compared

to macrophages from human primary tumors (**Fig. 4.13E** and **4.13F**). *IL1A* was enriched in both scaffolds and liver metastases compared to the primary tumor (**Fig. 4.13F** and **Fig. 4.8F**). *IL1A* has been associated with increasing metastatic spread *in vitro* in PDA (Melisi et al., 2009). Taken together, these data highlight the importance of both the similarities and differences in CQ-TAMs systemically in PDA.

Complement-high myeloid cells are elevated in the blood of pancreatic cancer patients

The notion that systemic changes in the immune/myeloid gene expression signature might reflect the presence of a primary tumor is potentially important to add to diagnostic/prognostic toolbox. We next assessed the macrophage gene expression signature in human blood. We utilized a published dataset of single cell RNA sequencing on PBMCs from healthy donors (n=4) and PDA patients (n=16) (Steele et al., 2020) and queried it for the expression of our signature genes: *C1QA, C1QB*, and *TREM2* (**Fig. 4.15A**). We observed highest expression of *C1QA, C1QB*, and *TREM2 in* circulating monocytes in human PBMCs (**Fig. 4.16A).** We identified four populations of circulating monocytes based on expression of *CD14* and *CD16* (*FCGR3A/B*) as previously defined (Wong et al., 2011) (**Fig. 4.16B**, **Fig. 4.15B**). Similar to the scaffold, liver and primary tumor, *C1QA*, *C1QB*, and *TREM2* marked only one subpopulation of monocytes (CQ-Monocytes) in human PBMCs (**Fig. 4.16C** and **Fig. 4.15B-D**). To assess whether these genes are upregulated in the blood of PDA patients we further compared PBMCs between healthy donors and PDA patients and saw higher normalized expression of *C1QA* and

C1QB, in patients, suggesting that the upregulation of these markers also applies to circulating monocytes (**Fig. 4.16D** and **Fig. 4.15E**).

In summary, we have identified a complement-high population of macrophages, CQ-TAMs, that exists both at the primary tumor and systemically in mouse and human pancreatic cancer. CQ-TAMs are enriched at the primary tumor and in circulation in human PDA patients, presenting a novel population of monocytes/macrophages that could potentially serve as indicators of disease state.

Discussion

In this study, we utilized bioengineered scaffolds as a tool to discover a novel gene signature that is associated with tumor-bearing mice, including elevated expression of *C1qa*, *C1qb*, and *Trem2*. By single cell RNA sequencing we mapped this signature to a population of infiltrating macrophages and determined that a corresponding TAM population is present at the primary tumor in mice. We then analyzed single cell RNA sequencing data from patient tumors (Steele et al., 2020) and novel single cell RNA sequencing data from liver metastases and identified macrophages expressing high levels of *C1QA*, *C1QB*, and *TREM2* in both primary tumor and metastases. Finally, we determined that a *C1QA*, *C1QB*, and *TREM2*-high monocyte population is enriched in pancreatic cancer patients compared with healthy individuals, suggesting that the elevation of these cells may serve as novel predictors of disease in PDA patients.

Biomaterial scaffolds model the pre-metastatic niche (Azarin et al., 2015; Bushnell et al., 2019; Rao et al., 2016) and allow for repeated sampling, and, thus, longitudinal analyses. Further, scaffolds model distal tissue and are distinct from blood, as recently

determined (Morris et al., 2020a; Oakes et al., 2020). Relevant to our study, myeloid cells entering scaffolds differentiate into macrophages, distinct from peripheral blood monocytes.

PDA is characterized by a dense, fibroinflammatory stroma, that contains a large infiltration of immunosuppressive myeloid cells. Myeloid cells are a heterogenous population consisting of myeloid-derived suppressor cells and tumor-associated macrophages that contribute to tumor progression and metastasis (Qian and Pollard, 2010). Although tumor-associated macrophages have been well-described as contributors to PDA tumor progression, no prior study has examined their role systemically in response to a primary tumor. Here, we have leveraged single cell RNA sequencing analysis to identify two distinct systemically induced macrophage populations that are specific to mouse and human pancreatic cancer. In mice one macrophage population upregulated *Chil3* (Chil-TAMs) in response to disease, whereas the other population upregulated *C1qa*, *C1qb*, and *Trem2* (Cq-TAMs) in mouse and PDA patients. The role for these genes is unknown in pancreatic cancer.

C1QA and C1QB are components of the complement cascade. The complement cascade is a crucial mediator of innate immunity and can be recruited by components of the adaptive immune system to combat microbial infection, but recently its role in cancer and the tumor microenvironment has been explored (Afshar-Kharghan, 2017; Bonavita et al., 2015). Upregulation of C1QB has been reported in PBMCs of melanoma patients (Luo et al., 2011). While C1QA and C1QB have not been extensively studied, a recent report examined the role of the complement cascade in PDA. Zhang *et al*. reported that TAMs help tumor cells avoid complement mediated cell death, providing mechanistic

insight into TAM and complement component cross-talk in pancreatic cancer (Zhang et al., 2019b). Our data provides evidence for upregulation of the complement components *C1QA* and *C1QB* in PDA tumor-associated macrophages systemically. Further work is needed to determine if the upregulation of complement components is a side effect of the systemic inflammation caused by PDA or if it is functionally contributing to carcinogenesis (Bettac et al., 2017).

To our knowledge, TREM2 has not been evaluated in pancreatic cancer, but has been shown to play an immunosuppressive role in other tumor types (Katzenelenbogen et al., 2020; Molgora et al., 2020). Its family member, Triggering Receptor Expressed on Myeloid Cells 1 (TREM1) however, has been implicated to reduce tumor burden in PDA (Shen and Sigalov, 2017). While understudied in PDA, TREM2 has been extensively evaluated in Alzheimer's disease, a neurodegenerative disease, that, like cancer, is marked by a chronic inflammatory response (Kinney et al., 2018). TREM2 is a risk factor for Alzheimer's disease and is believed to modulate the behavior of microglia to exacerbate the inflammatory response.

A similar single cell sequencing approach to ours previously identified two distinct macrophage subsets in normal renal tissue across multiple species (Zimmerman et al., 2019). The authors reported a population of inflammatory macrophages defined by high expression of *Ly6c*, *Plac8*, and *Chil3* and a resident macrophage subset defined by high expression of *Cd81, C1qa, C1qb,* and *C1qc*. Given the similarity of their finding to ours, these macrophage populations are likely relevant in other model systems. The gene signature presented here identified markers that define macrophage/monocyte subsets in mouse and human pancreatic cancer. The identification of a tumor associated

signature in blood monocytes will potentially be exploited for diagnostic and prognostic applications in pancreatic cancer patients.

Materials and Methods

Study approvals

All animal procedures and studies were performed at the University of Michigan (Protocol Number PRO00007983) in compliance with the Institutional Animal Care & Use Committee (IACUC) guidelines. For human research, this study included a dataset the included patients over the age of 18 who received diagnostic endoscopic ultrasound for a suspected pancreas mass who were consented under the Institutional Review Board (IRB) HUM00041280 (Two additional passes using a 22 Gauge SharkCore™ needle was performed for research once biopsy for clinical use was obtained). For surgically resected tissue, patients who underwent either Whipple of distal pancreatectomy were consented under IRB HUM00025339. For peripheral blood mononuclear cell collection, up to 40 ml of whole blood was collected pre- and intra-operatively for all consented patients. All patients provided written consent and procedures and studies performed were done in accordance with ethical standards. For liver metastasis samples, patients over the age of 18 referred for percutaneous liver biopsy of a mass suspected to be metastatic PDA were consented according to HUM00025339. Up to 2 extra biopsies were taken for research.

Scaffold fabrication

Implantable, biomaterial scaffolds were formed by mixing polycaprolactone microspheres with NaCl particles (250–425 μm) at a 1:30 (w/w) ratio as previously described (Rao et al., 2016). This mixture was then pressed into a 5 mm(diameter) by 2 mm (height) disc, heated at 60 °C for 5 minutes on each side, and submerged in water to remove salt particles, leaving a porous structure. The scaffolds were then sterilized in 70% ethanol and stored in -80 °C until surgical implantation.

Animal experiments

Mice

C57/BL6J mice (Jackson Laboratory stock number #000664), KPC (Hingorani et al., 2005), iKras* (Collins et al., 2012a), and iKras* p53* (Collins et al., 2012b) mice were used for mouse experiments. All mice were housed in the Rogel Cancer Center vivarium at the University of Michigan. Experimental mice were monitored daily.

Doxycycline treatment

iKras* and iKras* p53*mice were administered doxycycline chow (BioServ, F3949) to induce expression of $Kras^{G12D}$ for 72 hours, followed by two days of 8 intraperitoneal injections of caerulein (Sigma, 75 μg/kg) to induce pancreatitis, as previously described (Collins et al., 2012a). Control mice lacked the full set of alleles and were administered doxycycline chow and caerulein along with experimental animals. For early lesion samples, iKras* mice had doxycycline administered for 3 weeks. For tumor samples, iKras* p53* mice were administered doxycycline for 14 weeks. Scaffolds were

subcutaneously implanted into iKras* p53* mice that had been administered doxycycline for 15 weeks and harvested 3 weeks later.

Scaffold implantation

Mice were anesthetized using isoflurane and the surgical area was prepared using aseptic technique. Before implantation, scaffolds were warmed at room temperature (RT) for 30 seconds and then implanted subcutaneously in C57/BL6J or iKras* p53* mice. The incision site was closed using absorbable sutures (Ethicon #J303H). For all experiments, up to 4 scaffolds were implanted per mouse to allow enough cells for downstream analysis. For orthotopic tumor studies, 7940b (BL/6) cells derived from the *LSL-Kras*$^{G12D/+}$; *LSL-Trp53*$^{R172H/+}$; *Pdx1-Cre* (KPC) model of pancreatic cancer (A gift from Dr. Gregory Beatty, University of Pennsylvania) were orthotopically transplanted into the pancreas one week after scaffold implantation.

Orthotopic transplantation model

Orthotopic transplantation into the pancreas was performed as previously described (Aiello et al., 2016). Briefly, 5 x 10^4 7940b KPC (BL/6) cells were prepared in a 1:1 ratio of growth-factor reduced Matrigel and media (*Dulbecco's Modified Eagle Medium* (DMEM) supplemented with 10% FBS). Mice were anesthetized using isoflurane and the surgical area was prepared using aseptic technique. A tumor cell suspension of 50 µl was injected directly into the pancreas using an insulin syringe. Control, non-tumor bearing mice in scaffold experiments received injection of 50 µl of 50% Matrigel in media.

Histopathological analysis

Scaffolds were removed from -80 °C and stored on dry ice until embedding. For frozen sections, scaffolds were embedded in optimal cutting temperature (O.C.T) and allowed to solidify over dry ice, then stored at -80 °C until sectioning. Frozen sections were cut at 10 microns. For immunofluorescent staining on O.C.T embedded scaffolds, slides were brought to RT and then submerged in 4% paraformaldehyde (PFA) for 12 minutes at RT, then washed with three changes of PBS. Scaffolds were then blocked with 1% bovine serum albumin (BSA) in PBS for 1 hour at RT, followed by primary antibody incubation overnight at 4 °C and secondary antibody incubation for 45 minutes at RT. Cell nuclei were counterstained with Prolong Diamond Antifade Mountant with DAPI (Invitrogen). Tissues were fixed overnight in 10% buffered formalin, then transferred to 70% ethanol for paraffin embedding. Immunohistochemical staining was performed on tissue sections using the Ventana Discovery Ultra XT autostainer and counterstained with hematoxylin. Scaffolds and tissues were imaged on the Olympus BX53F microscope with the Olympus DP80 digital camera and CellSens Standard software using the 20x and 40x objectives. Quantitation of positive immunohistochemical stain was performed using Image J, Fiji V2.0.0-rc-69/1.52p on at least three 20x magnification fields per sample. For co-immunofluorescence, Alexa Fluor™ 488 Tyramide SuperBoost™ Kit (Invitrogen) with SignalStain® EDTA Unmasking Solution (Cell Signaling) were used for C1q staining according to manufacturer's protocols, then Alexa Fluor (Invitrogen) secondary antibodies were used for F4/80 and E-cad. Cell nuclei were counterstained with Prolong Diamond Antifade Mountant with DAPI (Invitrogen). Images were taken using Olympus BX53F microscope, Olympus DP80 digital camera, and CellSens Standard software.

Mass Cytometry (CyTOF)

To obtain a single cell suspension, scaffolds were first enzymatically digested with 1mg/ml Collagenase P in DMEM for 10 minutes at 37 °C under constant agitation. Scaffolds were then mechanically digested and allowed further enzymatic digestion for an additional 10 minutes. Cells are then filtered through 40 μM mesh. Preparation of the mouse tissue for CyTOF was performed as previously described (Zhang et al., 2020). Mouse livers were mechanically and enzymatically digested for 10 minutes at 37 °C under agitation and filtered through 40 μM mesh to obtain single cells. For mouse PBMCs, up to 1 mL of whole blood was obtained via cardiac puncture into EDTA-coated syringes and transferred to 1.5 mL tubes. Tubes were inverted 10 times and centrifuged at RT at 1700 x g for 20 minutes. Serum was then removed and the PBMC layer was transferred to a new tube. PBMCs were washed, underwent ammonium-chloride-potassium (ACK) lysis for 10 minutes at RT, and were then centrifuged at 300 x g for 5 minutes. For both scaffolds, PBMCs and tissues, up to 1 x 10^7 cells from the single cell suspension were stained with the live/dead marker, Cell-ID Cisplatin (Fluidigm, #201064) for 5 minutes at room temperature. Maxpar cell surface staining protocol was followed (PN 400276 A4). Cells were stained with a panel of surface antibodies for 30 minutes at RT, then stored in Cell-ID Intercalator-IR (Fluidigm, 201192A) until being shipped and acquired on the CyTOF2 Mass Cytometer at the University of Rochester Medical Center. Downstream analysis on normalized FCS files was performed using the Premium CytoBank Software V7.3.0 (cytobank.org).

Inflammatory gene array and signature

Scaffolds were removed from the subcutaneous space and flash frozen in liquid nitrogen, then stored at -80 °C. Scaffolds were submerged in TRI Reagent (#R2050-1-50) and mechanically homogenized. RNA was extracted using Direct-zol RNA miniprep (#R2051) with on column DNase I treatment. RNA quality was determined using both nanodrop results for concentration and purity, and RNA integrity number (RIN). Samples with a RIN greater than 7 underwent reverse transcription for cDNA synthesis. The University of Michigan Advanced Genomics Core measured gene expression using the Mouse Inflammation Taqman OpenArray® (#4475373), a high-throughput qRT-PCR of 648 inflammatory genes.

Selection of genes for scaffold gene signature

After OpenArray® analysis, Cq values were analyzed in MATLAB to create a gene signature in a manner similarly to that used previously (Morris et al., 2020a; Oakes et al., 2020). First, any genes that were not detected in more than two mice in either group were removed from further analysis, and 549 of the 648 genes on the OA chip were used for this study. For some downstream analysis (that requires complete matrices such as SVD), samples missing data for a particular gene were filled with the median of the entire dataset. Three reference genes were selected: Hmbs, Ubc, and Ywhaz and ΔC_q values were calculated for each gene from the average of the reference genes for that sample. Fold change (FC) and p-values were calculated for diseased vs control samples for each gene. To create the scaffold gene signature, genes with a FC > 1.5 and $p<0.1$ were

selected. This included: Ifng, Stat1, Ccr2, Irf7, Klrg7, Cx3cr1, Ccl4, Il12b, Cxcl10, Ccl11, Cxcl14, Csf3, Tnfsf11, Nfatc4, F2r, Nox4, Cxcr4, Il6ra, Il18bp, Chi3l3, and Ccrl1/Ackr4.

Gene signature scores and analysis

Unsupervised hierarchical clustering was performed using the clustergram tool in MATLAB to plot dendrograms. This process allows clustering analysis of genes that cluster together as well as samples and can indicate if diseased scaffolds appear different from healthy. Next, computational approaches were applied to create two metrics determined from the scaffolds to indicate whether a mouse was diseased or healthy. We first created a score with an unsupervised technique, singular value decomposition (SVD) using the svds function in MATLAB. Then we trained a bootstrap aggregated decision tree ensemble (Bagged Tree) with 100 learning cycles using MATLAB's fitcensemble function with the Bag method to classify samples as healthy or diseased. The bagged tree ensemble was fed the log2 transformed ΔCq values centered on the healthy controls as well as disease classification. This created our second score, a supervised machine learning metric that indicated the probability of disease.

Single-cell RNA sequencing

Scaffolds and human and mouse tissues were mechanically and enzymatically digested with collagenase P (1mg/mL) and filtered through a 40 μM mesh to obtain single cells. Dead cells were removed using MACS® Dead Cell Removal Kit (Miltenyi Biotec Inc.). The single cell cDNA libraries were prepared using the 10x Genomics platform at the University of Michigan, Advanced Genomics Core. All single cell RNA sequencing

samples were run using paired end 50 cycle reads on either the HiSeq 4000 or the NovaSeq 6000 (Illumina) to a depth of 100,000 reads. Raw data were aligned to either mm10 or hg19 for mouse and human, respectively. Data were then filtered using Cellranger count V3.0.0 with default settings at the University of Michigan, Advanced Genomics Core. Downstream analysis was performed using R Studio V3.5.1 and R package Seurat V3.0. Batch correction across samples was performed using the R package Harmony V1.0 (https://github.com/immunogenomics/harmony). Raw human data from the Steele *et al.* study (Steele et al., 2020) are available at the NIH dbGaP database under the accession phs002071.v1.p1 and processed data are available at NIH GEO database under the accession GSE155698. Raw and processed data from this study are available at the NCBI's Gene Expression Omnibus database under the accession GSE158356. Raw and processed data for the iKras* (3 week ON) samples are available under the accession GSE140628 (Zhang et al., 2020).

Statistics

GraphPad Prism V7 software was used for graphical representation and statistical analysis. Two-tailed Student's t-tests were performed. A $p<0.05$ was considered statistically significant. Data are presented as means ± standard error (SEM). Differential expression analysis in single cell RNA sequencing data was performed using Wilcoxon rank sum test, with adjusted p-values for multiple comparisons.

Author Contributions

MPdM and HCC directed the study. MPdM, HCC, LDS and SBK developed the study concept and design. GGB provided scaffold technical expertise. GGB and SMO provided biomaterial scaffolds. AHM and LDS developed the signature analysis pipeline. AHM and ZCN created the scaffold gene expression signature. SBK, NGS, CE, FL, and ESC processed and stained scaffolds and mouse tissue for CyTOF. SBK, NGS and FB analyzed CyTOF data. AR and ST developed single cell RNA sequencing analysis pipelines. SBK, NGS, KLD and VRS obtained and analyzed single cell RNA sequencing data. YZ, KB, AAG performed co-immunofluorescene on scaffolds and tissue samples. VS, ESC and VG consented and collected human patient samples. YZ and TLF, CAL provided study guidance. MPdM, HCC and SBK drafted the manuscript, which was then edited and approved by all co-authors.

Acknowledgments

We thank Matthew Cochran and Terry Wightman at the Flow Cytometry Core at the University of Rochester Medical Center for CyTOF acquisition. We thank Kevin Brown and Vinicius Motta from Fluidigm for their assistance in CyTOF antibody panel design as well as downstream analysis in Cytobank. We thank Dr. Gregory Beatty, at the University of Pennsylvania, for the 7940b (BL/6) cell line. This work was made possible by the Advanced Genomics core at the University of Michigan. **Funding:** This project was supported by NIH/NCI grants R01CA151588, R01CA198074 and the American Cancer Society to MPdM. This work was also supported by the NIH U01CA224145 and University of Michigan Cancer Center Support Grant (P30CA046592), including an Administrative

Supplement to HCC and MPdM. FB was funded by the Association of Academic Surgery Joel Roslyn Award. TLF was funded by K08CA201581. SBK was supported by NIH T32-GM113900 and NCI F31-CA247076. NGS, KLD and VRS were supported by T32-CA009676. NGS was funded by American Cancer Society Postdoctoral Award PF-19-096-01 and the Michigan Institute for Clinical and Healthy Research (MICHR) Postdoctoral Translational Scholar Program fellowship award. ESC was supported by the American College of Gastroenterology Clinical Research Award and by T32-DK094775. ZCN was supported by the Michigan Postdoctoral Pioneer Program, University of Michigan Medical School. AR and ST were funded by institutional startup funds from the University of Michigan, a gift from Agilent Technologies, NCI grant R37CA214955 and a Research Scholar Grant from the American Cancer Society (RSG-16-005-01). AHM received support from the Michigan Life Science Fellows award, NIH T32 grant DE007057-43, and NIBIB grant K99EB028840. The funders had no role in study design, data collection and analysis, decision to publish, or preparation of the manuscript.

Figures

Figure 4.1

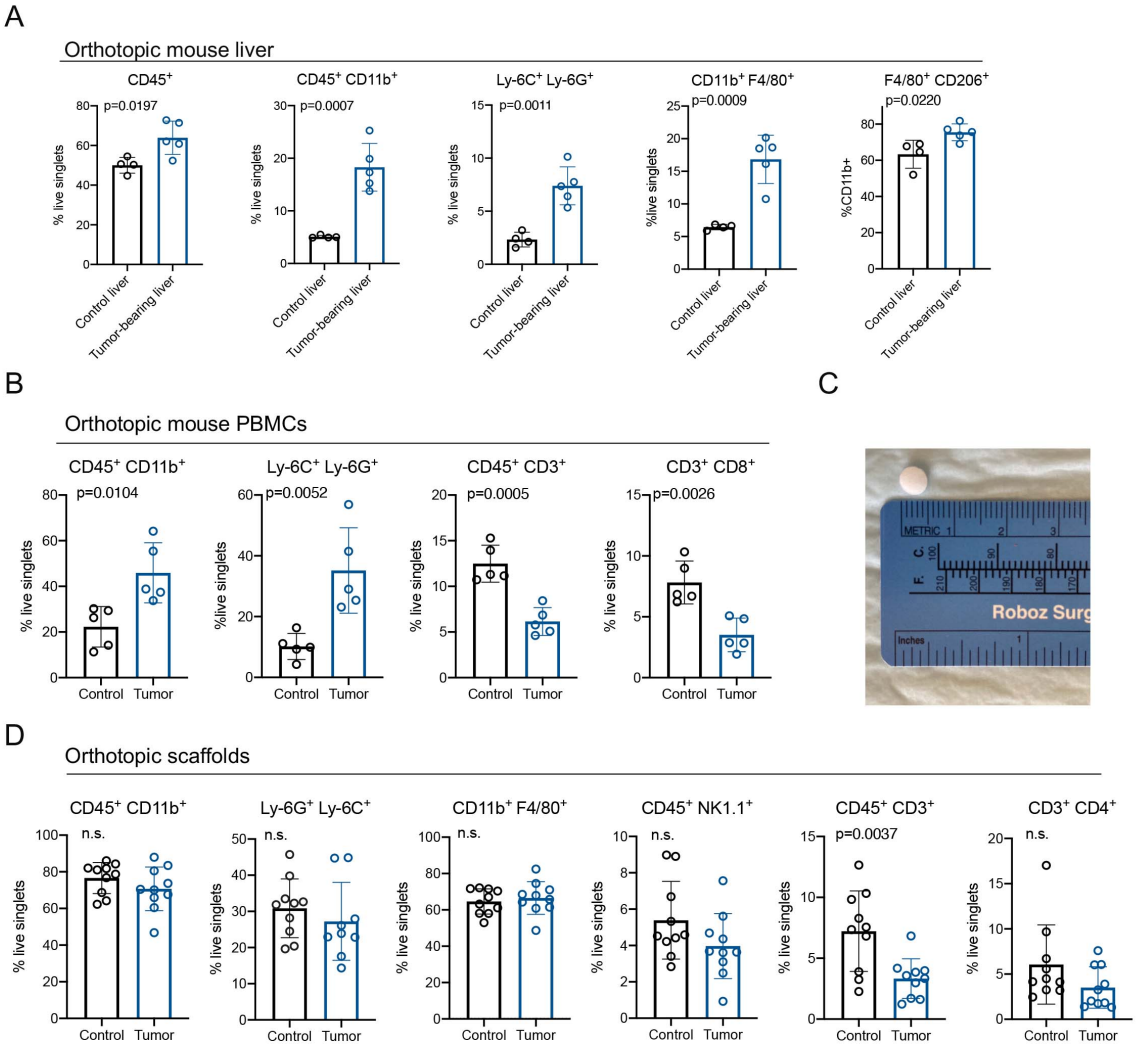

Figure 4.1 Immune characterization in liver, blood, and biomaterial scaffolds in tumor-bearing mice. (A) Manual gating of CyTOF results for total immune cells (CD45$^+$), myeloid cells (CD45$^+$ CD11b$^+$), MDSCs (Ly-6C$^+$ Ly-6G$^+$), total macrophages (CD11b$^+$ F4/80$^+$), and macrophage subset (F4/80$^+$ CD206$^+$) in control liver (n=4) compared to tumor-bearing liver (n=5) from an orthotopic mouse model of pancreatic cancer. Results are plotted as percent of total live singlets, except for CD206$^+$ macrophages, which are plotted as percent of total myeloid cells. Statistical significance was determined using two-tailed *t* tests. Data presented as means ± standard error (SEM) and $p<0.05$ was considered statistically significant. (B) Manual gating of CyTOF results for statistically significant changes in immune cell populations in PBMCS from control (n=5) and tumor-bearing (n=5) orthotopic mice. Results are plotted as percent of total live singlets, except for MDSCs, which are plotted as percent of total myeloid cells. Statistical significance was determined using two-tailed *t* tests. Data presented as means ± standard error (SEM) and $p<0.05$ was considered statistically significant. (C) Representation of scaffold size. (D) Manual gating of CyTOF results for total myeloid cells (CD45$^+$ CD11b$^+$), MDSCs (Ly-6G$^+$ Ly-6C$^+$), total macrophages (CD11b$^+$ F4/80$^+$), NK cells (CD45$^+$ NK1.1$^+$), total T cells (CD45$^+$ CD3$^+$), and CD4 T cells (CD3$^+$ CD4$^+$) in control scaffolds (n=10) compared to tumor-bearing scaffolds (n=9-10). Results are plotted as percent of total live singlets. Statistical significance was determined using two-tailed *t* tests. Data presented as means ± standard error (SEM) and $p<0.05$ was considered statistically significant.

Figure 4.2

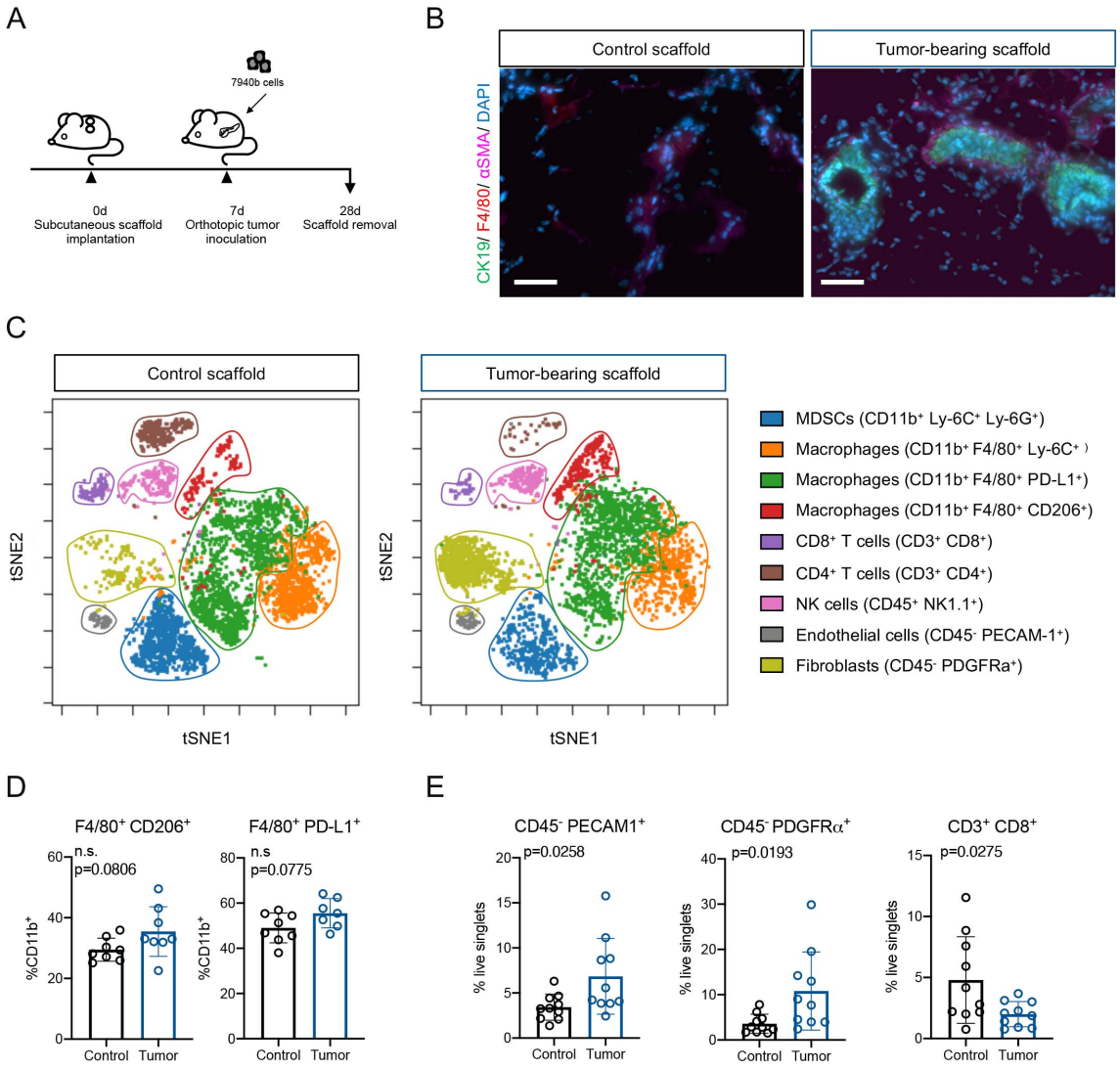

Figure 4.2 Biomaterial scaffolds harbor an immune-dense microenvironment in response to an orthotopic model of PDA.

(A) Experimental scheme. Scaffolds were subcutaneously implanted as described in the methods. 7940b (BL/6) cells derived from the *LSL-Kras*$^{G12D/+}$; *LSL-Trp53*$^{R172H/+}$; *Pdx1-Cre* (KPC) were orthotopically implanted into the pancreas. Scaffolds were harvested 3 weeks post tumor cell inoculation. (B) Co-immunofluorescence of scaffolds from animals who underwent mock-surgery (left) compared to tumor-bearing mice (right). Tumor cells are marked by CK19 (green), macrophages by F4/80 (red), fibroblasts by aSMA (pink), and nuclei by DAPI (blue). Scale bars, 50 μm. (C) Representative t-SNE plots for the scaffold infiltrate from control and tumor-bearing scaffolds. Identified populations include, MDSCs (blue), Ly-6C$^+$ macrophages (orange), PD-L1$^+$ macrophages (green), CD206$^+$ macrophages (red), CD8$^+$ T cells (purple), CD4$^+$ T cells (brown), NK cells (pink), endothelial cells (grey), and fibroblasts (light green). (D) Manual gating of CyTOF results for macrophage subsets (F4/80$^+$ CD206$^+$; F4/80$^+$ PD-L1$^+$) in control scaffold (n=8) compared to tumor-bearing scaffold (n=7-8). Results are plotted as percent of total myeloid cells (%CD11b$^+$). Statistical significance was determined using two-tailed *t* tests. Data presented as means ± standard error (SEM) and $p<0.05$ was considered statistically significant. (E) Manual gating of CyTOF results for endothelial cells (CD45$^-$ PECAM1$^+$), fibroblasts (CD45$^-$ PDGFRa$^+$) and CD8$^+$ T cells (CD3$^+$ CD8$^+$) in control scaffold (n=10) compared to tumor-bearing scaffold (n=10). Results are plotted as percent of total live singlets. Statistical significance was determined using two-tailed *t* tests. Data presented as means ± standard error (SEM) and $p<0.05$ was considered statistically significant.

Figure 4.3

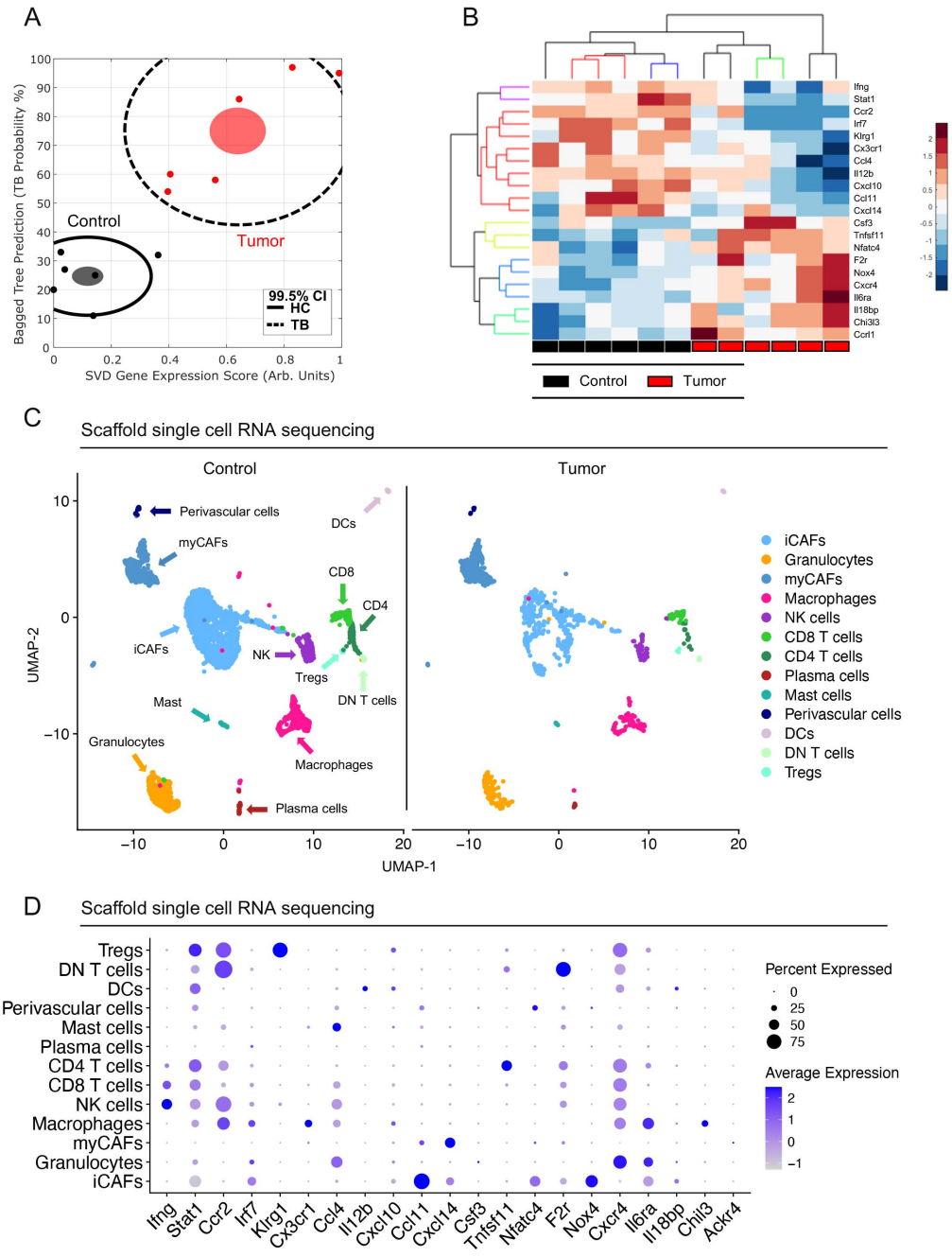

Figure 4.3 Identification of a pancreatic cancer-specific gene signature.
(A) Plot of Bagged Tree /SVD prediction produced from inflammatory gene OpenArray. Plot highlights the divergence of tumor-bearing (TB) scaffolds (red) from healthy control (HC) scaffolds (black). n=6 for control and n=6 for tumor-bearing scaffolds. Each dot represents a single mouse. Black line indicates 99.5% confidence intervals. Filled ovals denote the mean for control (black) and tumor-bearing (red) scaffolds for pooled control or tumor-bearing scaffolds. (B) Hierarchical clustering and heatmap of 21 inflammatory genes of interest in control (n=6) scaffolds compared to tumor-bearing scaffolds (n=6). (C) UMAP visualization of control scaffold (n=1) and tumor-bearing (n=1) scaffolds from an orthotopic mouse model of pancreatic cancer. (D) Dot plot shows average expression of scaffold signature in merged control and tumor-bearing scaffold infiltrate. Size of dot represents percent expressed. Color of dot represents average expression.

Figure 4.4

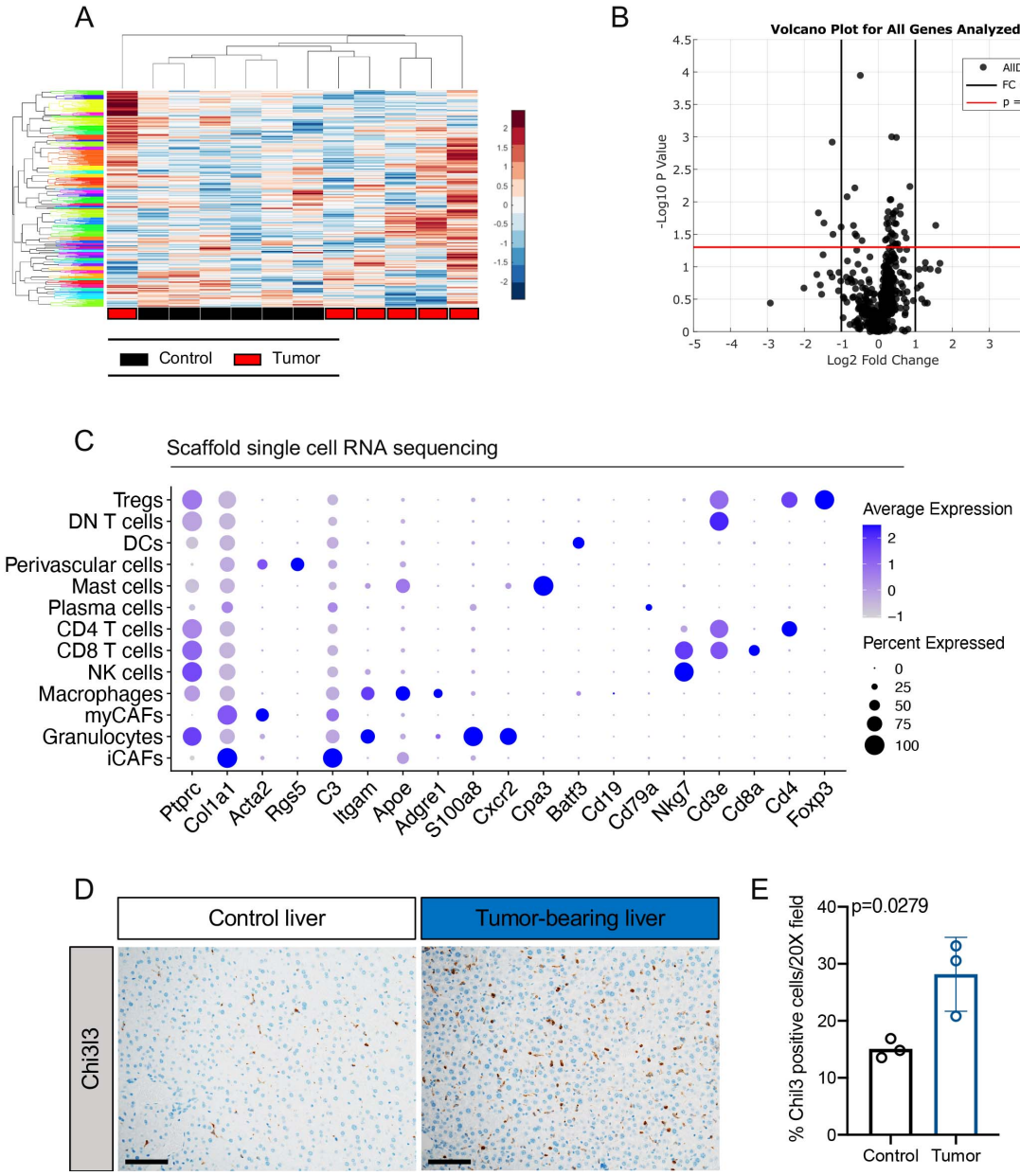

Figure 4.4 Heterogenous immune signature in tumor-bearing mice.
(A) Hierarchical clustering and heatmap analysis of all gene expression values from the OpenArray analysis. Black boxes indicate control scaffolds (n=6) and red boxes indicate tumor-bearing scaffolds (n=6). (B) Volcano plot analysis from all OpenArray gene expression data. Black lines indicate fold change of ± 2. Red line indicates p=0.05 determined by two-tailed *t* tests. (C) Dot plot of select lineage markers used to define captured cell populations. Color of the dot represents average expression. Size of the dot represents percent expressed. (D) Representative immunohistochemical analysis of Chil3/Chi3l3/Ym1 in control liver and tumor-bearing liver from mice with orthotopically transplanted PDA tumors. Scale bars, 100 μm. (E) Quantitation of %Chil3 positive cells in a 20x field in control (n= 3) and tumor-bearing livers (n=3).

Figure 4.5

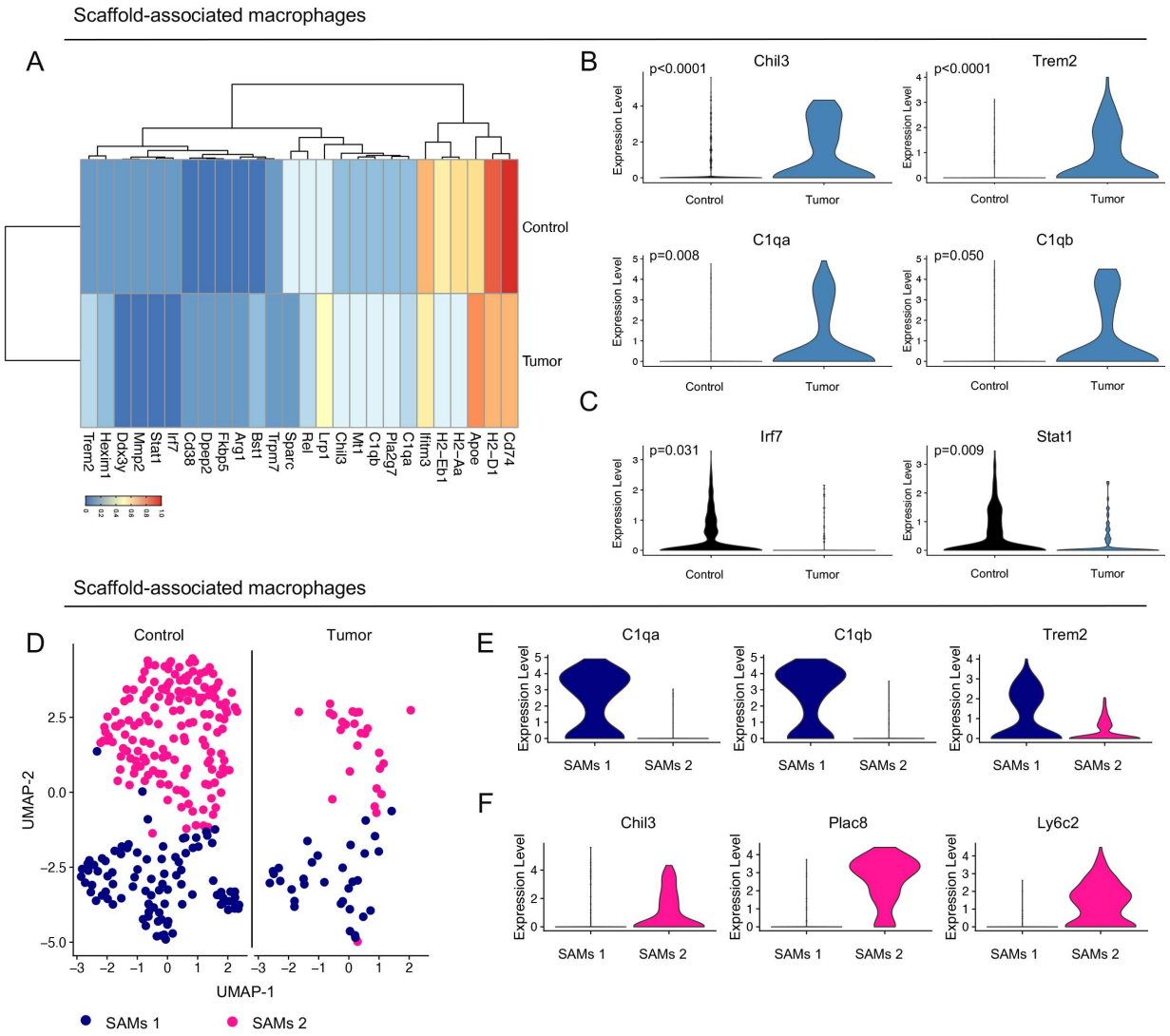

Figure 4.5 Identification of two distinct macrophage subsets in scaffold infiltrate.
(A) Average expression heatmap for select differentially expressed genes (DEGs) between macrophages from control and tumor-bearing scaffolds. Low expression in blue and high expression in red. All genes plotted are statistically significant, determined using non-parametric Wilcoxon rank sum test with a p-value cut off of p<0.05. (B) Violin plot of normalized gene expression of select upregulated and (C) downregulated genes in macrophages from control (black) and tumor-bearing (blue) scaffolds. Statistically significant genes were determined using non-parametric Wilcoxon rank sum test with a p-value cut off of p<0.05. (D) UMAP visualization of SAMs 1 (navy) and SAMs 2 (pink) subsets in control and tumor-bearing scaffolds. (E) Violin plots of normalized expression of *C1qa*, *C1qb*, and *Trem2* in SAMs 1 and (F) *Chil3*, *Plac8,* and *Ly6c2* in SAMs 2.

Figure 4.6

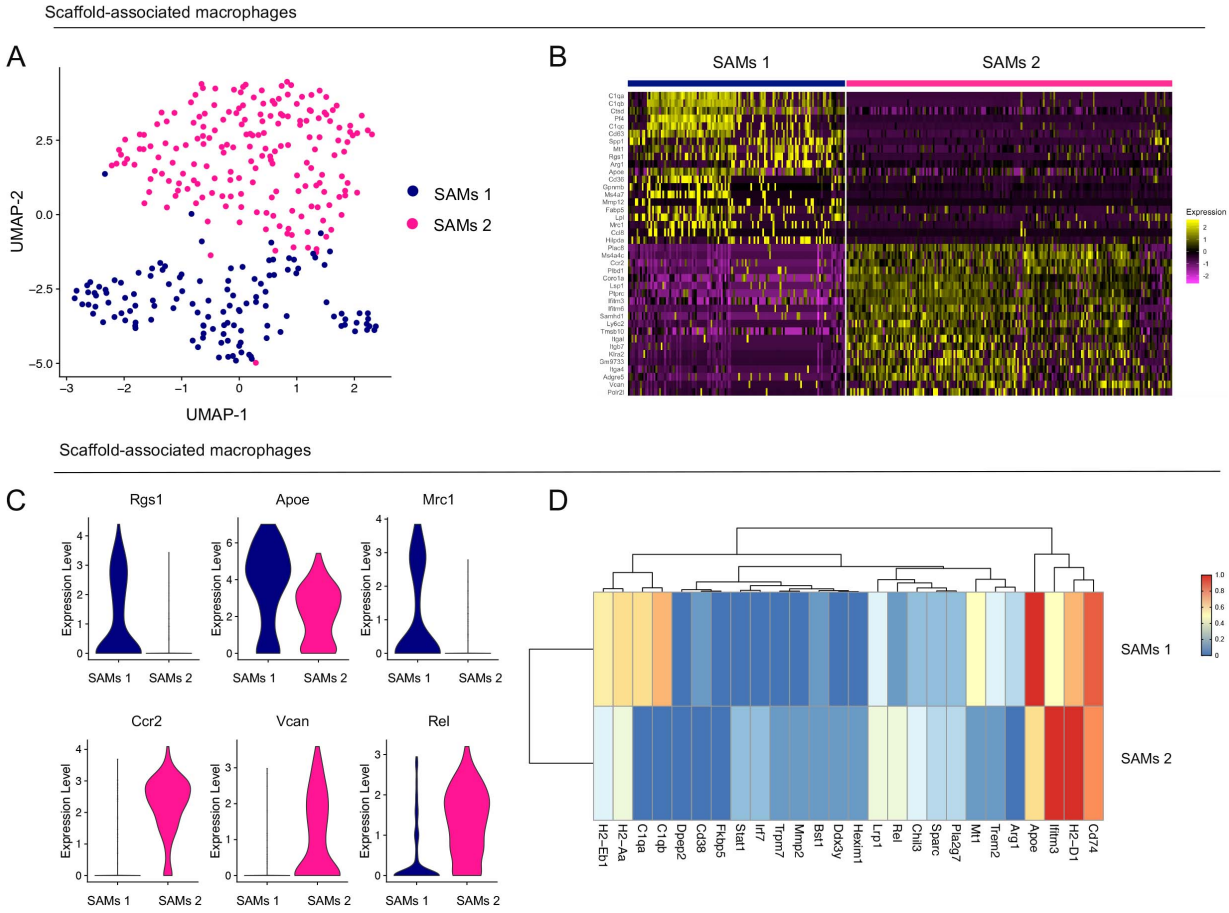

Figure 4.6 Single cell RNA sequencing analysis on scaffold associated macrophages.
(A) UMAP visualization of SAMs 1 (navy) and SAMs 2 (pink) macrophage subsets in merged control and tumor-bearing scaffolds. (B) Heatmap visualization at single cell resolution of the top 20 genes that unbiasedly define each scaffold macrophage subset. Low expression is in purple, while high expression is in yellow. (C) Violin plots of normalized expression for select macrophage markers in scaffold-associated macrophage subsets. (D) Heatmap visualization of average expression of macrophage differentially expressed genes between control and tumor-bearing scaffolds in SAMs 1 and SAMs 2 subsets.

Figure 4.7

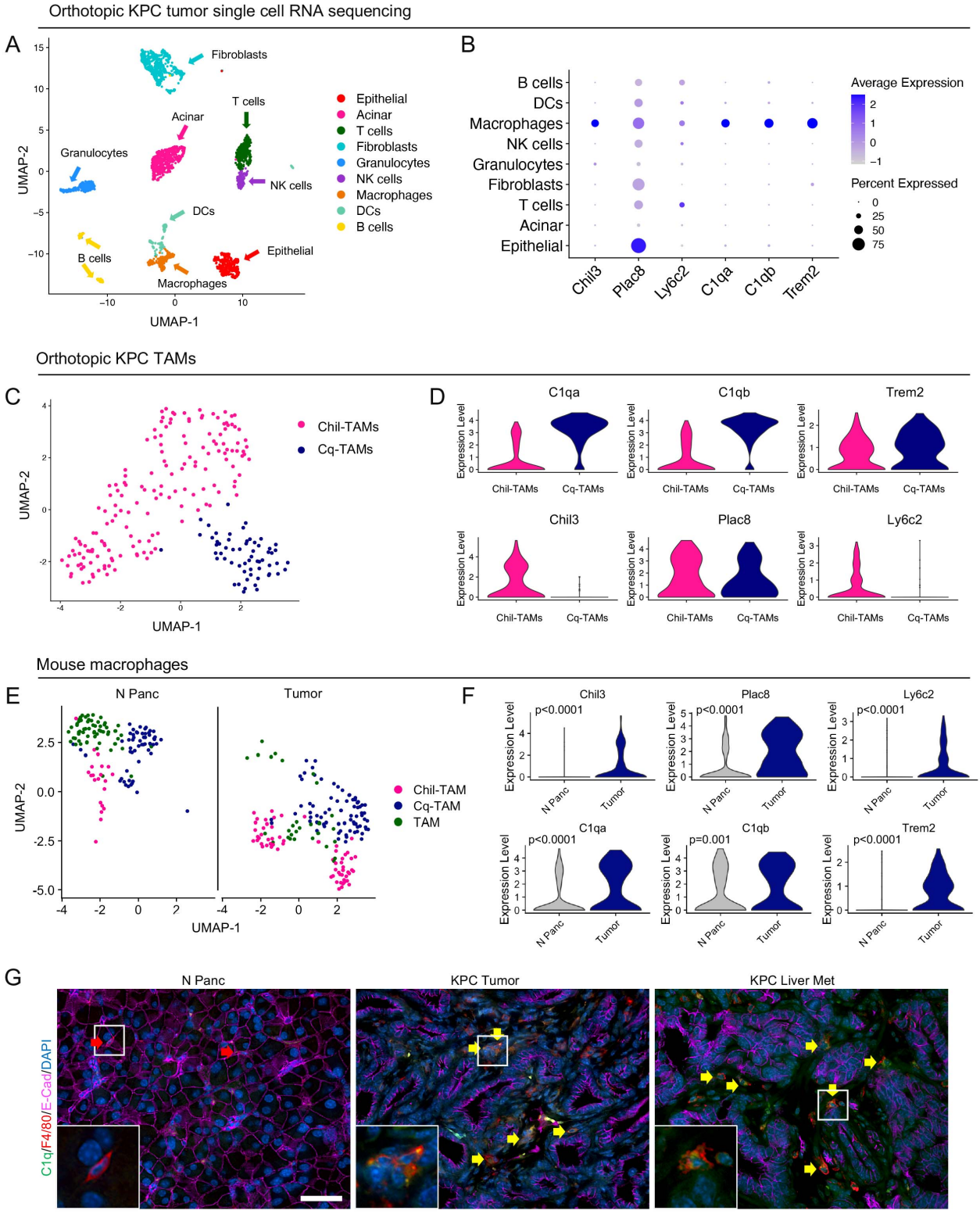
Orthotopic KPC tumor single cell RNA sequencing
A
Fibroblasts
T cells
Acinar
Granulocytes
NK cells
DCs
B cells
Epithelial
Macrophages
UMAP-1
UMAP-2
Epithelial
Acinar
T cells
Fibroblasts
Granulocytes
NK cells
Macrophages
DCs
B cells
B
B cells
DCs
Macrophages
NK cells
Granulocytes
Fibroblasts
T cells
Acinar
Epithelial
Chil3
Plac8
Ly6c2
C1qa
C1qb
Trem2
Average Expression
Percent Expressed
Orthotopic KPC TAMs
C
Chil-TAMs
Cq-TAMs
UMAP-1
UMAP-2
D
C1qa
C1qb
Trem2
Chil3
Plac8
Ly6c2
Expression Level
Chil-TAMs
Cq-TAMs
Mouse macrophages
E
N Panc
Tumor
Chil-TAM
Cq-TAM
TAM
UMAP-1
UMAP-2
F
Chil3
Plac8
Ly6c2
C1qa
C1qb
Trem2
p<0.0001
p=0.001
Expression Level
N Panc
Tumor
G
N Panc
KPC Tumor
KPC Liver Met
C1q/F4/80/E-Cad/DAPI

Figure 4.7 Macrophages in mouse pancreatic cancer tumors overexpress *TREM2* and complement genes.
(A) UMAP visualization of mouse orthotopic pancreatic cancer tumors (n=2). (B) Dot Plot of scaffold-associated macrophage signature, *Chil3*, Plac8, *Ly6c2, C1qa*, *C1qb*, and *Trem2* in identified cell populations in the orthotopic KPC tumors. Color represents average expression, while size of dot represents percent expressed. (C) UMAP visualization of Chil-TAMs (pink) and Cq-TAMs (navy) subsets in mouse orthotopic pancreatic cancer tumors. (D) Violin plots of *C1qa*, *C1qb, Trem2*, *Chil3*, *Plac8*, and *Ly6c2* across Chil-TAMs and Cq-TAMs. (E) UMAP visualization of Chil-TAM (pink), Cq-TAM (navy), and TAM (green) macrophage subsets in normal pancreas (n=1) and orthotopic tumors (n=2). (F) Violin plot of normalized gene expression of *Chil3*, *Plac8*, *Ly6c2, C1qa*, *C1qb,* and *Trem2* in macrophages from normal pancreas (grey) and orthotopic tumors (navy). Statistically significant genes were determined using non-parametric Wilcoxon rank sum test with a p-value cut off of $p<0.05$. (G) Co-immunofluorescence of normal mouse pancreas (N Panc), KPC tumor, and KPC liver metastasis samples of C1q (green), F4/80 (red), E-Cadherin (pink) and DAPI (blue). Red arrow denotes $C1q^{-}$ $F4/80^{+}$ macrophage in the normal pancreas. Yellow arrows denote $C1q^{+}$ $F4/80^{+}$ macrophages in KPC tumor and KPC liver metastasis. Inlets show higher magnification of select macrophages in boxed region. Scale bars, 50 μm.

Figure 4.8

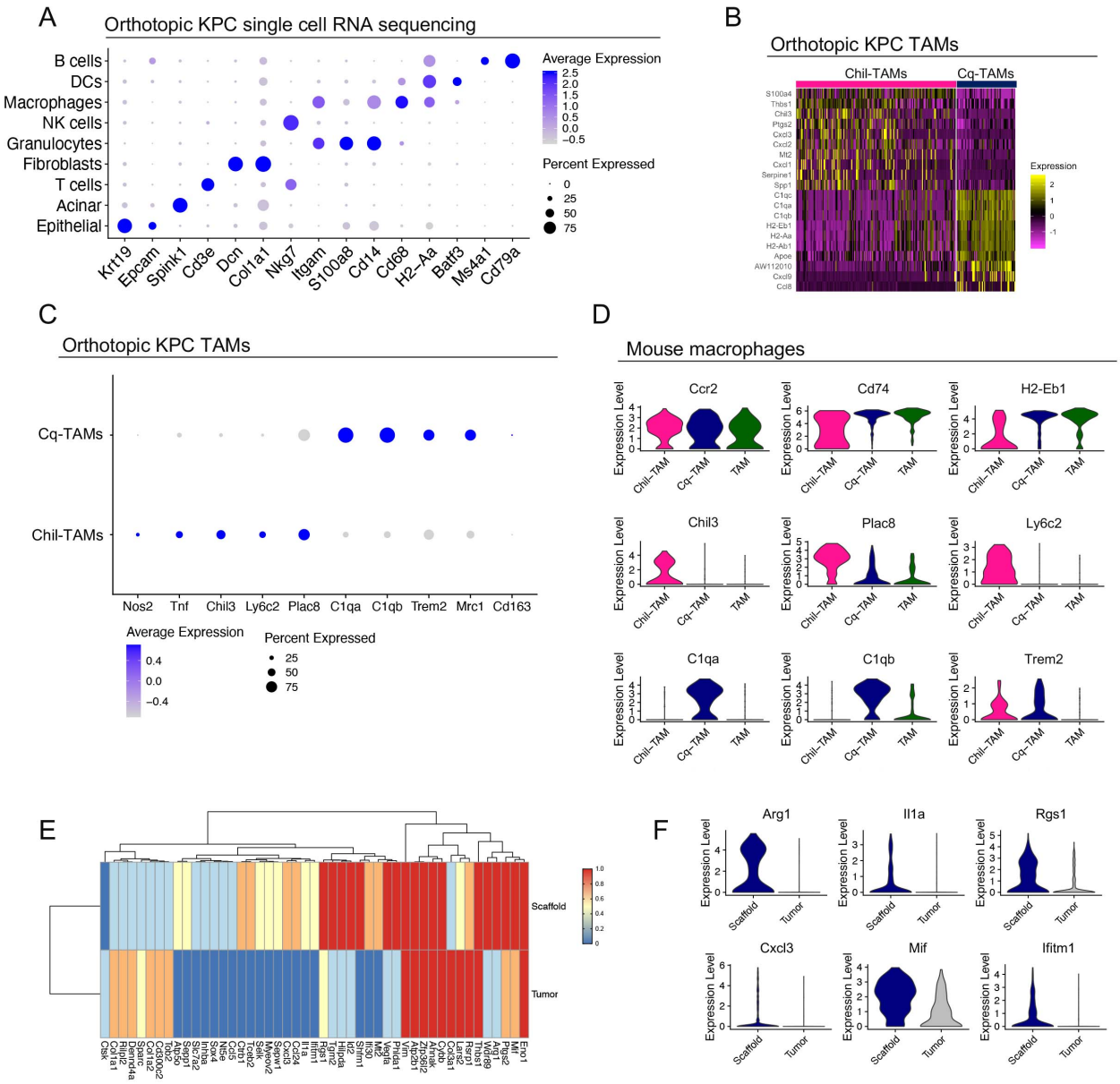

Figure 4.8 Single cell RNA sequencing analysis on mouse PDA macrophages.
(A) Dot plot of select lineage markers used to define captured cell populations in mouse orthotopic KPC tumors (n=2). Color of the dot represents average expression. Size of the dot represents percent expressed. (B) Heatmap visualization at single cell resolution of the top 10 genes that define Chil-TAMs and Cq-TAMs. Low expression is in purple, while high expression is in yellow. (C) Dot plot of *Nos2*, *Tnf*, *Chil3*, *Ly6c2*, *Plac8*, *C1qa*, *C1qb*, *Trem2*, *Mrc1*, and *Cd163* in Cq-TAMs and Chil-TAMs from orthotopic KPC tumors. Color of the dot represents average expression. Size of the dot represents percent expressed. (D) Violin plots for *Ccr2*, *Cd74*, *H2-Eb1*, *Chil3, Plac8*, *Ly6c2*, *C1qa*, *C1qb*, and *Trem2* in Chil-TAM (pink), Cq-TAM (navy), and TAM (green) subsets. (E) Average expression heatmap for select differentially expressed genes between macrophages from orthotopic scaffolds and mouse orthotopic primary tumors. Low expression in blue and high expression in red. All genes plotted are statistically significant, determined using non-parametric Wilcoxon rank sum test with a p-value cut off of $p<0.05$. (F) Violin plots of normalized expression for *Arg1*, *Il1a*, *Rgs1*, *Cxcl3*, *Mif*, and *Ifitm1* in macrophages from orthotopic scaffolds and mouse orthotopic primary tumors.

Figure 4.9

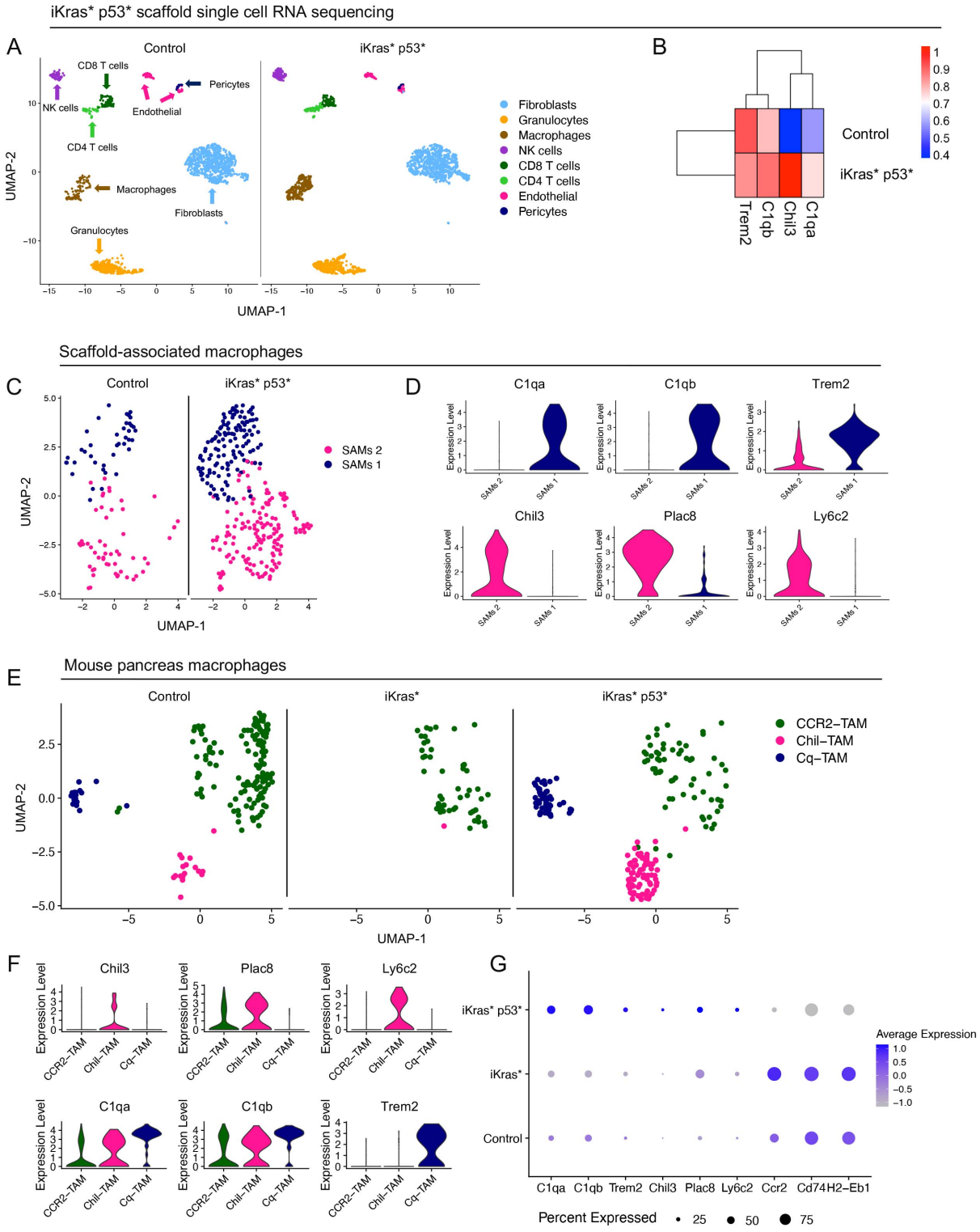
iKras* p53* scaffold single cell RNA sequencing
A
Control
iKras* p53*
CD8 T cells
Pericytes
NK cells
Endothelial
CD4 T cells
Macrophages
Fibroblasts
Granulocytes
UMAP-2
UMAP-1
Fibroblasts
Granulocytes
Macrophages
NK cells
CD8 T cells
CD4 T cells
Endothelial
Pericytes
B
Control
iKras* p53*
Trem2
C1qb
Chil3
C1qa
Scaffold-associated macrophages
C
Control
iKras* p53*
SAMs 2
SAMs 1
UMAP-2
UMAP-1
D
C1qa
C1qb
Trem2
Chil3
Plac8
Ly6c2
Expression Level
SAMs 2
SAMs 1
Mouse pancreas macrophages
E
Control
iKras*
iKras* p53*
CCR2–TAM
Chil–TAM
Cq–TAM
UMAP-2
UMAP-1
F
Chil3
Plac8
Ly6c2
C1qa
C1qb
Trem2
Expression Level
CCR2–TAM
Chil–TAM
Cq–TAM
G
iKras* p53*
iKras*
Control
C1qa
C1qb
Trem2
Chil3
Plac8
Ly6c2
Ccr2
Cd74
H2–Eb1
Average Expression
Percent Expressed
25
50
75

Figure 4.9 Cq-TAMs and Chil-TAMs are elevated in the iKras* p53* model of pancreatic cancer.
(A) UMAP visualization of scaffolds from control (n=1) and iKras* p53* mice (n=1). (B) Average expression heatmap of *Trem2*, *C1qb*, *Chil3*, and *C1qa* in control and iKras* p53* scaffolds. High expression is in red, while low expression is in blue. (C) UMAP visualization of SAMs 1 (navy) and SAMs 2 (pink) macrophage subsets in control and iKras* p53* scaffolds. (D) Violin plots of *C1qa*, *C1qb, Trem2*, *Chil3*, *Plac8*, and *Ly6c2* across SAMs 1 and SAMs 2. (E) UMAP visualization of CCR2-TAM (green), Chil-TAM (pink), and Cq-TAM (navy) macrophage subsets in control, iKras* and iKras* p53* pancreas samples. (F) Violin plots of *Chil3*, *Plac8*, *Ly6c2 C1qa*, *C1qb,* and *Trem2* across CCR2-TAM, Chil-TAM, and Cq-TAM macrophage subsets. (G) Dot plot of *C1qa*, *C1qb, Trem2*, *Chil3*, *Plac8*, *Ly6c2*, *Ccr2*, *Cd74*, and *H2-Eb1* in control, iKras* and iKras* p53* macrophages. Color represents average expression. Size of the dot represents percent expressed.

Figure 4.10

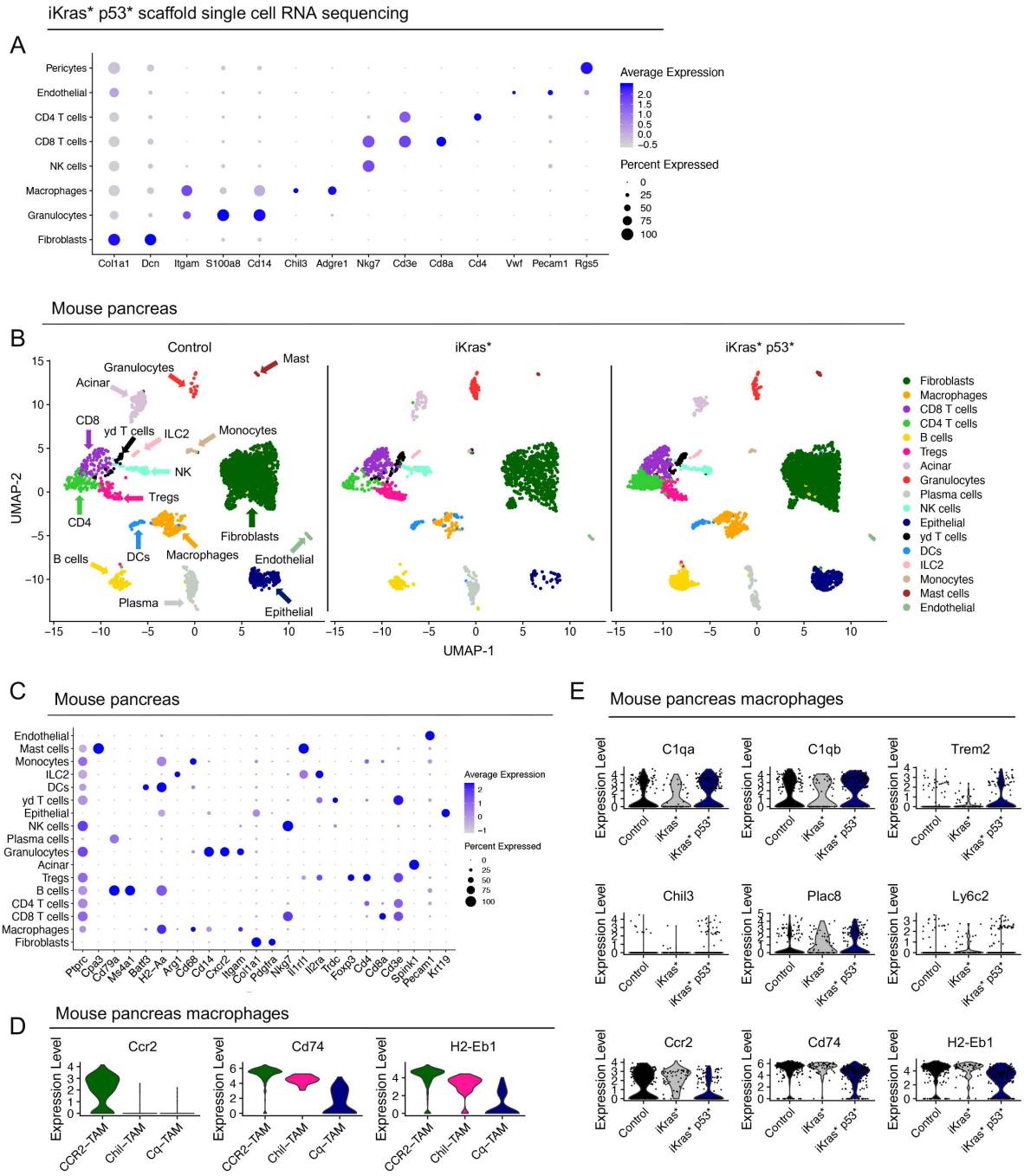

Figure 4.10 Immune infiltration in iKras* and iKras* p53* mice.
(A) Dot plot for lineage markers used to define identified cell populations in scaffolds from iKras* p53* mice. Color of the dot represents average expression. Size of the dot represents percent expressed. (B) UMAP visualization of from control/normal pancreas (n=2), iKras* (n=1), and iKras* p53* pancreas samples (n=2). (C) Dot plot for lineage markers used to define identified cell populations in control/normal pancreas, iKras*, and iKras* p53* pancreas samples. Color of the dot represents average expression. Size of the dot represents percent expressed. (D) Violin plots for *Ccr2*, *Cd74*, *H2-Eb1* in CCR2-TAM, Chil-TAM, and Cq-TAM subsets in mouse pancreas samples. (E) Violin plots for *C1qa*, *C1qb*, *Trem2*, *Chil3, Plac8*, *Ly6c2, Ccr2*, *Cd74*, and *H2-Eb1* in control/normal pancreas, iKras*, and iKras* p53* pancreas samples.

Figure 4.11

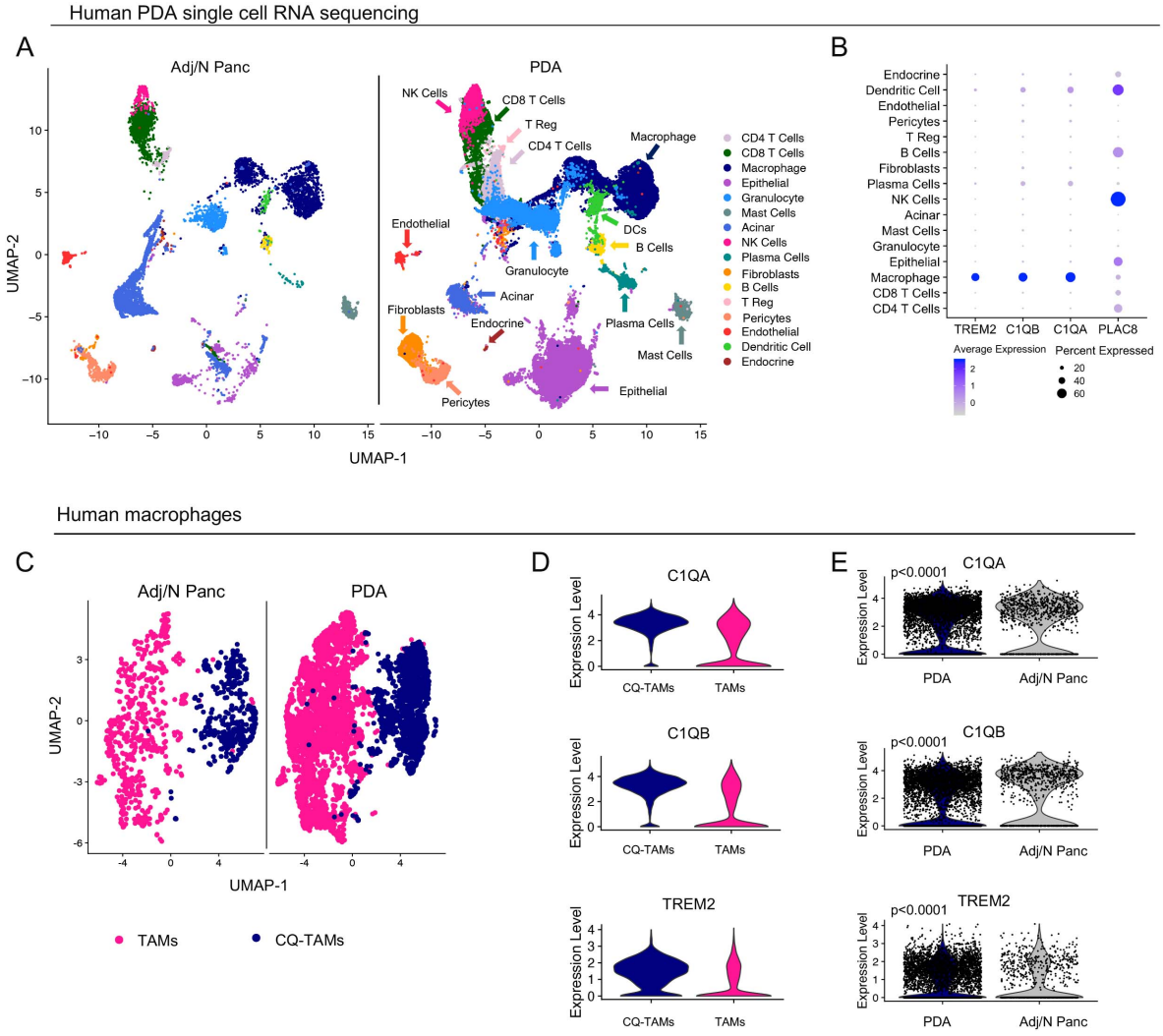

Figure 4.11 Macrophages in human pancreatic cancer tumors overexpress *TREM2* and complement genes. (A) UMAP visualization of Adj/Norm (n=3) and PDA tumors (n=16). (B) Dot plot of *TREM2*, *C1QB*, *C1QA*, *and PLAC8* in human PDA tumor cell populations. Color of the dot represents average expression, while the size of the dot represents average expression. (C) UMAP visualization of human TAMs (pink) and CQ-TAMs (navy) from adjacent normal pancreas (n=3) and human PDA tumors (n=16). (D) Violin plots of *C1QA*, *C1QB*, and *TREM2* in human TAMs and CQ-TAMs. (E) Violin plots of *C1QA*, *C1QB*, and *TREM2* in human macrophages from human PDA tumors compared to adjacent normal pancreas. Statistics were determined using non-parametric Wilcoxon rank sum test with a p-value of p<0.0001.

Figure 4.12

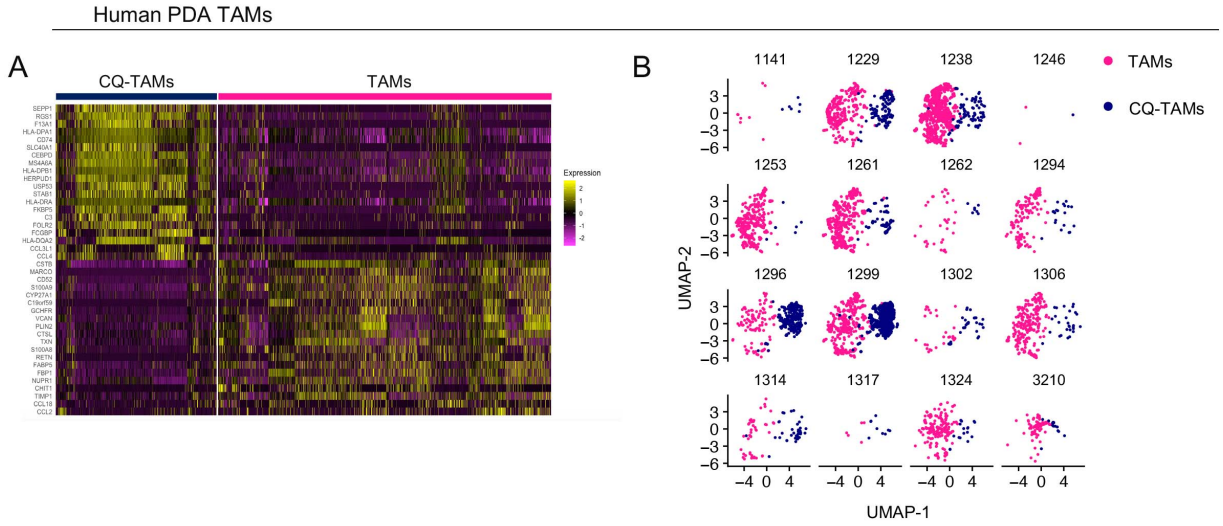

Figure 4.12 TAM populations are heterogenous in human PDA tumors.
(A) Heatmap visualization at single cell resolution of the top 20 genes that define human CQ-TAMs and TAMs. Low expression is in purple and high expression is in yellow. (B) UMAP visualization of human TAMs (pink) and CQ-TAMs (navy) from in individual human PDA tumors (n=16). The four-digit number represents the de-identified patient ID.

Figure 4.13

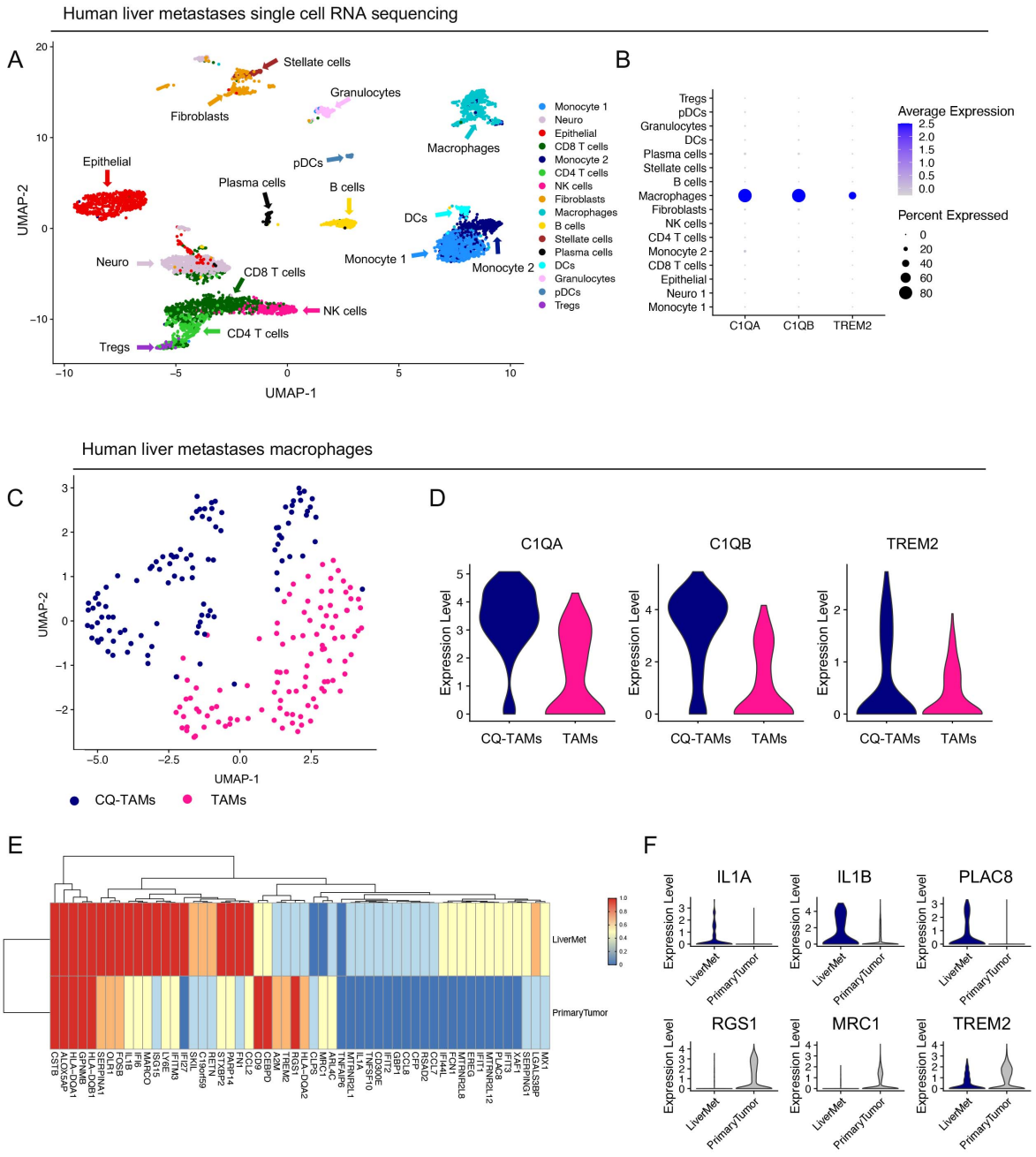

Figure 4.13 Macrophages in human liver metastases express high levels of *TREM2* and complement genes and are distinct from primary tumor macrophages.
(A) UMAP visualization of human liver metastasis samples (n=5) from PDA patients. (B) Violin plots of normalized expression of *C1QA*, *C1QB*, and *TREM2* in identified cell populations in the liver metastasis lesions from human PDA patients (n=5). (C) UMAP visualization of CQ-TAMs (navy) and TAMs (pink) identified in human liver metastasis samples. (D) Violin plots of normalized expression for *C1QA*, *C1QB*, and *TREM2* in CQ-TAMs and TAMs from liver metastasis samples. (E) Average expression heatmap for select differentially expressed genes between macrophages from human liver metastases and human primary tumors. Low expression in blue and high expression in red. All genes plotted are statistically significant, determined using non-parametric Wilcoxon rank sum test with a p-value cut off of p<0.05. (F) Violin plots of normalized expression for *IL1A*, *IL1B*, *PLAC8*, *RGS1*, *MRC1*, and *TREM2* in macrophages from human liver metastasis and primary tumor samples.

Figure 4.14

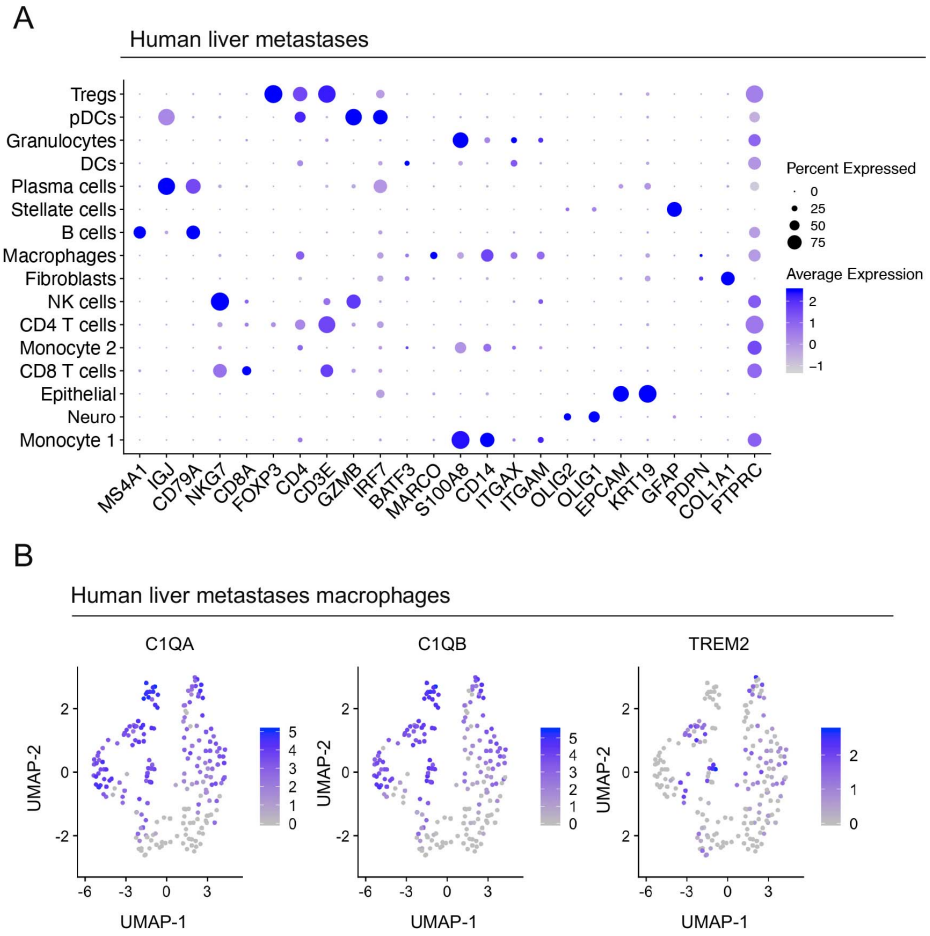

Figure 4.14 Single cell RNA sequencing of human liver metastases.
(A) Dot plot of lineage markers used to define populations in human liver metastases from PDA patients (n=5). Color of the dot represents average expression, while the size of the dot represents average expression. (B) Feature plots of *C1QA*, *C1QB*, and *TREM2* in human liver metastases. Blue is high expression, while grey is low expression.

Figure 4.15

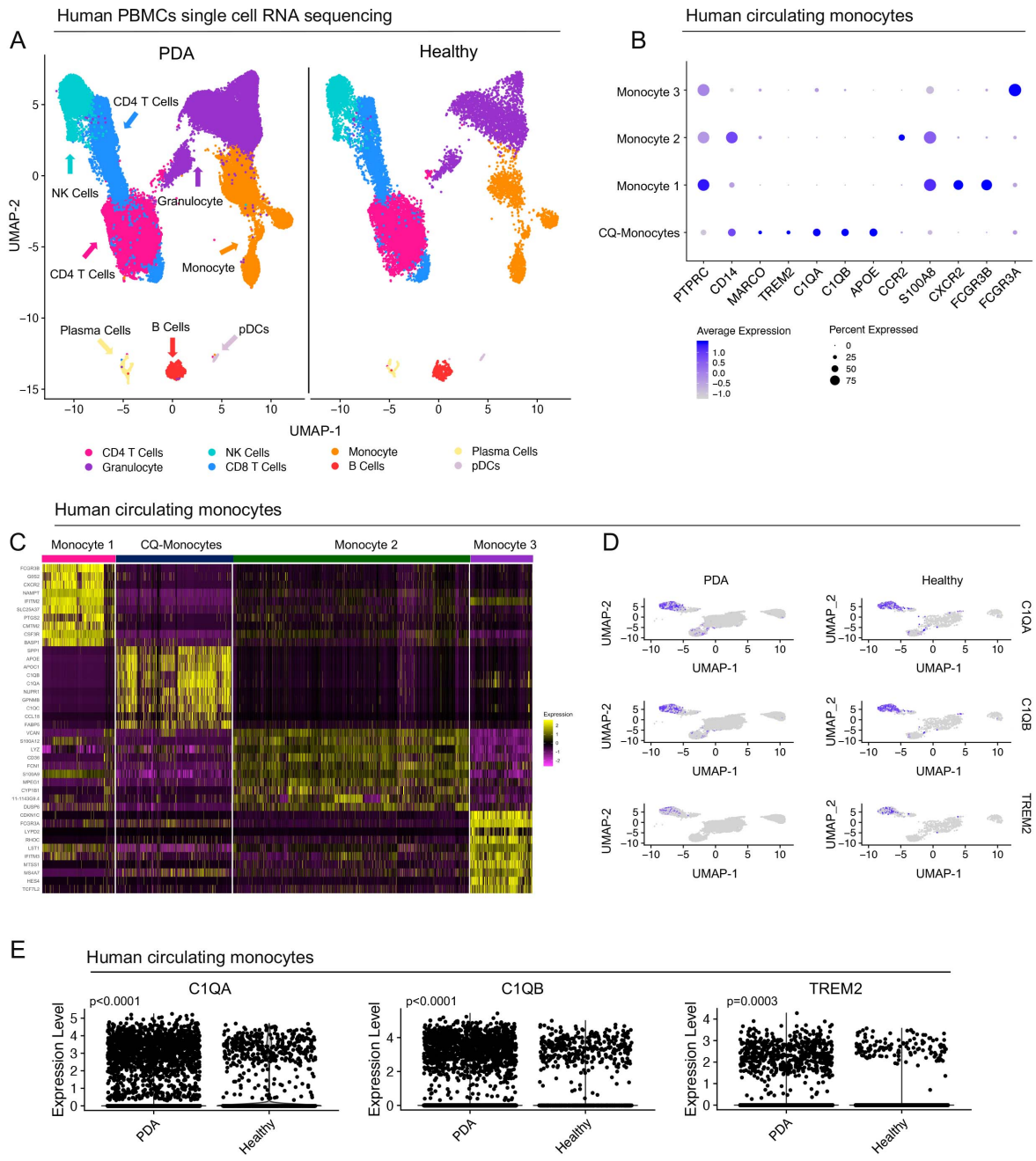

Figure 4.15 Complement genes mark one population of circulating monocytes in PDA patients.
(A) UMAP visualization of PDA PBMCs (n=16) and healthy PBMCs (n=4). (B) Dot plot analysis for lineage markers used to define human monocyte subsets in the blood. Color of the dot represents average expression, while the size of the dot represents average expression. (C) Heatmap visualization at single cell resolution of the top 10 genes that define human monocyte subsets. Low expression is in purple, while high expression is in yellow. (D) Feature plot of *C1QA*, *C1QB*, and *TREM2* in human monocyte subsets in the blood of healthy donors and PDA patients. Blue is high expression and grey is low expression. (E) Violin plots of *C1QA*, *C1QB*, and *TREM2* in human circulating monocytes from PDA patients compared to healthy donors. Statistics were determined using non-parametric Wilcoxon rank sum test.

Figure 4.16

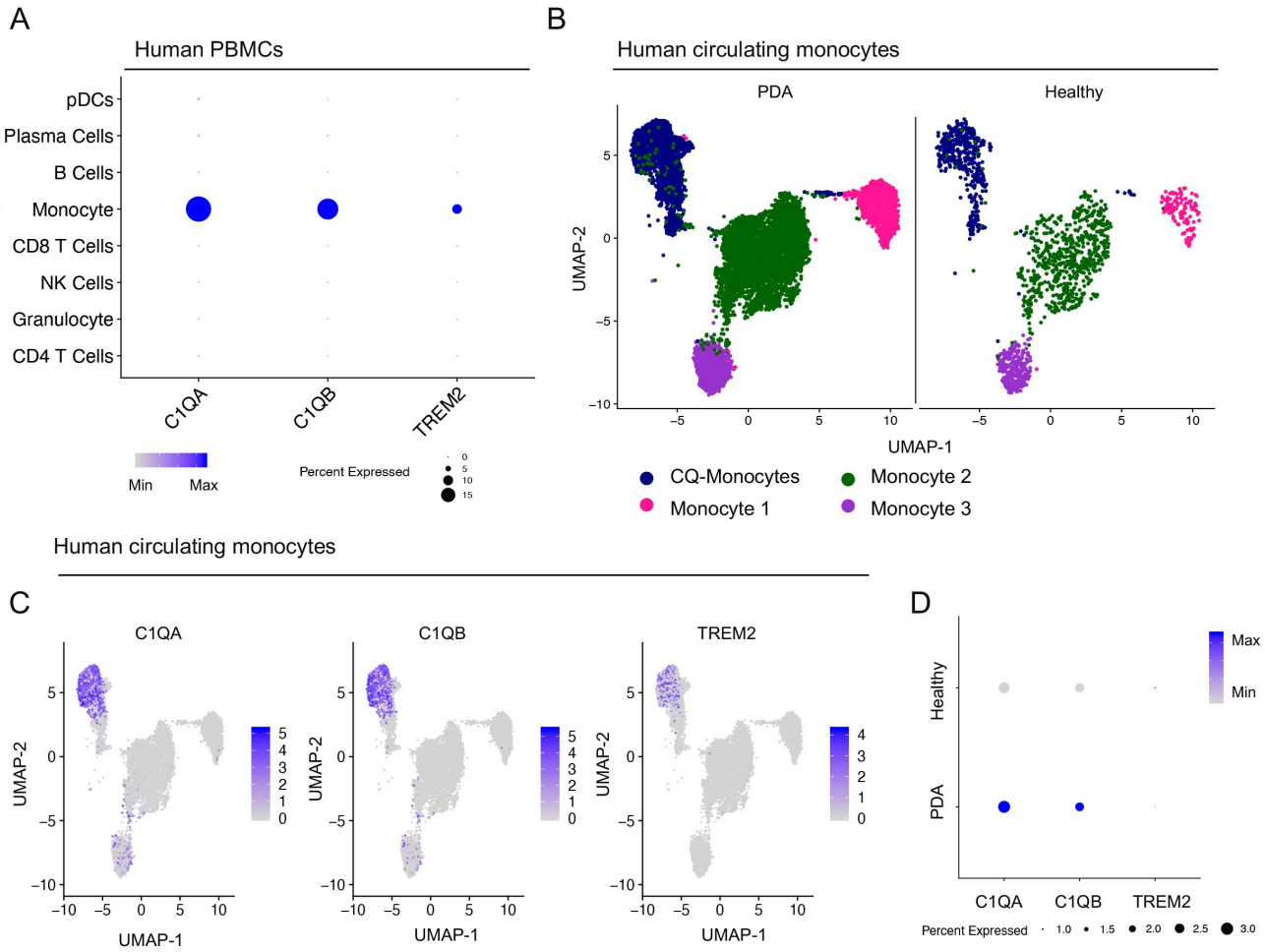

Figure 4.16 Complement-high myeloid cells are elevated in the blood of pancreatic cancer patients.
(A) Dot plot of *C1QA*, *C1QB*, and *TREM2* in identified populations in human PBMCs. Color of the dot represents average expression, while the size of the dot represents average expression. (B) UMAP visualization of CQ-monocytes (navy), Monocyte 1 (pink), Monocyte 2 (green), and Monocyte 3 (purple) in human PBMCs in PDA (n=16) and healthy (n=4). (C) Feature plot of *C1QA*, *C1QB*, and *TREM2* in human monocyte subsets in the blood. Blue is high expression and grey is low expression. (D) Dot plot of *C1QA*, *C1QB*, and *TREM2* in PBMCs from healthy donors and PDA patients. High expression is in blue, low expression is in grey. Size of the dot represents percent expressed.

Chapter 5 Discussion and Future Directions

The most common type of pancreatic cancer, pancreatic ductal adenocarcinoma (PDA) is a lethal malignancy that warrants a deeper biological understanding. PDA has an infiltration of myeloid cells and sparse infiltration of T cells. This inverse correlation between myeloid cells and T cells contributes to the robust immune suppression that characterizes the disease. Immune therapy has not been beneficial in PDA so far, and thus further evaluation for mechanisms mediating immune suppression is critical. In this dissertation I have discussed our work evaluating both T cell and myeloid cell mediated immune suppression mechanisms in mouse and human PDA. In this section I summarize the major findings in each chapter and present future directions and questions for each project.

Multi-modal Mapping of the Tumor and Peripheral Blood Immune Landscape in Human Pancreatic Cancer

In Chapter 2 of this thesis I discuss our comprehensive mapping of the immune landscape in PDA. The transcriptional analysis at a single cell resolution allowed us to evaluate immune cell and immune checkpoint heterogeneity. Immune checkpoint blockade has not been beneficial in PDA thus far. The work presented in Chapter 2 identified TIGIT as an understudied immune checkpoint that should be considered in PDA treatment. In our data, $TIGIT^+$ $CD8^+$ T cells were elevated in PDA compared to normal pancreas samples, and further, there was a positive correlation of $TIGIT^+$ $CD8^+$ T cells in

matched blood and tumors from patients. The multi-modal approach used here allowed us to perform a large characterization study of the human immune response in PDA. Further, these data and the dataset as a whole resulted in multiple hypotheses and many open questions.

To fully elucidate the role of TIGIT in PDA immune suppression more mechanistic studies are needed. A limitation to human research is the amount of research specimen that is available and also consideration of the variable nature of available samples. With that limitation in place, the published data in Chapter 2, was largely descriptive in nature. Future directions to study TIGIT mechanistically would provide evidence for targeting TIGIT in PDA patients.

One open question is how TIGIT promotes immune suppression mechanistically. To further study TIGIT in PDA immune suppression, $TIGIT^+$ $CD8^+$ and $TIGIT^-$ $CD8^+$ T cells can be isolated from patient tumors and blood using fluorescence-activated cell sorting (FACS). The sorted T cells could then be plated in culture with matched patient-derived organoids and T cell activation can be determined through enzyme-linked immunospot (ELISpot) assay for IFN-γ levels. Given the immunosuppressive ability of $TIGIT^+$ $CD8^+$ T cells, compared to $TIGIT^-$ $CD8^+$ T cells, it is expected there will be lower levels of IFN-γ compared to $TIGIT^-$ $CD8^+$ T cells when cultured with organoids. To provide further evidence of the immunosuppressive abilities of TIGIT, a blocking antibody could be added to the co-cultures, followed by ELISpot for IFN-γ levels. Blockade of TIGIT on exhausted $CD8^+$ T cells is expected to revert the T cells to their effector function, resulting in an increase in IFN-γ levels.

The data in Chapter 2 are solely from human samples, and while this is biologically relevant and highly translational, human data has its limitations. For this reason, moving into a mouse model willl provide an avenue to further mechanistically evaluate the role of TIGIT on PDA immune suppression. We first performed syngeneic orthotopic transplantation of mouse PDA cells into C57/BL6J mice and treated the mice with either IgG control (BioXCell #BE0083) or anti-TIGIT (BioXCell #BE0274). After 3 weeks we weighed the tumors and detected no difference in final tumor weight (**Fig. 5.1A**). Given its immunosuppressive role this was not our expected hypothesis, however this finding could be because TIGIT is not only expressed in $CD8^+$ T cells, but also NK cells and Tregs, so it is possible there is compartment specific functions (Kurtulus et al., 2015). Further understanding the role of TIGIT in Tregs is an important question that still remains. Parallelling the human data, immune checkpoint expression on $CD8^+$ T cells in mouse tumors is also heterogenous (**Fig. 5.1B**). The heterogeneity of TIGIT expression in mouse PDA could be another factor for why blocking TIGIT did not result in decreased tumor burden.

In summary, Chapter 2 presents a multimodal approach to understanding the immune landscape in PDA. With this pipeline we highlighted the heterogeneity of PDA patients and identified TIGIT as a potential therapeutic target. Future experiments are needed to elucidate the immunosuppressive mechanism and compartment specific role of TIGIT in the PDA TME. Mouse modeling and *in vitro* techniques could provide additional evidence on TIGIT as a therapeutic target. Importantly, we showed that $TIGIT^+$ $CD8^+$ T cells are highly expressed in metastatic and locally advanced patients, compared

to patients with resectable disease, suggesting TIGIT could be useful in treating patients with advanced stage of disease.

Apolipoprotein E promotes immune suppression through NF-kB mediated CXCL1 production in pancreatic cancer

In Chapter 3 of this thesis I discuss ApoE as a novel mediator of immune suppression in PDA. Prior to this work, ApoE had yet to be evaluated in PDA, and we provided the first functional study on ApoE in the PDA TME. Loss of ApoE from the TME resulted in reduced fibrosis, fewer M-MDSCs, and an increase in $CD8^+$ T cells. Previous studies in the field have identified the CXCL1-CXCR2 axis is essential for the recruitment of MDSCs and subsequent blockade of tumoral T cell infiltration in PDA (Li et al., 2018a; Steele et al., 2016). This work in Chapter 3 builds upon that mechanism, identifying ApoE as critical for the secretion of CXCL1 via LDLR and NF-κB signaling. In this chapter I discuss the mechanism behind ApoE in PDA immune suppression, however this work opens up many questions that are of interest for further studies.

First, the mouse data presented in Chapter 3 were performed using a full body knock-out of ApoE. We have shown that ApoE is expressed predominately by macrophages and iCAFs in the TME. Our approach is limited by being able to determine which cellular source is driving the T cell phenotype. Future studies could use a conditional knock-out ApoE allele (Jax #028530) to evaluate the role of ApoE from myeloid cells and fibroblasts separately. To evaluate the role of ApoE in myeloid cells and fibroblasts separately, Apoe-floxed mice can be crossed with a myeloid specific Cre (LysMcre, Jax #004781) or a fibroblast specific Cre (PDGFRa-Cre, Jax #013148). Using

this conditional knock-out approach will allow the evaluation of the cellular source of ApoE that drives the immunosuppressive phenotype discussed in Chapter 3.

Chapter 3 discusses changes to macrophage polarization with loss of ApoE, however we did not evalaute changes in fibroblasts deficient in ApoE. Due to the heterogeneity of fibroblasts, it is more technically challenging to assess the loss of ApoE in fibroblasts as ApoE is only present in iCAFs. *In vitro*, myCAFs grow in 2-D, while iCAFs form in 3-D, and this is believed to be a plastic process. Fibroblasts can be sorted from WT and $APOE^{-/-}$ mice and plated in 3-D matrigel domes. Once cultures are established, bulk sequencing can be performed to evaluate changes to fibroblasts without ApoE. In Chapter 3 I showed when ApoE is added to fibroblasts, fibroblasts secrete higher levels of IL-6, suggesting ApoE is making the fibroblasts more immunosuppressive. It would be expected that fibroblasts deficient in ApoE would have less immunosuppressive markers such as IL-6 and leukemia inhibitory factor (LIF) (Biffi et al., 2019).

In addition to ApoE being expressed by fibroblasts, ELISA analysis on iCAF conditioned-media would confirm that like macrophages, ApoE is secreted by fibroblasts. The mechanistic work detailed in Chapter 3 looked at ApoE signaling to tumor cells specificallly through LDLR and NF-κB. We did not evaluate the signaling pathway that ApoE activates to induce Cxcl1 expression in fibroblasts. While LDLR is also expressed in fibroblasts, the most predominately expressed ApoE receptor in fibroblasts is LRP1. It is possible that ApoE binds to either LDLR or LRP1 on fibroblasts to increase Cxcl1 production. ApoE is present in fibroblasts and given that one of the findings in Chapter 3 was a loss of fibrosis in ApoE deficient animals it is important to consider the functional implications on fibroblasts due to loss of ApoE.

Given that ApoE seems to promote immune suppression, we hypothesized that loss of ApoE would sensitize tumors to immunotherapy approaches. However when ApoE$^{-/-}$ mice were treated with αPD-1 we saw no difference in tumor size (**Fig. 5.2A**). Data from Chapter 2 revealed the heterogeneity of immune checkpoints in humans, so we hypothesized that single agent immunotherapy was potentially not sufficient. Combination immunotherapy approaches treating with α-CD40, α-CTLA-4, and α-PD-1 (FCP) have shown success in mouse models of PDA (Li et al., 2018a; Winograd et al., 2015). We thus treated ApoE$^{-/-}$ mice with the combination immunotherapy (FCP) treatment (**Fig. 5.2B**). FCP treatment, while effective at reducing tumor burden, we were unable to compare WT and APOE$^{-/-}$ conditions as FCP eliminated almost the entirety of the tumor in both conditions (**Fig. 5.2B**). PDA tumors that have a low T cell infiltration do not respond to FCP treatment (Li et al., 2018a). Future studies could orthotopically transplant a T cell low cell line into ApoE$^{-/-}$ mice and determine if loss of ApoE sensitizes the tumors to combination immune therapy (FCP).

Further, given the immunosuppressive role of MDSCs, we treated WT and ApoE$^{-/-}$ mice with α-Ly-6G, to deplete the PMN-MDSCs, in combination with α-PD-1 (**Fig. 5.3C**). Neither α-Ly-6G, or combination α-Ly-6G and α-PD-1 resulted in smaller tumors (**Fig. 5.3C**). As discussed in Chapter 1, MDSCs have two main subsets, M-MDSC and PMN-MDSCs. It has been established M-MDSCs have increased immunosuppressive functions compared to PMN-MDSCs. Given that ApoE$^{-/-}$ mice have fewer M-MDSCs, and unchanged PMN-MDSCs infiltration it can be hypothesized that ApoE specifically affects M-MDSCs in the TME. Blockade of Ly-6G specifically targeted the PMN-MDSCs, which was not sufficient to reduce tumor size. Future studies could instead use a small molecule

inhibitor (AstraZeneca, AZD5069) that antagonizes CXCR2 on all MDSC subsets, allowing for inhibtion of M-MDSCs and PMN-MDSCs (Steele et al., 2016).

Another remaining question is if ApoE binding to LDLR activates NF-κB. Data from Chapter 3 show that partial knock-down of LDLR reduces Cxcl1 secretion and that inhibition of NF-κB signaling through an IKK inhibitor also reduces Cxcl1 levels in tumor cells. However, we did not directly link LDLR and NF-κB signaling together. Existing literature has also not linked LDLR and NF-κB signaling. We used siRNA to knock-down LDLR in tumor cells and then treated the cells with recombinant ApoE (**Fig. 5.3A**). We stained the tumor cells for the NF-κB mediator, p65 and measured nuclear translocation as a read-out for active NF-κB signaling. Tumor cells treated with ApoE have increased nuclear p65, providing evidence that ApoE promotes NF-κB signaling (**Fig. 5.3A** and **5.3B**). When we treated tumor cells with partial loss of LDLR we saw a decrease in nuclear p65, suggesting that ApoE binding to LDLR activates NF-κB signaling in tumor cells (**Fig. 5.3A** and **5.3B**).

Pancreatic cancer is marked by complement-high tumor associated macrophages in primary and metastatic tumors and blood monocytes

In Chapter 4 of this thesis I discuss the identification of a myeloid gene signature (*C1QA*, *C1QB*, and *TREM2*) that marks a distinct population of monocytes in the blood and macrophages in the tissue. The immune response at the primary tumor has been well studied, however the changes to the immune system systemically in PDA have been understudied. As the majority of patients either present with metastatic disease or ultimately relapse with metastasis post surgery, it is critical we understand the systemic

immune changes in PDA. While metastasis has dire outcomes, it is a stochastic and ultimately inefficient process, which make studying metastatic dissemination difficult. Some approaches to studying metastatic disease use techniques including injection of tumor cells into the tail vein or portal vein to ensure metastatic dissemination to the liver. This method though misses the critical steps of the metastatic cascade where tumor cells must first break apart from the primary tumor and intravasate into the blood stream. Methods to study metastasis that by pass these intial steps do not fully recapitulate the biological process.

In Chapter 4 we utilized implantable biomaterial scaffolds, a novel device that recapitulates the metastatic site, to evaluate the immune changes when the metastatic cascade is intact. With this approach we identifed an immune signature that is unique to tumor-bearing animals compared to controls. Using single cell RNA sequencing on the scaffold infiltrate we focused specifically on the macrophages within the infiltrate, which we called scaffold-associated macrophages (SAMs). Further analysis revealed two distinct SAM populations, one defined by *Chil3*, *Ly6c2*, and *Plac8* (Chil-TAM), and the other defined by *C1qa*, *C1qb*, and *Trem2* (Cq-TAM). Using mouse models we determined these macrophages populations, Chil-TAMs and Cq-TAMs are also present in early and late stages of PDA, and they upregulate *Chil3*, *C1qa*, *C1qb*, and *Trem2* expression with disease progression. We further showed, these distinct macrophage populations in human primary tumors and human liver metastases, providing translational relevance for these populations in human disease. Further, in the peripheral blood *C1QA*, *C1QB*, and *TREM2* marked one population of circulating monocytes. *C1QA*, *C1QB*, and *TREM2*

expression was upregulated in the blood of patients, suggesting these markers could be used for potential diagnostic and prognostic applications.

The data in Chapter 4 described a unique macrophage signature. One remaining question is the functional implication of C1QA, C1QB, and TREM2 in PDA. TREM2 has been associated with promoting immune suppression in other cancers, but not PDA (Katzenelenbogen et al., 2020; Molgora et al., 2020). We isolated bone marrow-derived macrophages and polarized to either M0 with M-CSF or TAM with tumor cell conditioned-media and measured expression of *C1qa*, *C1qb*, and *Trem2* (**Fig. 5.4A**). With our limited samples, we detected an upward trend in *C1qa* and *C1qb*, and a significant increase in *Trem2* in TAMs compared to M0 macrophages (**Fig. 5.4A**). These data provide further evidence that the macrophage signature we identified in Chapter 4 is elevated in response to PDA.

We identifed the elevation of the signature genes, *C1QA*, *C1QB*, and *TREM2* in our human PDA samples, and hypothesized it could be used for diagnostics and prognostic applications. We isolated serum samples from healthy volunteers, chronic pancreatitis patients, and PDA patients and measured the levels of C1Q. We did not detect a difference in C1Q serum levels in patients compared to healthy volunteers or chronic pancreatitis patients or a difference based on disease stage (**Fig. 5.5A** and **Fig. 5.5B**). However we did identify that PDA patients who had non-progressive disease had higher serum levels of C1Q compared to patients with complete response or progressive disease (**Fig. 5.5C**). Survival analysis did not reveal any significant difference when patients were stratified by C1Q levels, however patients with high levels of C1Q had a trend for better overall survival (**Fig. 5.5D**). Patients with high serum C1Q also had fewer

$CD4^+$ T cells and $CD16^+$ monocytes in their blood (**Fig. 5.5E**). These data suggest high serum C1Q levels could correlate with more favorable outcomes, however more experiments are needed. Future studies could utilize C1qa knock-out mice (JAX #031675) with syngeneic transplantation of PDA tumor cells to evaluate C1qa on tumor growth and immune infiltration. C1qa can further be crossed into spontaneous mouse models of PDA to evaluate its role on disease progression and metastatic dissemination. The data in Chapter 4 suggest further evaluation of the complement system in PDA.

Summary

PDA is an almost universally lethal disease, and it is critical for us to understand the biology behind immune suppression in PDA. The data presented in this thesis provide further evidence of the complex cellular crosstalk in PDA that promotes immune suppression. The use of multimodal approaches using both mouse and human systems provided a unique opportunity to generate hypotheses and then evaluate them. This work has identified novel proteins of interest in mediating immune suppression, such as TIGIT, APOE, C1QA/B, and TREM2. Chapter 3 describes the mechanisms behind APOE in mediating immune suppression, but the other genes identified throughout this thesis need to be mechanistically evaluated for their functional relevance in PDA. Taken together, this thesis identifies novel mediators of immune suppression in both mouse and human PDA.

Figures

Figure 5.1

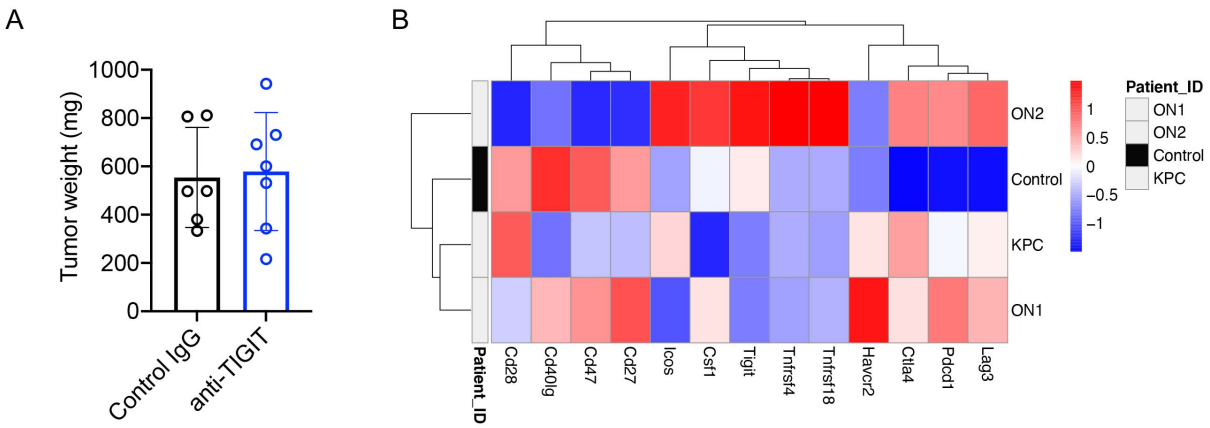

Figure 5.1 Depletion of TIGIT did not alter tumor growth in an orthotopic mouse model of PDA.
(A) 10,000 7940b KPC cells were implanted into the pancreas of C57/BL6J mice and treated with 200ug of either IgG (n=6) or α–TIGIT (7) every 3 days. Final tumor weight was plotted in mg between the two conditions. There was no statistically significant difference in tumor weight determined by Student's t test. (B) Average expression heatmap of immune checkpoints in $CD8^+$ T cells from iKras* p53* tumors (n=2, ON1, ON2), KPC tumor (n=1), and control pancreas (n=1). High expression is in red. Low expression is in blue.

Figure 5.2

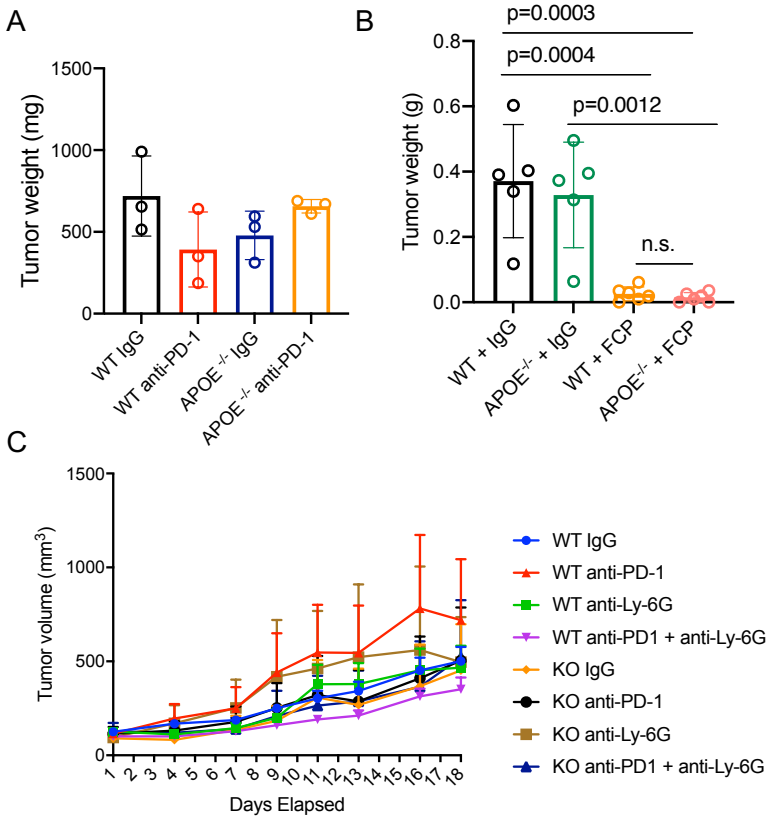

Figure 5.2 Immunotherapy approaches in APOE deficient mice.
(A) Final orthotopic tumor weight (mg) from C57/BL6J and APOE$^{-/-}$ mice treated with IgG or α-PD-1. (B) Final orthotopic tumor weight (g) from C57/BL6J and APOE$^{-/-}$ mice treated with IgG or FCP (α-CD40, α-CTLA-4, α-PD-1). One-way ANOVA was used to determine statistical significance. (C) Subcutaneous tumor volume (mm^3) from C57/BL6J and APOE$^{-/-}$ (KO) mice treated with IgG, α-PD-1, α-Ly-6G, or combination α-PD-1 and α-Ly-6G.

Figure 5.3

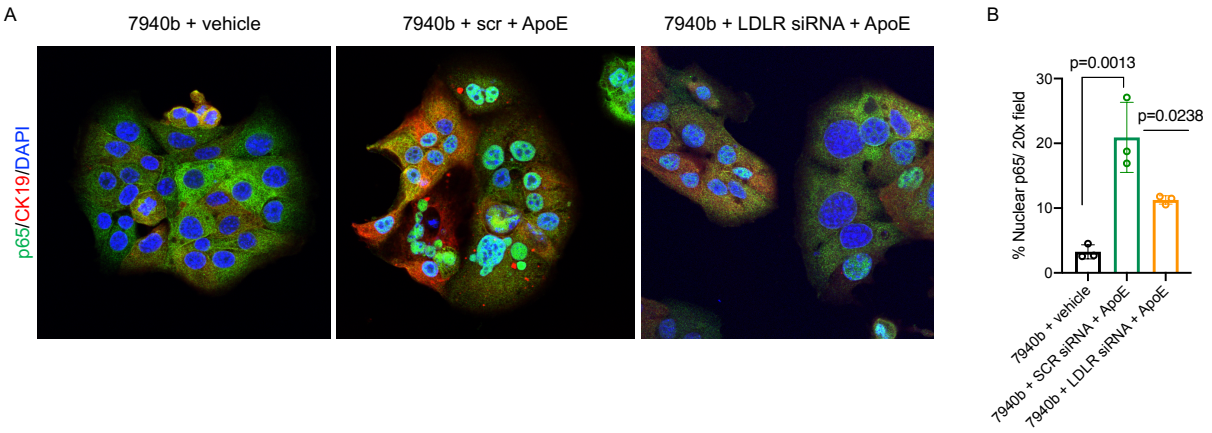

Figure 5.3 LDLR knockdown results in reduced p65 nuclear translocation.
(A) Co-immunofluorescence for p65 (green), CK19 (red) and DAPI (blue) on 7940b tumor cells treated with vehicle (left), scramble siRNA (scr, middle), or LDLR siRNA (right). Recombinant ApoE (0.3ug/mL) was spiked into the media of scramble and LDLR siRNA for one hour. (B) Quantitation of %nuclear p65 in a 20x field across conditions.

Figure 5.4

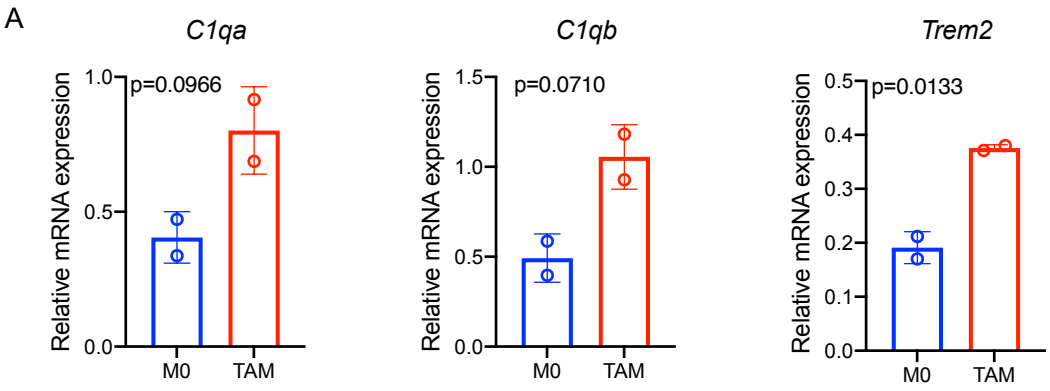

Figure 5.4 Bone marrow-derived TAMs upregulate complement components and *Trem2* compared to M0 macrophages.
(A) qRT-PCR analysis of C1qa, C1qb, and Trem2 on M0 macrophages compared to TAMs. Data were normalized to *Cyclophilin A*. Statistics were determined using Student's *t* test.

Figure 5.5

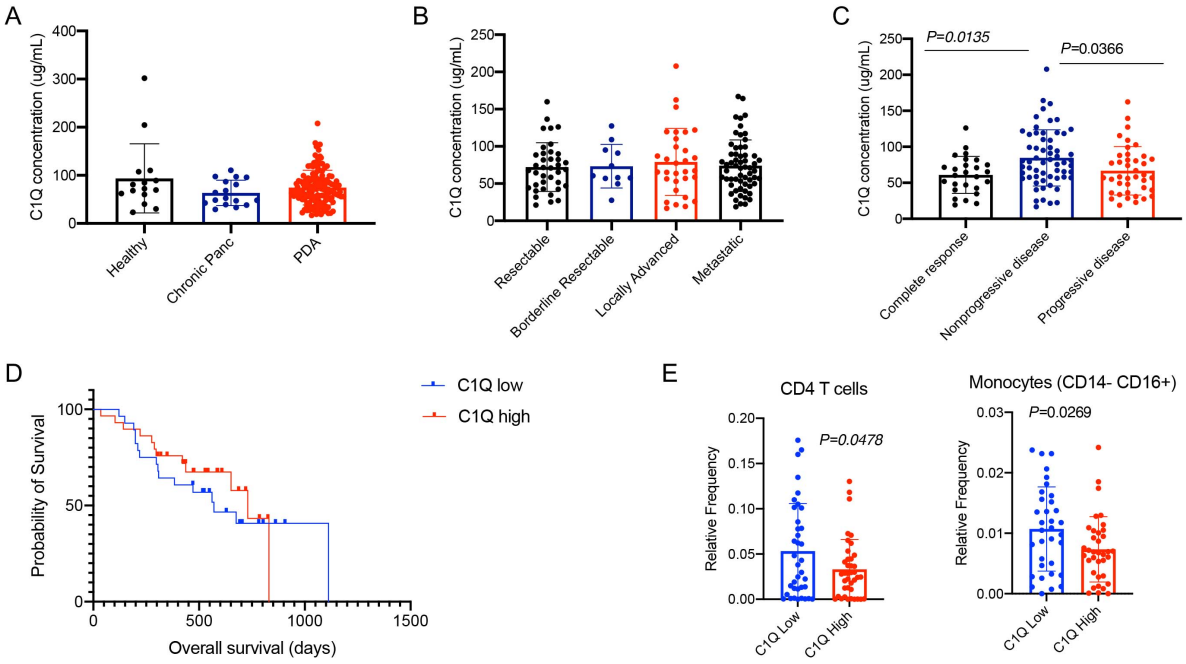

Figure 5.5 C1Q levels in human PDA serum.
(A) C1Q concentration (ug/mL) in serum from healthy (n=15), chronic pancreatitis (n=17) and PDA (n=140) patients. (B) C1Q concentration (ug/mL) in serum from PDA patients stratified by disease stage (resectable (n=38), borderline resectable (n=11), locally advanced (n=31), metastatic (n=60)). (C) C1Q concentration (ug/mL) in serum from PDA patients stratified by RECIST criteria (complete response (n=26), nonprogressive disease (n=60), progressive disease (n=40). (D) Survival analysis on PDA patients stratified by C1Q serum levels. (E) Relative frequency of CD4 T cells and $CD14^{-}$ $CD16^{+}$ monocytes in the peripheral blood of PDA patients stratified by C1Q levels.

Bibliography

Afshar-Kharghan, V. 2017. The role of the complement system in cancer. *J Clin Invest* 127:780-789.

Aguado, B.A., G.G. Bushnell, S.S. Rao, J.S. Jeruss, and L.D. Shea. 2017. Engineering the pre-metastatic niche. *Nat Biomed Eng* 1:

Aguirre, A.J., N. Bardeesy, M. Sinha, L. Lopez, D.A. Tuveson, J. Horner, M.S. Redston, and R.A. DePinho. 2003. Activated Kras and Ink4a/Arf deficiency cooperate to produce metastatic pancreatic ductal adenocarcinoma. *Genes Dev* 17:3112-3126.

Aiello, N.M., A.D. Rhim, and B.Z. Stanger. 2016. Orthotopic Injection of Pancreatic Cancer Cells. *Cold Spring Harb Protoc* 2016:pdb prot078360.

Almoguera, C., D. Shibata, K. Forrester, J. Martin, N. Arnheim, and M. Perucho. 1988. Most human carcinomas of the exocrine pancreas contain mutant c-K-ras genes. *Cell* 53:549-554.

Amir, E.D., B. Lee, P. Badoual, M. Gordon, X.V. Guo, M. Merad, and A.H. Rahman. 2019. Development of a Comprehensive Antibody Staining Database Using a Standardized Analytics Pipeline. *Front Immunol* 10:1315.

Ardito, C.M., B.M. Gruner, K.K. Takeuchi, C. Lubeseder-Martellato, N. Teichmann, P.K. Mazur, K.E. Delgiorno, E.S. Carpenter, C.J. Halbrook, J.C. Hall, D. Pal, T. Briel, A. Herner, M. Trajkovic-Arsic, B. Sipos, G.Y. Liou, P. Storz, N.R. Murray, D.W. Threadgill, M. Sibilia, M.K. Washington, C.L. Wilson, R.M. Schmid, E.W. Raines,

H.C. Crawford, and J.T. Siveke. 2012. EGF receptor is required for KRAS-induced pancreatic tumorigenesis. *Cancer Cell* 22:304-317.

Arlettaz, L., S. Degermann, C. De Rham, E. Roosnek, and B. Huard. 2004. Expression of inhibitory KIR is confined to CD8+ effector T cells and limits their proliferative capacity. *Eur J Immunol* 34:3413-3422.

Azarin, S.M., J. Yi, R.M. Gower, B.A. Aguado, M.E. Sullivan, A.G. Goodman, E.J. Jiang, S.S. Rao, Y. Ren, S.L. Tucker, V. Backman, J.S. Jeruss, and L.D. Shea. 2015. In vivo capture and label-free detection of early metastatic cells. *Nat Commun* 6:8094.

Bailey, P., D.K. Chang, K. Nones, A.L. Johns, A.M. Patch, M.C. Gingras, D.K. Miller, A.N. Christ, T.J. Bruxner, M.C. Quinn, C. Nourse, L.C. Murtaugh, I. Harliwong, S. Idrisoglu, S. Manning, E. Nourbakhsh, S. Wani, L. Fink, O. Holmes, V. Chin, M.J. Anderson, S. Kazakoff, C. Leonard, F. Newell, N. Waddell, S. Wood, Q. Xu, P.J. Wilson, N. Cloonan, K.S. Kassahn, D. Taylor, K. Quek, A. Robertson, L. Pantano, L. Mincarelli, L.N. Sanchez, L. Evers, J. Wu, M. Pinese, M.J. Cowley, M.D. Jones, E.K. Colvin, A.M. Nagrial, E.S. Humphrey, L.A. Chantrill, A. Mawson, J. Humphris, A. Chou, M. Pajic, C.J. Scarlett, A.V. Pinho, M. Giry-Laterriere, I. Rooman, J.S. Samra, J.G. Kench, J.A. Lovell, N.D. Merrett, C.W. Toon, K. Epari, N.Q. Nguyen, A. Barbour, N. Zeps, K. Moran-Jones, N.B. Jamieson, J.S. Graham, F. Duthie, K. Oien, J. Hair, R. Grutzmann, A. Maitra, C.A. Iacobuzio-Donahue, C.L. Wolfgang, R.A. Morgan, R.T. Lawlor, V. Corbo, C. Bassi, B. Rusev, P. Capelli, R. Salvia, G. Tortora, D. Mukhopadhyay, G.M. Petersen, I. Australian Pancreatic Cancer Genome, D.M. Munzy, W.E. Fisher, S.A. Karim, J.R. Eshleman, R.H. Hruban, C.

Pilarsky, J.P. Morton, O.J. Sansom, A. Scarpa, E.A. Musgrove, U.M. Bailey, O. Hofmann, R.L. Sutherland, D.A. Wheeler, A.J. Gill, R.A. Gibbs, J.V. Pearson, N. Waddell, A.V. Biankin, and S.M. Grimmond. 2016. Genomic analyses identify molecular subtypes of pancreatic cancer. *Nature* 531:47-52.

Balachandran, V.P., M. Luksza, J.N. Zhao, V. Makarov, J.A. Moral, R. Remark, B. Herbst, G. Askan, U. Bhanot, Y. Senbabaoglu, D.K. Wells, C.I.O. Cary, O. Grbovic-Huezo, M. Attiyeh, B. Medina, J. Zhang, J. Loo, J. Saglimbeni, M. Abu-Akeel, R. Zappasodi, N. Riaz, M. Smoragiewicz, Z.L. Kelley, O. Basturk, I. Australian Pancreatic Cancer Genome, R. Garvan Institute of Medical, H. Prince of Wales, H. Royal North Shore, G. University of, H. St Vincent's, Q.B.M.R. Institute, C.f.C.R. University of Melbourne, I.f.M.B. University of Queensland, H. Bankstown, H. Liverpool, C.O.B.L. Royal Prince Alfred Hospital, H. Westmead, H. Fremantle, H. St John of God, H. Royal Adelaide, C. Flinders Medical, P. Envoi, H. Princess Alexandria, H. Austin, I. Johns Hopkins Medical, A.R.-N.C.f.A.R.o. Cancer, M. Gonen, A.J. Levine, P.J. Allen, D.T. Fearon, M. Merad, S. Gnjatic, C.A. Iacobuzio-Donahue, J.D. Wolchok, R.P. DeMatteo, T.A. Chan, B.D. Greenbaum, T. Merghoub, and S.D. Leach. 2017. Identification of unique neoantigen qualities in long-term survivors of pancreatic cancer. *Nature* 551:512-516.

Balli, D., A.J. Rech, B.Z. Stanger, and R.H. Vonderheide. 2017. Immune Cytolytic Activity Stratifies Molecular Subsets of Human Pancreatic Cancer. *Clin Cancer Res* 23:3129-3138.

Bayne, L.J., G.L. Beatty, N. Jhala, C.E. Clark, A.D. Rhim, B.Z. Stanger, and R.H. Vonderheide. 2012. Tumor-derived granulocyte-macrophage colony-stimulating

factor regulates myeloid inflammation and T cell immunity in pancreatic cancer. *Cancer Cell* 21:822-835.

Beatty, G.L., E.G. Chiorean, M.P. Fishman, B. Saboury, U.R. Teitelbaum, W. Sun, R.D. Huhn, W. Song, D. Li, L.L. Sharp, D.A. Torigian, P.J. O'Dwyer, and R.H. Vonderheide. 2011. CD40 agonists alter tumor stroma and show efficacy against pancreatic carcinoma in mice and humans. *Science* 331:1612-1616.

Beatty, G.L., R. Winograd, R.A. Evans, K.B. Long, S.L. Luque, J.W. Lee, C. Clendenin, W.L. Gladney, D.M. Knoblock, P.D. Guirnalda, and R.H. Vonderheide. 2015. Exclusion of T Cells From Pancreatic Carcinomas in Mice Is Regulated by Ly6C(low) F4/80(+) Extratumoral Macrophages. *Gastroenterology* 149:201-210.

Bendall, S.C., E.F. Simonds, P. Qiu, A.D. Amir el, P.O. Krutzik, R. Finck, R.V. Bruggner, R. Melamed, A. Trejo, O.I. Ornatsky, R.S. Balderas, S.K. Plevritis, K. Sachs, D. Pe'er, S.D. Tanner, and G.P. Nolan. 2011. Single-cell mass cytometry of differential immune and drug responses across a human hematopoietic continuum. *Science* 332:687-696.

Bengsch, F., D.M. Knoblock, A. Liu, F. McAllister, and G.L. Beatty. 2017. CTLA-4/CD80 pathway regulates T cell infiltration into pancreatic cancer. *Cancer Immunol Immunother* 66:1609-1617.

Benoit, M.E., E.V. Clarke, P. Morgado, D.A. Fraser, and A.J. Tenner. 2012. Complement protein C1q directs macrophage polarization and limits inflammasome activity during the uptake of apoptotic cells. *J Immunol* 188:5682-5693.

Bettac, L., S. Denk, T. Seufferlein, and M. Huber-Lang. 2017. Complement in Pancreatic Disease—Perpetrator or Savior? *Frontiers in Immunology* 8:

Biasci, D., M. Smoragiewicz, C.M. Connell, Z. Wang, Y. Gao, J.E.D. Thaventhiran, B. Basu, L. Magiera, T.I. Johnson, L. Bax, A. Gopinathan, C. Isherwood, F.A. Gallagher, M. Pawula, I. Hudecova, D. Gale, N. Rosenfeld, P. Barmpounakis, E.C. Popa, R. Brais, E. Godfrey, F. Mir, F.M. Richards, D.T. Fearon, T. Janowitz, and D.I. Jodrell. 2020. CXCR4 inhibition in human pancreatic and colorectal cancers induces an integrated immune response. *Proc Natl Acad Sci U S A* 117:28960-28970.

Biffi, G., T.E. Oni, B. Spielman, Y. Hao, E. Elyada, Y. Park, J. Preall, and D.A. Tuveson. 2019. IL1-Induced JAK/STAT Signaling Is Antagonized by TGFbeta to Shape CAF Heterogeneity in Pancreatic Ductal Adenocarcinoma. *Cancer Discov* 9:282-301.

Blando, J., A. Sharma, M.G. Higa, H. Zhao, L. Vence, S.S. Yadav, J. Kim, A.M. Sepulveda, M. Sharp, A. Maitra, J. Wargo, M. Tetzlaff, R. Broaddus, M.H.G. Katz, G.R. Varadhachary, M. Overman, H. Wang, C. Yee, C. Bernatchez, C. Iacobuzio-Donahue, S. Basu, J.P. Allison, and P. Sharma. 2019. Comparison of immune infiltrates in melanoma and pancreatic cancer highlights VISTA as a potential target in pancreatic cancer. *Proc Natl Acad Sci U S A* 116:1692-1697.

Bonavita, E., S. Gentile, M. Rubino, V. Maina, R. Papait, P. Kunderfranco, C. Greco, F. Feruglio, M. Molgora, I. Laface, S. Tartari, A. Doni, F. Pasqualini, E. Barbati, G. Basso, M.R. Galdiero, M. Nebuloni, M. Roncalli, P. Colombo, L. Laghi, J.D. Lambris, S. Jaillon, C. Garlanda, and A. Mantovani. 2015. PTX3 is an extrinsic oncosuppressor regulating complement-dependent inflammation in cancer. *Cell* 160:700-714.

Bouma, M.E., M. Pessah, G. Renaud, N. Amit, D. Catala, and R. Infante. 1988. Synthesis and secretion of lipoproteins by human hepatocytes in culture. *In Vitro Cell Dev Biol* 24:85-90.

Brahmer, J.R., S.S. Tykodi, L.Q. Chow, W.J. Hwu, S.L. Topalian, P. Hwu, C.G. Drake, L.H. Camacho, J. Kauh, K. Odunsi, H.C. Pitot, O. Hamid, S. Bhatia, R. Martins, K. Eaton, S. Chen, T.M. Salay, S. Alaparthy, J.F. Grosso, A.J. Korman, S.M. Parker, S. Agrawal, S.M. Goldberg, D.M. Pardoll, A. Gupta, and J.M. Wigginton. 2012. Safety and activity of anti-PD-L1 antibody in patients with advanced cancer. *N Engl J Med* 366:2455-2465.

Bronte, V., S. Brandau, S.H. Chen, M.P. Colombo, A.B. Frey, T.F. Greten, S. Mandruzzato, P.J. Murray, A. Ochoa, S. Ostrand-Rosenberg, P.C. Rodriguez, A. Sica, V. Umansky, R.H. Vonderheide, and D.I. Gabrilovich. 2016. Recommendations for myeloid-derived suppressor cell nomenclature and characterization standards. *Nat Commun* 7:12150.

Bronte, V., and P. Zanovello. 2005. Regulation of immune responses by L-arginine metabolism. *Nat Rev Immunol* 5:641-654.

Burke, S.J., D. Lu, T.E. Sparer, T. Masi, M.R. Goff, M.D. Karlstad, and J.J. Collier. 2014. NF-kappaB and STAT1 control CXCL1 and CXCL2 gene transcription. *Am J Physiol Endocrinol Metab* 306:E131-149.

Burris, H.A., 3rd, M.J. Moore, J. Andersen, M.R. Green, M.L. Rothenberg, M.R. Modiano, M.C. Cripps, R.K. Portenoy, A.M. Storniolo, P. Tarassoff, R. Nelson, F.A. Dorr, C.D. Stephens, and D.D. Von Hoff. 1997. Improvements in survival and clinical

benefit with gemcitabine as first-line therapy for patients with advanced pancreas cancer: a randomized trial. *J Clin Oncol* 15:2403-2413.

Bushnell, G.G., T.P. Hardas, R.M. Hartfield, Y. Zhang, R.S. Oakes, S. Ronquist, H. Chen, I. Rajapakse, M.S. Wicha, J.S. Jeruss, and L.D. Shea. 2019. Biomaterial Scaffolds Recruit an Aggressive Population of Metastatic Tumor Cells In Vivo. *Cancer Res* 79:2042-2053.

Candido, J.B., J.P. Morton, P. Bailey, A.D. Campbell, S.A. Karim, T. Jamieson, L. Lapienyte, A. Gopinathan, W. Clark, E.J. McGhee, J. Wang, M. Escorcio-Correia, R. Zollinger, R. Roshani, L. Drew, L. Rishi, R. Arkell, T.R.J. Evans, C. Nixon, D.I. Jodrell, R.W. Wilkinson, A.V. Biankin, S.T. Barry, F.R. Balkwill, and O.J. Sansom. 2018. CSF1R(+) Macrophages Sustain Pancreatic Tumor Growth through T Cell Suppression and Maintenance of Key Gene Programs that Define the Squamous Subtype. *Cell Rep* 23:1448-1460.

Carlson, C.M., B.T. Endrizzi, J. Wu, X. Ding, M.A. Weinreich, E.R. Walsh, M.A. Wani, J.B. Lingrel, K.A. Hogquist, and S.C. Jameson. 2006. Kruppel-like factor 2 regulates thymocyte and T-cell migration. *Nature* 442:299-302.

Carstens, J.L., P. Correa de Sampaio, D. Yang, S. Barua, H. Wang, A. Rao, J.P. Allison, V.S. LeBleu, and R. Kalluri. 2017. Spatial computation of intratumoral T cells correlates with survival of patients with pancreatic cancer. *Nat Commun* 8:15095.

Chan-Seng-Yue, M., J.C. Kim, G.W. Wilson, K. Ng, E.F. Figueroa, G.M. O'Kane, A.A. Connor, R.E. Denroche, R.C. Grant, J. McLeod, J.M. Wilson, G.H. Jang, A. Zhang, A. Dodd, S.B. Liang, A. Borgida, D. Chadwick, S. Kalimuthu, I. Lungu, J.M.S. Bartlett, P.M. Krzyzanowski, V. Sandhu, H. Tiriac, F.E.M. Froeling, J.M.

Karasinska, J.T. Topham, D.J. Renouf, D.F. Schaeffer, S.J.M. Jones, M.A. Marra, J. Laskin, R. Chetty, L.D. Stein, G. Zogopoulos, B. Haibe-Kains, P.J. Campbell, D.A. Tuveson, J.J. Knox, S.E. Fischer, S. Gallinger, and F. Notta. 2020. Transcription phenotypes of pancreatic cancer are driven by genomic events during tumor evolution. *Nat Genet* 52:231-240.

Chao, T., E.E. Furth, and R.H. Vonderheide. 2016. CXCR2-Dependent Accumulation of Tumor-Associated Neutrophils Regulates T-cell Immunity in Pancreatic Ductal Adenocarcinoma. *Cancer Immunol Res* 4:968-982.

Chen, Y., Y. Song, W. Du, L. Gong, H. Chang, and Z. Zou. 2019. Tumor-associated macrophages: an accomplice in solid tumor progression. *J Biomed Sci* 26:78.

Chu, G.C., A.C. Kimmelman, A.F. Hezel, and R.A. DePinho. 2007. Stromal biology of pancreatic cancer. *J Cell Biochem* 101:887-907.

Clark, C.E., S.R. Hingorani, R. Mick, C. Combs, D.A. Tuveson, and R.H. Vonderheide. 2007. Dynamics of the immune reaction to pancreatic cancer from inception to invasion. *Cancer Res* 67:9518-9527.

Cohen, M., A. Giladi, A.D. Gorki, D.G. Solodkin, M. Zada, A. Hladik, A. Miklosi, T.M. Salame, K.B. Halpern, E. David, S. Itzkovitz, T. Harkany, S. Knapp, and I. Amit. 2018. Lung Single-Cell Signaling Interaction Map Reveals Basophil Role in Macrophage Imprinting. *Cell* 175:1031-1044 e1018.

Collin, M., and V. Bigley. 2018. Human dendritic cell subsets: an update. *Immunology* 154:3-20.

Collins, M.A., F. Bednar, Y. Zhang, J.C. Brisset, S. Galban, C.J. Galban, S. Rakshit, K.S. Flannagan, N.V. Adsay, and M. Pasca di Magliano. 2012a. Oncogenic Kras is

required for both the initiation and maintenance of pancreatic cancer in mice. *J Clin Invest* 122:639-653.

Collins, M.A., J.C. Brisset, Y. Zhang, F. Bednar, J. Pierre, K.A. Heist, C.J. Galban, S. Galban, and M.P. di Magliano. 2012b. Metastatic pancreatic cancer is dependent on oncogenic Kras in mice. *PLoS One* 7:e49707.

Collins, M.A., W. Yan, J.S. Sebolt-Leopold, and M. Pasca di Magliano. 2014. MAPK signaling is required for dedifferentiation of acinar cells and development of pancreatic intraepithelial neoplasia in mice. *Gastroenterology* 146:822-834 e827.

Condeelis, J., and J.W. Pollard. 2006. Macrophages: obligate partners for tumor cell migration, invasion, and metastasis. *Cell* 124:263-266.

Conroy, T., F. Desseigne, M. Ychou, O. Bouche, R. Guimbaud, Y. Becouarn, A. Adenis, J.L. Raoul, S. Gourgou-Bourgade, C. de la Fouchardiere, J. Bennouna, J.B. Bachet, F. Khemissa-Akouz, D. Pere-Verge, C. Delbaldo, E. Assenat, B. Chauffert, P. Michel, C. Montoto-Grillot, M. Ducreux, U. Groupe Tumeurs Digestives of, and P. Intergroup. 2011. FOLFIRINOX versus gemcitabine for metastatic pancreatic cancer. *N Engl J Med* 364:1817-1825.

Conroy, T., P. Hammel, M. Hebbar, M. Ben Abdelghani, A.C. Wei, J.L. Raoul, L. Chone, E. Francois, P. Artru, J.J. Biagi, T. Lecomte, E. Assenat, R. Faroux, M. Ychou, J. Volet, A. Sauvanet, G. Breysacher, F. Di Fiore, C. Cripps, P. Kavan, P. Texereau, K. Bouhier-Leporrier, F. Khemissa-Akouz, J.L. Legoux, B. Juzyna, S. Gourgou, C.J. O'Callaghan, C. Jouffroy-Zeller, P. Rat, D. Malka, F. Castan, J.B. Bachet, G. Canadian Cancer Trials, and G.I.P.G. the Unicancer. 2018. FOLFIRINOX or

Gemcitabine as Adjuvant Therapy for Pancreatic Cancer. *N Engl J Med* 379:2395-2406.

Corder, E.H., A.M. Saunders, N.J. Risch, W.J. Strittmatter, D.E. Schmechel, P.C. Gaskell, Jr., J.B. Rimmler, P.A. Locke, P.M. Conneally, K.E. Schmader, and et al. 1994. Protective effect of apolipoprotein E type 2 allele for late onset Alzheimer disease. *Nat Genet* 7:180-184.

Costa-Silva, B., N.M. Aiello, A.J. Ocean, S. Singh, H. Zhang, B.K. Thakur, A. Becker, A. Hoshino, M.T. Mark, H. Molina, J. Xiang, T. Zhang, T.M. Theilen, G. Garcia-Santos, C. Williams, Y. Ararso, Y. Huang, G. Rodrigues, T.L. Shen, K.J. Labori, I.M. Lothe, E.H. Kure, J. Hernandez, A. Doussot, S.H. Ebbesen, P.M. Grandgenett, M.A. Hollingsworth, M. Jain, K. Mallya, S.K. Batra, W.R. Jarnagin, R.E. Schwartz, I. Matei, H. Peinado, B.Z. Stanger, J. Bromberg, and D. Lyden. 2015. Pancreatic cancer exosomes initiate pre-metastatic niche formation in the liver. *Nat Cell Biol* 17:816-826.

Coussens, L.M., and Z. Werb. 2002. Inflammation and cancer. *Nature* 420:860-867.

Das, S., B. Shapiro, E.A. Vucic, S. Vogt, and D. Bar-Sagi. 2020. Tumor Cell-Derived IL1beta Promotes Desmoplasia and Immune Suppression in Pancreatic Cancer. *Cancer Res* 80:1088-1101.

DeNardo, D.G., and B. Ruffell. 2019. Macrophages as regulators of tumour immunity and immunotherapy. *Nat Rev Immunol* 19:369-382.

Deng, M., X. Gui, J. Kim, L. Xie, W. Chen, Z. Li, L. He, Y. Chen, H. Chen, W. Luo, Z. Lu, J. Xie, H. Churchill, Y. Xu, Z. Zhou, G. Wu, C. Yu, S. John, K. Hirayasu, N. Nguyen, X. Liu, F. Huang, L. Li, H. Deng, H. Tang, A.H. Sadek, L. Zhang, T. Huang, Y. Zou,

B. Chen, H. Zhu, H. Arase, N. Xia, Y. Jiang, R. Collins, M.J. You, J. Homsi, N. Unni, C. Lewis, G.Q. Chen, Y.X. Fu, X.C. Liao, Z. An, J. Zheng, N. Zhang, and C.C. Zhang. 2018. LILRB4 signalling in leukaemia cells mediates T cell suppression and tumour infiltration. *Nature* 562:605-609.

Deshmane, S.L., S. Kremlev, S. Amini, and B.E. Sawaya. 2009. Monocyte chemoattractant protein-1 (MCP-1): an overview. *J Interferon Cytokine Res* 29:313-326.

Dominguez, C.X., S. Muller, S. Keerthivasan, H. Koeppen, J. Hung, S. Gierke, B. Breart, O. Foreman, T.W. Bainbridge, A. Castiglioni, Y. Senbabaoglu, Z. Modrusan, Y. Liang, M.R. Junttila, C. Klijn, R. Bourgon, and S.J. Turley. 2020. Single-Cell RNA Sequencing Reveals Stromal Evolution into LRRC15(+) Myofibroblasts as a Determinant of Patient Response to Cancer Immunotherapy. *Cancer Discov* 10:232-253.

Dove, A. 2000. CD18 trials disappoint again. *Nat Biotechnol* 18:817-818.

Ducimetiere, L., M. Vermeer, and S. Tugues. 2019. The Interplay Between Innate Lymphoid Cells and the Tumor Microenvironment. *Front Immunol* 10:2895.

Duffield, J.S., S.J. Forbes, C.M. Constandinou, S. Clay, M. Partolina, S. Vuthoori, S. Wu, R. Lang, and J.P. Iredale. 2005. Selective depletion of macrophages reveals distinct, opposing roles during liver injury and repair. *J Clin Invest* 115:56-65.

Elyada, E., M. Bolisetty, P. Laise, W.F. Flynn, E.T. Courtois, R.A. Burkhart, J.A. Teinor, P. Belleau, G. Biffi, M.S. Lucito, S. Sivajothi, T.D. Armstrong, D.D. Engle, K.H. Yu, Y. Hao, C.L. Wolfgang, Y. Park, J. Preall, E.M. Jaffee, A. Califano, P. Robson, and D.A. Tuveson. 2019. Cross-Species Single-Cell Analysis of Pancreatic Ductal

Adenocarcinoma Reveals Antigen-Presenting Cancer-Associated Fibroblasts. *Cancer Discov* 9:1102-1123.

Feig, C., J.O. Jones, M. Kraman, R.J. Wells, A. Deonarine, D.S. Chan, C.M. Connell, E.W. Roberts, Q. Zhao, O.L. Caballero, S.A. Teichmann, T. Janowitz, D.I. Jodrell, D.A. Tuveson, and D.T. Fearon. 2013. Targeting CXCL12 from FAP-expressing carcinoma-associated fibroblasts synergizes with anti-PD-L1 immunotherapy in pancreatic cancer. *Proc Natl Acad Sci U S A* 110:20212-20217.

Fourcade, J., Z. Sun, J.M. Chauvin, M. Ka, D. Davar, O. Pagliano, H. Wang, S. Saada, C. Menna, R. Amin, C. Sander, J.M. Kirkwood, A.J. Korman, and H.M. Zarour. 2018. CD226 opposes TIGIT to disrupt Tregs in melanoma. *JCI Insight* 3:

Gabitova-Cornell, L., A. Surumbayeva, S. Peri, J. Franco-Barraza, D. Restifo, N. Weitz, C. Ogier, A.R. Goldman, T.R. Hartman, R. Francescone, Y. Tan, E. Nicolas, N. Shah, E.A. Handorf, K.Q. Cai, A.M. O'Reilly, I. Sloma, R. Chiaverelli, R.A. Moffitt, V. Khazak, C.Y. Fang, E.A. Golemis, E. Cukierman, and I. Astsaturov. 2020. Cholesterol Pathway Inhibition Induces TGF-beta Signaling to Promote Basal Differentiation in Pancreatic Cancer. *Cancer Cell* 38:567-583 e511.

Gabrilovich, D.I., and S. Nagaraj. 2009. Myeloid-derived suppressor cells as regulators of the immune system. *Nat Rev Immunol* 9:162-174.

Garcia, P.E., M.K. Scales, B.L. Allen, and M. Pasca di Magliano. 2020. Pancreatic Fibroblast Heterogeneity: From Development to Cancer. *Cells* 9:

Georgoudaki, A.M., K.E. Prokopec, V.F. Boura, E. Hellqvist, S. Sohn, J. Ostling, R. Dahan, R.A. Harris, M. Rantalainen, D. Klevebring, M. Sund, S.E. Brage, J. Fuxe, C. Rolny, F. Li, J.V. Ravetch, and M.C. Karlsson. 2016. Reprogramming Tumor-

Associated Macrophages by Antibody Targeting Inhibits Cancer Progression and Metastasis. *Cell Rep* 15:2000-2011.

Gilmore, T.D. 2006. Introduction to NF-kappaB: players, pathways, perspectives. *Oncogene* 25:6680-6684.

Goldstein, D., R.H. El-Maraghi, P. Hammel, V. Heinemann, V. Kunzmann, J. Sastre, W. Scheithauer, S. Siena, J. Tabernero, L. Teixeira, G. Tortora, J.L. Van Laethem, R. Young, D.N. Penenberg, B. Lu, A. Romano, and D.D. Von Hoff. 2015. nab-Paclitaxel plus gemcitabine for metastatic pancreatic cancer: long-term survival from a phase III trial. *J Natl Cancer Inst* 107:

Gonzalez, H., C. Hagerling, and Z. Werb. 2018. Roles of the immune system in cancer: from tumor initiation to metastatic progression. *Genes Dev* 32:1267-1284.

Gordon, S. 2003. Alternative activation of macrophages. *Nat Rev Immunol* 3:23-35.

Griesmann, H., C. Drexel, N. Milosevic, B. Sipos, J. Rosendahl, T.M. Gress, and P. Michl. 2017. Pharmacological macrophage inhibition decreases metastasis formation in a genetic model of pancreatic cancer. *Gut* 66:1278-1285.

Gui, X., M. Deng, H. Song, Y. Chen, J. Xie, Z. Li, L. He, F. Huang, Y. Xu, Y. Anami, H. Yu, C. Yu, L. Li, Z. Yuan, X. Xu, Q. Wang, Y. Chai, T. Huang, Y. Shi, K. Tsuchikama, X.C. Liao, N. Xia, G.F. Gao, N. Zhang, C.C. Zhang, and Z. An. 2019. Disrupting LILRB4/APOE Interaction by an Efficacious Humanized Antibody Reverses T-cell Suppression and Blocks AML Development. *Cancer Immunol Res* 7:1244-1257.

Halbrook, C.J., C. Pontious, I. Kovalenko, L. Lapienyte, S. Dreyer, H.J. Lee, G. Thurston, Y. Zhang, J. Lazarus, P. Sajjakulnukit, H.S. Hong, D.M. Kremer, B.S. Nelson, S.

Kemp, L. Zhang, D. Chang, A. Biankin, J. Shi, T.L. Frankel, H.C. Crawford, J.P. Morton, M. Pasca di Magliano, and C.A. Lyssiotis. 2019. Macrophage-Released Pyrimidines Inhibit Gemcitabine Therapy in Pancreatic Cancer. *Cell Metab* 29:1390-1399 e1396.

Hanahan, D., and R.A. Weinberg. 2011. Hallmarks of cancer: the next generation. *Cell* 144:646-674.

Hata, T., M. Suenaga, L. Marchionni, A. Macgregor-Das, J. Yu, K. Shindo, K. Tamura, R.H. Hruban, and M. Goggins. 2018. Genome-Wide Somatic Copy Number Alterations and Mutations in High-Grade Pancreatic Intraepithelial Neoplasia. *Am J Pathol* 188:1723-1733.

Hegde, S., V.E. Krisnawan, B.H. Herzog, C. Zuo, M.A. Breden, B.L. Knolhoff, G.D. Hogg, J.P. Tang, J.M. Baer, C. Mpoy, K.B. Lee, K.A. Alexander, B.E. Rogers, K.M. Murphy, W.G. Hawkins, R.C. Fields, C.J. DeSelm, J.K. Schwarz, and D.G. DeNardo. 2020. Dendritic Cell Paucity Leads to Dysfunctional Immune Surveillance in Pancreatic Cancer. *Cancer Cell* 37:289-307 e289.

Hezel, A.F., A.C. Kimmelman, B.Z. Stanger, N. Bardeesy, and R.A. Depinho. 2006. Genetics and biology of pancreatic ductal adenocarcinoma. *Genes Dev* 20:1218-1249.

Highfill, S.L., Y. Cui, A.J. Giles, J.P. Smith, H. Zhang, E. Morse, R.N. Kaplan, and C.L. Mackall. 2014. Disruption of CXCR2-mediated MDSC tumor trafficking enhances anti-PD1 efficacy. *Sci Transl Med* 6:237ra267.

Hingorani, S.R., E.F. Petricoin, A. Maitra, V. Rajapakse, C. King, M.A. Jacobetz, S. Ross, T.P. Conrads, T.D. Veenstra, B.A. Hitt, Y. Kawaguchi, D. Johann, L.A. Liotta, H.C.

Crawford, M.E. Putt, T. Jacks, C.V. Wright, R.H. Hruban, A.M. Lowy, and D.A. Tuveson. 2003. Preinvasive and invasive ductal pancreatic cancer and its early detection in the mouse. *Cancer Cell* 4:437-450.

Hingorani, S.R., L. Wang, A.S. Multani, C. Combs, T.B. Deramaudt, R.H. Hruban, A.K. Rustgi, S. Chang, and D.A. Tuveson. 2005. Trp53R172H and KrasG12D cooperate to promote chromosomal instability and widely metastatic pancreatic ductal adenocarcinoma in mice. *Cancer Cell* 7:469-483.

Hinz, B., G. Celetta, J.J. Tomasek, G. Gabbiani, and C. Chaponnier. 2001. Alpha-smooth muscle actin expression upregulates fibroblast contractile activity. *Mol Biol Cell* 12:2730-2741.

Hiratsuka, S., K. Nakamura, S. Iwai, M. Murakami, T. Itoh, H. Kijima, J.M. Shipley, R.M. Senior, and M. Shibuya. 2002. MMP9 induction by vascular endothelial growth factor receptor-1 is involved in lung-specific metastasis. *Cancer Cell* 2:289-300.

Hiratsuka, S., A. Watanabe, H. Aburatani, and Y. Maru. 2006. Tumour-mediated upregulation of chemoattractants and recruitment of myeloid cells predetermines lung metastasis. *Nat Cell Biol* 8:1369-1375.

Hoffman, M.T., S.B. Kemp, D.J. Salas-Escabillas, Y. Zhang, N.G. Steele, S. The, D. Long, S. Benitz, W. Yan, R.F. Margolskee, F. Bednar, M. Pasca di Magliano, H.J. Wen, and H.C. Crawford. 2020. The Gustatory Sensory G-Protein GNAT3 Suppresses Pancreatic Cancer Progression in Mice. *Cell Mol Gastroenterol Hepatol*

Hosein, A.N., H. Huang, Z. Wang, K. Parmar, W. Du, J. Huang, A. Maitra, E. Olson, U. Verma, and R.A. Brekken. 2019. Cellular heterogeneity during mouse pancreatic ductal adenocarcinoma progression at single-cell resolution. *JCI Insight* 5:

Huber, S., N. Gagliani, L.A. Zenewicz, F.J. Huber, L. Bosurgi, B. Hu, M. Hedl, W. Zhang, W. O'Connor, Jr., A.J. Murphy, D.M. Valenzuela, G.D. Yancopoulos, C.J. Booth, J.H. Cho, W. Ouyang, C. Abraham, and R.A. Flavell. 2012. IL-22BP is regulated by the inflammasome and modulates tumorigenesis in the intestine. *Nature* 491:259-263.

Ijichi, H., A. Chytil, A.E. Gorska, M.E. Aakre, B. Bierie, M. Tada, D. Mohri, K. Miyabayashi, Y. Asaoka, S. Maeda, T. Ikenoue, K. Tateishi, C.V. Wright, K. Koike, M. Omata, and H.L. Moses. 2011. Inhibiting Cxcr2 disrupts tumor-stromal interactions and improves survival in a mouse model of pancreatic ductal adenocarcinoma. *J Clin Invest* 121:4106-4117.

Ino, Y., R. Yamazaki-Itoh, K. Shimada, M. Iwasaki, T. Kosuge, Y. Kanai, and N. Hiraoka. 2013. Immune cell infiltration as an indicator of the immune microenvironment of pancreatic cancer. *Br J Cancer* 108:914-923.

Israel, A. 2010. The IKK complex, a central regulator of NF-kappaB activation. *Cold Spring Harb Perspect Biol* 2:a000158.

Jaeschke, H., A. Farhood, A.P. Bautista, Z. Spolarics, J.J. Spitzer, and C.W. Smith. 1993. Functional inactivation of neutrophils with a Mac-1 (CD11b/CD18) monoclonal antibody protects against ischemia-reperfusion injury in rat liver. *Hepatology* 17:915-923.

Jang, J.E., C.H. Hajdu, C. Liot, G. Miller, M.L. Dustin, and D. Bar-Sagi. 2017. Crosstalk between Regulatory T Cells and Tumor-Associated Dendritic Cells Negates Anti-tumor Immunity in Pancreatic Cancer. *Cell Rep* 20:558-571.

Jansen, C.S., N. Prokhnevska, V.A. Master, M.G. Sanda, J.W. Carlisle, M.A. Bilen, M. Cardenas, S. Wilkinson, R. Lake, A.G. Sowalsky, R.M. Valanparambil, W.H. Hudson, D. McGuire, K. Melnick, A.I. Khan, K. Kim, Y.M. Chang, A. Kim, C.P. Filson, M. Alemozaffar, A.O. Osunkoya, P. Mullane, C. Ellis, R. Akondy, S.J. Im, A.O. Kamphorst, A. Reyes, Y. Liu, and H. Kissick. 2019. An intra-tumoral niche maintains and differentiates stem-like CD8 T cells. *Nature* 576:465-470.

Kalluri, R. 2016. The biology and function of fibroblasts in cancer. *Nat Rev Cancer* 16:582-598.

Kaplan, R.N., R.D. Riba, S. Zacharoulis, A.H. Bramley, L. Vincent, C. Costa, D.D. MacDonald, D.K. Jin, K. Shido, S.A. Kerns, Z. Zhu, D. Hicklin, Y. Wu, J.L. Port, N. Altorki, E.R. Port, D. Ruggero, S.V. Shmelkov, K.K. Jensen, S. Rafii, and D. Lyden. 2005. VEGFR1-positive haematopoietic bone marrow progenitors initiate the pre-metastatic niche. *Nature* 438:820-827.

Katzenelenbogen, Y., F. Sheban, A. Yalin, I. Yofe, D. Svetlichnyy, D.A. Jaitin, C. Bornstein, A. Moshe, H. Keren-Shaul, M. Cohen, S.Y. Wang, B. Li, E. David, T.M. Salame, A. Weiner, and I. Amit. 2020. Coupled scRNA-Seq and Intracellular Protein Activity Reveal an Immunosuppressive Role of TREM2 in Cancer. *Cell* 182:872-885 e819.

Kinney, J.W., S.M. Bemiller, A.S. Murtishaw, A.M. Leisgang, A.M. Salazar, and B.T. Lamb. 2018. Inflammation as a central mechanism in Alzheimer's disease. *Alzheimers Dement (N Y)* 4:575-590.

Kleeff, J., M. Korc, M. Apte, C. La Vecchia, C.D. Johnson, A.V. Biankin, R.E. Neale, M. Tempero, D.A. Tuveson, R.H. Hruban, and J.P. Neoptolemos. 2016. Pancreatic cancer. *Nat Rev Dis Primers* 2:16022.

Kondo, T., H. Takata, and M. Takiguchi. 2007. Functional expression of chemokine receptor CCR6 on human effector memory CD8+ T cells. *Eur J Immunol* 37:54-65.

Kopp, J.L., G. von Figura, E. Mayes, F.F. Liu, C.L. Dubois, J.P.t. Morris, F.C. Pan, H. Akiyama, C.V. Wright, K. Jensen, M. Hebrok, and M. Sander. 2012. Identification of Sox9-dependent acinar-to-ductal reprogramming as the principal mechanism for initiation of pancreatic ductal adenocarcinoma. *Cancer Cell* 22:737-750.

Kraman, M., P.J. Bambrough, J.N. Arnold, E.W. Roberts, L. Magiera, J.O. Jones, A. Gopinathan, D.A. Tuveson, and D.T. Fearon. 2010. Suppression of antitumor immunity by stromal cells expressing fibroblast activation protein-alpha. *Science* 330:827-830.

Krzywinski, M., J. Schein, I. Birol, J. Connors, R. Gascoyne, D. Horsman, S.J. Jones, and M.A. Marra. 2009. Circos: an information aesthetic for comparative genomics. *Genome Res* 19:1639-1645.

Kumar, V., S. Patel, E. Tcyganov, and D.I. Gabrilovich. 2016. The Nature of Myeloid-Derived Suppressor Cells in the Tumor Microenvironment. *Trends Immunol* 37:208-220.

Kurahara, H., H. Shinchi, Y. Mataki, K. Maemura, H. Noma, F. Kubo, M. Sakoda, S. Ueno, S. Natsugoe, and S. Takao. 2011. Significance of M2-polarized tumor-associated macrophage in pancreatic cancer. *J Surg Res* 167:e211-219.

Kurtulus, S., K. Sakuishi, S.F. Ngiow, N. Joller, D.J. Tan, M.W. Teng, M.J. Smyth, V.K. Kuchroo, and A.C. Anderson. 2015. TIGIT predominantly regulates the immune response via regulatory T cells. *J Clin Invest* 125:4053-4062.

Kzhyshkowska, J., A. Gratchev, and S. Goerdt. 2007. Human chitinases and chitinase-like proteins as indicators for inflammation and cancer. *Biomark Insights* 2:128-146.

Lane-Donovan, C., and J. Herz. 2017. ApoE, ApoE Receptors, and the Synapse in Alzheimer's Disease. *Trends Endocrinol Metab* 28:273-284.

Lazarus, J., T. Maj, J.J. Smith, M. Perusina Lanfranca, A. Rao, M.I. D'Angelica, L. Delrosario, A. Girgis, C. Schukow, J. Shia, I. Kryczek, J. Shi, I. Wasserman, H. Crawford, H. Nathan, M. Pasca Di Magliano, W. Zou, and T.L. Frankel. 2018. Spatial and phenotypic immune profiling of metastatic colon cancer. *JCI Insight* 3:

Lee, J., M.H. Rhee, E. Kim, and J.Y. Cho. 2012. BAY 11-7082 is a broad-spectrum inhibitor with anti-inflammatory activity against multiple targets. *Mediators Inflamm* 2012:416036.

Lee, J.J., R.M. Perera, H. Wang, D.C. Wu, X.S. Liu, S. Han, J. Fitamant, P.D. Jones, K.S. Ghanta, S. Kawano, J.M. Nagle, V. Deshpande, Y. Boucher, T. Kato, J.K. Chen, J.K. Willmann, N. Bardeesy, and P.A. Beachy. 2014. Stromal response to Hedgehog signaling restrains pancreatic cancer progression. *Proc Natl Acad Sci U S A* 111:E3091-3100.

Lee, J.W., M.L. Stone, P.M. Porrett, S.K. Thomas, C.A. Komar, J.H. Li, D. Delman, K. Graham, W.L. Gladney, X. Hua, T.A. Black, A.L. Chien, K.S. Majmundar, J.C. Thompson, S.S. Yee, M.H. O'Hara, C. Aggarwal, D. Xin, A. Shaked, M. Gao, D.

Liu, M.J. Borad, R.K. Ramanathan, E.L. Carpenter, A. Ji, M.C. de Beer, F.C. de Beer, N.R. Webb, and G.L. Beatty. 2019a. Hepatocytes direct the formation of a pro-metastatic niche in the liver. *Nature* 567:249-252.

Lee, J.W., M.L. Stone, P.M. Porrett, S.K. Thomas, C.A. Komar, J.H. Li, D. Delman, K. Graham, W.L. Gladney, X. Hua, T.A. Black, A.L. Chien, K.S. Majmundar, J.C. Thompson, S.S. Yee, M.H. O'Hara, C. Aggarwal, D. Xin, A. Shaked, M. Gao, D. Liu, M.J. Borad, R.K. Ramanathan, E.L. Carpenter, A. Ji, M.C. de Beer, F.C. de Beer, N.R. Webb, and G.L. Beatty. 2019b. Hepatocytes direct the formation of a pro-metastatic niche in the liver. *Nature*

Lee, P.Y., J.X. Wang, E. Parisini, C.C. Dascher, and P.A. Nigrovic. 2013. Ly6 family proteins in neutrophil biology. *J Leukoc Biol* 94:585-594.

Li, J., K.T. Byrne, F. Yan, T. Yamazoe, Z. Chen, T. Baslan, L.P. Richman, J.H. Lin, Y.H. Sun, A.J. Rech, D. Balli, C.A. Hay, Y. Sela, A.J. Merrell, S.M. Liudahl, N. Gordon, R.J. Norgard, S. Yuan, S. Yu, T. Chao, S. Ye, T.S.K. Eisinger-Mathason, R.B. Faryabi, J.W. Tobias, S.W. Lowe, L.M. Coussens, E.J. Wherry, R.H. Vonderheide, and B.Z. Stanger. 2018a. Tumor Cell-Intrinsic Factors Underlie Heterogeneity of Immune Cell Infiltration and Response to Immunotherapy. *Immunity* 49:178-193 e177.

Li, J., Y. He, J. Hao, L. Ni, and C. Dong. 2018b. High Levels of Eomes Promote Exhaustion of Anti-tumor CD8(+) T Cells. *Front Immunol* 9:2981.

Li, J., S. Yuan, R.J. Norgard, F. Yan, Y.H. Sun, I.K. Kim, A.J. Merrell, Y. Sela, Y. Jiang, N.V. Bhanu, B.A. Garcia, R.H. Vonderheide, A. Blanco, and B.Z. Stanger. 2020a. Epigenetic and transcriptional control of the epidermal growth factor receptor

(EGFR) regulates the tumor immune microenvironment in pancreatic cancer. *Cancer Discov*

Li, S., K.W. Fong, G. Gritsina, A. Zhang, J.C. Zhao, J. Kim, A. Sharp, W. Yuan, C. Aversa, X.J. Yang, P.S. Nelson, F.Y. Feng, A.M. Chinnaiyan, J.S. de Bono, C. Morrissey, M.B. Rettig, and J. Yu. 2020b. Correction: Activation of MAPK Signaling by CXCR7 Leads to Enzalutamide Resistance in Prostate Cancer. *Cancer Res* 80:2072.

Ligorio, M., S. Sil, J. Malagon-Lopez, L.T. Nieman, S. Misale, M. Di Pilato, R.Y. Ebright, M.N. Karabacak, A.S. Kulkarni, A. Liu, N. Vincent Jordan, J.W. Franses, J. Philipp, J. Kreuzer, N. Desai, K.S. Arora, M. Rajurkar, E. Horwitz, A. Neyaz, E. Tai, N.K.C. Magnus, K.D. Vo, C.N. Yashaswini, F. Marangoni, M. Boukhali, J.P. Fatherree, L.J. Damon, K. Xega, R. Desai, M. Choz, F. Bersani, A. Langenbucher, V. Thapar, R. Morris, U.F. Wellner, O. Schilling, M.S. Lawrence, A.S. Liss, M.N. Rivera, V. Deshpande, C.H. Benes, S. Maheswaran, D.A. Haber, C. Fernandez-Del-Castillo, C.R. Ferrone, W. Haas, M.J. Aryee, and D.T. Ting. 2019. Stromal Microenvironment Shapes the Intratumoral Architecture of Pancreatic Cancer. *Cell* 178:160-175 e127.

Ling, J., Y. Kang, R. Zhao, Q. Xia, D.F. Lee, Z. Chang, J. Li, B. Peng, J.B. Fleming, H. Wang, J. Liu, I.R. Lemischka, M.C. Hung, and P.J. Chiao. 2012. KrasG12D-induced IKK2/beta/NF-kappaB activation by IL-1alpha and p62 feedforward loops is required for development of pancreatic ductal adenocarcinoma. *Cancer Cell* 21:105-120.

Liou, G.Y., L. Bastea, A. Fleming, H. Doppler, B.H. Edenfield, D.W. Dawson, L. Zhang, N. Bardeesy, and P. Storz. 2017. The Presence of Interleukin-13 at Pancreatic

ADM/PanIN Lesions Alters Macrophage Populations and Mediates Pancreatic Tumorigenesis. *Cell Rep* 19:1322-1333.

Liou, G.Y., H. Doppler, B. Necela, B. Edenfield, L. Zhang, D.W. Dawson, and P. Storz. 2015. Mutant KRAS-induced expression of ICAM-1 in pancreatic acinar cells causes attraction of macrophages to expedite the formation of precancerous lesions. *Cancer Discov* 5:52-63.

Liou, G.Y., H. Doppler, B. Necela, M. Krishna, H.C. Crawford, M. Raimondo, and P. Storz. 2013. Macrophage-secreted cytokines drive pancreatic acinar-to-ductal metaplasia through NF-kappaB and MMPs. *J Cell Biol* 202:563-577.

Luo, Y., S. Robinson, J. Fujita, L. Siconolfi, J. Magidson, C.K. Edwards, K. Wassmann, K. Storm, D.A. Norris, D. Bankaitis-Davis, W.A. Robinson, and M. Fujita. 2011. Transcriptome profiling of whole blood cells identifies PLEK2 and C1QB in human melanoma. *PLoS One* 6:e20971.

Macy, M., Y. Okano, A.D. Cardin, E.M. Avila, and J.A. Harmony. 1983. Suppression of lymphocyte activation by plasma lipoproteins. *Cancer Res* 43:2496s-2502s.

Mahley, R.W. 1988. Apolipoprotein E: cholesterol transport protein with expanding role in cell biology. *Science* 240:622-630.

Mahley, R.W. 2016. Apolipoprotein E: from cardiovascular disease to neurodegenerative disorders. *J Mol Med (Berl)* 94:739-746.

Mahley, R.W., and S.C. Rall, Jr. 2000. Apolipoprotein E: far more than a lipid transport protein. *Annu Rev Genomics Hum Genet* 1:507-537.

Maier, H.J., M. Wagner, T.G. Schips, H.H. Salem, B. Baumann, and T. Wirth. 2013. Requirement of NEMO/IKKgamma for effective expansion of KRAS-induced precancerous lesions in the pancreas. *Oncogene* 32:2690-2695.

Maiguel, D., M.H. Faridi, C. Wei, Y. Kuwano, K.M. Balla, D. Hernandez, C.J. Barth, G. Lugo, M. Donnelly, A. Nayer, L.F. Moita, S. Schurer, D. Traver, P. Ruiz, R.I. Vazquez-Padron, K. Ley, J. Reiser, and V. Gupta. 2011. Small molecule-mediated activation of the integrin CD11b/CD18 reduces inflammatory disease. *Sci Signal* 4:ra57.

Maitra, A., and R.H. Hruban. 2008. Pancreatic cancer. *Annu Rev Pathol* 3:157-188.

Maj, T., W. Wang, J. Crespo, H. Zhang, W. Wang, S. Wei, L. Zhao, L. Vatan, I. Shao, W. Szeliga, C. Lyssiotis, J.R. Liu, I. Kryczek, and W. Zou. 2017. Oxidative stress controls regulatory T cell apoptosis and suppressor activity and PD-L1-blockade resistance in tumor. *Nat Immunol* 18:1332-1341.

Malanchi, I., A. Santamaria-Martinez, E. Susanto, H. Peng, H.A. Lehr, J.F. Delaloye, and J. Huelsken. 2011. Interactions between cancer stem cells and their niche govern metastatic colonization. *Nature* 481:85-89.

Manieri, N.A., E.Y. Chiang, and J.L. Grogan. 2017. TIGIT: A Key Inhibitor of the Cancer Immunity Cycle. *Trends Immunol* 38:20-28.

Mantovani, A., S. Sozzani, M. Locati, P. Allavena, and A. Sica. 2002. Macrophage polarization: tumor-associated macrophages as a paradigm for polarized M2 mononuclear phagocytes. *Trends Immunol* 23:549-555.

Marvel, D., and D.I. Gabrilovich. 2015. Myeloid-derived suppressor cells in the tumor microenvironment: expect the unexpected. *J Clin Invest* 125:3356-3364.

Mathew, E., Y. Zhang, A.M. Holtz, K.T. Kane, J.Y. Song, B.L. Allen, and M. Pasca di Magliano. 2014. Dosage-dependent regulation of pancreatic cancer growth and angiogenesis by hedgehog signaling. *Cell Rep* 9:484-494.

Mauer, J., B. Chaurasia, J. Goldau, M.C. Vogt, J. Ruud, K.D. Nguyen, S. Theurich, A.C. Hausen, J. Schmitz, H.S. Bronneke, E. Estevez, T.L. Allen, A. Mesaros, L. Partridge, M.A. Febbraio, A. Chawla, F.T. Wunderlich, and J.C. Bruning. 2014. Signaling by IL-6 promotes alternative activation of macrophages to limit endotoxemia and obesity-associated resistance to insulin. *Nat Immunol* 15:423-430.

Maurer, C., S.R. Holmstrom, J. He, P. Laise, T. Su, A. Ahmed, H. Hibshoosh, J.A. Chabot, P.E. Oberstein, A.R. Sepulveda, J.M. Genkinger, J. Zhang, A.C. Iuga, M. Bansal, A. Califano, and K.P. Olive. 2019. Experimental microdissection enables functional harmonisation of pancreatic cancer subtypes. *Gut* 68:1034-1043.

McCarthy, D.J., Y. Chen, and G.K. Smyth. 2012. Differential expression analysis of multifactor RNA-Seq experiments with respect to biological variation. *Nucleic Acids Res* 40:4288-4297.

McMahon, C.W., A.J. Zajac, A.M. Jamieson, L. Corral, G.E. Hammer, R. Ahmed, and D.H. Raulet. 2002. Viral and bacterial infections induce expression of multiple NK cell receptors in responding CD8(+) T cells. *J Immunol* 169:1444-1452.

Melani, C., S. Sangaletti, F.M. Barazzetta, Z. Werb, and M.P. Colombo. 2007. Amino-biphosphonate-mediated MMP-9 inhibition breaks the tumor-bone marrow axis responsible for myeloid-derived suppressor cell expansion and macrophage infiltration in tumor stroma. *Cancer Res* 67:11438-11446.

Melisi, D., J. Niu, Z. Chang, Q. Xia, B. Peng, S. Ishiyama, D.B. Evans, and P.J. Chiao. 2009. Secreted interleukin-1alpha induces a metastatic phenotype in pancreatic cancer by sustaining a constitutive activation of nuclear factor-kappaB. *Mol Cancer Res* 7:624-633.

Messmer, M.N., C.S. Netherby, D. Banik, and S.I. Abrams. 2015. Tumor-induced myeloid dysfunction and its implications for cancer immunotherapy. *Cancer Immunol Immunother* 64:1-13.

Mitchem, J.B., D.J. Brennan, B.L. Knolhoff, B.A. Belt, Y. Zhu, D.E. Sanford, L. Belaygorod, D. Carpenter, L. Collins, D. Piwnica-Worms, S. Hewitt, G.M. Udupi, W.M. Gallagher, C. Wegner, B.L. West, A. Wang-Gillam, P. Goedegebuure, D.C. Linehan, and D.G. DeNardo. 2013. Targeting tumor-infiltrating macrophages decreases tumor-initiating cells, relieves immunosuppression, and improves chemotherapeutic responses. *Cancer Res* 73:1128-1141.

Molgora, M., E. Esaulova, W. Vermi, J. Hou, Y. Chen, J. Luo, S. Brioschi, M. Bugatti, A.S. Omodei, B. Ricci, C. Fronick, S.K. Panda, Y. Takeuchi, M.M. Gubin, R. Faccio, M. Cella, S. Gilfillan, E.R. Unanue, M.N. Artyomov, R.D. Schreiber, and M. Colonna. 2020. TREM2 Modulation Remodels the Tumor Myeloid Landscape Enhancing Anti-PD-1 Immunotherapy. *Cell* 182:886-900 e817.

Moncada, R., D. Barkley, F. Wagner, M. Chiodin, J.C. Devlin, M. Baron, C.H. Hajdu, D.M. Simeone, and I. Yanai. 2020. Integrating microarray-based spatial transcriptomics and single-cell RNA-seq reveals tissue architecture in pancreatic ductal adenocarcinomas. *Nat Biotechnol* 38:333-342.

Morris, A.H., K.R. Hughes, R.S. Oakes, M.M. Cai, S.D. Miller, D.N. Irani, and L.D. Shea. 2020a. Engineered immunological niches to monitor disease activity and treatment efficacy in relapsing multiple sclerosis. *Nat Commun* 11:3871.

Morris, A.H., S.M. Orbach, G.G. Bushnell, R.S. Oakes, J.S. Jeruss, and L.D. Shea. 2020b. Engineered Niches to Analyze Mechanisms of Metastasis and Guide Precision Medicine. *Cancer Res* 80:3786-3794.

Murray, P.J., and T.A. Wynn. 2011. Protective and pathogenic functions of macrophage subsets. *Nat Rev Immunol* 11:723-737.

Nielsen, S.R., V. Quaranta, A. Linford, P. Emeagi, C. Rainer, A. Santos, L. Ireland, T. Sakai, K. Sakai, Y.S. Kim, D. Engle, F. Campbell, D. Palmer, J.H. Ko, D.A. Tuveson, E. Hirsch, A. Mielgo, and M.C. Schmid. 2016. Macrophage-secreted granulin supports pancreatic cancer metastasis by inducing liver fibrosis. *Nat Cell Biol* 18:549-560.

Nowicka, M., C. Krieg, H.L. Crowell, L.M. Weber, F.J. Hartmann, S. Guglietta, B. Becher, M.P. Levesque, and M.D. Robinson. 2017. CyTOF workflow: differential discovery in high-throughput high-dimensional cytometry datasets. *F1000Res* 6:748.

Noy, R., and J.W. Pollard. 2014. Tumor-associated macrophages: from mechanisms to therapy. *Immunity* 41:49-61.

Nywening, T.M., B.A. Belt, D.R. Cullinan, R.Z. Panni, B.J. Han, D.E. Sanford, R.C. Jacobs, J. Ye, A.A. Patel, W.E. Gillanders, R.C. Fields, D.G. DeNardo, W.G. Hawkins, P. Goedegebuure, and D.C. Linehan. 2018. Targeting both tumour-associated CXCR2(+) neutrophils and CCR2(+) macrophages disrupts myeloid

recruitment and improves chemotherapeutic responses in pancreatic ductal adenocarcinoma. *Gut* 67:1112-1123.

Nywening, T.M., A. Wang-Gillam, D.E. Sanford, B.A. Belt, R.Z. Panni, B.M. Cusworth, A.T. Toriola, R.K. Nieman, L.A. Worley, M. Yano, K.J. Fowler, A.C. Lockhart, R. Suresh, B.R. Tan, K.H. Lim, R.C. Fields, S.M. Strasberg, W.G. Hawkins, D.G. DeNardo, S.P. Goedegebuure, and D.C. Linehan. 2016. Targeting tumour-associated macrophages with CCR2 inhibition in combination with FOLFIRINOX in patients with borderline resectable and locally advanced pancreatic cancer: a single-centre, open-label, dose-finding, non-randomised, phase 1b trial. *Lancet Oncol* 17:651-662.

Oakes, R.S., G.G. Bushnell, S.M. Orbach, P. Kandagatla, Y. Zhang, A.H. Morris, M.S. Hall, P. LaFaire, J.T. Decker, R.M. Hartfield, M.D. Brooks, M.S. Wicha, J.S. Jeruss, and L.D. Shea. 2020. Metastatic Conditioning of Myeloid Cells at a Subcutaneous Synthetic Niche Reflects Disease Progression and Predicts Therapeutic Outcomes. *Cancer Res* 80:602-612.

Ohlund, D., A. Handly-Santana, G. Biffi, E. Elyada, A.S. Almeida, M. Ponz-Sarvise, V. Corbo, T.E. Oni, S.A. Hearn, E.J. Lee, Chio, II, C.I. Hwang, H. Tiriac, L.A. Baker, D.D. Engle, C. Feig, A. Kultti, M. Egeblad, D.T. Fearon, J.M. Crawford, H. Clevers, Y. Park, and D.A. Tuveson. 2017. Distinct populations of inflammatory fibroblasts and myofibroblasts in pancreatic cancer. *J Exp Med* 214:579-596.

Orecchioni, M., Y. Ghosheh, A.B. Pramod, and K. Ley. 2019. Macrophage Polarization: Different Gene Signatures in M1(LPS+) vs. Classically and M2(LPS-) vs. Alternatively Activated Macrophages. *Front Immunol* 10:1084.

Ostendorf, B.N., J. Bilanovic, N. Adaku, K.N. Tafreshian, B. Tavora, R.D. Vaughan, and S.F. Tavazoie. 2020. Common germline variants of the human APOE gene modulate melanoma progression and survival. *Nat Med* 26:1048-1053.

Ozdemir, B.C., T. Pentcheva-Hoang, J.L. Carstens, X. Zheng, C.C. Wu, T.R. Simpson, H. Laklai, H. Sugimoto, C. Kahlert, S.V. Novitskiy, A. De Jesus-Acosta, P. Sharma, P. Heidari, U. Mahmood, L. Chin, H.L. Moses, V.M. Weaver, A. Maitra, J.P. Allison, V.S. LeBleu, and R. Kalluri. 2014. Depletion of carcinoma-associated fibroblasts and fibrosis induces immunosuppression and accelerates pancreas cancer with reduced survival. *Cancer Cell* 25:719-734.

Panni, R.Z., J.M. Herndon, C. Zuo, S. Hegde, G.D. Hogg, B.L. Knolhoff, M.A. Breden, X. Li, V.E. Krisnawan, S.Q. Khan, J.K. Schwarz, B.E. Rogers, R.C. Fields, W.G. Hawkins, V. Gupta, and D.G. DeNardo. 2019. Agonism of CD11b reprograms innate immunity to sensitize pancreatic cancer to immunotherapies. *Sci Transl Med* 11:

Pencheva, N., H. Tran, C. Buss, D. Huh, M. Drobnjak, K. Busam, and S.F. Tavazoie. 2012. Convergent multi-miRNA targeting of ApoE drives LRP1/LRP8-dependent melanoma metastasis and angiogenesis. *Cell* 151:1068-1082.

Perusina Lanfranca, M., Y. Zhang, A. Girgis, S. Kasselman, J. Lazarus, I. Kryczek, L. Delrosario, A. Rhim, L. Koneva, M. Sartor, L. Sun, C. Halbrook, H. Nathan, J. Shi, H.C. Crawford, M. Pasca di Magliano, W. Zou, and T.L. Frankel. 2020. Interleukin 22 Signaling Regulates Acinar Cell Plasticity to Promote Pancreatic Tumor Development in Mice. *Gastroenterology* 158:1417-1432 e1411.

Pollard, J.W. 2004. Tumour-educated macrophages promote tumour progression and metastasis. *Nat Rev Cancer* 4:71-78.

Porembka, M.R., J.B. Mitchem, B.A. Belt, C.S. Hsieh, H.M. Lee, J. Herndon, W.E. Gillanders, D.C. Linehan, and P. Goedegebuure. 2012. Pancreatic adenocarcinoma induces bone marrow mobilization of myeloid-derived suppressor cells which promote primary tumor growth. *Cancer Immunol Immunother* 61:1373-1385.

Porta, C., F.M. Consonni, S. Morlacchi, S. Sangaletti, A. Bleve, M.G. Totaro, P. Larghi, M. Rimoldi, C. Tripodo, L. Strauss, S. Banfi, M. Storto, T. Pressiani, L. Rimassa, S. Tartari, A. Ippolito, A. Doni, G. Solda, S. Duga, V. Piccolo, R. Ostuni, G. Natoli, V. Bronte, F. Balzac, E. Turco, E. Hirsch, M.P. Colombo, and A. Sica. 2020. Tumor-Derived Prostaglandin E2 Promotes p50 NF-kappaB-Dependent Differentiation of Monocytic MDSCs. *Cancer Res* 80:2874-2888.

Pylayeva-Gupta, Y., K.E. Lee, C.H. Hajdu, G. Miller, and D. Bar-Sagi. 2012. Oncogenic Kras-induced GM-CSF production promotes the development of pancreatic neoplasia. *Cancer Cell* 21:836-847.

Qian, B.Z., and J.W. Pollard. 2010. Macrophage diversity enhances tumor progression and metastasis. *Cell* 141:39-51.

Rahib, L., B.D. Smith, R. Aizenberg, A.B. Rosenzweig, J.M. Fleshman, and L.M. Matrisian. 2014. Projecting cancer incidence and deaths to 2030: the unexpected burden of thyroid, liver, and pancreas cancers in the United States. *Cancer Res* 74:2913-2921.

Ramilowski, J.A., T. Goldberg, J. Harshbarger, E. Kloppmann, M. Lizio, V.P. Satagopam, M. Itoh, H. Kawaji, P. Carninci, B. Rost, and A.R. Forrest. 2015. A draft network of ligand-receptor-mediated multicellular signalling in human. *Nat Commun* 6:7866.

Rao, S.S., G.G. Bushnell, S.M. Azarin, G. Spicer, B.A. Aguado, J.R. Stoehr, E.J. Jiang, V. Backman, L.D. Shea, and J.S. Jeruss. 2016. Enhanced Survival with Implantable Scaffolds That Capture Metastatic Breast Cancer Cells In Vivo. *Cancer Res* 76:5209-5218.

Ren, L., J. Yi, W. Li, X. Zheng, J. Liu, J. Wang, and G. Du. 2019. Apolipoproteins and cancer. *Cancer Med* 8:7032-7043.

Rhim, A.D., E.T. Mirek, N.M. Aiello, A. Maitra, J.M. Bailey, F. McAllister, M. Reichert, G.L. Beatty, A.K. Rustgi, R.H. Vonderheide, S.D. Leach, and B.Z. Stanger. 2012. EMT and dissemination precede pancreatic tumor formation. *Cell* 148:349-361.

Rhim, A.D., P.E. Oberstein, D.H. Thomas, E.T. Mirek, C.F. Palermo, S.A. Sastra, E.N. Dekleva, T. Saunders, C.P. Becerra, I.W. Tattersall, C.B. Westphalen, J. Kitajewski, M.G. Fernandez-Barrena, M.E. Fernandez-Zapico, C. Iacobuzio-Donahue, K.P. Olive, and B.Z. Stanger. 2014. Stromal elements act to restrain, rather than support, pancreatic ductal adenocarcinoma. *Cancer Cell* 25:735-747.

Robinson, M.D., D.J. McCarthy, and G.K. Smyth. 2010. edgeR: a Bioconductor package for differential expression analysis of digital gene expression data. *Bioinformatics* 26:139-140.

Rodriguez, P.C., and A.C. Ochoa. 2008. Arginine regulation by myeloid derived suppressor cells and tolerance in cancer: mechanisms and therapeutic perspectives. *Immunol Rev* 222:180-191.

Rogers, C., E.R. Edelman, and D.I. Simon. 1998. A mAb to the beta2-leukocyte integrin Mac-1 (CD11b/CD18) reduces intimal thickening after angioplasty or stent implantation in rabbits. *Proc Natl Acad Sci U S A* 95:10134-10139.

Rosenberg, S.A. 2014. Decade in review-cancer immunotherapy: entering the mainstream of cancer treatment. *Nat Rev Clin Oncol* 11:630-632.

Roszer, T. 2015. Understanding the Mysterious M2 Macrophage through Activation Markers and Effector Mechanisms. *Mediators Inflamm* 2015:816460.

Royal, R.E., C. Levy, K. Turner, A. Mathur, M. Hughes, U.S. Kammula, R.M. Sherry, S.L. Topalian, J.C. Yang, I. Lowy, and S.A. Rosenberg. 2010. Phase 2 trial of single agent Ipilimumab (anti-CTLA-4) for locally advanced or metastatic pancreatic adenocarcinoma. *J Immunother* 33:828-833.

Saka, D., M. Gokalp, B. Piyade, N.C. Cevik, E. Arik Sever, D. Unutmaz, G.O. Ceyhan, I.E. Demir, and H. Asimgil. 2020. Mechanisms of T-Cell Exhaustion in Pancreatic Cancer. *Cancers (Basel)* 12:

Sanford, D.E., B.A. Belt, R.Z. Panni, A. Mayer, A.D. Deshpande, D. Carpenter, J.B. Mitchem, S.M. Plambeck-Suess, L.A. Worley, B.D. Goetz, A. Wang-Gillam, T.J. Eberlein, D.G. Denardo, S.P. Goedegebuure, and D.C. Linehan. 2013. Inflammatory monocyte mobilization decreases patient survival in pancreatic cancer: a role for targeting the CCL2/CCR2 axis. *Clin Cancer Res* 19:3404-3415.

Sarkar, S., V. Kalia, W.N. Haining, B.T. Konieczny, S. Subramaniam, and R. Ahmed. 2008. Functional and genomic profiling of effector CD8 T cell subsets with distinct memory fates. *J Exp Med* 205:625-640.

Schlesinger, Y., O. Yosefov-Levi, D. Kolodkin-Gal, R.Z. Granit, L. Peters, R. Kalifa, L. Xia, A. Nasereddin, I. Shiff, O. Amran, Y. Nevo, S. Elgavish, K. Atlan, G. Zamir, and O. Parnas. 2020. Single-cell transcriptomes of pancreatic preinvasive lesions and cancer reveal acinar metaplastic cells' heterogeneity. *Nat Commun* 11:4516.

Schreck, R., and P.A. Baeuerle. 1990. NF-kappa B as inducible transcriptional activator of the granulocyte-macrophage colony-stimulating factor gene. *Mol Cell Biol* 10:1281-1286.

Schreiber, R.D., L.J. Old, and M.J. Smyth. 2011. Cancer immunoediting: integrating immunity's roles in cancer suppression and promotion. *Science* 331:1565-1570.

Sckisel, G.D., A. Mirsoian, C.M. Minnar, M. Crittenden, B. Curti, J.Q. Chen, B.R. Blazar, A.D. Borowsky, A.M. Monjazeb, and W.J. Murphy. 2017. Differential phenotypes of memory CD4 and CD8 T cells in the spleen and peripheral tissues following immunostimulatory therapy. *J Immunother Cancer* 5:33.

Shen, Z.T., and A.B. Sigalov. 2017. Novel TREM-1 Inhibitors Attenuate Tumor Growth and Prolong Survival in Experimental Pancreatic Cancer. *Mol Pharm* 14:4572-4582.

Shi, C., and E.G. Pamer. 2011. Monocyte recruitment during infection and inflammation. *Nat Rev Immunol* 11:762-774.

Siegel, R.L., K.D. Miller, and A. Jemal. 2020. Cancer statistics, 2020. *CA Cancer J Clin* 70:7-30.

Smith, S.L., P.R. Kennedy, K.B. Stacey, J.D. Worboys, A. Yarwood, S. Seo, E.H. Solloa, B. Mistretta, S.S. Chatterjee, P. Gunaratne, K. Allette, Y.C. Wang, M.L. Smith, R. Sebra, E.M. Mace, A. Horowitz, W. Thomson, P. Martin, S. Eyre, and D.M. Davis.

2020. Diversity of peripheral blood human NK cells identified by single-cell RNA sequencing. *Blood Adv* 4:1388-1406.

Solomon, B.L., and I. Garrido-Laguna. 2018. TIGIT: a novel immunotherapy target moving from bench to bedside. *Cancer Immunol Immunother* 67:1659-1667.

Steele, C.W., S.A. Karim, J.D.G. Leach, P. Bailey, R. Upstill-Goddard, L. Rishi, M. Foth, S. Bryson, K. McDaid, Z. Wilson, C. Eberlein, J.B. Candido, M. Clarke, C. Nixon, J. Connelly, N. Jamieson, C.R. Carter, F. Balkwill, D.K. Chang, T.R.J. Evans, D. Strathdee, A.V. Biankin, R.J.B. Nibbs, S.T. Barry, O.J. Sansom, and J.P. Morton. 2016. CXCR2 Inhibition Profoundly Suppresses Metastases and Augments Immunotherapy in Pancreatic Ductal Adenocarcinoma. *Cancer Cell* 29:832-845.

Steele, N.G., E.S. Carpenter, S.B. Kemp, V.R. Sirihorachai, S. The, L. Delrosario, J. Lazarus, E.-a.D. Amir, V. Gunchick, C. Espinoza, S. Bell, L. Harris, F. Lima, V. Irizarry-Negron, D. Paglia, J. Macchia, A.K.Y. Chu, H. Schofield, E.-J. Wamsteker, R. Kwon, A. Schulman, A. Prabhu, R. Law, A. Sondhi, J. Yu, A. Patel, K. Donahue, H. Nathan, C. Cho, M.A. Anderson, V. Sahai, C.A. Lyssiotis, W. Zou, B.L. Allen, A. Rao, H.C. Crawford, F. Bednar, T.L. Frankel, and M. Pasca di Magliano. 2020. Multimodal mapping of the tumor and peripheral blood immune landscape in human pancreatic cancer. *Nature Cancer* 1:1097-1112.

Storz, P. 2017. Acinar cell plasticity and development of pancreatic ductal adenocarcinoma. *Nat Rev Gastroenterol Hepatol* 14:296-304.

Strittmatter, W.J., A.M. Saunders, D. Schmechel, M. Pericak-Vance, J. Enghild, G.S. Salvesen, and A.D. Roses. 1993. Apolipoprotein E: high-avidity binding to beta-

amyloid and increased frequency of type 4 allele in late-onset familial Alzheimer disease. *Proc Natl Acad Sci U S A* 90:1977-1981.

Stromnes, I.M., J.S. Brockenbrough, K. Izeradjene, M.A. Carlson, C. Cuevas, R.M. Simmons, P.D. Greenberg, and S.R. Hingorani. 2014. Targeted depletion of an MDSC subset unmasks pancreatic ductal adenocarcinoma to adaptive immunity. *Gut* 63:1769-1781.

Stromnes, I.M., A. Hulbert, R.H. Pierce, P.D. Greenberg, and S.R. Hingorani. 2017. T-cell Localization, Activation, and Clonal Expansion in Human Pancreatic Ductal Adenocarcinoma. *Cancer Immunol Res* 5:978-991.

Stuart, T., and R. Satija. 2019. Integrative single-cell analysis. *Nat Rev Genet* 20:257-272.

Takeuchi, S., M. Baghdadi, T. Tsuchikawa, H. Wada, T. Nakamura, H. Abe, S. Nakanishi, Y. Usui, K. Higuchi, M. Takahashi, K. Inoko, S. Sato, H. Takano, T. Shichinohe, K. Seino, and S. Hirano. 2015. Chemotherapy-Derived Inflammatory Responses Accelerate the Formation of Immunosuppressive Myeloid Cells in the Tissue Microenvironment of Human Pancreatic Cancer. *Cancer Res* 75:2629-2640.

Tavazoie, M.F., I. Pollack, R. Tanqueco, B.N. Ostendorf, B.S. Reis, F.C. Gonsalves, I. Kurth, C. Andreu-Agullo, M.L. Derbyshire, J. Posada, S. Takeda, K.N. Tafreshian, E. Rowinsky, M. Szarek, R.J. Waltzman, E.A. McMillan, C. Zhao, M. Mita, A. Mita, B. Chmielowski, M.A. Postow, A. Ribas, D. Mucida, and S.F. Tavazoie. 2018. LXR/ApoE Activation Restricts Innate Immune Suppression in Cancer. *Cell* 172:825-840 e818.

Trovato, R., A. Fiore, S. Sartori, S. Cane, R. Giugno, L. Cascione, S. Paiella, R. Salvia, F. De Sanctis, O. Poffe, C. Anselmi, F. Hofer, S. Sartoris, G. Piro, C. Carbone, V. Corbo, R. Lawlor, S. Solito, L. Pinton, S. Mandruzzato, C. Bassi, A. Scarpa, V. Bronte, and S. Ugel. 2019. Immunosuppression by monocytic myeloid-derived suppressor cells in patients with pancreatic ductal carcinoma is orchestrated by STAT3. *J Immunother Cancer* 7:255.

Tsujikawa, T., S. Kumar, R.N. Borkar, V. Azimi, G. Thibault, Y.H. Chang, A. Balter, R. Kawashima, G. Choe, D. Sauer, E. El Rassi, D.R. Clayburgh, M.F. Kulesz-Martin, E.R. Lutz, L. Zheng, E.M. Jaffee, P. Leyshock, A.A. Margolin, M. Mori, J.W. Gray, P.W. Flint, and L.M. Coussens. 2017. Quantitative Multiplex Immunohistochemistry Reveals Myeloid-Inflamed Tumor-Immune Complexity Associated with Poor Prognosis. *Cell Rep* 19:203-217.

Turnbull, I.R., S. Gilfillan, M. Cella, T. Aoshi, M. Miller, L. Piccio, M. Hernandez, and M. Colonna. 2006. Cutting edge: TREM-2 attenuates macrophage activation. *J Immunol* 177:3520-3524.

van der Laan, L.J., E.A. Dopp, R. Haworth, T. Pikkarainen, M. Kangas, O. Elomaa, C.D. Dijkstra, S. Gordon, K. Tryggvason, and G. Kraal. 1999. Regulation and functional involvement of macrophage scavenger receptor MARCO in clearance of bacteria in vivo. *J Immunol* 162:939-947.

van der Leun, A.M., D.S. Thommen, and T.N. Schumacher. 2020. CD8(+) T cell states in human cancer: insights from single-cell analysis. *Nat Rev Cancer* 20:218-232.

Van Gassen, S., B. Callebaut, M.J. Van Helden, B.N. Lambrecht, P. Demeester, T. Dhaene, and Y. Saeys. 2015. FlowSOM: Using self-organizing maps for visualization and interpretation of cytometry data. *Cytometry A* 87:636-645.

Veglia, F., and D.I. Gabrilovich. 2017. Dendritic cells in cancer: the role revisited. *Curr Opin Immunol* 45:43-51.

Veglia, F., M. Perego, and D. Gabrilovich. 2018. Myeloid-derived suppressor cells coming of age. *Nat Immunol* 19:108-119.

Von Hoff, D.D., T. Ervin, F.P. Arena, E.G. Chiorean, J. Infante, M. Moore, T. Seay, S.A. Tjulandin, W.W. Ma, M.N. Saleh, M. Harris, M. Reni, S. Dowden, D. Laheru, N. Bahary, R.K. Ramanathan, J. Tabernero, M. Hidalgo, D. Goldstein, E. Van Cutsem, X. Wei, J. Iglesias, and M.F. Renschler. 2013. Increased survival in pancreatic cancer with nab-paclitaxel plus gemcitabine. *N Engl J Med* 369:1691-1703.

Vonderheide, R.H. 2018. The Immune Revolution: A Case for Priming, Not Checkpoint. *Cancer Cell* 33:563-569.

Waldman, A.D., J.M. Fritz, and M.J. Lenardo. 2020. A guide to cancer immunotherapy: from T cell basic science to clinical practice. *Nat Rev Immunol* 20:651-668.

Werb, Z., J.R. Chin, R. Takemura, R.L. Oropeza, D.F. Bainton, P. Stenberg, J.M. Taylor, and C. Reardon. 1986. The cell and molecular biology of apolipoprotein E synthesis by macrophages. *Ciba Found Symp* 118:155-171.

Wherry, E.J., S.J. Ha, S.M. Kaech, W.N. Haining, S. Sarkar, V. Kalia, S. Subramaniam, J.N. Blattman, D.L. Barber, and R. Ahmed. 2007. Molecular signature of CD8+ T cell exhaustion during chronic viral infection. *Immunity* 27:670-684.

Winograd, R., K.T. Byrne, R.A. Evans, P.M. Odorizzi, A.R. Meyer, D.L. Bajor, C. Clendenin, B.Z. Stanger, E.E. Furth, E.J. Wherry, and R.H. Vonderheide. 2015. Induction of T-cell Immunity Overcomes Complete Resistance to PD-1 and CTLA-4 Blockade and Improves Survival in Pancreatic Carcinoma. *Cancer Immunol Res* 3:399-411.

Wong, K.L., J.J. Tai, W.C. Wong, H. Han, X. Sem, W.H. Yeap, P. Kourilsky, and S.C. Wong. 2011. Gene expression profiling reveals the defining features of the classical, intermediate, and nonclassical human monocyte subsets. *Blood* 118:e16-31.

Wynn, T.A., A. Chawla, and J.W. Pollard. 2013. Macrophage biology in development, homeostasis and disease. *Nature* 496:445-455.

Xu, J., H. Sai, Y. Li, A.C. Jordan, S.E. McGettigan, J.H. Chen, F. Bedoya, J.A. Fraietta, W.L. Gladney, J.J. Melenhorst, and G.L. Beatty. 2019. Peripheral Blood T-Cell Fitness Is Diminished in Patients With Pancreatic Carcinoma but Can Be Improved With Homeostatic Cytokines. *Cell Mol Gastroenterol Hepatol* 8:656-658 e656.

Yamamoto, T., H.W. Choi, and R.O. Ryan. 2008. Apolipoprotein E isoform-specific binding to the low-density lipoprotein receptor. *Anal Biochem* 372:222-226.

Youn, J.I., S. Nagaraj, M. Collazo, and D.I. Gabrilovich. 2008. Subsets of myeloid-derived suppressor cells in tumor-bearing mice. *J Immunol* 181:5791-5802.

Yu, X., K. Harden, L.C. Gonzalez, M. Francesco, E. Chiang, B. Irving, I. Tom, S. Ivelja, C.J. Refino, H. Clark, D. Eaton, and J.L. Grogan. 2009. The surface protein TIGIT suppresses T cell activation by promoting the generation of mature immunoregulatory dendritic cells. *Nat Immunol* 10:48-57.

Zhang, Q., J. Bi, X. Zheng, Y. Chen, H. Wang, W. Wu, Z. Wang, Q. Wu, H. Peng, H. Wei, R. Sun, and Z. Tian. 2018. Blockade of the checkpoint receptor TIGIT prevents NK cell exhaustion and elicits potent anti-tumor immunity. *Nat Immunol* 19:723-732.

Zhang, Q., Y. He, N. Luo, S.J. Patel, Y. Han, R. Gao, M. Modak, S. Carotta, C. Haslinger, D. Kind, G.W. Peet, G. Zhong, S. Lu, W. Zhu, Y. Mao, M. Xiao, M. Bergmann, X. Hu, S.P. Kerkar, A.B. Vogt, S. Pflanz, K. Liu, J. Peng, X. Ren, and Z. Zhang. 2019a. Landscape and Dynamics of Single Immune Cells in Hepatocellular Carcinoma. *Cell* 179:829-845 e820.

Zhang, Q., M.J. Lenardo, and D. Baltimore. 2017a. 30 Years of NF-kappaB: A Blossoming of Relevance to Human Pathobiology. *Cell* 168:37-57.

Zhang, R., Q. Liu, J. Peng, M. Wang, X. Gao, Q. Liao, and Y. Zhao. 2019b. Pancreatic cancer-educated macrophages protect cancer cells from complement-dependent cytotoxicity by up-regulation of CD59. *Cell Death Dis* 10:836.

Zhang, Y., H.C. Crawford, and M. Pasca di Magliano. 2019c. Epithelial-Stromal Interactions in Pancreatic Cancer. *Annu Rev Physiol* 81:211-233.

Zhang, Y., J. Lazarus, N.G. Steele, W. Yan, H.J. Lee, Z.C. Nwosu, C.J. Halbrook, R.E. Menjivar, S.B. Kemp, V.R. Sirihorachai, A. Velez-Delgado, K. Donahue, E.S. Carpenter, K.L. Brown, V. Irizarry-Negron, A.C. Nevison, A. Vinta, M.A. Anderson, H.C. Crawford, C.A. Lyssiotis, T.L. Frankel, F. Bednar, and M. Pasca di Magliano. 2020. Regulatory T-cell Depletion Alters the Tumor Microenvironment and Accelerates Pancreatic Carcinogenesis. *Cancer Discov* 10:422-439.

Zhang, Y., A. Velez-Delgado, E. Mathew, D. Li, F.M. Mendez, K. Flannagan, A.D. Rhim, D.M. Simeone, G.L. Beatty, and M. Pasca di Magliano. 2017b. Myeloid cells are

required for PD-1/PD-L1 checkpoint activation and the establishment of an immunosuppressive environment in pancreatic cancer. *Gut* 66:124-136.

Zhang, Y., W. Yan, E. Mathew, F. Bednar, S. Wan, M.A. Collins, R.A. Evans, T.H. Welling, R.H. Vonderheide, and M.P. di Magliano. 2014. CD4+ T lymphocyte ablation prevents pancreatic carcinogenesis in mice. *Cancer Immunol Res* 2:423-435.

Zhang, Y., W. Yan, E. Mathew, K.T. Kane, A. Brannon, 3rd, M. Adoumie, A. Vinta, H.C. Crawford, and M. Pasca di Magliano. 2017c. Epithelial-Myeloid cell crosstalk regulates acinar cell plasticity and pancreatic remodeling in mice. *Elife* 6:

Zhou, Q., X. Tao, S. Xia, F. Guo, C. Pan, H. Xiang, and D. Shang. 2020. T Lymphocytes: A Promising Immunotherapeutic Target for Pancreatitis and Pancreatic Cancer? *Front Oncol* 10:382.

Zhu, Y., J.M. Herndon, D.K. Sojka, K.W. Kim, B.L. Knolhoff, C. Zuo, D.R. Cullinan, J. Luo, A.R. Bearden, K.J. Lavine, W.M. Yokoyama, W.G. Hawkins, R.C. Fields, G.J. Randolph, and D.G. DeNardo. 2017. Tissue-Resident Macrophages in Pancreatic Ductal Adenocarcinoma Originate from Embryonic Hematopoiesis and Promote Tumor Progression. *Immunity* 47:323-338 e326.

Zhu, Y., B.L. Knolhoff, M.A. Meyer, T.M. Nywening, B.L. West, J. Luo, A. Wang-Gillam, S.P. Goedegebuure, D.C. Linehan, and D.G. DeNardo. 2014. CSF1/CSF1R blockade reprograms tumor-infiltrating macrophages and improves response to T-cell checkpoint immunotherapy in pancreatic cancer models. *Cancer Res* 74:5057-5069.

Zimmerman, K.A., M.R. Bentley, J.M. Lever, Z. Li, D.K. Crossman, C.J. Song, S. Liu, M.R. Crowley, J.F. George, M. Mrug, and B.K. Yoder. 2019. Single-Cell RNA

Sequencing Identifies Candidate Renal Resident Macrophage Gene Expression Signatures across Species. *J Am Soc Nephrol* 30:767-781.